U.S. Department of Energy - National Energy Technology Laboratory

Final Technical Report
Report Number: DOE-REI-29162-1

DOE Cooperative Agreement No: DE-FE0029162

Characterizing Impacts of Dry Coal Feeding
in High Pressure Oxy-Coal Combustion Systems

Principal Investigator
Kevin A. Davis, Ph.D.
Senior Principal and Co-President
davis@reaction-eng.com
801-364-6925 ext. 23

Submitting Official
Andrew P. Chiodo
Project Manager and Engineer
chiodo@reaction-eng.com
801-364-6925 ext. 46

December 23, 2022

DUNS Number: 612498220

Reaction Engineering International
189 E. Fort Union Blvd., Suite 201
Midvale, UT 84047

Project Period of Performance: October 1, 2016 – September 30, 2022

Signature of Submitting Official: Andrew P. Chiodo

AKNOWLEDGEMENT

This material is based upon work supported by the Department of Energy, National Energy Technology Laboratory, under Award Number DE-FE0029162.

DISCLAIMER

TABLE OF CONTENTS

TABLE OF FIGURES

LIST OF TABLES

ABSTRACT

Reaction Engineering International (REI) has managed a team of experts from the University of Utah, Southeast University (SEU) in Nanjing, China, Electric Power Research Institute (EPRI), Corrosion Management Ltd. (C-M), Praxair, and Brigham Young University (BYU) to investigate dry pulverized coal feeding for pressurized oxy-coal combustion. Dry feed firing systems for entrained flow, pressurized, oxy-coal combustors have not been well developed, although related technologies have been used in the Shell Gasification Process and for pressurized fluid bed combustion. DOE-funded research recently completed at REI and the University of Utah focused on characterizing impacts of high temperatures and pressures in oxy-coal combustion systems. For high pressure combustion, that research used a coal slurry feed into a 17 bar pressurized combustor. As a consequence of that research, it was identified that fuel feeding and firing system flexibility are challenges that require attention. Based on that experience, the approach of using a coal slurry feed system leads to challenges in producing consistent atomization of the slurry, which causes burnout problems, especially at high pressures. In addition, slurry atomization processes may be difficult to scale to sizes appropriate for practical commercial use. Dry pressurized coal burner systems, on the other hand, have the potential to yield efficiency gains, improve flexibility and facilitate applications at larger scales.

Experimental work was conducted at the University of Utah Industrial Combustion and Gasification Research Facility as well as the 100 kW pressurized oxy-coal combustor (POC) facility at Brigham Young University. Mechanism development and CFD-based combustion and dense-phase flow modeling were performed at REI.

Successful completion of the project objectives has resulted in the following key deliverables:

1) Design and prototype of a pressurized pulverized coal feeding and oxy-firing system
2) Data from a 100kW, pressurized (15 bar) entrained flow reactor with a dry feeding delivery and burner system that describes flame characteristics, radiative heat flux profiles, carbon burnout, along with characteristics of ash aerosols, fouling, and slagging.
3) Validated and transportable models that describe the relevant conditions in pressurized oxy-combustion systems and that can be used for scale-up and optimization.
4) Principles to guide design of high pressure, pilot-scale and full-scale coal oxy-firing systems.
5) Assessment of pressurized oxy-combustion impacts on key parameters relevant to oxy-coal fired utility boilers such as coal devolatilization, char oxidation, mineral matter transformation, deposition, and corrosion.

The experimental data, pressurized oxy-firing system principles, and process mechanisms provided by this work can be used by electric utilities, boiler OEMs, equipment suppliers, design firms, software vendors, consultants and government agencies to assess the use of high temperature and high pressure oxy-combustion in current research and to guide development of new oxy-coal boiler designs.

INTRODUCTION

The future use of coal as a fuel for power generation in the US depends on the availability of financially viable technologies for capture and storage of CO_2 emissions from power plants. The first-generation candidates for CO_2 capture technology includes oxy-firing of coal applied to existing units, using flue gas recycle (FGR) to regulate flame temperatures. Key second generation candidates for CO_2 capture include pressurized oxy-firing of coal. Application of this technology to steam generation is promising because of their potential to increase efficiency, lower capital costs, avoid air ingress and reduce oxygen requirements.

This project, directed towards the future commercialization of a second generation pressurized oxy-coal combustion process and comprises an expansion of a preceding DOE Cooperative Agreement No: DE-FE0025168 entitled "Characterizing Impacts of High Temperatures and Pressures in Oxy-Coal Combustion"[1]. Whereas that project was divided into research on high temperature, minimum recycle, atmospheric oxy-coal combustion processes and high temperature, high pressure, coal slurry fed oxy-coal combustion processes, this project focused solely on high pressure, dry pulverized coal fed, oxy-coal combustion processes. The preceding work relied upon a coal slurry feed and burner system primarily because that is the approach used by most commercial high pressure pulverized coal conversion systems. However, this work was motivated by the assertion that it is critically important to extend the slurry fed approach to dry feed conditions because:

1) There are efficiency gains to be obtained by eliminating the water introduced with the coal slurry.
2) There are challenges related to coal slurry atomization and carbon burnout with the slurry injection.
3) Poor atomization under pressurized conditions will have effects on ash aerosol size distribution and hence ash deposition rates.
4) Coal slurry atomization processes do not easily lend themselves to scale up, especially under pressurized conditions.
5) Burner designs and the accompanying near field burner aerodynamics can be scaled up more easily for dry feed systems than for wet slurry feed systems, primarily because the slurry atomization/evaporation/dispersion phenomena are not well understood at pressurized conditions.

This project produced data used to describe (1) performance of dry pulverized coal feeding systems designed for pressurized conditions as well as applicability over a range of conditions and (2) pressurized oxy-coal combustion with a dry feed. The first step in the research was to determine a dry feed system design appropriate for the scale of the program's experimental combustion facilities. The next step was to perform "cold" tests where the capabilities of dry feed system design were evaluated for consistency and reliability in coal transport. Finally, combustion experiments were performed to understand the combustion environment created when dry pulverized coal is fed into a pressurized combustor. The impacts determined are on a) flame stability and radiative heat transfer as a function of flame aerodynamics, b) ash

transformation as functions of pressure and coal composition, and c) high temperature corrosion on metal surfaces typically used in industrial furnaces.

The primary goal of the program involved coupling experiments with development of mechanisms suitable for inclusion in CFD models or process models. The data and tools produced were focused on characterization of flame behavior, heat transfer, ash deposition, ash chemistry, coal devolatilization, char oxidation, and corrosion under pressurized oxy-coal combustion conditions. These aspects must be understood and controlled to enable application of pressurized oxy-combustion in full-scale systems.

The project team included personnel from Reaction Engineering International (REI), the University of Utah, Brigham Young University, Southeast University in Nanjing, China, Electric Power Research Institute, Corrosion Management Ltd. and Praxair. Experimental work on dry pulverized coal feed system technology was performed at the University of Utah's Industrial Combustion and Gasification Research Facility (ICGRF) while dry-fed pressurized oxy-coal combustion experiments were performed in the 100 kW pressurized oxy combustor at Brigham Young University. The experiments with dry feed systems at the University of Utah and Brigham Young University were devised to determine dry feed system design specifications and operating parameters to produce stable and consistent coal feed rates in a pressurized environment. The combustion experiments were designed to provide a comprehensive data set describing heat release profiles, material temperatures, mineral matter behavior, and high temperature corrosion under elevated temperature and high pressure flames generated by oxygen combustion of dry-fed pulverized coal.

The work conducted in this project received funding from the Department of Energy under cooperative agreement No: DE-FE0029162 with a performance period that began on October 1, 2016 and concluded on September 30, 2022.

ACCOMPLISHMENTS

Major goals of the project

The major goals of this project are to conduct pilot-scale experiments of coal oxygen combustion in a pressurized reactor with a dry pulverized coal feed and couple the results with the development of mechanisms tailored for CFD and process modeling tools. The data and tools generated during the project will be capable of characterizing flame behavior, heat transfer, ash deposition, ash chemistry, char oxidation, and corrosion of furnace surfaces under high temperature pressurized oxy-coal combustion.

Accomplishments under the goals

This report is comprised of detailed discussions of the project's technical tasks. The report is broken into sections describing the accomplishments in each of the following technical tasks:

- Task 2. Design, construction and shakedown of a dry feeding system
- Task 3. Pressurized Reactor Preparation
- Task 4. Design, Installation, and Testing of Pressurized Oxy-coal Burner
- Task 5. Pressurized Oxy-coal Testing with Dry Feed
- Task 6. Model Extension and Validation

A tabulation of all project tasks along with a brief description is shown in Table 1.

Table 1. Project Tasks in *Characterizing Impacts of Dry Coal Feeding in High Pressure Oxy-Coal Combustion Systems*

Task Number	Task Title	Description	Comment
1	Program Management and Reporting	Coordinate and manage the overall work effort	**Task Completed**: All contractually required reports and forms were prepared and distributed in the required formats
2	Design, Construction and Shakedown of a Dry Feeding System	Design, construct, test, and integrate dry feed system into pressurized combustor	**Task Completed**: Design completed, system constructed, system performance test results interrogated
3	Pressurized Reactor Preparation	Modify, as necessary, the instrumentation and flue gas handling equipment for use in the proposed high pressure oxy-coal combustion conditions	**Task Completed**: Reactor modifications complete and furnace ready for pressurized oxy coal combustion testing
4	Design, Installation, and Testing of Pressurized Oxy-coal Burner	Leverage existing models and experience to design burner	**Task Completed**: CFD simulations of entrained flow pressurized reactor (EFPR) completed. Simulations to guide burner design complete.
5	Pressurized Oxy-coal Testing with Dry Feed	Conduct pressurized oxy-coal combustion experiments with a dry feed and characterize heat flux, particle/deposition, and corrosion	**Task Completed**: Testing in the BYU pressurized oxy-coal (POC) system completed

Task Number	Task Title	Description	Comment
6	Model Extension and Validation	Validate the applicability of the model across a range of scales ensuring that the model can be used with confidence in extension to full-scale applications.	**Task Completed**: High pressure char combustion data used to validate the Chemical Percolation Devolatilization (CPD) model implementation into REI's CFD modeling tools

Task 2 – Design, construction and shakedown of a dry feeding system

Objective: Design, construct and operate a dry pulverized coal feed system for pressurized combustion

Subtask 2.1 – Design and construction of three-hopper pulverized coal feeder

Project partner Southeast University (SEU) developed an initial design for the pulverized coal dry feed system based on design specifications from the University of Utah (UofU). The new pressurized dry feed system built under this program was critical to successful operation and data acquisition, not only for the specific pilot-scale system being used in this program but also as proof-of-concept for larger-scale pressurized oxy-coal systems. Although SEU has demonstrated controlled feed of coal powder under pressurized conditions for gasification applications using a similar design, this would be the first time that this design would be used for oxy-coal combustion.

The design shown in Figure 1 centered on a cone-shaped pressure vessel approximately 5 feet high and 2 feet diameter. The vessel serves both as the fuel hopper and as an integral part of the feed system. Three pressurized gas lines carrying CO_2 are used to pneumatically convey the pulverized fuel and balance the pressure around the system. At the bottom of the cone taper, fluidizing gas passes through a distributor mounted inside the vessel to locally fluidize the fine coal powder. The primary coal feed tube extends from the top of the vessel down to just above the distributor where the coal in its fluidized state is swept into the narrow-diameter tube and out of the vessel. A higher flow of supplementary gas is mixed with the primary coal feed to dilute the flow and increase the velocity to ensure stable, plug-free flow as the coal is conveyed to the burner of the reactor. A visualization chamber and a special flowmeter developed by SEU is installed on the transport line to the reactor for system control and troubleshooting. A third independent gas line is connected to the top of the hopper to maintain pressure within the system.

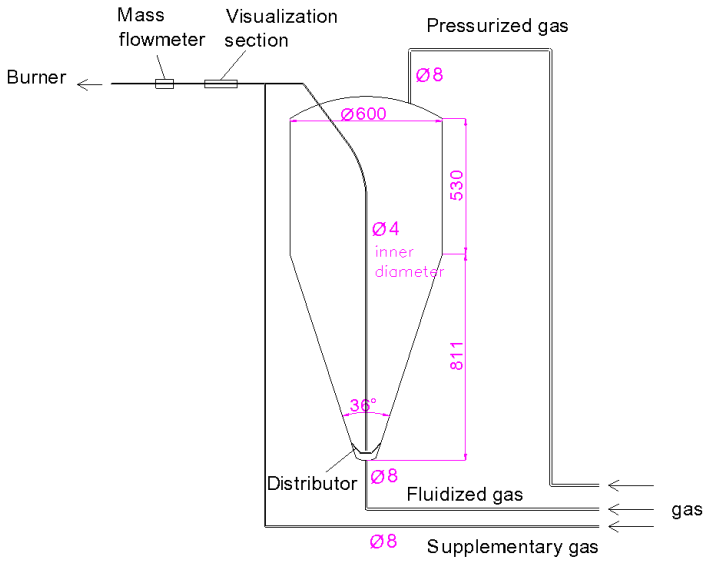

Figure 1. Design of pressurized dry feed system for University of Utah EFPR system. Dimensions shown are in millimeters.

The initial design called for a single hopper, which was sized to allow for approximately six hours of continuous operation. To achieve continuous operation, multiple hoppers are configured in parallel with one in use for feeding while the others are either being refilled or maintained. Multiple hoppers also offer flexibility when testing different fuel types. SEU operates a multiple hopper feed system in their dense phase conveying test facility in Nanjing, China as shown in Figure 2.

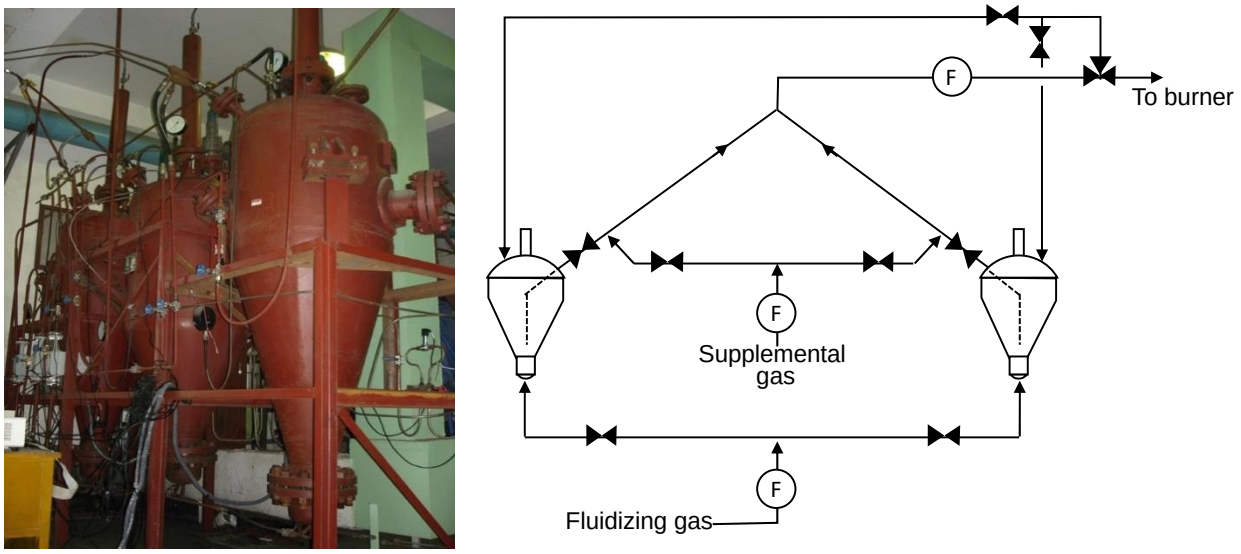

Figure 2. Multiple-hopper pulverized coal feed system (left) at SEU dense phase conveying test facility and schematic for 2-hopper continuous feed system (right).

At the onset of the program, it was determined that tests would be performed with the single-hopper system to confirm that coal could be fed controllably and with little interruption before any additional hoppers would be considered for the University of Utah system. Any design changes deemed necessary would be incorporated into the newer hoppers as they are introduced into the system.

In accordance with the SEU design of a single fluidization hopper, CAD design drawings were generated. Component sizing and materials selection were performed in conjunction with the design drawings. The design constructed for the University of Utah is shown in Figure 3.

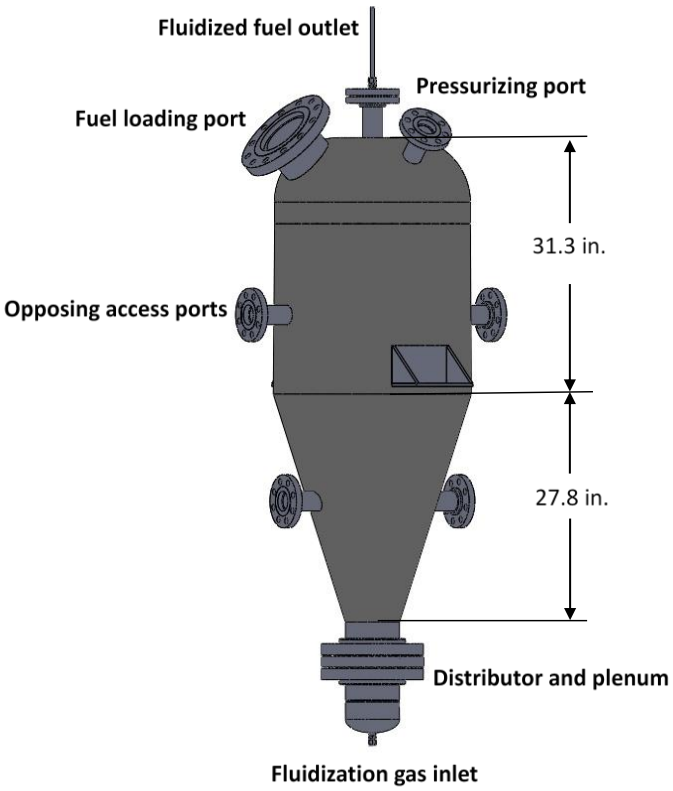

Figure 3. Design of pressurized dry feed system hopper for University of Utah EFPR system.

The ports for the opposing access, pressurizing and fuel outlet are comprised of 2 inch class 300 flanges. The fuel loading port is an 8 inch class 300 flange. The distributor and plenum section are assembled from 6 inch class 300 flanges and 6 inch pipe. The fluidization gas into the plenum and the fluidized fuel out of the top of the hopper are through 0.5 inch stainless steel tube with 0.049 inch wall thickness. Unless otherwise stated, materials for the hopper are schedule 80 carbon steel or the equivalent thereof. The hopper assembly was fabricated locally by a company licensed in pressure vessel assembly and professionally stamped as such. The plenum and distributor section dimensions are less than the 6 inch ID required for a pressure vessel stamp and hydrostat rating.

Cutaway views for the hopper and the distributor and plenum section are shown in Figure 4. A 0.5 inch fluidized fuel transfer tube extends through the top of the hopper and terminates in the zone of local fluidization, just above the sintered distributor cup.

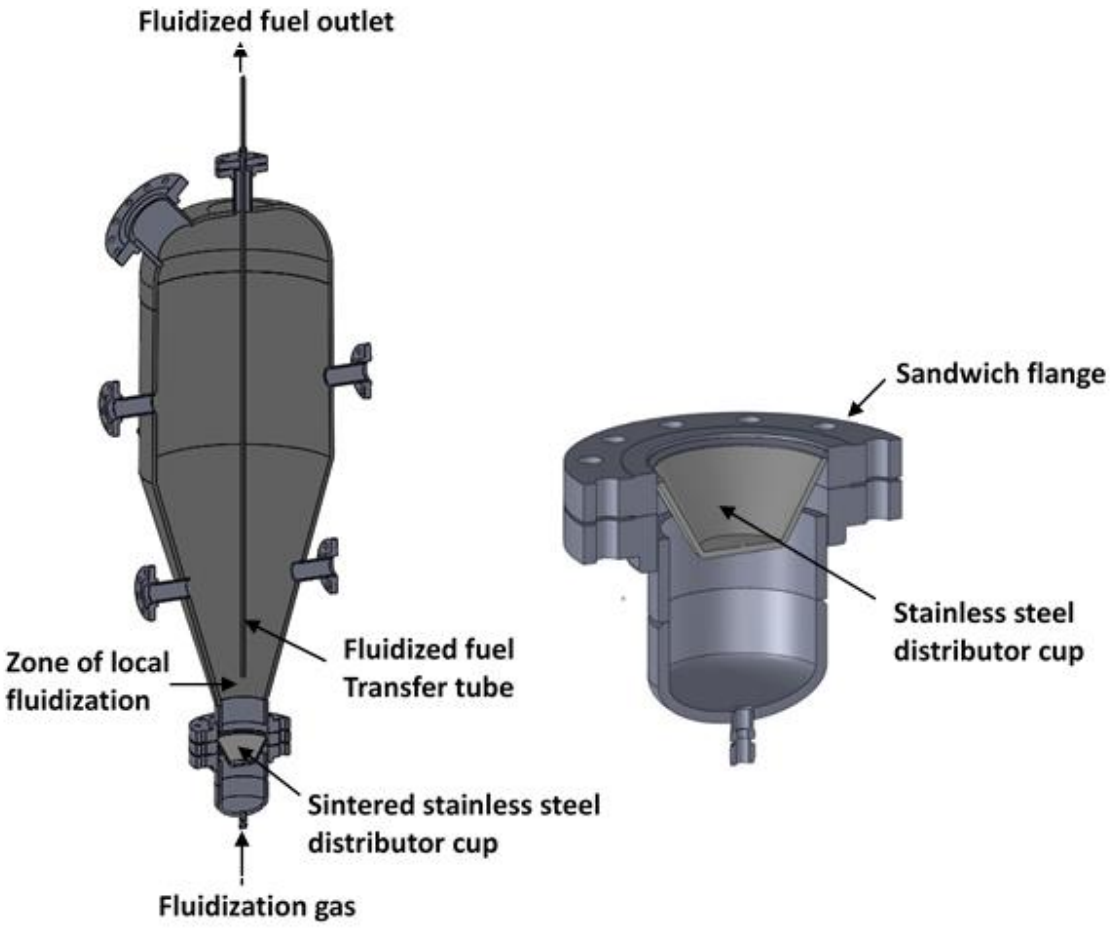

Figure 4. Cutaway views of fluidization hopper and plenum and distributor section

The initial design of the fluidized feeder body was sent out to relevant parties for final approval. Two 1 inch flanged ports were added to the top of the vessel. Once given an ASME pressure stamp, modifications would have to be performed by the original fabricators. These ports were added for access to the vessel to address unanticipated events and troubleshooting. The location and geometry of these ports are shown in Figure 5 and Figure 6.

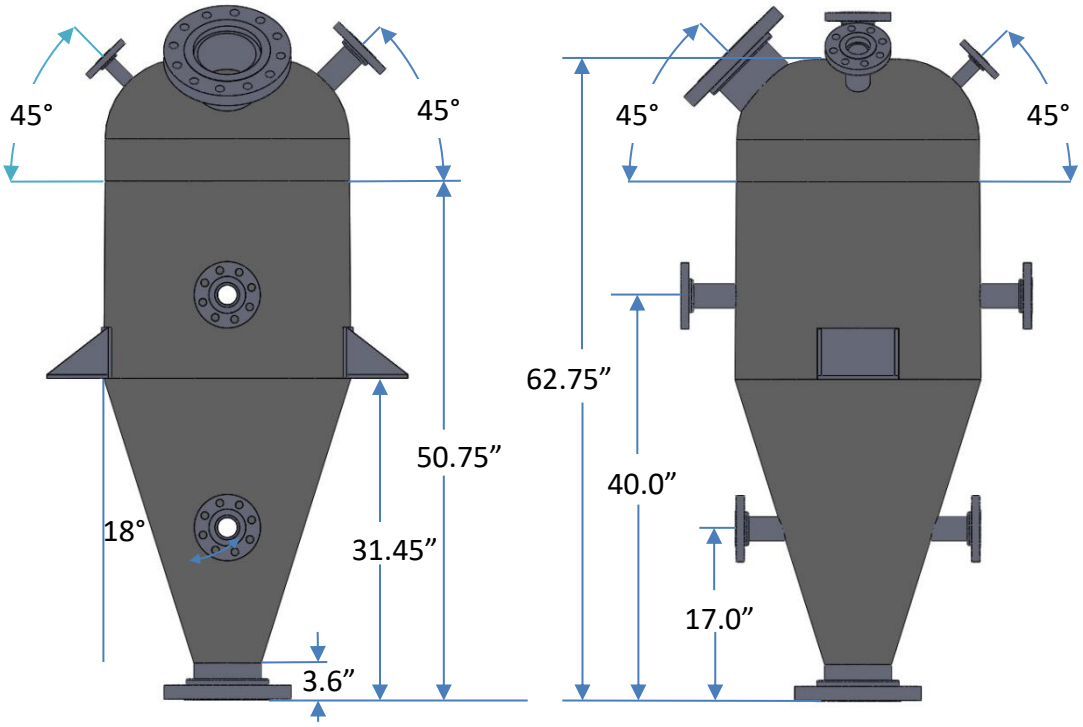

Figure 5. Final design of fluidized feeder body sent out for fabrication.

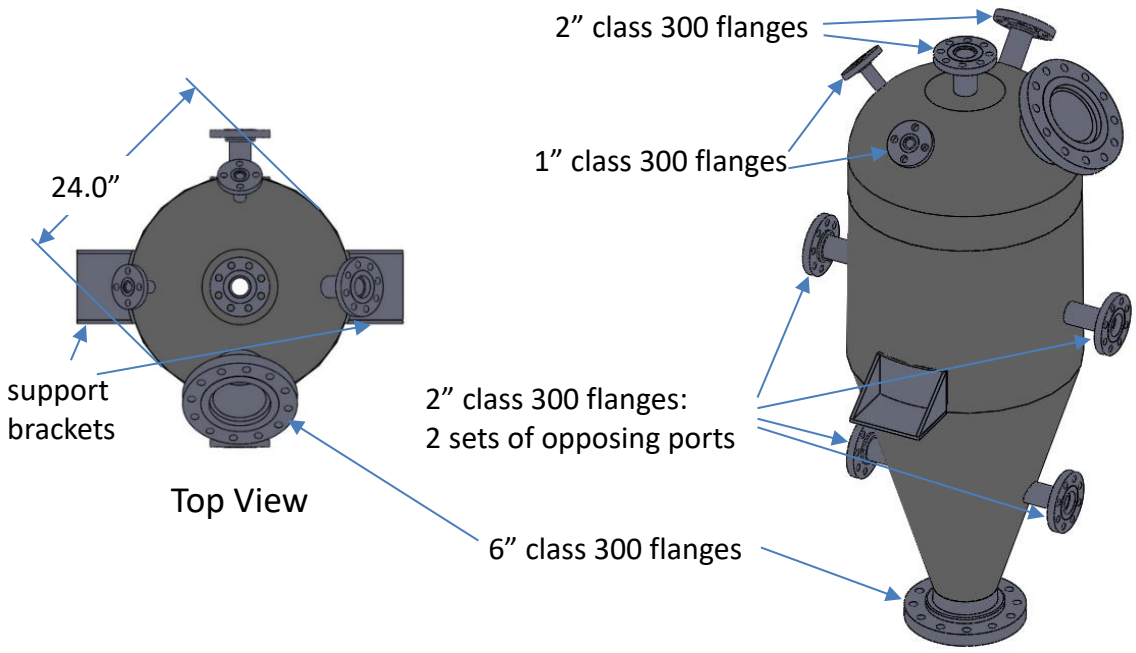

Figure 6. Port location and dimensions for fluidized feeder body

The initial design of the support structure for the porous stainless-steel distributor cup involved welding the cup in a flange sandwiched between the bottom flange of the fluidized feeder body and plenum section. Project partner SEU was tasked with fabricating the cup assembly. Owing to the lack of uniformity of commonly available pipe and flanges between the University of Utah and SEU, the design of the cup support assembly is the original SEU configuration shown in Figure 7. The figure shows cutaway views of the cup and support assembly, as well as the placement in the plenum while the photograph in Figure 8 shows the completed distributor cup assembly.

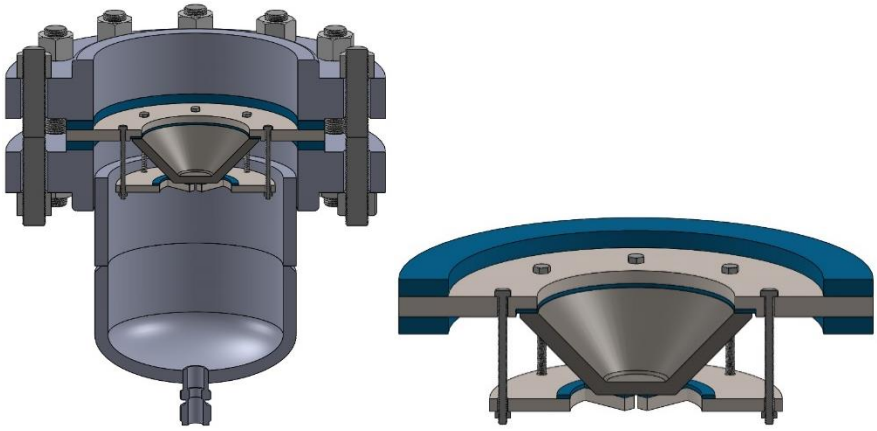

Figure 7. Distributor cup assembly and position in plenum

Figure 8. Completed distributor cup assembly

Mass flow controllers (MFC) for the fluidization and supplemental gases were acquired and the location of these components is shown in the Figure 9 P&ID. The visualization section indicated in the diagram and shown in Figure 10 was fabricated and delivered by SEU. The visualization window allows for observation of flow patterns in dense-phase conveying.

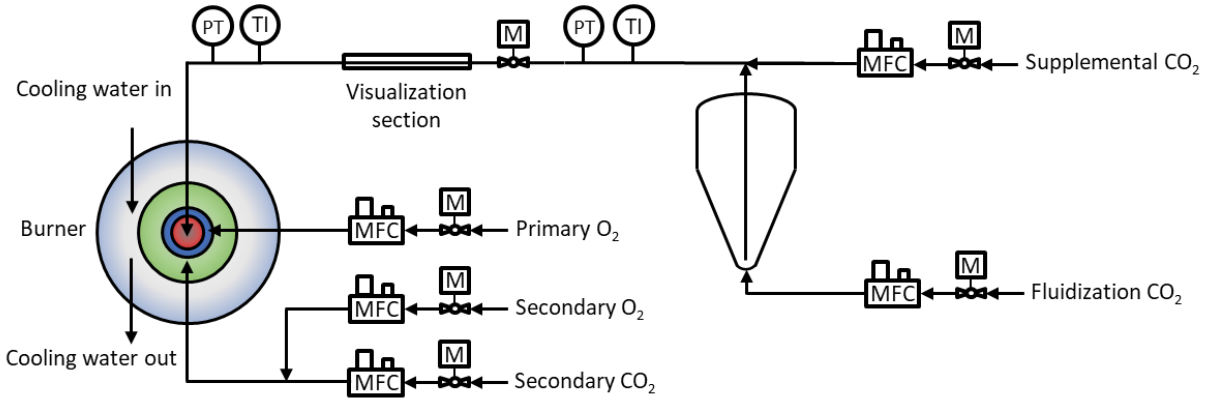

Figure 9. Preliminary P&ID for the dry feeding system in the 300 kW EFPR

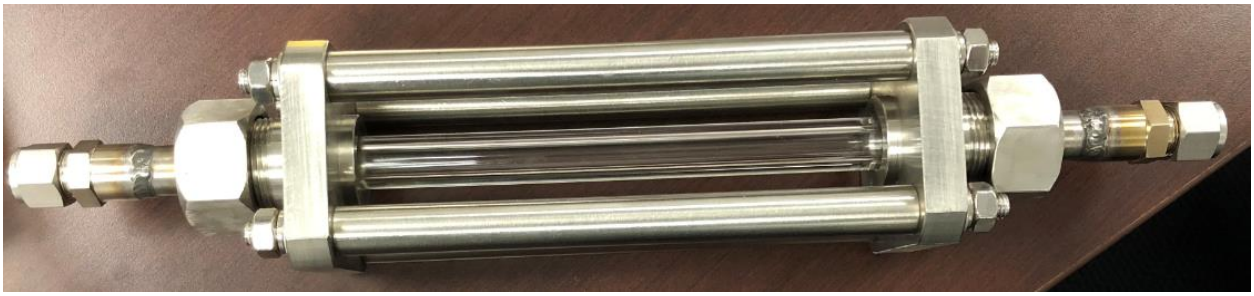

Figure 10. Visualization section for identification of dense-phase solid-gas flow patterns

The mass flow meters for the CO_2 microbulk tank were tested and verified to perform according to factory calibrations. A persistent issue with the mass flow control of the fluidization CO_2 line complicated the pressurization of the dry feed hopper. An undesirable design feature of the mass flow controller is that the mass flow meter closes when a pressure drop of 8 bar (116 psi) exists across it. This cap on pressure drop led to difficulties bringing the hopper up to the desired pressure. A resolution to this is illustrated in Figure 11 and involves routing the fluidizing CO_2 through a three-way solenoid to a back-pressure regulator that maintains a pressure drop below 8 bar across the mass flow controller as the hopper is brought to the desired pressure. Once the hopper reaches the pressure setpoint on the regulator, the solenoid is switched to a line with no regulator. At that point, finer control of the fluidization CO_2 proceeds unimpeded.

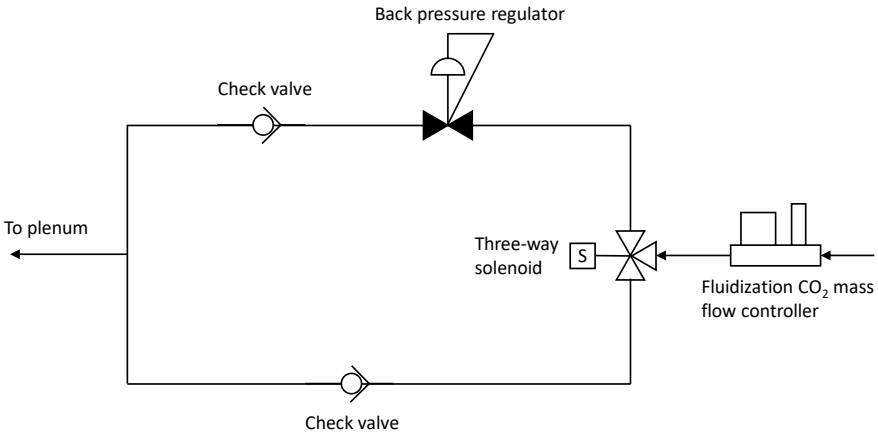

Figure 11. Modification to address pressure drop cap on fluidization CO_2 mass flow controller.

An important design feature of the dry feed system involves the capability to finely tune and maintain the pressure drop between the feed hopper and the reactor. In migrating the SEU design to the University of Utah system, a mass flow meter for pressurization gas was eliminated with the belief that the hopper to reactor pressure drop could be controlled with additional supplemental CO_2. This is not the case. Initial design drawings excluded the existence of an exhaust port, sized such that an input of CO_2 through the pressurization line maintains the pressure in the hopper to allow for precise control of fuel transport. Discussions with SEU led to the selection of an appropriately sized pressurizing CO_2 mass flow controller for the exhaust port specifications. In addition, a small baghouse was installed downstream of the exhaust port to collect particulate entrained in the exhaust gas.

In an attempt to simulate pressurized conditions and shakedown the coal feed process, the fuel line from the feed hopper was connected to a high pressure filter with a large surface area. A back pressure regulator set to appoximately 17 bar was placed on the outlet of the filter housing. Tests at atmospheric pressure were carried out using flow rates adjusted for the gas density under a high pressure regime. Fuel flow rates as a function of pressure drop were determined during the tests and results were reproducible.

A bridge connecting the fluidized hopper and the reactor is shown in Figure 12. The bridge contains the safety fuel shutoff valve, high pressure nitrogen purge lines for pressure transducers, shop compressed air for pneumatic components and signal wire for thermocouples and transducers. The hopper positioned adjacent to the reactor and not visible in the figure weighs approximately 1,400 lb when fully loaded with coal. Load cells installed on the feed hopper with a collective range of 2,000 lb allow for a measurement of the coal feed rate, which could be resolved to within 7 lb/h by utilizing an averaging table in the OPTO 22 control system and adjusting the reporting intervals.

Figure 12. Instrumentation and fuel line bridge

Once the dry feed system was fully assembled, initial tests were completed to characterize coal transport by CO_2 carrier gas. The initial test of conveying pulverized Utah Sufco coal from the new feed hopper of the pressurized entrained flow reactor system into an ambient environment (Figure 13) confirmed basic operation of the hopper system. The tests were carried out at different hopper pressures to allow a range of coal flow rates, yielding coal feeding rates from 25 to 300 lb/hr, as shown in Table 2. Although operating variables were expected to differ for feed to a high pressure reactor, these initial tests were a necessary first step toward the development of protocols for controlling coal flow from the hopper to the high pressure reactor. The purpose of these tests was to observe how the fluidized bed feeding system functioned and acquire an understanding of effective approaches for controlling the dry coal feed rates. In general, these tests were successful and showed that this dry feeding system holds promise.

Figure 13. Coal transport into ambient environment

Table 2. Coal feeding rates in initial testing of dry feed system

Coal feeding rate (lb/hr)	Pressure drop (psi)	Fluidization CO_2 flow rate (lb/hr)	Supplemental CO_2 flow rate (lb/hr)
25	1.9	5	16
40	2.3	5	16
90	3.4	5	16
300	9.0	5	16

Although the flow rates of the fluidization and supplemental CO_2 were not at design values and the downstream environment was not pressurized, this test clearly indicated that the coal feeding rate is determined by the pressure drop along the transport line as determined by the hopper pressure. Operational experience from SEU also confirmed that the pressure difference is the most critical factor affecting coal feeding rate.

Based on communications with SEU, a revised pressure control configuration on the dry-feeding system was proposed and is shown in Figure 14. The pressurized gas line shown is used to build up and maintain the hopper pressure. The pressure difference between the hopper and the combustor measured by a pressure difference transducer (dP) along with the hopper pressure monitored by a pressure transducer (P), provide the feedback signals on flow control of the pressurized gas. The exhaust line with a dust filter is used only when the hopper pressure needs to be reduced or quickly released. A coiled tube between the hopper and reactor was added to produce a suitable pressure drop to achieve stable coal transport.

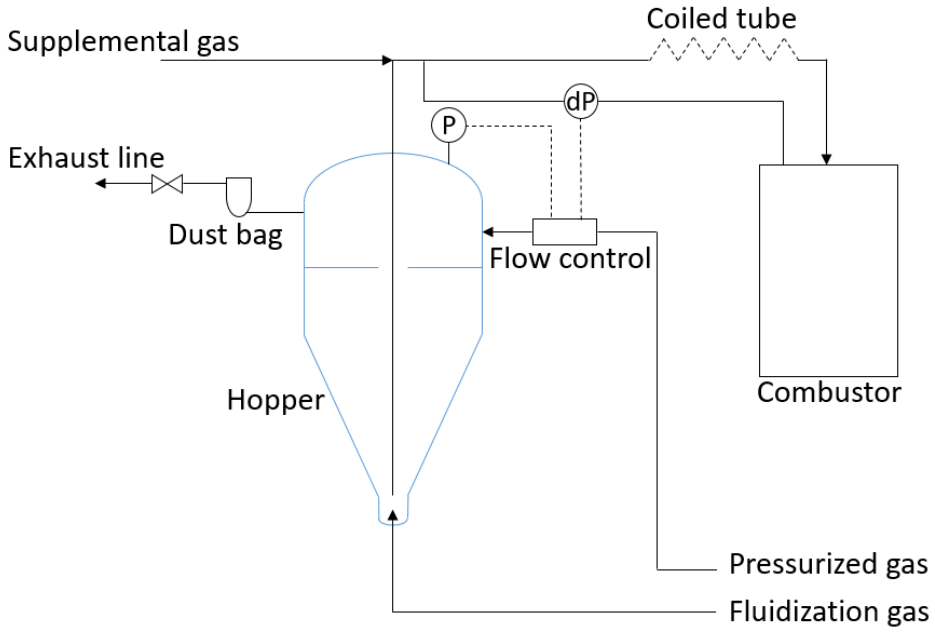

Figure 14. Proposed feeding system revision

To have a thorough understanding of the pressure drop induced by the coiled tube between the feed hopper and the EFPR combustor, pressure tests were conducted. A pressure gauge was initially used to measure pressure upstream the coil at atmospheric pressure. Then a differential pressure transducer with a range of 27 psi and a pressure transducer with range of 725 psi were installed and connected to the OPTO 22 distributed control system.

The test system is shown in Figure 15. The coil was made of 3/8" tube with a total length of 50 feet. A mass flow controller (MFC) controlled the flow rate of CO_2 gas. A regulator was installed on the outlet of the coil to adjust the back pressure, which represents the high pressure that would be observed in the combustor. For these tests, CO_2 downstream of the backpressure regulator was released to the atmosphere. The pressure transducer measured the downstream pressure and the differential pressure transducer measured the pressure drop.

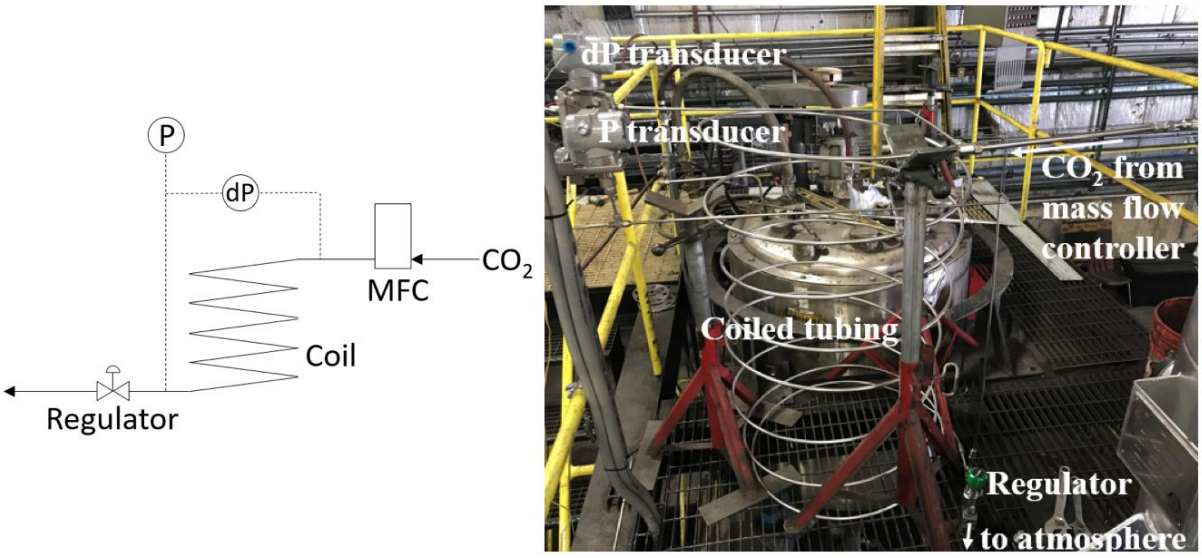

Figure 15. Pressure-drop test set-up

Theoretical pressure drops were calculated using Darcy-Weisbach equation:

$$\Delta p = f_D \cdot \frac{\rho v^2}{2} \cdot \frac{L}{D} \quad (1)$$

where f_D is the Darcy friction factor.

With the CO_2 flow rate ranging from 60 to 600 SLPM, the pressure drops over the 50 feet of coiled tube versus flow rate were obtained. The back pressure was set from 0 psig (without the downstream regulator) to 280 psig. Test results are plotted alongside calculated values in Figure 16.

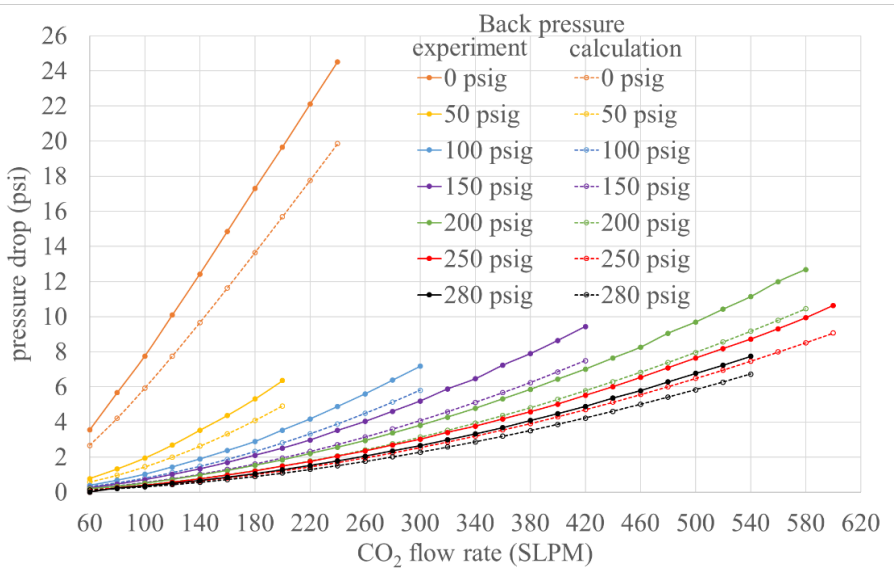

Figure 16. Pressure drop across the coil vs. CO_2 flow rate

The target condition in EFPR test would be 17 bar (247 psi). The results show that a pressure drop around 8 psi is expected under such a back pressure with CO_2 flow being at 500 SLPM. In the dry-feeding system, there are additional tubes and fittings between the coil and the burner, which will add to the total pressure drop. Control of the hopper pressure and the coal feed rate improves at larger pressure drops, so an objective of the system design was to produce a pressure drop significantly large enough to achieve the best level of control on the coal flow rate. The length of the coiled tube as well as the tube diameter were identified as parameters that could be adjusted to achieve the pressure drops needed to fine tune control of the coal flow.

Cold-flow Visualization of Dry Feed Hopper

Bench-scale research was conducted to gain a better understanding of the fluidized bed region in the bottom of the conical section of the hopper to compliment the design engineering on the pilot-scale system. The fluidization zone is a critical component to the dry feed system and it was decided to construct an acrylic cold-flow mockup of the bottom part of the hopper in order to better understand dynamics of the pulverized coal in the hopper. Objectives from this model included confirmation that undesirable effects such as bridging or ratholing was not occurring and to help define the operating window and range of fluidization velocities that give acceptable performance. The cold-flow system matches the geometry of the actual pressurized feed system and includes the fluidizing distributor, coal take-up tube and supplemental gas. Although the system did not operate under pressure, the lower gas density in the cold flow system was expected to have minimal impact on the dynamics of the coal bed, fluidization region and transport of coal. Importantly, the cold-flow model allowed for visualization of the coal in the bottom of the bed where there should be a mildly fluidized region enabling pneumatic coal transport.

Assembly of the main parts of the cold flow system are shown in Figure 17. The body of the system was constructed of acrylic plate and acrylic tubing. The cone-shaped part of the system

was custom-made by cutting a 1/4-inch thick plate of acrylic with a laser cutter into an open wedge shape. The piece was then heated until soft such that it could be formed around a wooden mandrel built specifically for shaping that piece. The seam was then glued to close the structure. The flanges were cut from 1/2-inch thick acrylic using a laser cutter. To simulate the distributor, a piece of dense fabric was sandwiched between two perforated plates, and instated into the plenum section made of aluminum.

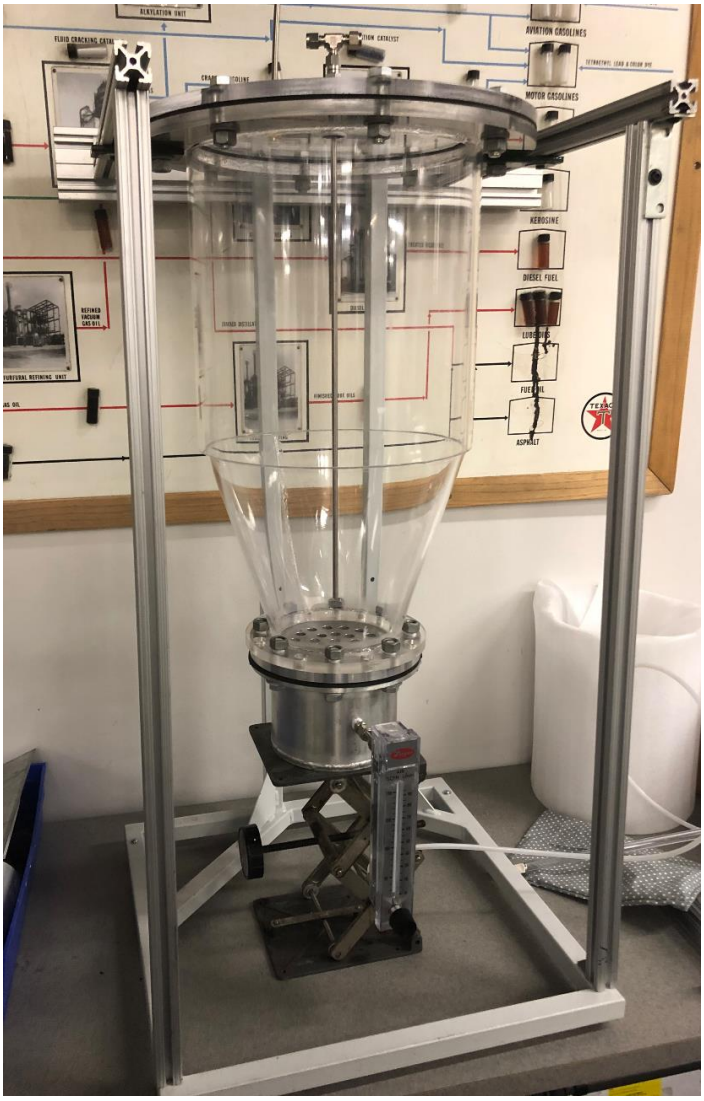

Figure 17. Acrylic cold-flow model of dry feed system hopper

Proof-of-concept feeding using the cold-flow model was confirmed with flow rates for fluidizing gas and supplemental gas regulated with rotameters. The plumbing and flow control was representative of that on the full-scale system and included fluidization air, an adjustable-height dip tube to transport powder from the hopper, supplemental air connected by a tee downstream of the hopper, a long length of tubing to produce pressure drop for flow stability, and measurement of the pressure difference between the hopper and the exit of the transport tubing.

Fine ceramic powder was used to represent pulverized coal. The material was loaded into the hopper and fluidization was initiated as shown in Figure 18. Initial tests were performed with a low level of particles, but in later testing the acrylic hopper was filled approximately half full as would be the case in the full-scale feeder.

Figure 18. Fluidization of surrogate pulverized coal. The level of material in the photo is lower than during normal operation so that the fluidization can be seen.

It was demonstrated that the ceramic powder could be stably fed by the system and at no point was there any blockage or cessation of flow. Initial data indicates that the flow rate of supplemental air has little influence on coal feed rate, which aligns with expectations of the system design.

Computational Fluid Dynamics Modeling of the Dry Feeder System

In parallel with the cold flow modeling effort, a three-dimensional computational model of the dry feeder system was developed to evaluate particle-fluid hydrodynamics under different feeder operating conditions using CPFD's Barracuda VR code. The code employs an Eulerian-Lagrangian approach to solve the fluid and particle momentum equations in three dimensions with strong, bi-directional coupling between the fluid phase and solid particles. The multiphase-particle in cell (MP-PIC) method is used to describe a computational particle cloud defined as a Lagrangian entity in which particle with the same properties such as composition, size, density, and temperature are grouped.

Figure 19 shows the computational model developed for the dry feeder. The model of the vessel is approximately 1.63 m high with a cylindrical shape in the upper section and a conical shape in the lower section. A particle take-up tube is oriented along the central axis of the vessel and the lower end of the tube is located immediately above the distributor cup at the bottom of the vessel. Fluidization flow comes in through the distributor cup at the bottom and supplemental gas flows through the tube above the vessel. Figure 20 shows the initial

conditions used in the simulation. The inside of the vessel is initially filled with CO_2 at 101,325 Pa and 300K. The vessel is also filled with 165.49 kg of coal particles with a particle close pack volume fraction of 0.6. Table 3 and Table 4 show the sieve analysis of the coal and the modeled coal particle size distribution, respectively.

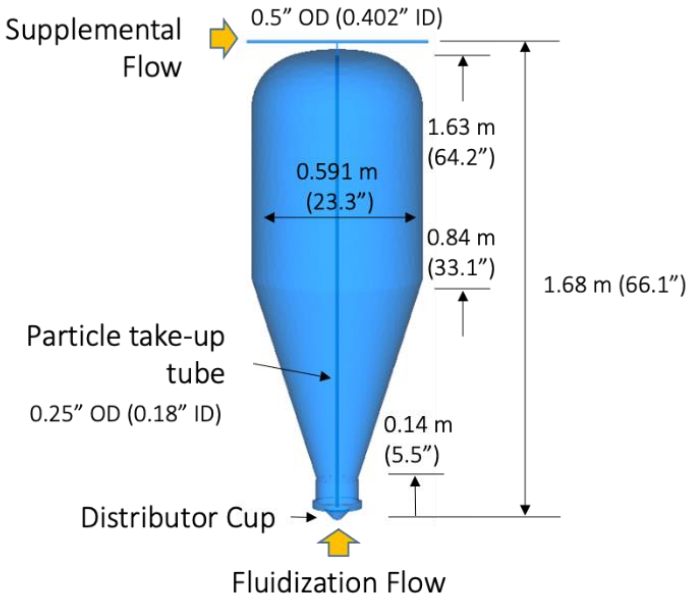

Figure 19. A computational model of the dry feeder.

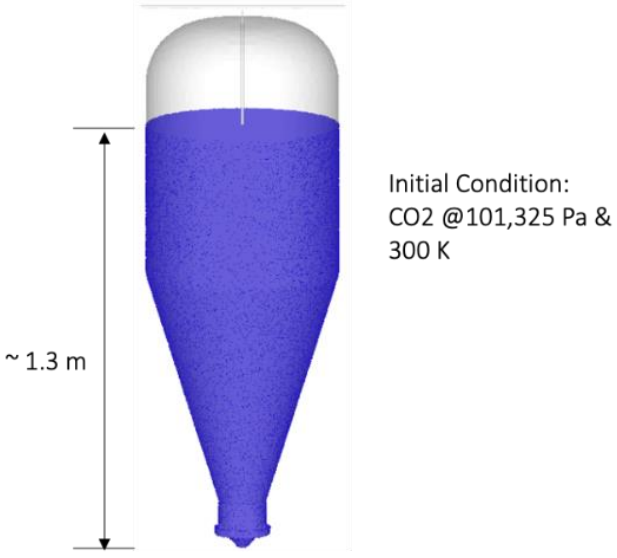

Figure 20. Initial conditions of the dry feeder showing the vessel filled with coal particles up to about 1.3 m.

Table 3. Coal particle sieve analysis.

Mesh	% not through	Mass fraction (%)
100	7.9	7.89
150	15.2	7.31
200	29.2	14.04
275	44.4	15.20
325	63.7	19.30
400	65.5	1.75
pan	100	34.50

Table 4. Modeled coal particle size distribution.

Bin Mass Fraction	Particle Diameter (μm)
0.025	8.4
0.050	15.5
0.075	21.3
0.100	27.7
0.150	36.3
0.200	49.8
0.150	69.1
0.100	91.2
0.075	118.5
0.050	160.3
0.025	242.4

Operating conditions for a baseline case is shown in Table 5. Baseline has 76.6 and 8.5 lb/hr for fluidization flow and supplemental flow, respectively. The fluidization flow in Baseline is relatively high at 90% of the total flow entering the system. CO_2 enters at 300K for both flows.

Table 5. Operating conditions for simulation.

	Baseline	
	Flow Rate, lb/hr	Flow Split, %
Fluidization Flow	76.6	90
Supplemental Flow	8.5	10

Baseline reached a steady-state at about 11-12 seconds of simulation time and the case was further simulated close to 25 seconds. Figure 21 shows the pressure changes at various locations in the vessel and the pipe as a function of time. As fluidization flow enters into the vessel, the pressure builds and increases up to 5-6 times the initial pressure due to the flow

blockage from the dense coal particle bed. The pressure inside of the pipe reaches a maximum at 6-7 seconds, then fluctuates when particles that are present in the particle take-up tube begin moving upward. When these particles in the tube have all exited, no particles are removed from the vessel until around 10 seconds when large pressure release occurs. Figure 22 shows a) system mass flow change, b) exiting mass flow, c) cumulative exiting mass flow, and d) integrated exiting particle by size from the baseline simulation. As shown in Figure 22 a), the system mass decreases at around 6-7 seconds followed by no change until 10 seconds, then a steady system mass decrease appears. This is consistent with exiting mass flow changes in Figure 22 b) and cumulative exiting fluid and particle mass in Figure 22 c). Figure 22 d) shows the integrated existing particle mass by particle size illustrating that some particle sizes may exit early while other particles exit more slowly.

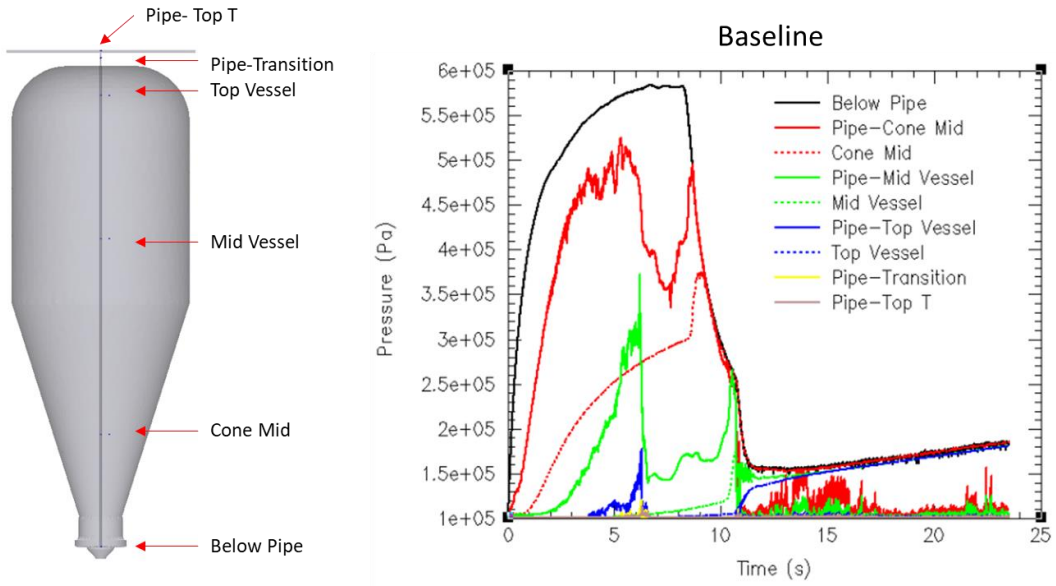

Figure 21. Pressure changes at various locations in the dry feeder as a function of time from Baseline.

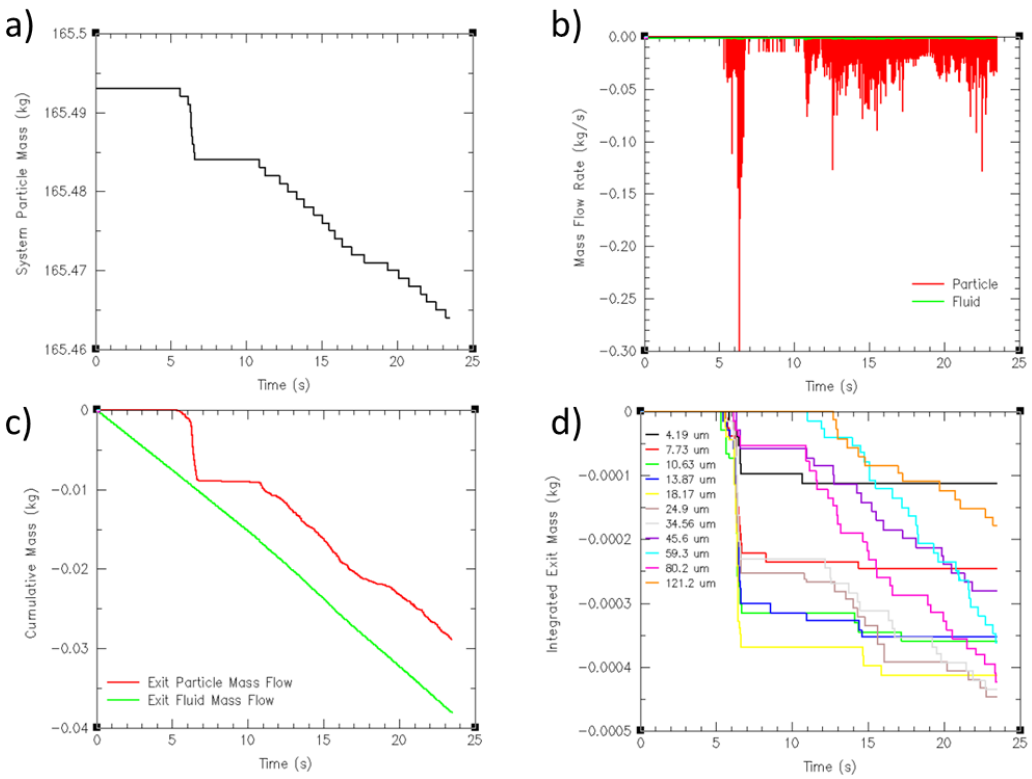

Figure 22. Baseline particle and fluid mass flow changes: a) system mass flow, b) existing mass flow, c) cumulative exiting mass flow, and d) integrated exiting particle by size.

Figure 23 shows the particles at the beginning and at 20.5 seconds of simulation time colored by particle size. Fluidization occurs as pressure builds up inside and the periphery region of the vessel cone has more intermediate particles (greenish color) while the bottom has larger particles (reddish color). As the pressure builds and fluidization occurs at the bottom of the vessel, some particles in the center are lifted up and splash the ceiling of the vessel. In fact, there is some channeling in the center of the vessel. Figure 24 shows the particles at the center slice of the vessel at 11.35 and 16.4 seconds. Some channeling occurs along the particle take-up pipe in the center. Particles near the center pipe flow upward, while the particles in the periphery flow downward. Figure 25 compares the particle size distributions of input and exiting particles. The median size of the exiting particles shifts to larger sizes, which implies larger particles are transported in greater quantities under the baseline operating conditions. This preferential removal of the certain sizes from the feeder may be determined by the operating conditions such as the fluidization flow rate and the location of the particle take-up pipe location.

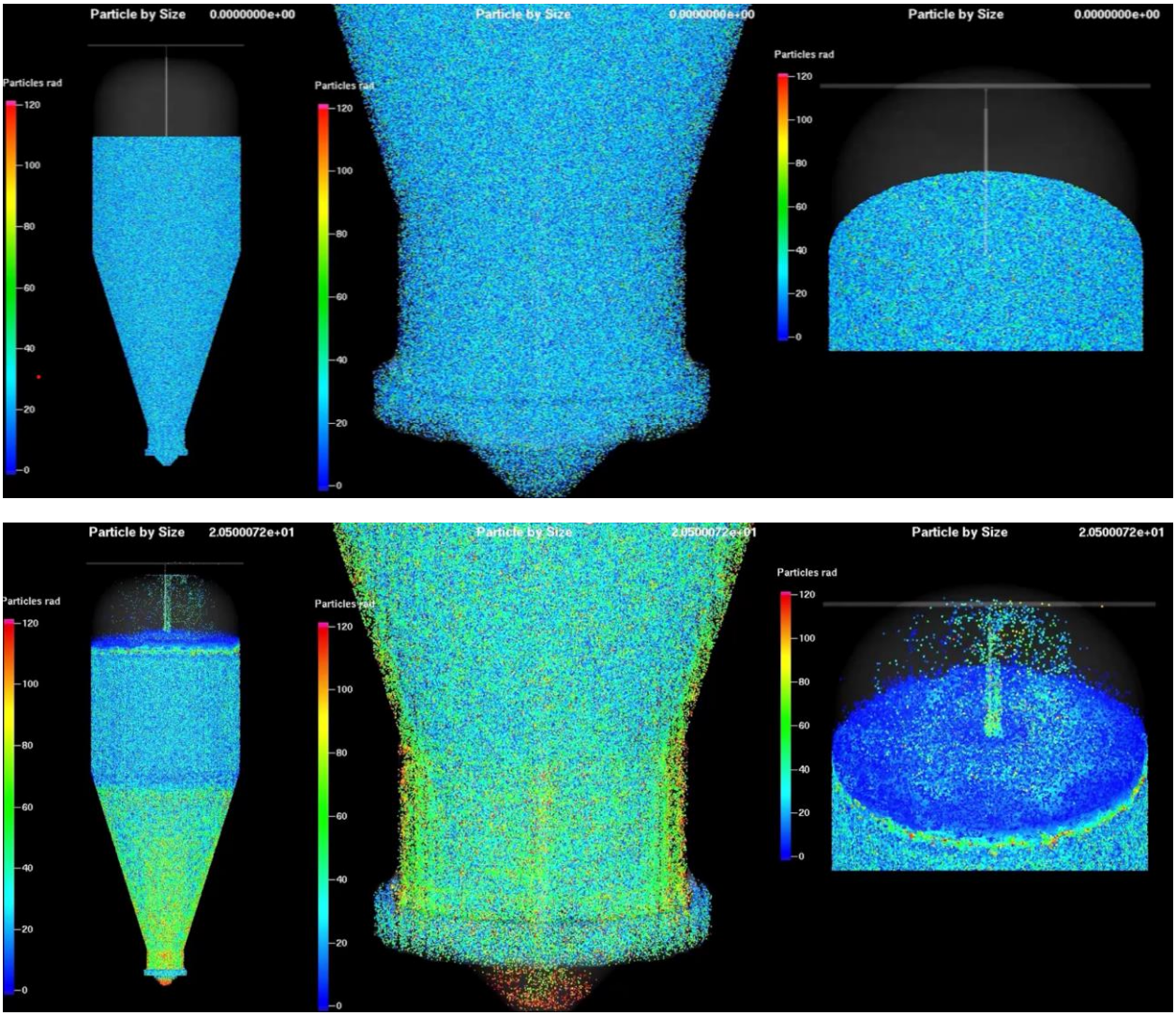

Figure 23. Baseline particle distribution in the feeder at 0 sec (top) and 20.5 sec (bottom).

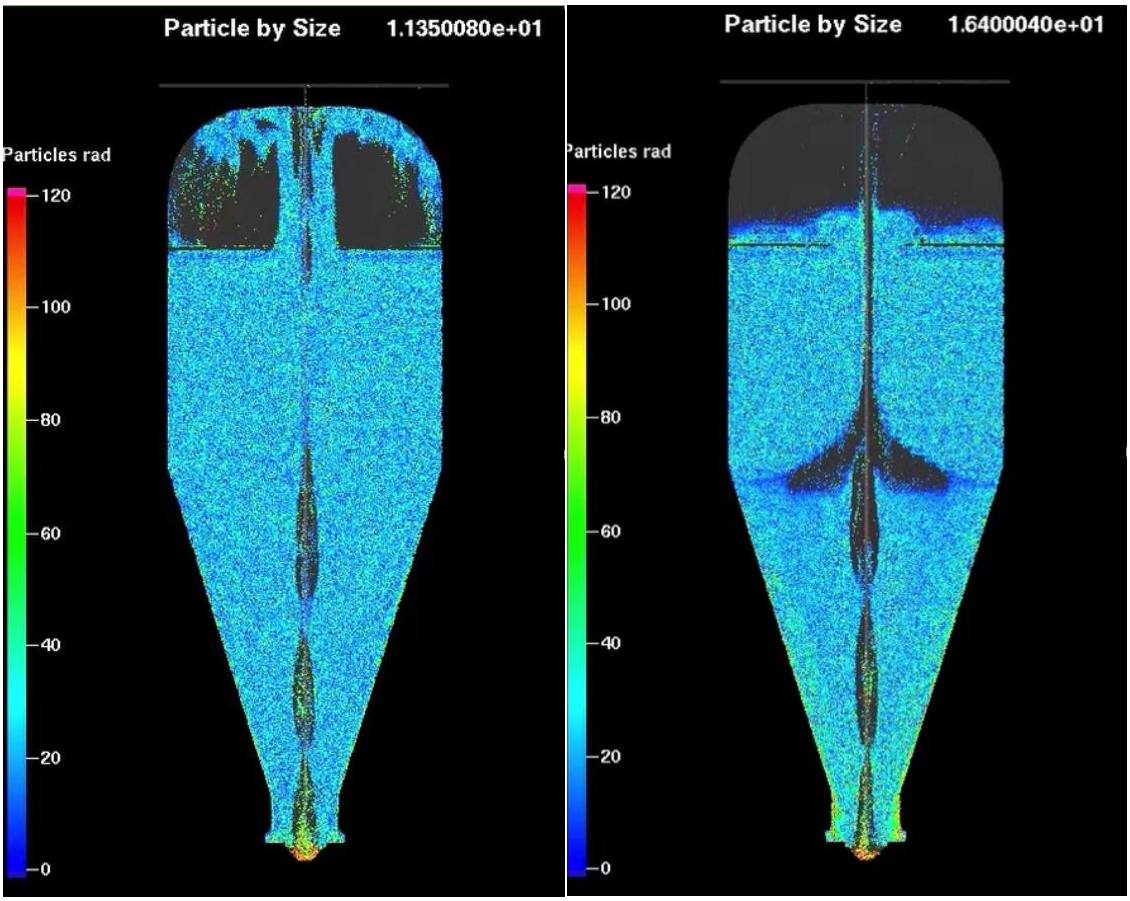

Figure 24. Channeling behavior from the baseline simulation showing particles at 11.35 and 16.4 seconds.

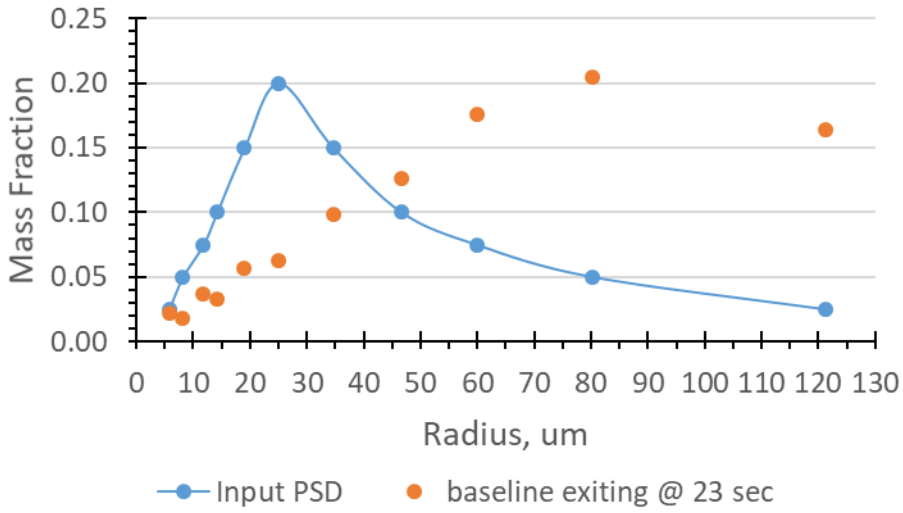

Figure 25. Input and exiting particle size distribution from the baseline simulation.

In order to understand the impact of the fluidization flow, a parametric case was simulated under the reduced fluidization flow rate. In Param 1, the fluidization flow rate is reduced from 76.6 to 13.8 lb/hr while the supplemental flow rate increased from 8.5 to 88 lb/hr. The fluidization flow rate is about 14% of the total gas flow inlet compared to 90% in Baseline. Due to the reduced fluidization flow rate, the pressure build-up rate inside the vessel and pipe is relatively slow and reaches up to twice the initial pressure at the bottom as shown in Figure 26. The pressure in the pipe increases first and then decreases at approximately 10 seconds when the initial particles already in the pipe start exiting. This behavior is similar to Baseline, but occurs at a slower pace due to the reduced fluidization flow rate. Once all the particles that were already in the pipe are gone, the pressure increases again as the particles taken up from the vessel are exiting. Figure 27 shows a) system mass flow change, b) exiting mass flow, c) cumulative exiting mass flow, and d) integrated exiting particle by size from Param 1.

Figure 28 shows the particle size distributions of the input and the exiting particles from Baseline and Param 1. As Param 1 is showing the exiting particles mostly from the particles placed inside the pipe through initialization of the simulation, the distribution is similar to the input particle size distribution.

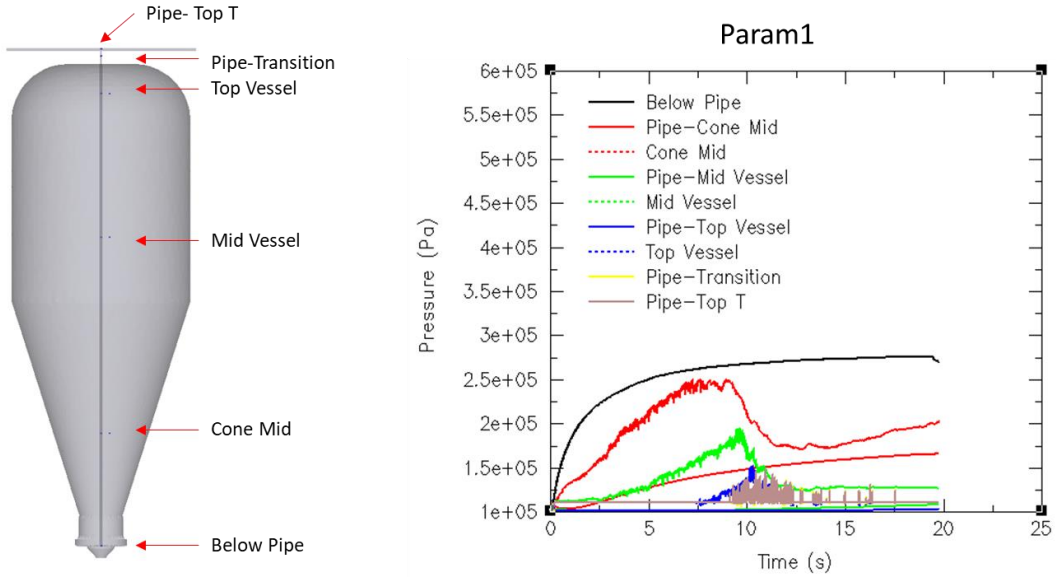

Figure 26. Pressure changes at various locations in the feeder as a function of time from the param1 simulation.

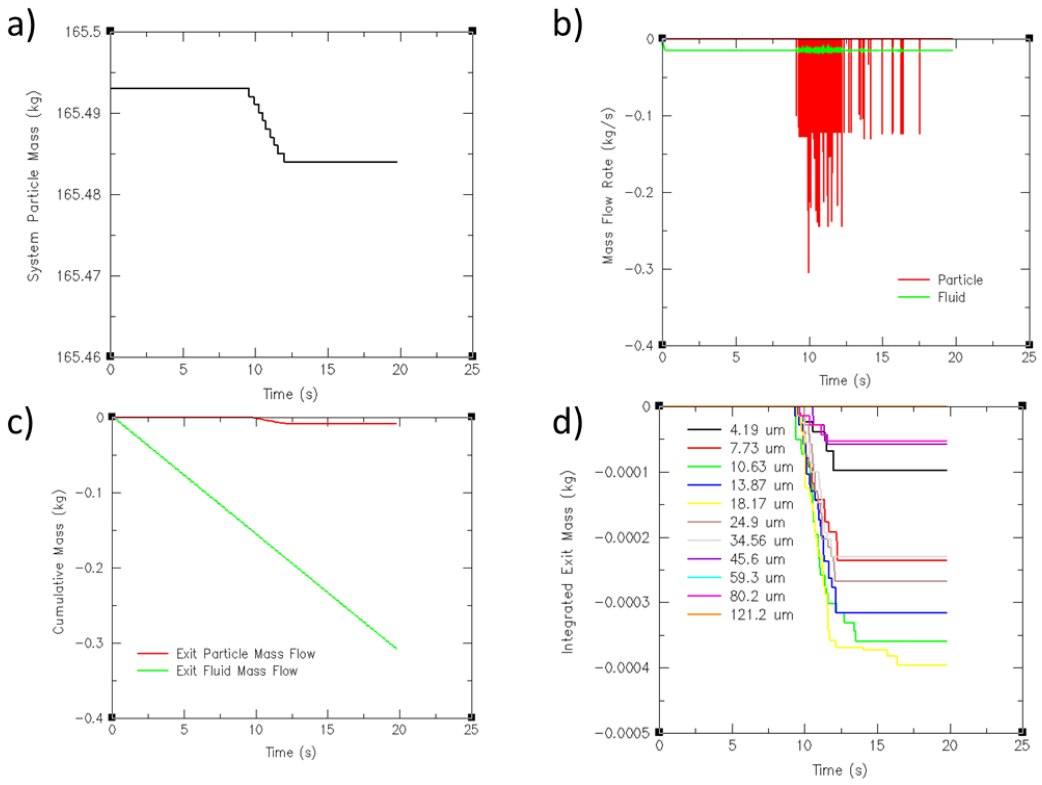

Figure 27. Parametric case (param1) mass flow changes: a) system mass flow, b) existing mass flow, c) cumulative exiting mass flow, and d) integrated exiting particle by size.

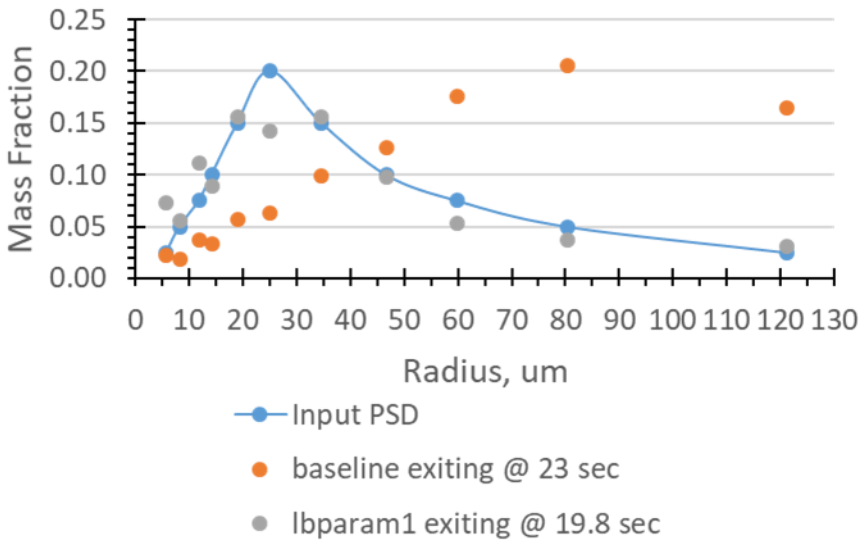

Figure 28. Input and exiting particle size distributions from baseline and param1.

Param 2 to Param 4 were added to investigate the sensitivities to the fluidization CO_2 flows entering the hopper. Table 5 shows the key operating conditions for these cases. Param 1 has 13.8 and 88.0 lb/hr for fluidization flow and supplemental flow, respectively. Both fluidization and supplemental flows are made of 100% CO_2 injected at 300K. In Param 2 through 4, the fluidization flow is modified with the same total flow as in Param 1. Fluidization flow is increased to 45.2 lb/hr (or 44% of the total flow) in Param 2, 29.5 lb/hr (or 29% of the total flow) in Param 3, and 72.3 lb/hr (or 71% of the total flow) in Param 4 from Param 1. Also, the outlet pressure is increased to actual operating conditions, 227 psi (about 10 psi over the reactor pressure).

Table 6. Operating conditions for parametric simulations

	Param1		**Param2**		**Param3**		**Param4**	
	Flow Rate (lb/h)	Flow Split	Flow Rate (lb/h)	Flow Split	Flow Rate (lb/h)	Flow Split	Flow Rate (lb/h)	Flow Split
Fluidization Flow	13.8	14%	45.2	44%	29.5	29%	72.3	71%
Supplemental Flow	88.0	86%	56.6	56%	72.3	71%	29.5	29%
Sum	101.8	100%	101.8	100%	101.8	100%	101.8	100%
Outlet Pressure (psi)	14.696		226.98		226.98		226.9	

Figure 29 shows the integrated particle mass and particle mass flow rates as a function of simulation for each case. Results are presented in order of increasing fluidization flow rate: Param1 < Param 3 < Param 2 < Param4. As the particles leave the computational domain, the outlet mass flow rates show as negative values. In Param 1, particle output starts around 9 seconds: these particles are from those already in the take-up tube through model initialization. After the exit of these particles, the particle exit flow rate is reduced significantly to 0.196 lb/hr (about 0.7 kW firing rate) and the case was stopped at 27 sec as computational time was impractical (overall 45 hours per 1 second simulation). In Param 3, particles start leaving the feeder at around 49 seconds. As in Param1, these particles are those already in the take-up tube through model initialization. After the particles initially in the take-up tube reach the exit, the particle output rate reduces to 0.904 lb/hr (about 3 kW firing rate). In Param 2, output of particles initialized in the take-up tube starts around 57 seconds. As pressure builds in the vessel, output rates slow until the simulation reaches 110 sec where the particle flow increases to 53 lb/hr. Beyond the large increase at 110 sec, the particle output rates slow to 13.6 lb/hr (about 47 kW firing rate). In Param 4, with the highest fluidization flow rates used in the current simulation set, the particle output rate is approximately 35 lb/hr (122 kW). The trend from these simulations clearly show output rates increasing with higher fluidization flow rates.

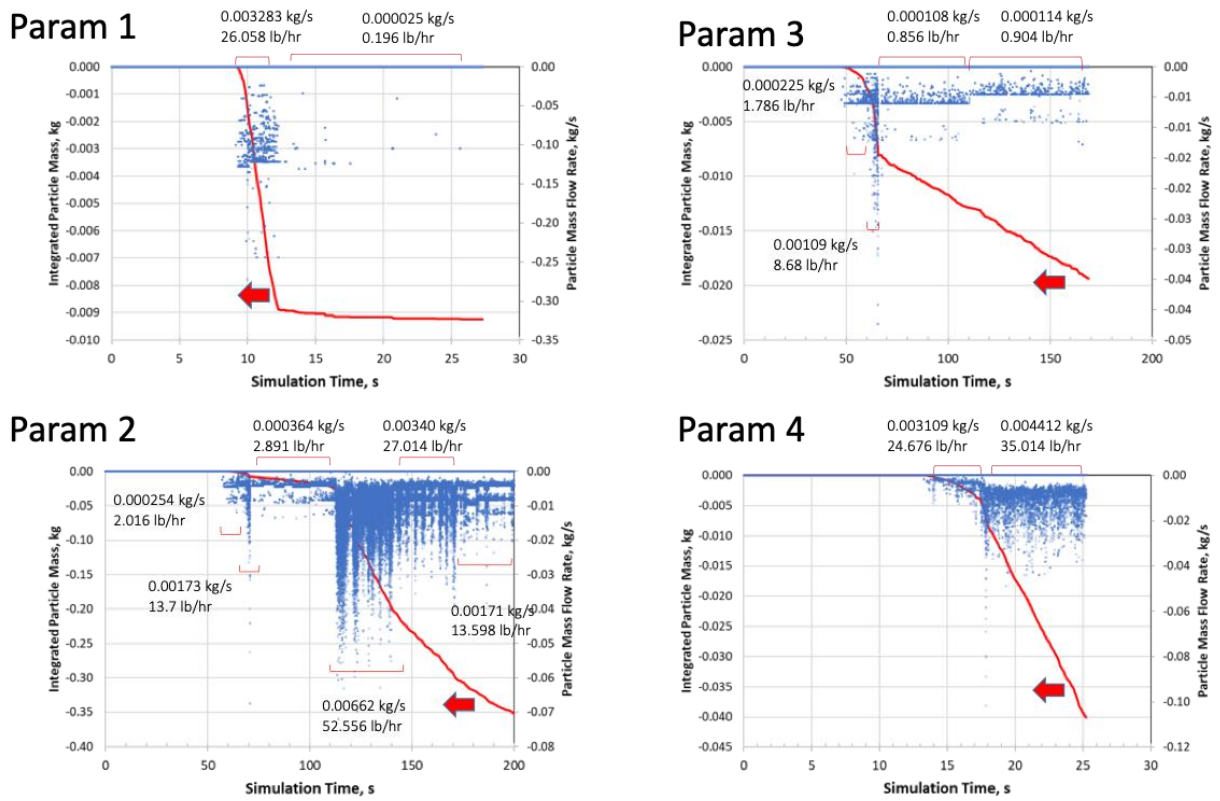

Figure 29. Integrated particle mass and particle mass flow rates as a function of simulation time for Param 1 through Param 4.

Figure 30 shows snapshots of particle distribution at the center plane of each case. With increasing fluidization flow rates, the stronger channeling along the central take-tube occurs. Figure 31 shows the integrated mass of the exiting particles by size and Figure 32 shows the accumulated particle size distribution of the exiting particles. The particles are leaving the computational domain and the integrated mass shows as negative values. In Param 1, most of the exiting particles are from those initialized in the take-up tube and, as shown in Figure 32, the particle size distribution is similar to the original coal particle size distribution. The figure shows that in Param 3, mid-range particles (24.9 and 34.6 µm) exit preferentially. Param 2 shows a shift of the size distribution of the exiting particles toward the larger particles while Param 4 shows mid to large particles exit more with a higher fluidization rate than Param 3.

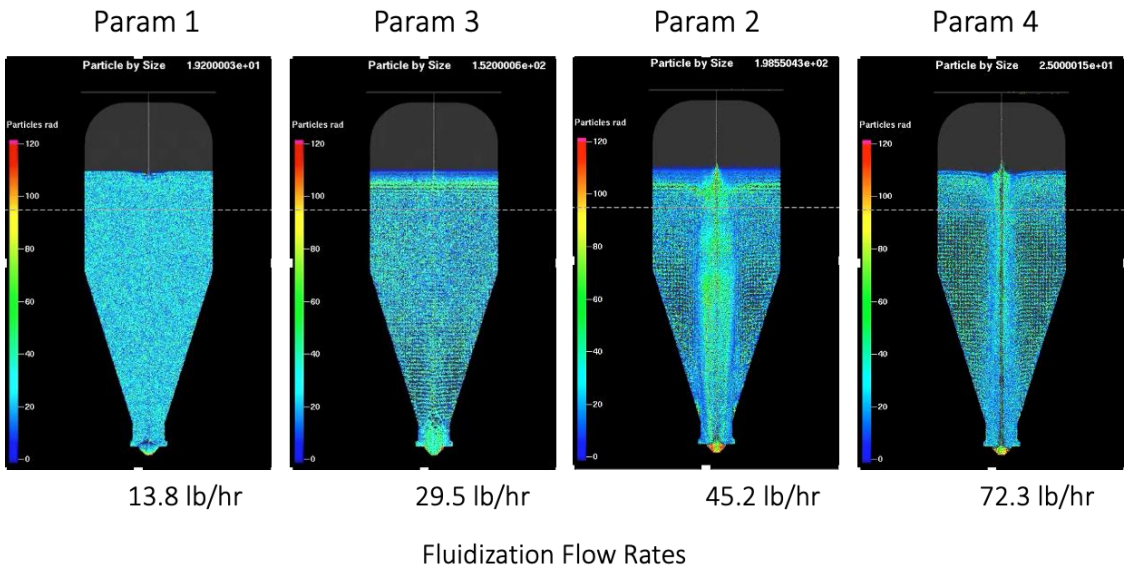

Figure 30. Particles at the center slice from each case in the order of increasing fluidization flow rates.

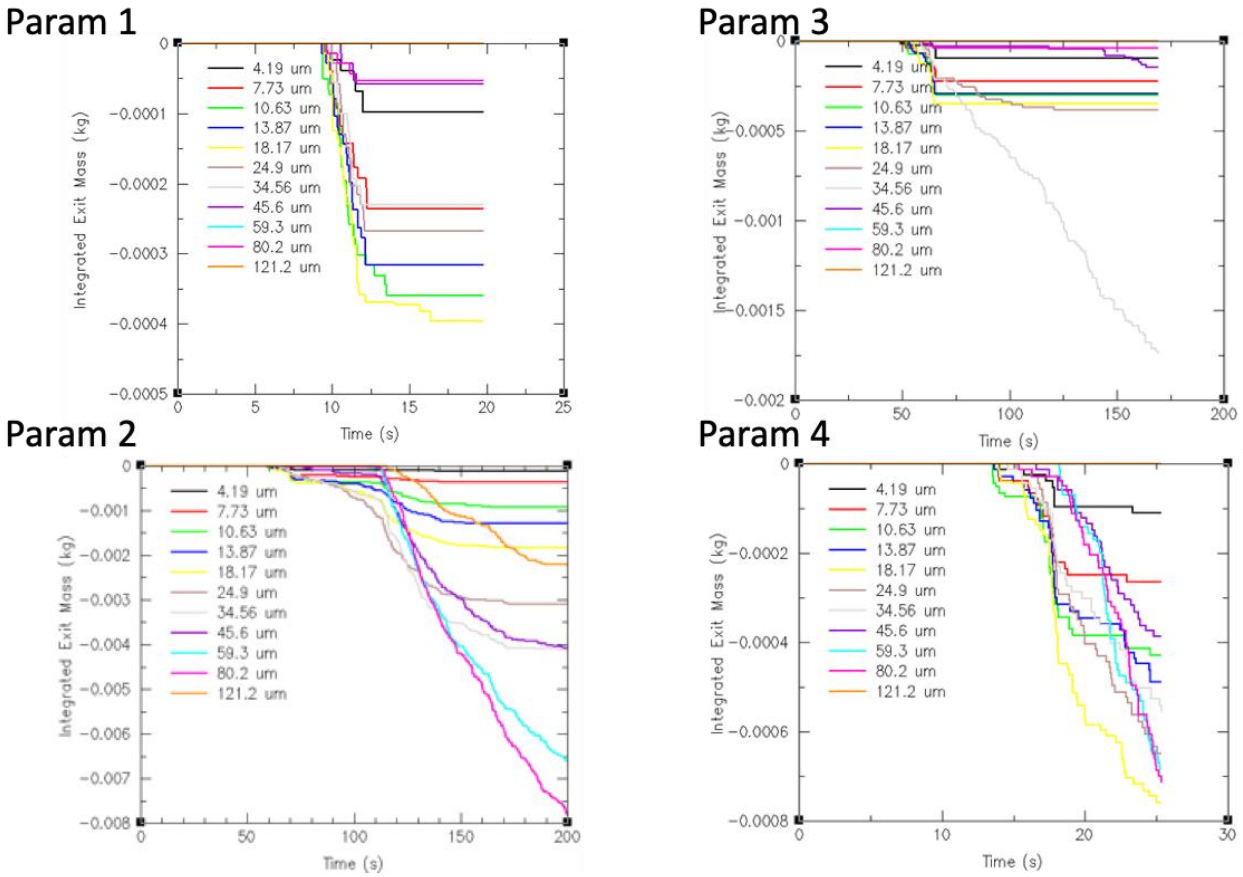

Figure 31. The integrated mass of the exiting particles by size for each case.

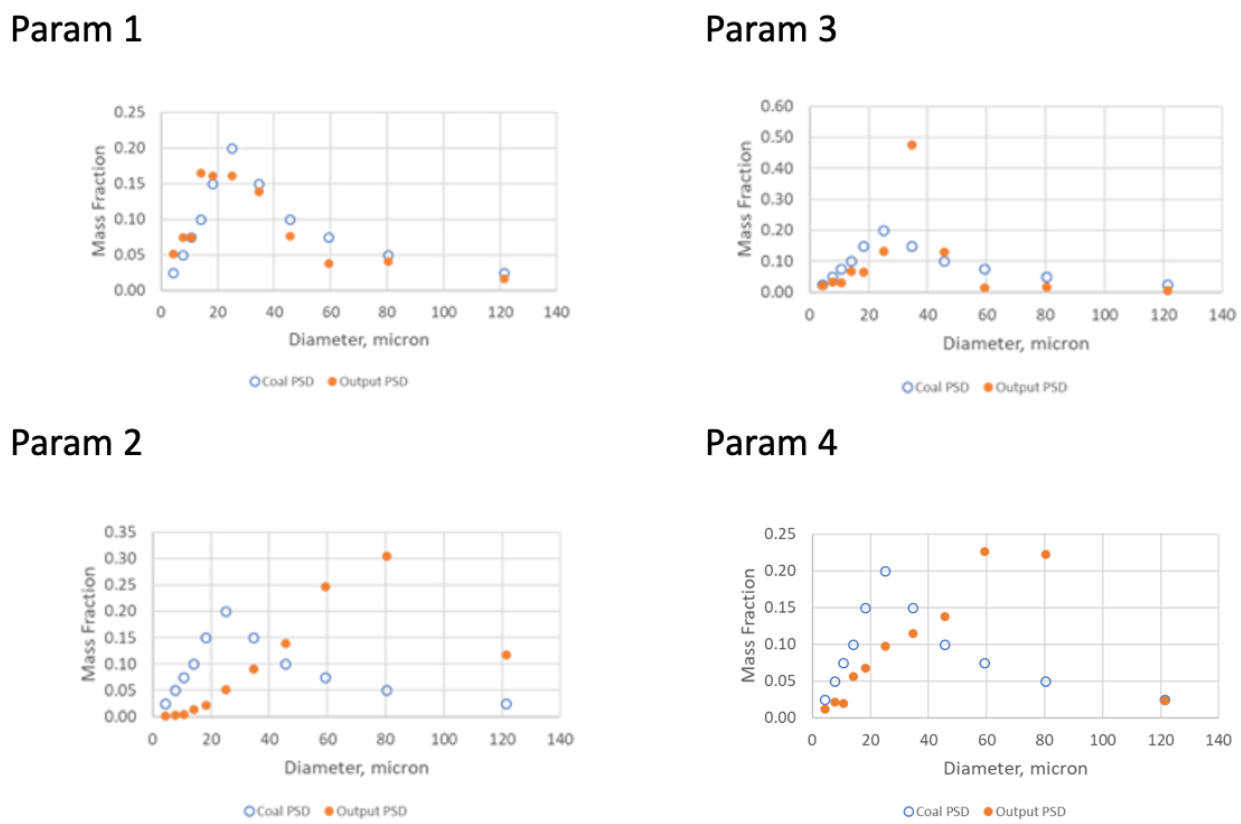

Figure 32. Accumulated size distributions of the exiting particles for each case.

Figure 33 illustrates how the simulation results indicate that the higher fluidization flow rates increase the coal flow rates from the feeder, but with a particle size distribution biased toward the larger particles. This is due to particle segregation from fluidization resulting in larger particles settling down at the bottom part of the feeder vessel. Figure 34 shows the particle size distribution colored by size at 190 second simulation time for Param 2. The particles initially started with a uniform distribution in the vessel, but the larger particles (reddish colors) settle at the bottom part of the feeder near the distributor cup, while smaller particles (bluish colors) reside in the upper part through fluidization. The inlet of the take-up pipe is located near the distributor cup and can pick up larger particles more easily. The combination of the fluidization flow rates and the take-up pipe location should be considered to reach the conditions that provide the most efficient and consistent operation of the combustion system.

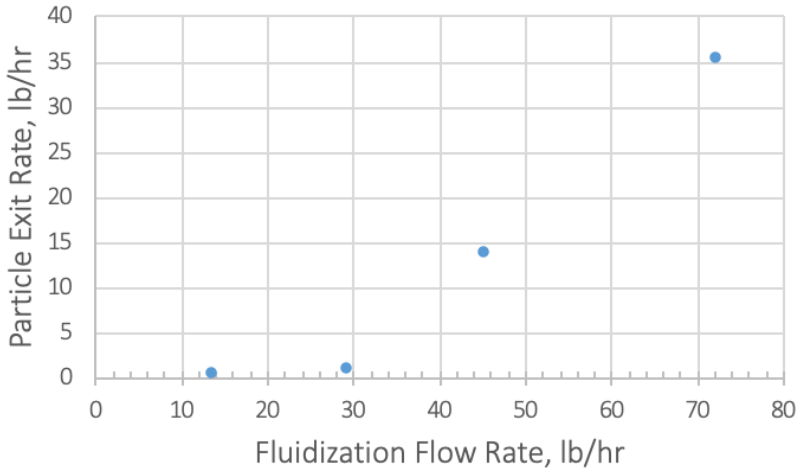

Figure 33. Particle exit flow rates as a function of fluidization flow rate.

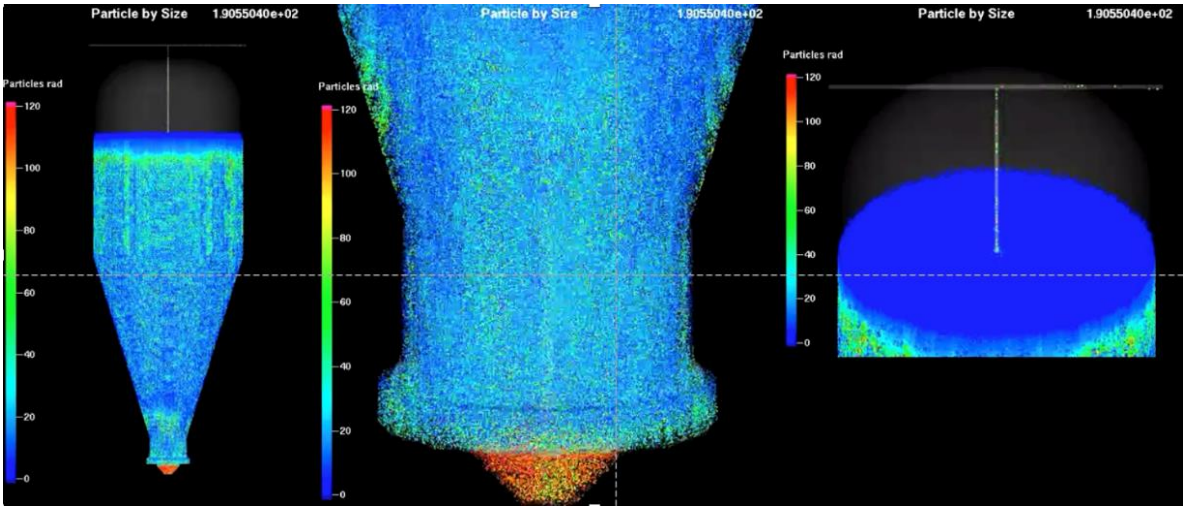

Figure 34. Particle distribution by size for Param 2 at 190 second simulation time.

Subtask 2.2 - Engineering and integration of dry feeding system

The dry feeding system requires high pressure CO_2 both for pressurized pneumatic transport of the pulverized coal and for mixing with O_2 for combustion. The capacity and pressure of CO_2 necessary for pilot-scale testing exceeds that which can be reasonably delivered by standard CO_2 dewars. At room temperature, the vapor pressure of CO_2 is approximately 800 psi so CO_2 is supplied as a liquid and must be vaporized either by electric heating or by using an ambient vaporizer of aluminum finned tube design.

For this project, a dedicated CO_2 "microbulk" tank system has been engineered. Project partner Praxair worked with the University of Utah to identify an affordable solution that would satisfy

the pressure and capacity requirements of the system. The microbulk tank provided by project partner, Praxair is shown in Figure 35. At a nominal firing rate of 200 kW dry coal, the expected CO_2 feed rate would be 400 lb/hr when combusting with 27% O_2 in CO_2 and 100 lb/hr when combusting with 60% O_2 in CO_2. A full microbulk tank would provide between 11 and 60 hours of CO_2, which is sufficient for 1-2 weeks of testing at 4-6 hours per day, 3-4 days per week. The microbulk tank and vaporizer installed on-site at the University of Utah laboratories was integrated into the dry feed system and Praxair provided refills of the tank when necessary.

Figure 35. Placement of CO_2 microbulk tank at the University of Utah's Industrial Combustion and Gasification Research Facility

As the hopper design work was occurring, an assessment of the appropriate location for the hopper in the laboratory was completed. The hopper was located such that 1) existing support structures surrounding the reactor could be utilized; and 2) transport lines for coal conveyance from the hopper to the reactor would be minimized. The determination for the location of the hopper and its position relative to the reactor is illustrated in Figure 36.

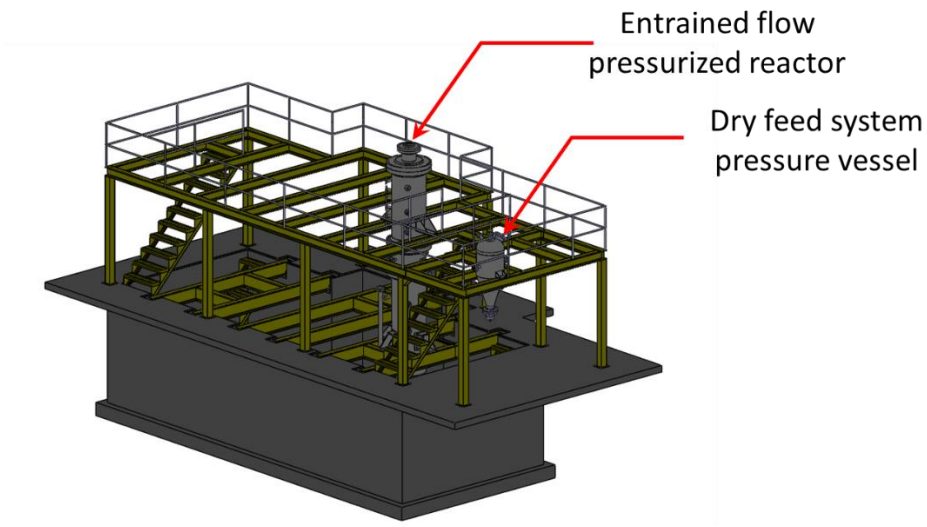

Figure 36. Support structure and hopper location at the University of Utah's Industrial Combustion and Gasification Research Facility

A process and instrumentation diagram (P&ID) is provided in Figure 39 with descriptions of lines, instrumentation, and equipment in Figure 40. Inspection of the diagram reveals an emphasis on the solids sampling system. Finalization of the P&ID involved reconfiguring natural gas and air lines to accommodate the burner for idling the reactor when not firing on coal

The reactor port assignments are shown in Figure 37. A UV flame detector was installed to monitor the natural gas flame when heating up and idling between each day's experiments. This UV detector was mounted behind a pressure-rated sapphire window. Its primary function was flame monitoring when the reactor was idling unattended at atmospheric pressure. However, the UV detector could additionally serve to detect a coal flame during the experiments under pressurized conditions. Immediately below the UV detector is a port for a removable 10,000 VDC igniter for cold start on the gas flame. The igniter was not intended for use during pressurized operation and would be removed before bringing the reactor up to pressure. The upper 4 ports shown are reserved for radiometers while the 5th port from the top is the location designated for the solids sampling probe. Type B thermocouples run through pressure fittings are embedded in the inner refractory, recessed 3/8 inch from the hot face.

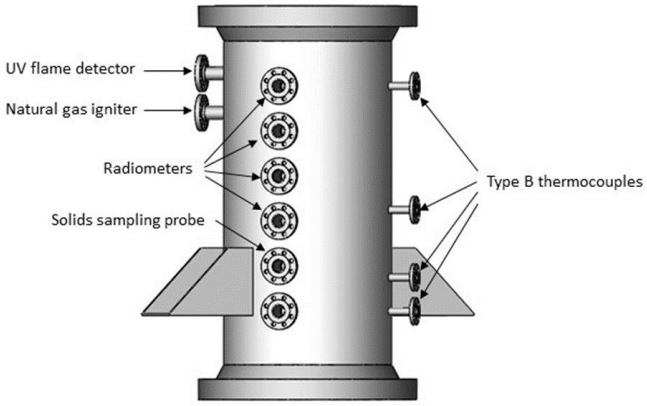

Figure 37. Port assignments on reactor section of Entrained Flow Gasifier

A key component of the instrumentation was a set of radiometers. Figure 38 shows the hardware used in the radiometer calibrations. The approach consists of measurements with a black body radiator and separate calibrations for the radiometers' field of view and view angle. The figure shows the overall calibration setup with the alignment tube for access to the black body radiator. Also shown is the calibration assembly with a cowling to adjust ambient temperatures. The field of view and view angle is calibrated using the glowing rod shown.

Figure 38. Hardware used in radiometer calibrations

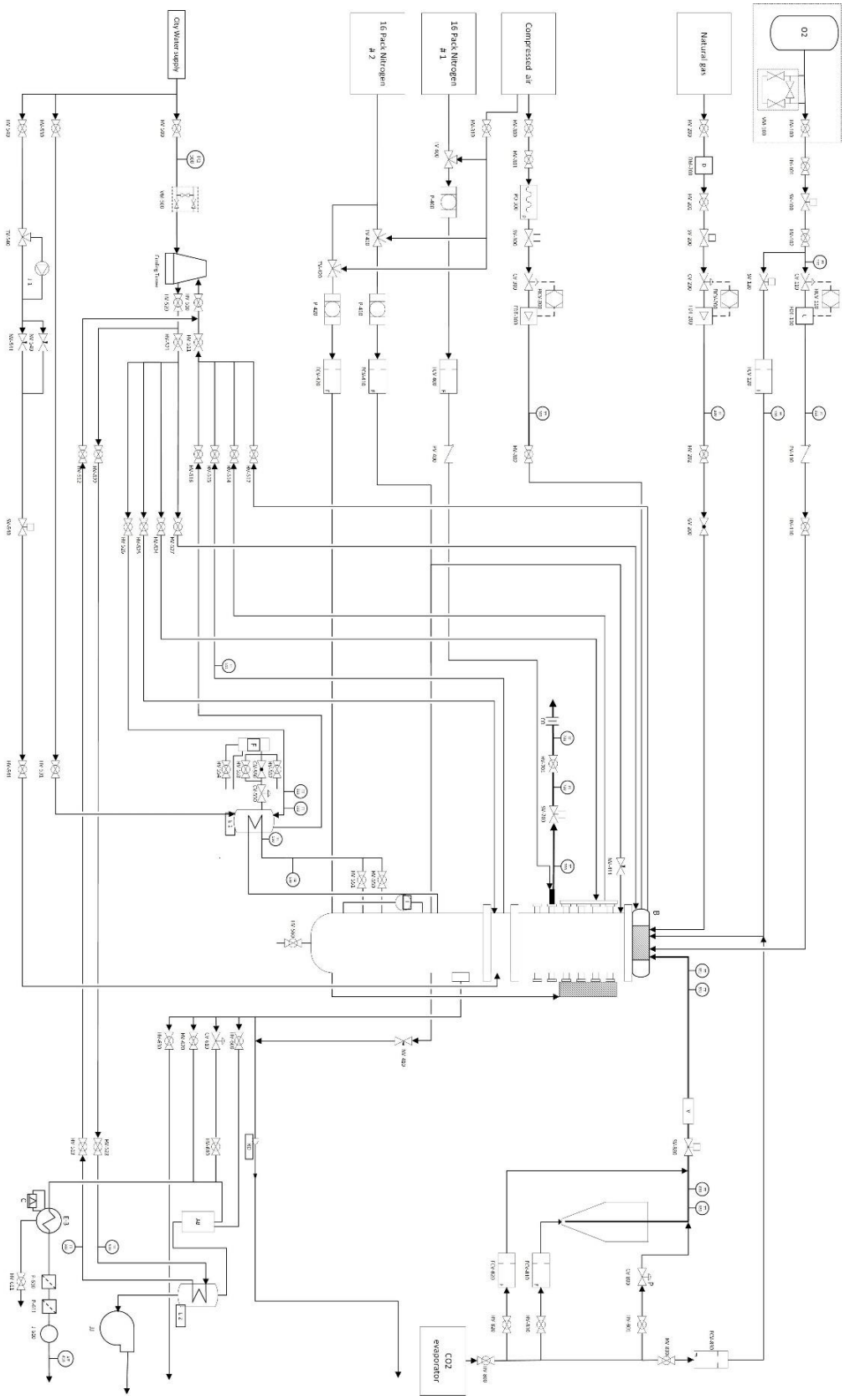
City Water supply
16 Pack Nitrogen # 2
16 Pack Nitrogen # 1
Compressed air
Natural gas
O2
CO2 evaporator

Figure 39. Process and Instrumentation Diagram for Dry Feed System

Instruments

Symbol	Description
AIT	Gas Analyzer
FCV	Mass Flow Controller
FDT	V-Cone/Coriolis
FICV	OPTO-Controlled Flow
PO	Regulator
PT	Pressure Transmitter
TT	Temperature Transmitter
DM	Diaphragm Meter

Valves

Symbol	Description
CV	Control Valve
HV	Hand/Ball Valve
NV	Needle Valve
PV	Check Valve
SV	Solenoid
TV	Three-way Valve
GV	Globe Valve
VM	Valve Manifold

Equipment

Symbol	Description
E	Heat Exchanger
J	Pump
JJ	Fan
P	Filter
R	Reactor
B	Burner
AB	After-burner
F	Flush Tank
RD	Rupture Disc

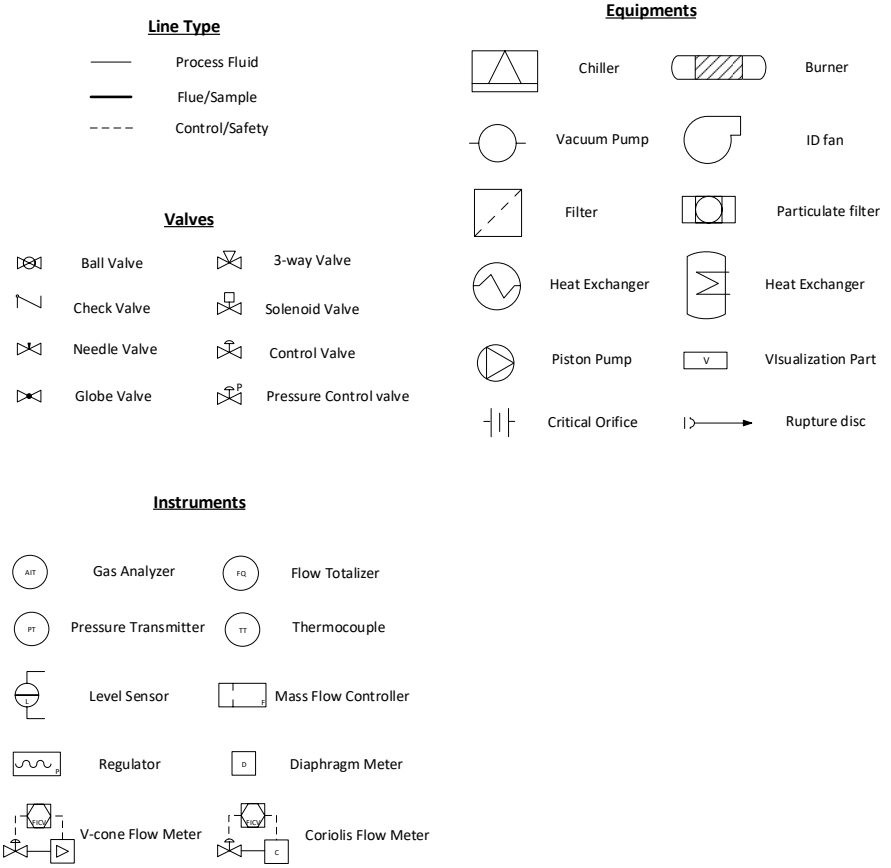

Figure 40. Description of components in process and instrumentation diagram for dry feed system

As the work on the integrated system progressed, the process instrumentation for coal transport from the pressurized fluidized bed feeder to the EFPR was refined. An update to the simple preliminary process flow diagram in Figure 9 was produced that includes equipment and instrumentation for the integrated system. The updated process flow diagram is shown in Figure 41.

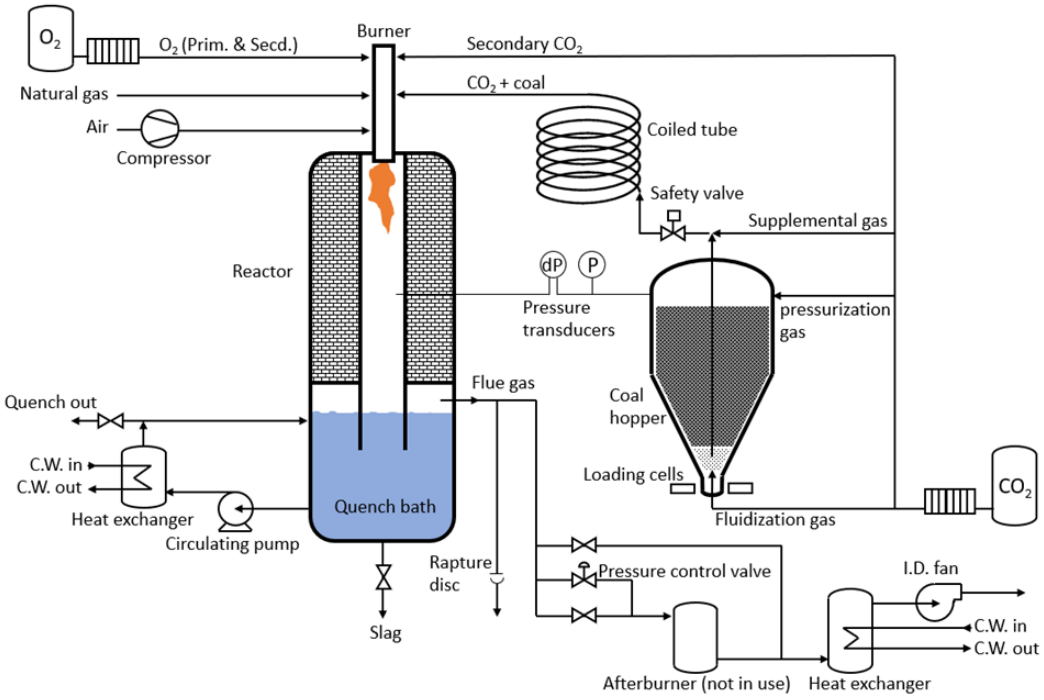

Figure 41. Process flow diagram of the integrated dry pulverized coal feeder and the entrained flow pressurized reactor

As mentioned above, communications with SEU led to the development of a control scheme where pressure difference transducers measuring the pressure drop between the feeder and the reactor provide the feedback signals on flow control of the pressurizing gas. The pressure difference transducer along with the hopper pressure transducer were installed.

The coiled tube shown between the hopper and reactor in Figure 41 was added to produce a suitable pressure drop to achieve stable coal transport. Completion of the coiled tube connection included installation of a safety valve between the feeder and the reactor. The placement of the coiled tubing relative to the feeder hopper and the reactor is shown in Figure 42.

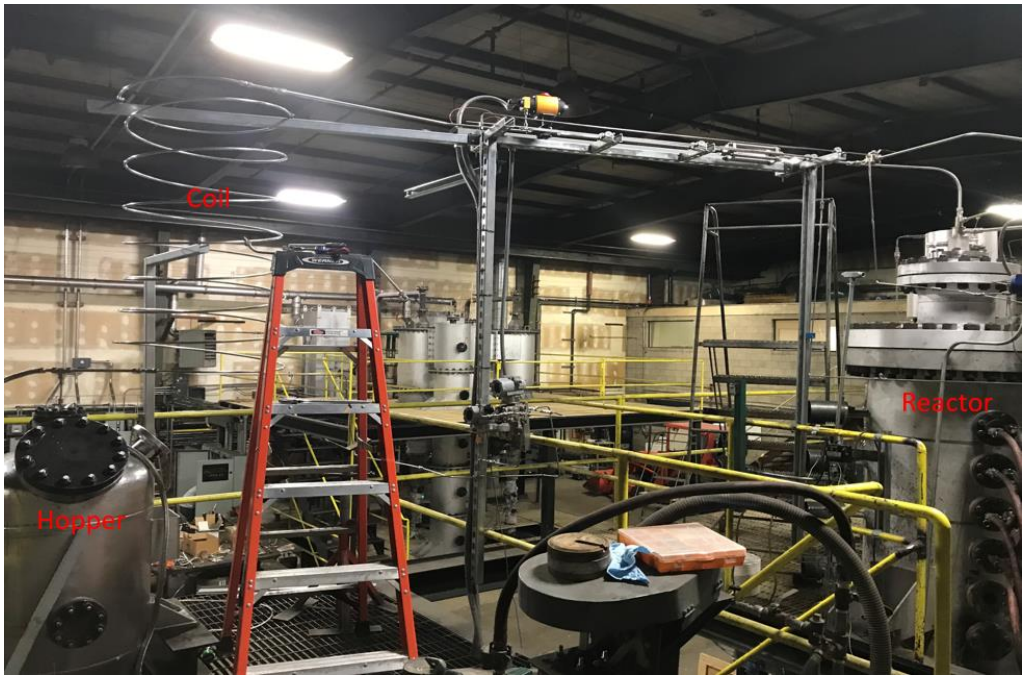

Figure 42. Integration of the dry feed system with the combustor showing the feeder hopper, coiled tubing, and EFPR

Initial Testing of the Dry Feed System

An initial test of the dry feed system was carried out at atmospheric pressure. The test involved feeding coal from the dry feed hopper through the pressure-drop coil into a receiver barrel capped with a bag filter. The test setup is illustrated in Figure 43 showing the hopper, the coil and the barrel used to collect the coal flowing from the hopper. As shown on the right side of the figure, the barrel was set on a digital scale displaying the mass change during the test.

Figure 43. Setup of the initial coal transport test at atmospheric pressure

Results of the test are shown in Table 7. The coal flow was maintained at a steady 27.6 lb/h feeding rate, which would correspond to a furnace firing rate close to 93.5 kW. The pressurization, fluidization and supplemental CO_2 flows are as shown. Relatively high pressure drop allows for increased control over the flow. As shown, the initial test had 14.9 psi of pressure loss between the hopper and the barrel used to collect the coal.

Table 7. Conditions for the initial coal transport test at atmospheric pressure

Coal feeding rate (lb/hr)	Pressurization flow rate (SLPM)	Fluidization flow rate (SLPM)	Supplemental flow rate (SLPM)	dP hopper to barrel (psi)
27.6	5	5	50	14.9

The visualization module installed in the coal transport path is shown in Figure 44. The visualization section was used to monitor the flow of the coal between the coiled tube and the reactor during the test. Figure 45 is a photograph of the visualization section during the test. The glass tube allows for confirmation of the presence of coal flow as well as inspection of coal transport consistency.

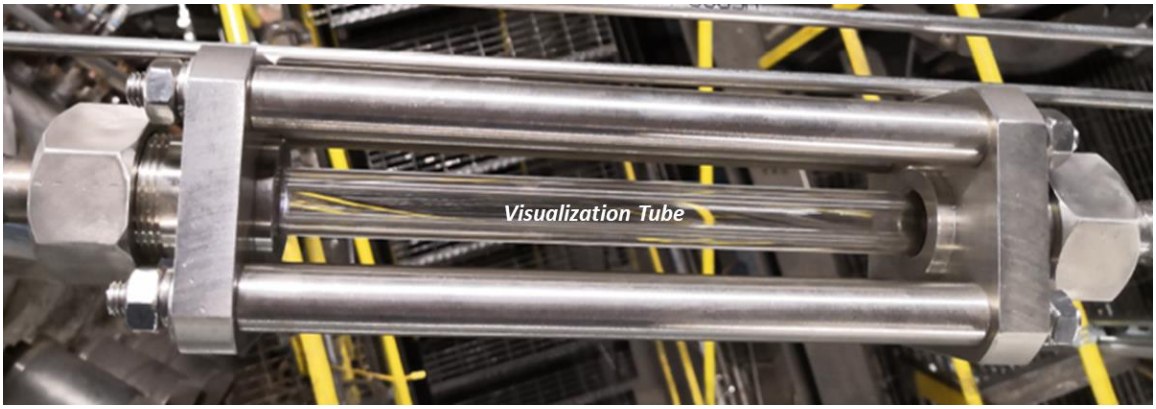

Figure 44. Visualization section for monitoring coal flow from the hopper to the reactor

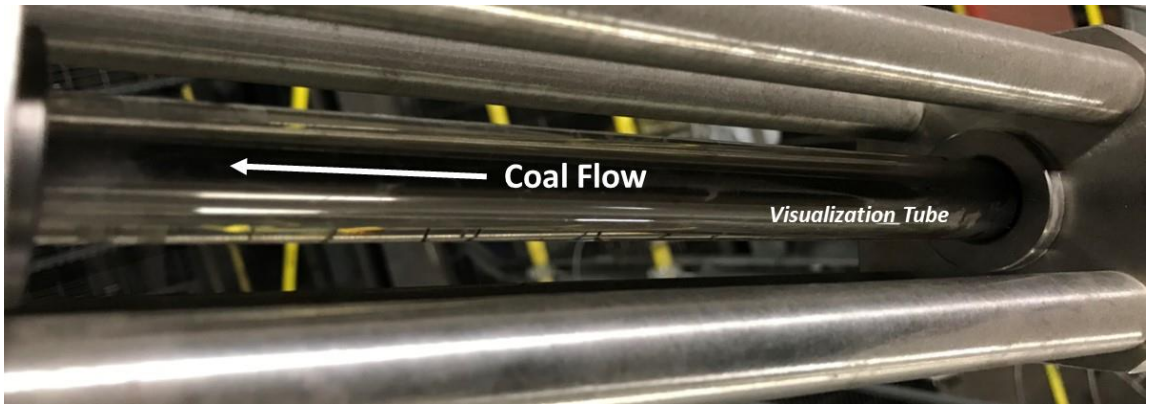

Figure 45. Visualization section with coal flowing from the hopper

Load cells have been mounted to the bottom of the hopper to measure hopper mass. The coal feeding rate was automatically calculated by the control system, using the mass loss divided by time lag. The accuracy of the total mass reading was ± 0.05% with a full range of 2000 lb. This relatively low refinement in the measurement made it difficult to obtain an accurate feeding rate each second, which is why a digital scale was used to measure the coal flow rate in the test. To improve the resolution on coal feeding rate, a summing box was installed on site to reduce signal noise from the load cells and a new calculation strategy was updated on the control side.

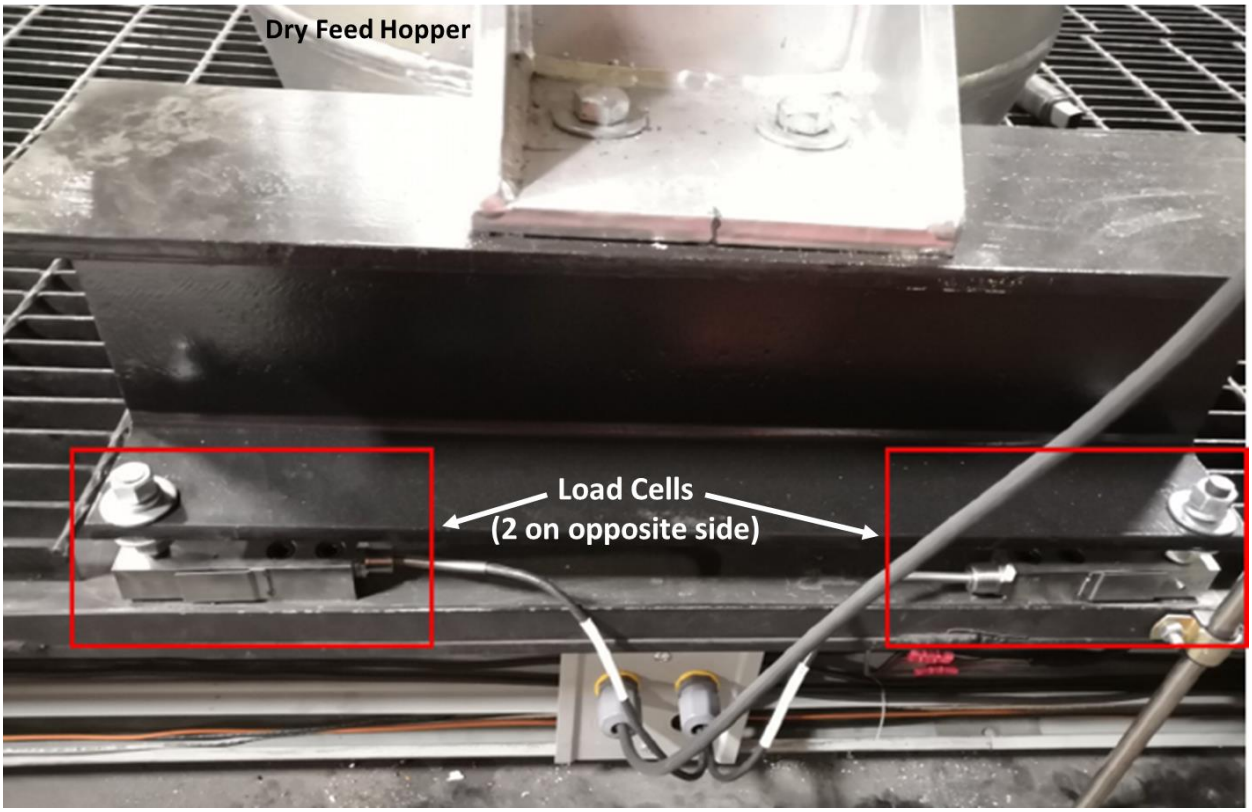

Figure 46. Load cells mounted to the bottom of the hopper

Integration of averaging function into load cell signal for real time feed rate

The original approach for determining the coal flow rate involved recording the mass of the hopper over specific time intervals. This calculation method, however, was susceptible to the signal noise of the load cells, which have maximum ratings of 500 lb and are accurate to within 0.1%. The sum of the 4 load cells (1 in each corner of the hopper) gives a maximum hopper mass of 2000 lb and a resultant margin of error of +/- 2 lb being read by the controls system, which translates into an error of +/- 1400 lb/h on the coal flow rate. This is unacceptably high error relative to the target, which is approximately 45 lb/h. Signal noise could be dampened by increasing the time intervals between measurements, but this would hinder timely adjustments to operation in response to transient fluctuations in the system.

Shown in Figure 47 is the recorded data from the load cells with no flow or mass change to the hopper. The figure shows the magnitude of the signal noise at this resolution with fluctuations of approximately 1 pound between readings.

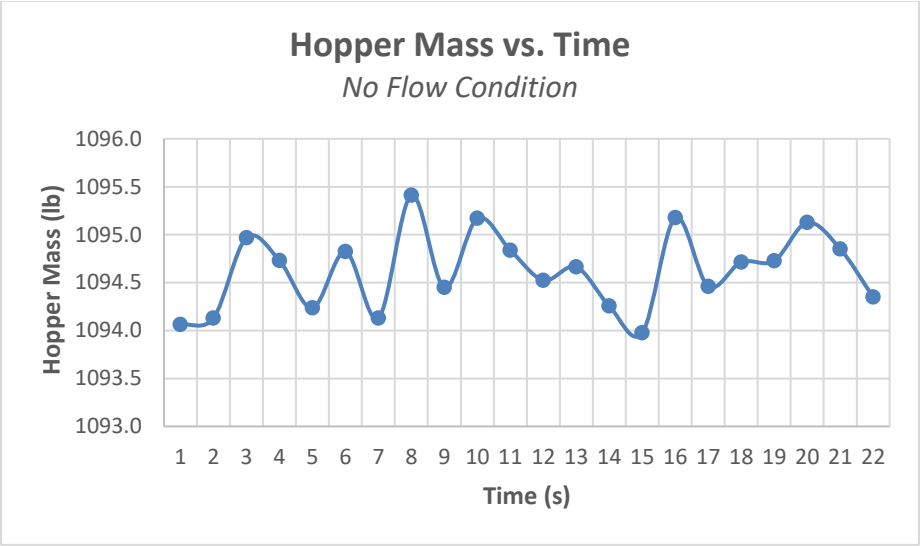

Figure 47. Signal noise for hopper mass measurement

An averaging technique was implemented as an initial step in dampening the signal noise. When hopper mass was recorded, a series of 50 values were taken over a 200-millisecond time step rather than a single value. These 50 values are then averaged, and that averaged hopper mass would be the value entered into the flow rate equation. In theory, this would solve the problem because even though the load cells produced a noisy signal, the averaged mass should remain constant as the error fluctuated around the true hopper mass. Shown in Figure 48 are multiple time step averages. These averages helped to reduce the magnitude of the noise by dampening large spikes in the signal. However, the averages still showed discrepancies of +/- 0.4 lb. With no change to the hopper mass, this averaging technique on the mass taken over time would produce a calculated flow rate of 140 lb/h, which is still unacceptably high relative to the flow rate targeted for the combustion tests.

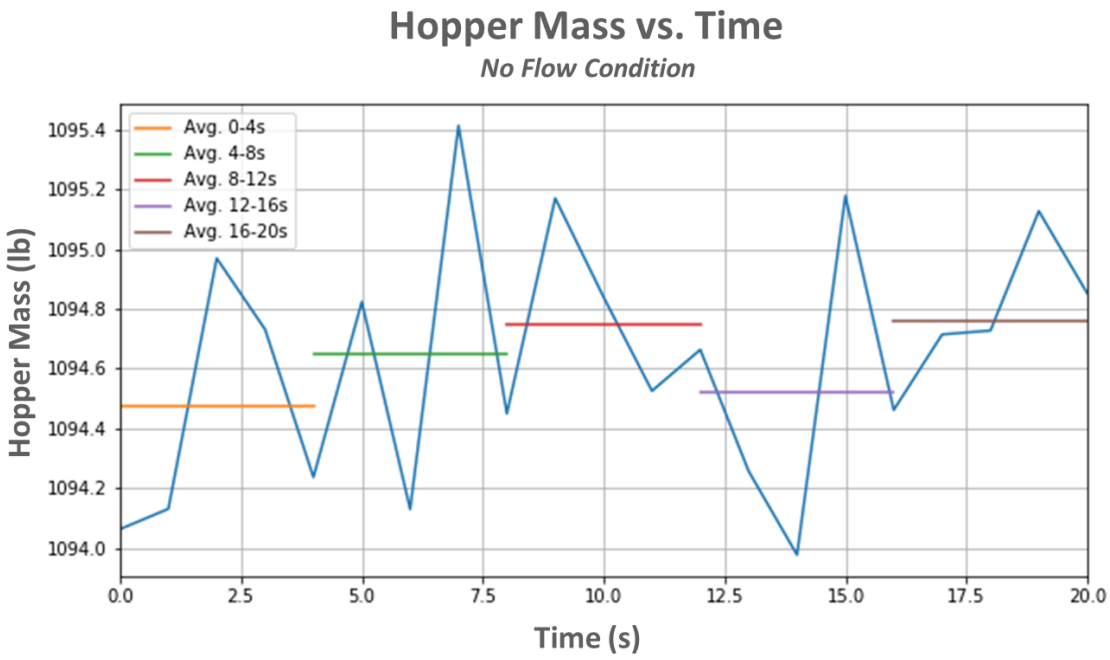

Figure 48. Signal noise for hopper mass measurement with time step averages

An approach to smooth the flow rate calculations is to increase the time step between mass readings as this decreases the impact the signal noise has on the calculated value. This approach by itself is impractical because it has the effect of reducing insight into the operating conditions and limit the ability of the operator to quickly respond to changes in the system. However, a combined approach involving longer time steps between measurements and the averaging technique described above held promise for dampening the signal noise and improving the accuracy of the mass measurement.

In the original averaging technique concept, the control software would delete the recorded mass values and start again from scratch after both mass values were collected and the flow rate calculated. This means that all prior data of the hopper's mass would be lost, and the next flow calculation susceptible to the same amount of noise as the previous.

The averaging technique was adapted to incorporate the ability of the longer time steps to mitigate the signal noise. When a flow rate was calculated, the averaged mass readings were saved to an array. The code would then repeat the flow rate calculation. On the second iteration instead of calculating a single flow rate, the method would calculate two flow rates. The first flow rate being the standard averaging calculation, while the second flow rate was calculated between the current hopper mass and the saved initial hopper mass. This second flow rate is smoothed because the time step is now doubled. This process is repeated every 5 seconds so by the 12^{th} iteration, the flow rate calculation is incorporating mass values collected one-minute prior.

The formula for this approach is Equation 2. This formula was implemented into the strategy and a calibration setup was created. A water-filled bucket was suspended from the hopper and

a constant flow was drained onto a scale. A manual stopwatch was used for calibration and a time interval of 5 minutes was set. Initial mass of the calibration scale was recorded, and the flow calculation strategy was run. The mass flow rate recorded by the calibration scale and the calculated values from the adapted formula were compared. Across 5 separate runs with flow rates ranging from 20 – 75 lb/h, the adapted formula was within +/- 1 lb of the calibration. With the adapted formula, the signal noise was successfully mitigated bringing the +/- 1400 lb/h theoretical maximum error to 1 lb/h.

$$\dot{Q} = \frac{\sum_{n=N-1}^{1} \frac{(M_{n\_}M_N)}{\Delta t \cdot (N-n)}}{N} \frac{3600s}{h} \qquad \mathbf{2}$$

Where $M_1, M_2 \ldots M_N$ is the hopper mass from initial to current N.

The reason this method can produce a sensible value is due to averaging. The adapted formula is the average of the sum of the difference of averages. This means that any sudden changes to the flow rate will not be immediately seen. The magnitude of a sudden change would be dampened in the averaging so it would require some iterations for the change to be noticed. The longer the method runs, the more accurate it would become. Initially, there will be a relatively large amount of signal noise. The calculated flow value would then become more reasonable as more data is collected.

Cold testing of the dry feeding system was accomplished using a high-pressure filter previously used at the ICGRF. The high pressure filter essentially acted as a surrogate for the pressurized reactor, which enabled an assessment of system performance and control. The objective of the cold testing was to establish operational experience and develop control methodologies in advance of the combustion experiments. Development of an understanding of system behavior is greatly simplified and economical when the added complexities associated with combustion in the pressurized reactor is excluded.

The filter assembly shown in Figure 49 was previously used on a fluidized bed gasifier to remove tars at high temperatures. To repurpose the filter, the coal transport line was run to the bottom of the filter assembly where the seven stainless steel candle filters shown in Figure 50 retained the coal that was subsequently carried to the bottom of the assembly. The filtered stream exited the top plenum with system pressure maintained with a back pressure imposed on the filter assembly outlet.

Figure 49. Candle Filter Assembly

Figure 50. Stainless steel candle filters

The collector section of the filter assembly holds up to 120 lb of coal before removal is necessary. The contents of the assembly are emptied through a series of pneumatic lock hoppers. This arrangement allows for retrieval of the transported coal.

Initial transport tests using the candle filter assembly and back pressure regulator was successful as coal was transported through the ¼-inch stainless steel coal feed tube that is inserted through the top of the vessel and penetrates into the fluidization zone of the hopper. The inlet of the feed tube was located 1 inch from the bottom of the distributor cup for these calibration tests.

An additional differential pressure transducer was installed to refine pressure measurements on the system. This pressure transducer has a range of 150 inches of water (5.41 psi) and helps indicate plugging issues in the feed tube. The pressure at the high-pressure port is essentially the hopper pressure and the low-pressure port is at the top of the feed tube where it exits the hopper. Table 8 summarizes the pressure transducers installed on the current coal feeding system. The pressure measurements for the coal feed tests are shown in Figure 51. The feed tube differential pressure transducer is labeled P4.

Table 8. Pressure transducers installed on the coal feeding system

Transducer	Range (psi)	Location	Measurement
P1	725	Hopper top zone	P in the hopper
P2	500	Hopper top zone	P in the hopper
P3	725	Transporting line above reactor	P in "reactor"
ΔP1	27.1	Between hopper outlet and "reactor"	ΔP between hopper outlet and "reactor"
ΔP2 (P4)	5.41	Between hopper inside and feed tube top	ΔP on vertical feed tube

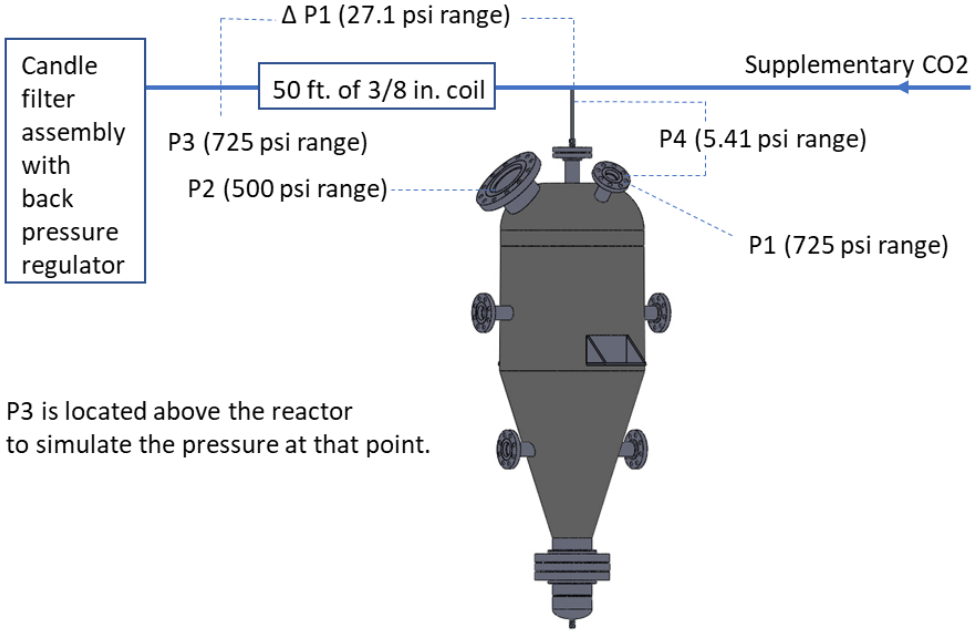

Figure 51. Coal feed tests pressure measurement points

In the event the system will need to be depressurized quickly, an exhaust line was installed. Figure 52 shows the exhaust line in relation to the hopper and the candle filter. A bag filter has been installed prior to the gas outlet to collect coal particles carried by the gas.

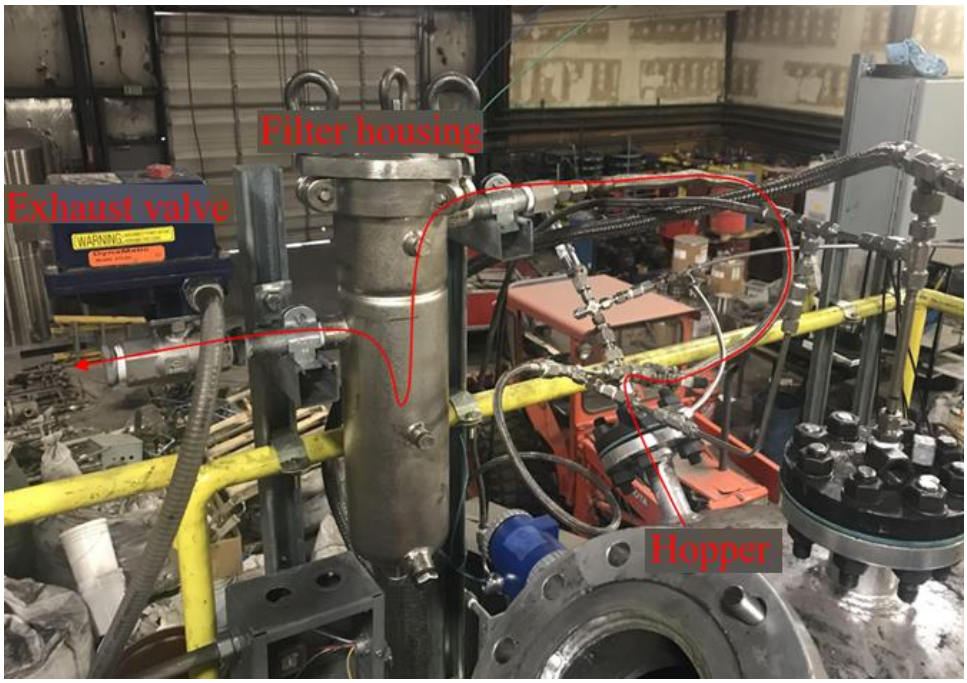

Figure 52. Exhaust line on the hopper

A camera was installed to observe the visualization tube on the coal transport line in order to remotely monitor the coal flow. Figure 53 shows images of the tube with no coal flowing versus a time when coal was transported through the tube.

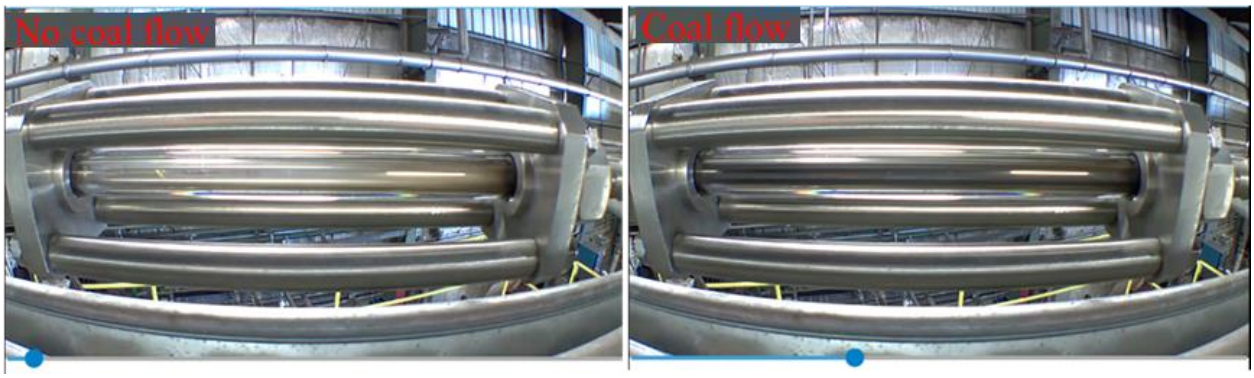

Figure 53. Visualization tube on transporting line (left: no coal flow; right: with coal flow)

The system as shown in Figure 54 was used for the high-pressure coal transport tests. The back pressure at which the coal was fed from the hopper into the candle filter was controlled by a regulator at gas outlet. The pressure measurements in Figure 54 represent hopper pressure (P1, P2), back ("reactor") pressure (P3) and pressure difference between the hopper outlet and the "reactor" (ΔP1), which are described in Figure 51 and Table 8.

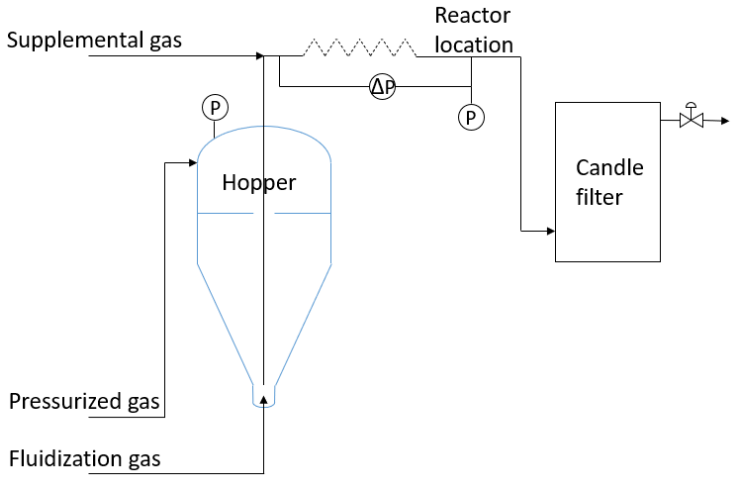

Figure 54. High-pressure coal feeding test system

Initially, some pressure measurements were taken without coal feeding to ensure the system was appropriately pressurized. Table 9 shows pressure drops under various flow conditions for the fluidization, pressurization, and supplemental CO_2 streams. Included in the tests were design target rates for 250 psi operation: 58 lpm for the fluidization CO_2, 20 lpm for the pressurization CO_2 and 370 lpm for supplemental CO_2. A test run at the target flow rates produced a 5.68 psi pressure drop across the transport line from the hopper outlet to the reactor location. The pressure drops recorded over the matrix of tests indicate that the system is adequately pressurized with proper controls over the respective CO_2 inlet streams.

Table 9. Pressure measurements of CO_2 flow in the feeding system under high pressure

Back pressure (psi)	Fluidization CO_2 (LPM)	Pressurization CO_2 (LPM)	Supplemental CO_2 (LPM)	Hopper Pressure (psi)	ΔP (psi)
50.0	15	5	100	53.6	3.23
99.8	25	10	150	103.4	3.08
150.2	35	15	230	154.9	3.91
200.3	45	20	300	206.4	4.83
250.6	58	20	370	257.1	5.68
300.4	70	20	257	303.9	2.91

Two configurations were used for these initial coal feeding tests. The first configuration involved the geometrical description of the dry feed system provided above and coal with a fineness of 70% passing 200 mesh (74 μm). The coal feeding test for Configuration 1 at 250 psi back pressure was started with CO_2 flow rates being set at the target values. Illinois #6 bituminous coal with 4.48% moisture (as received) was loaded into the hopper and tested. Over the course of 11 minutes, coal was fed at rates varying from 188 to 299 lb/h. CO_2 flow rate, hopper weight and pressure measurements are shown in Figure 54, Figure 55, and Figure

56, respectively. The coal feed rate is calculated based on hopper weight loss measured by filtered load cell readings.

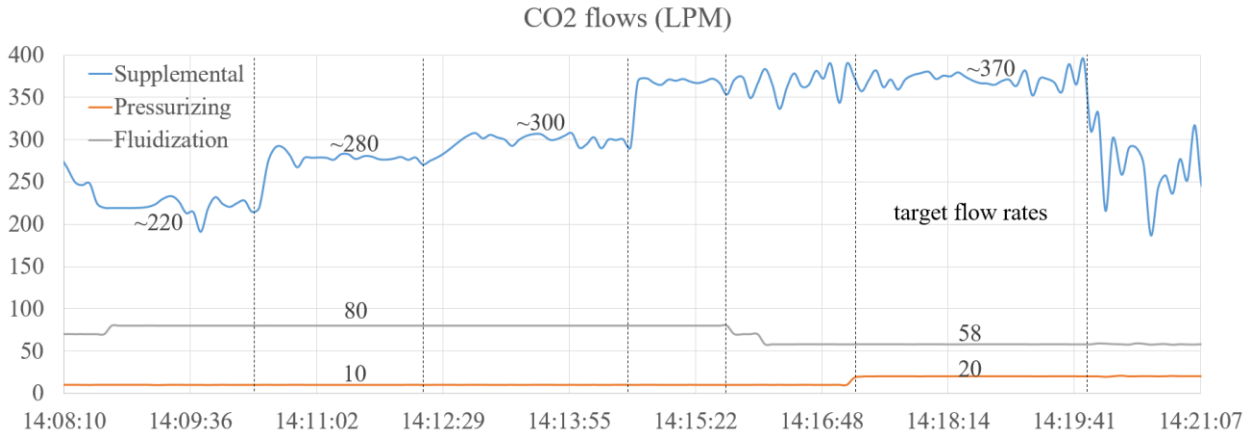

Figure 55. CO_2 flows during coal transport tests at elevated pressure for test Configuration 1

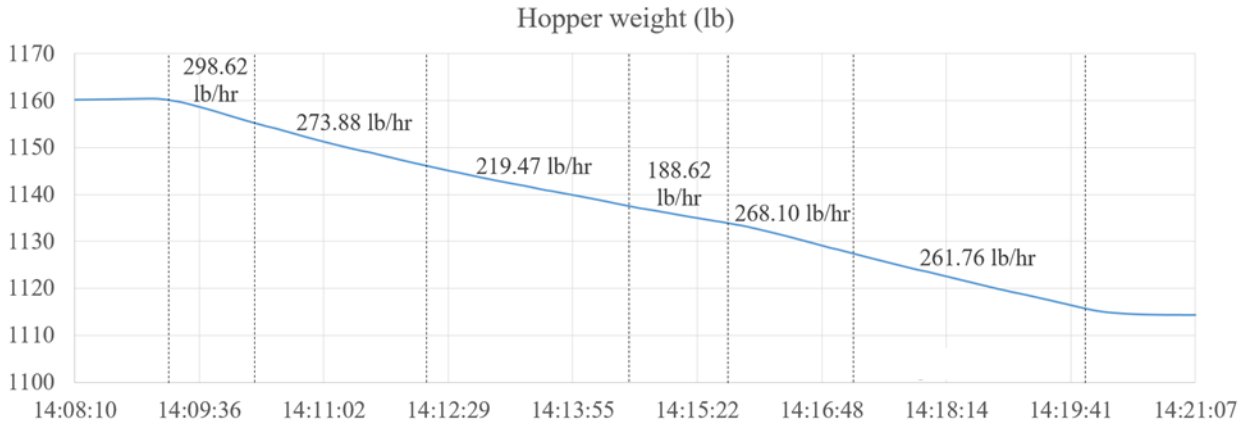

Figure 56. Hopper weight during coal transport tests at elevated pressure for test Configuration 1

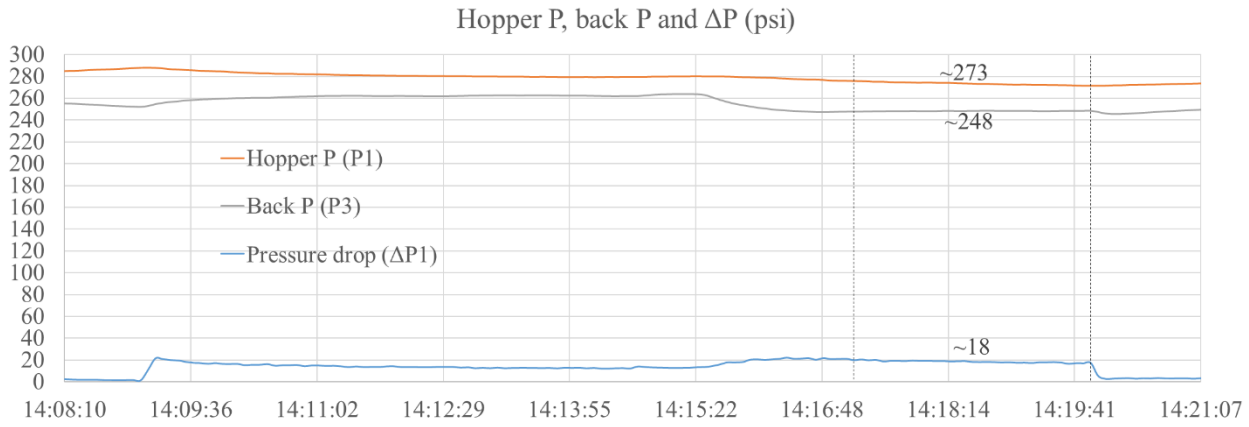

Figure 57. Pressure measurements during coal transport tests at elevated pressure for test Configuration 1

As shown in Figure 56, the 3-minute time window at the target flow rates yielded a feeding rate at 261.76 lb/h which is much higher than the target ~60 lb/h at 200kW firing rate. After the test transported all the coal from the hopper to the candle filter, the system was depressurized, and the coal was recovered from the filter lock hoppers and loaded back into the feeding hopper. In a subsequent test, plugging of the vertical feed tube occurred. This led to the modifications in Configuration 2. The original ¼-inch feed tube was replaced with a ⅜-inch tube to provide a larger cross-sectional area, and the coal was sifted through a 30 mesh screen (590 μm) to remove large particles that may be contributing to clogging of the transport line. When the coal was sifted, a noteworthy quantity of particles were retained and subsequently removed from the batch.

After the larger vertical feed tube had been installed and finer coal feedstock introduced into the hopper, a test was conducted at 250 psi. As shown Figure 58 - Figure 60, the feeding time window of 48 minutes is divided into three stages. In stage 1, the coal feeding was started and maintained by the supplemental gas, with or without fluidization/pressurization gas. As shown in Figure 60, lowering the back pressure induced coal flow with a ΔP between 10 and 20 psi. During stage 2, behavior was observed with fluidization gas at 3 set points: the 58 lpm target value, and lower flows of 40 lpm and 20 lpm. As the fluidization gas flow was varied, the supplemental CO_2 was held constant at 100 lpm and the pressurization gas set to 0 lpm. In stage 3, the supplemental CO_2 mass flow controller gave stable flows only when the hopper pressure was below 240 psi (back pressure below 232 psi). During this stage, the coal feeding rate was approximately 167 lb/h with ΔP at 8.34 psi.

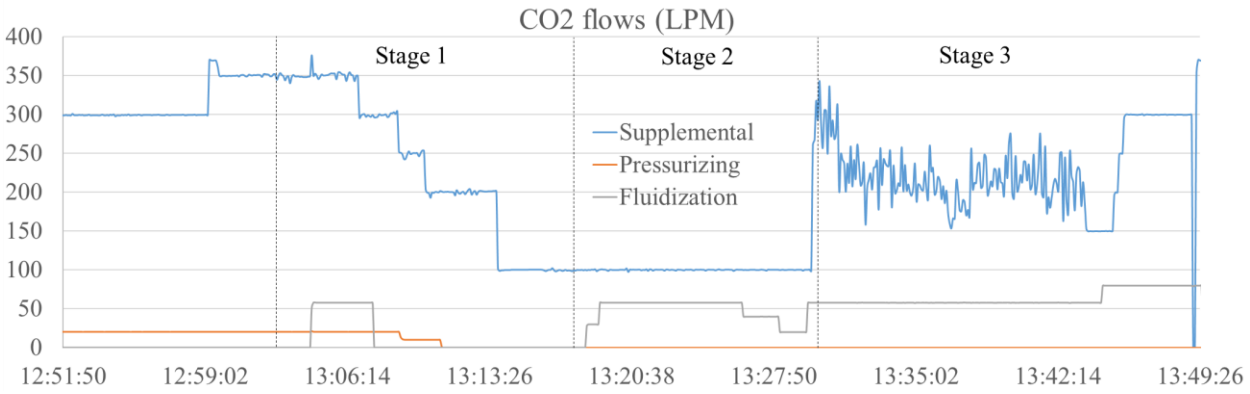

Figure 58. CO_2 flows during coal transport tests at elevated pressure for test Configuration 2

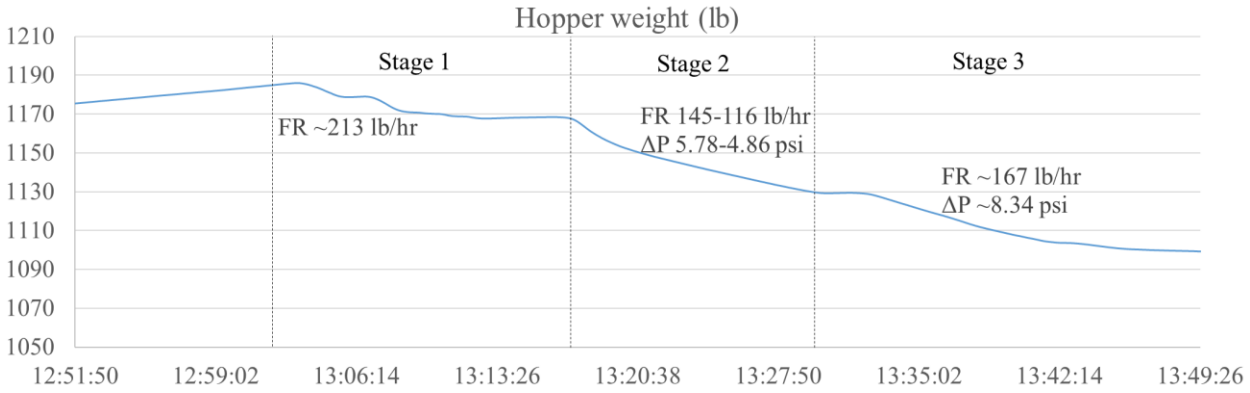

Figure 59. Hopper weight during coal transport tests at elevated pressure for test Configuration 2 (FR = Feed Rate)

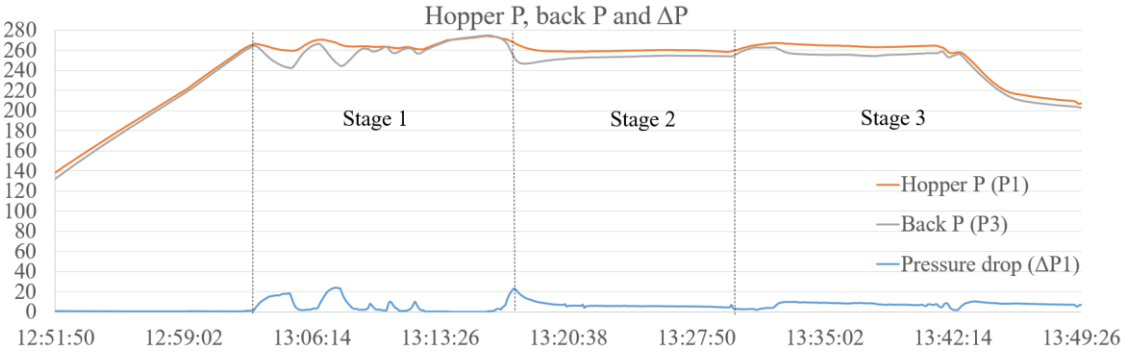

Figure 60. Pressure measurements during coal transport tests at elevated pressure for test Configuration 2

Figure 61 depicts the coal feeding rate calculated as hopper weight loss during stage 2 of the 48 minute run where the fluidization CO_2 flow rate was varied. Measurements indicate that a lower fluidization flow rate reduces the coal feeding rate as the supplemental and pressurization gas flows are held constant. This may suggest that the best approach is to use lower fluidization flow in combination with higher supplemental gas flow to reduce the coal feeding rate to the desired range while staying above the saltation velocity in the transport lines.

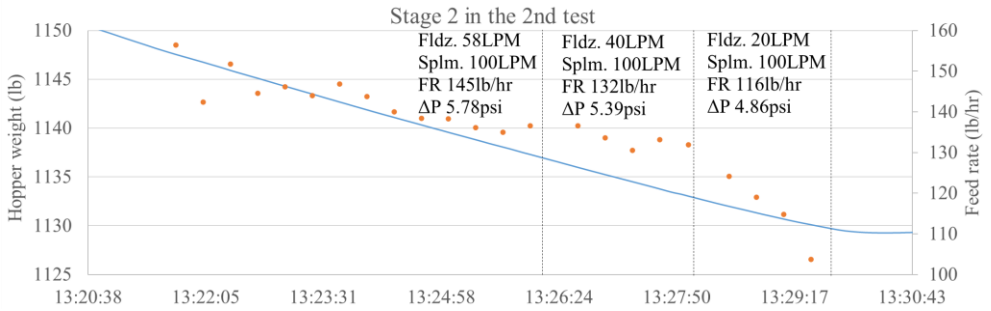

Figure 61. Coal feeding rates in Stage 2 during tests with Configuration 2

The challenges encountered in reducing the coal feed rate to the desired range, prompted several modifications to the system including the coal transport lines, valving and flow regulators. Regarding the coal transport lines, the feed tube in the center of the pressure vessel was changed back to a ¼-inch stainless steel tube with 0.035 inch wall thickness since the ⅜-inch feed tube that was previously in place entrained too much coal at low hopper/filter assembly pressure differences. In addition to a smaller diameter feed tube, the coil used to create a pressure drop was replaced. The existing coil was 50 feet of ⅜-inch tube. This tube was replaced with 40 feet of ½-inch x 0.035 wall stainless steel tubing. This reduced the back pressure on the supplemental CO_2 line. These modifications are shown in Figure 62.

Upon startup, the feed hopper and the candle filter assembly (surrogate for the reactor) are pressurized simultaneously, which necessitated the introduction of the burner secondary CO_2 between the overhead pneumatic safety ball valve and the candle filter assembly. With the overhead pneumatic safety ball valve closed, the filter assembly and hopper can be pressurized by the burner secondary CO_2 and pressurizing/supplemental CO_2, respectively. The ball valve is opened when both the filter assembly and hopper are pressurized, and a reasonable pressure difference is achieved.

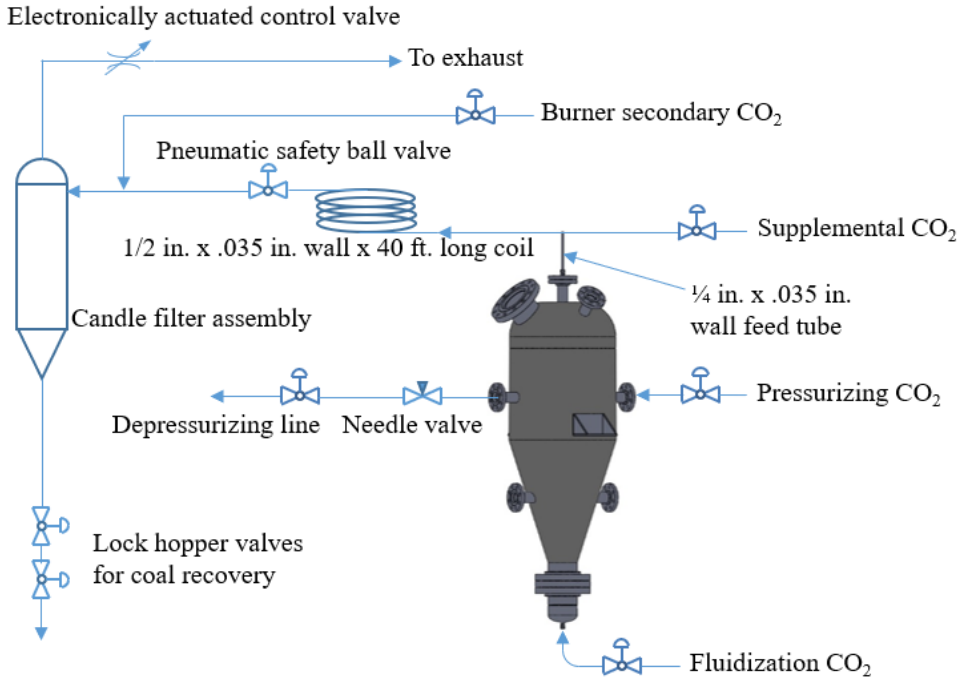

Figure 62. Modifications to Dry Feed coal delivery system

A needle valve was installed on the outlet of the depressurizing line on the feed hopper. The flow from this line was formerly controlled with a manual ball valve. The needle valve allows for finer control of the hopper pressure as well as slower depressurization. The candle filter assembly pressure was previously controlled with a manual back pressure regulator, but this manual approach produced instabilities in the hopper/filter pressure differential. The back pressure regulator was subsequently removed and the filter exit was plumbed into an

electronically actuated control valve. In previous experimental campaigns gasification and combustion campaigns involving the pressurized reactor, the Badger valve shown in Figure 63 was used to control the pressure inside the reactor by restricting the high-pressure exhaust. Use of this valve is a superior option to the manual back pressure regulator as it can be controlled in the distributed control system, OPTO 22, which will allow for much better control over the filter/hopper pressure differential.

Figure 63. Electronically actuated control valve (Badger valve)

An update to the dry feed pressure measurement points is shown in Figure 64. Previously, the hopper/reactor differential pressure was measured between the candle filter inlet and the point where the feed tube connects to the supplemental CO_2 line above the hopper. This arrangement resulted in unstable pressure differential measurements. The high side of this pressure differential, the hopper, was moved from the top of the feed tube to the hopper body. This change provided a more representative measurement of the pressure differential and better control.

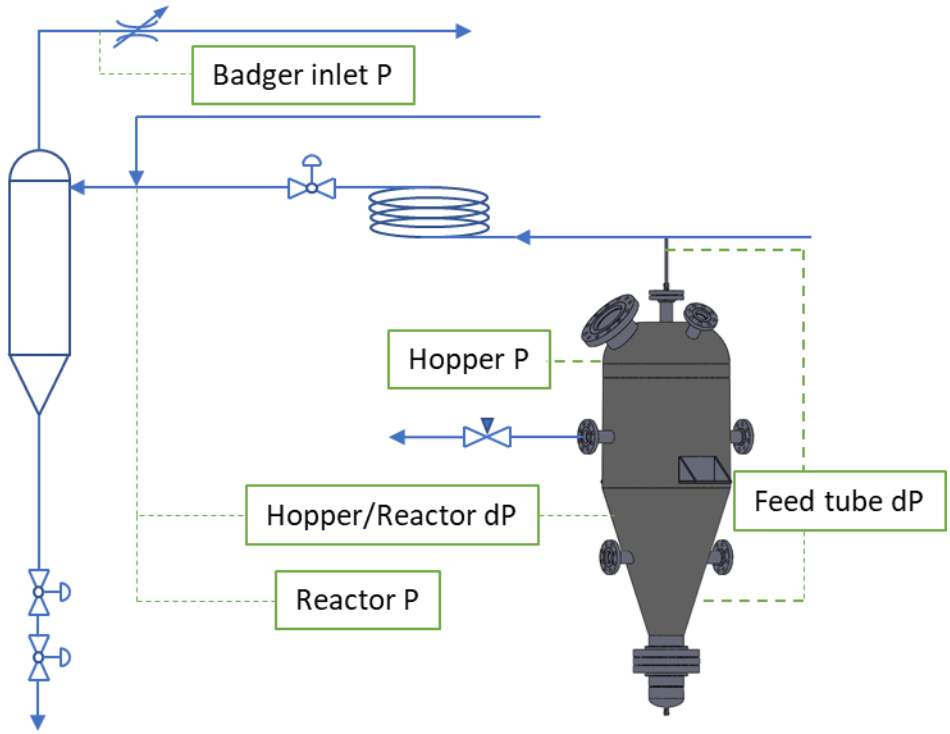

Figure 64. Dry Feed pressure measurement locations

A pressure transducer was located at the inlet of the electronically actuated control valve. This provided an indication of the pressure drop across the filter elements of the candle filter housing. The filter has no pulse jets to blow the coal off the elements and this pressure differential is an indicator of the filters plugging.

Instability observed in the coal flow led to the supposition that poor fluidization was occurring above the sintered distributor cup. To confirm this assertion, the feed hopper plenum was removed and inspected. The plenum was placed on a bench and the fluidization CO_2 line was connected and run though the cup. The fluidization was not uniform and showed a circular pattern around the periphery of the cup. Upon closer inspection, it was found that the majority of the CO_2 leaked through the rubber gasket between the cup and the mounting flange, which short-circuited the fluidization. Figure 65 shows the cup flange assembly and the uneven fluidization caused by the circular leak.

Figure 65. Cup flange assembly (left) and uneven fluidization pattern caused by gasket leaks on sintered cup (right)

Different gasket materials were attempted to stop this leak to no avail. As a next step, the cup and flange were taken to a welding and machine shop at the University of Utah where an attempt was made to weld the cup to the flange. Due to challenges working with sintered metal, the welds were not successful at eliminating the short circuit and the circular pattern persisted. To reduce leakage around the edges of the cup, an epoxy product commercially named JB Weld was applied to the outer edges of the cup. This stopped the perimeter leaks and created a more evenly distributed fluidization CO_2 gas. As shown in Figure 66, the sintered cup is now connected to the mounting flange by welding, instead of using bolts and gaskets. The photo on the right shows the improved fluidization of the coal particles.

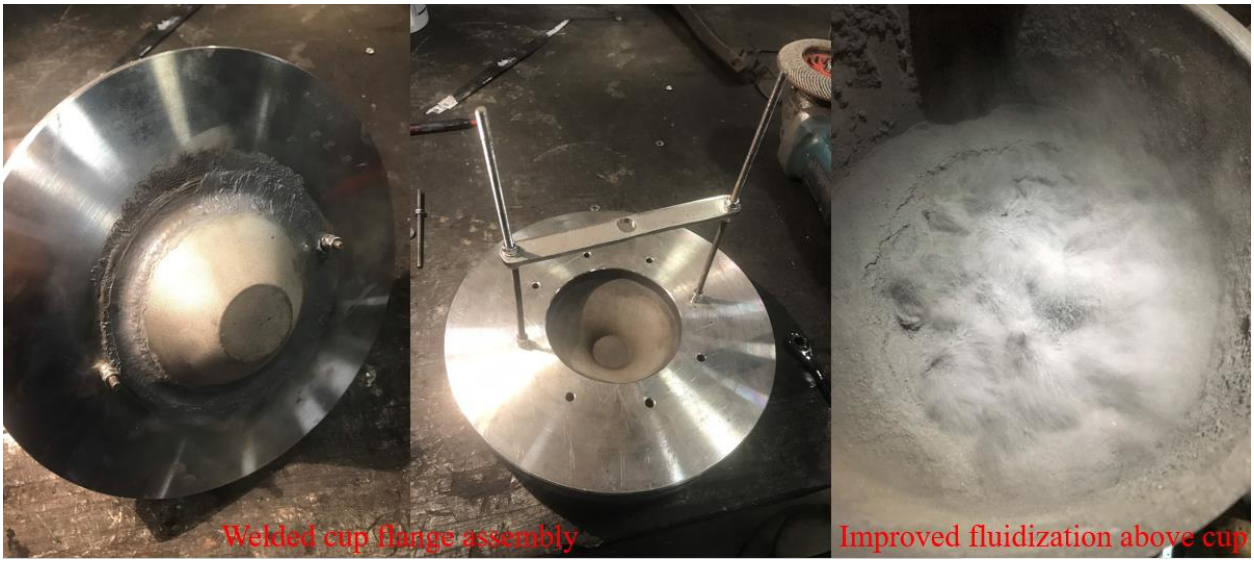

Figure 66. The welded cup flange assembly and improve fluidization.

P&ID of EFPR System

The piping and instrumentation diagram for the EFPR system is shown in Figure 67. It illustrates the process flows, measurements and control equipment in the system. The dry feeding of pulverized coal and aerosol sampling system are integrated within this system. Each pipeline, valve and instrument on the P&ID is assigned a specific number, which are labeled accordingly in the physical system for operation convenience.

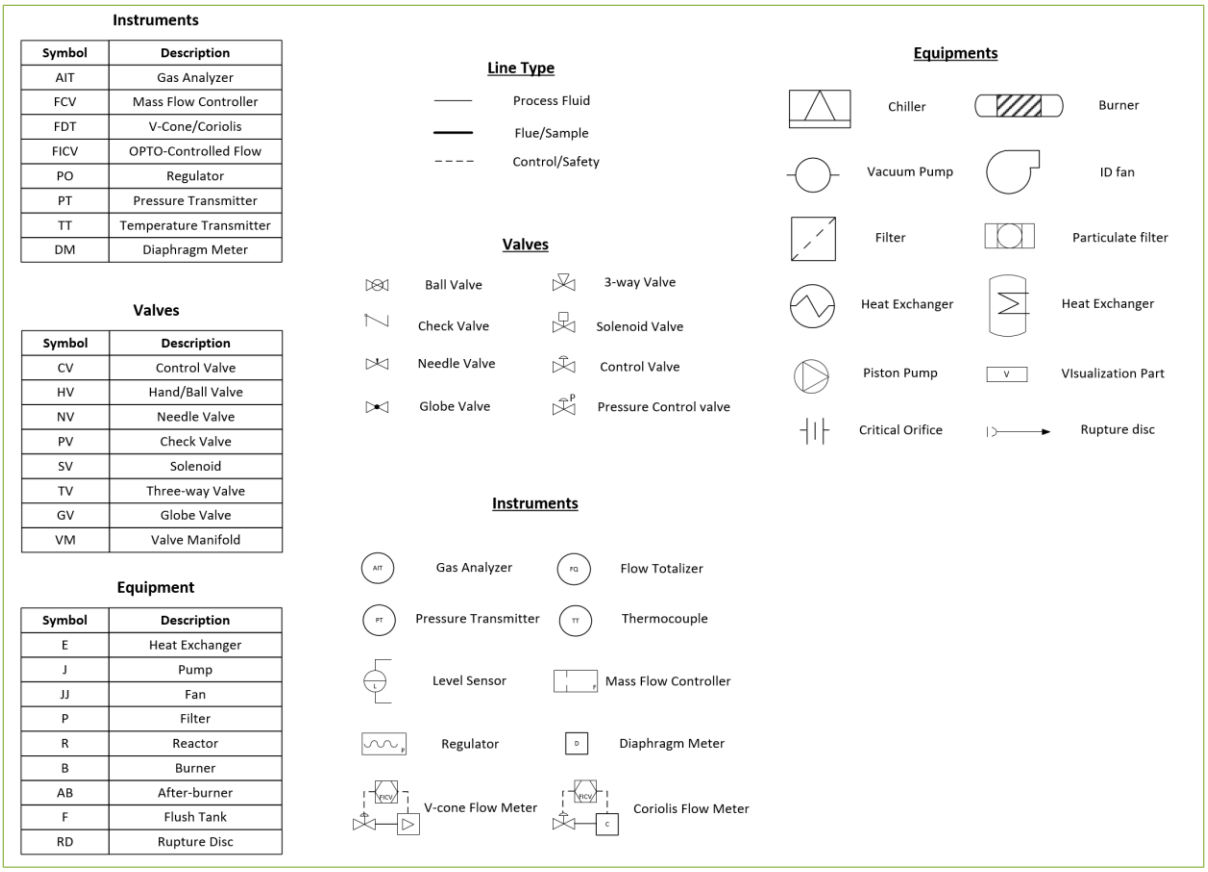

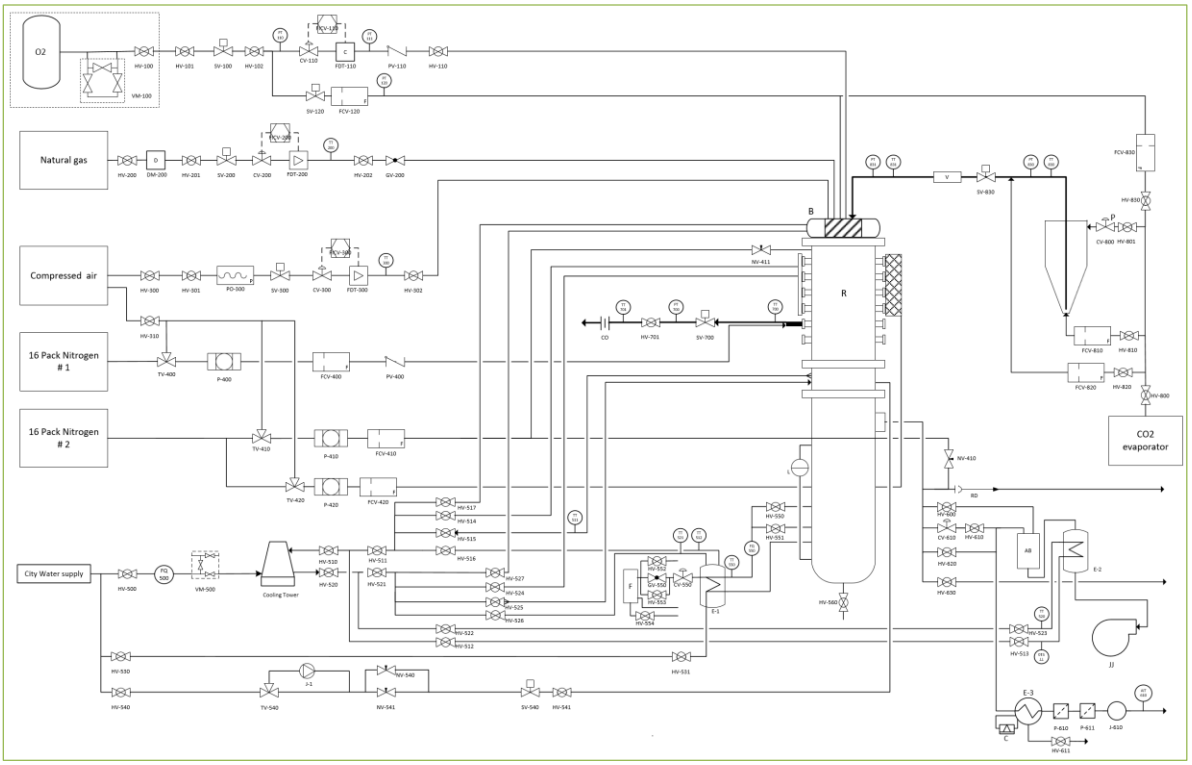

Figure 67. P&ID of dry feeding EFPR

Testing Coal Transport at High Pressure

Multiple tests were conducted to transport coal from the hopper to the candle filter assembly under high pressure conditions. Tests in the early stage yielded high feed rates, all above 100 lb/h, similar to those previously reported and thus will not be reported here. With all the above modifications except for the depressurizing needle valve, candle filter outlet control valve and the replaced coil, some tests produced coal feed rates over a wide range from 13 lb/h to 150 lb/h. Figure 68 and Figure 69 show the hopper weight loss and hopper/reactor dP during tests of reactor pressure at 200 and 230 psi, respectively. The feed rate (FR) and dP values labeled on the figures are averaged over the corresponding time period.

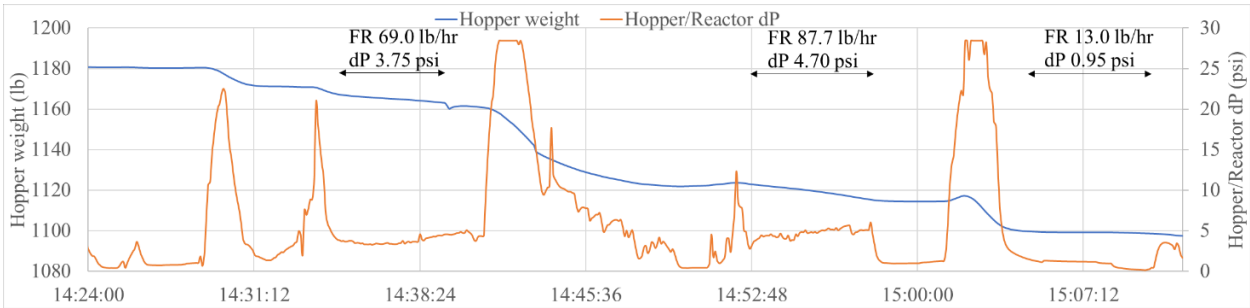

Figure 68. Test results at 200 psi reactor pressure

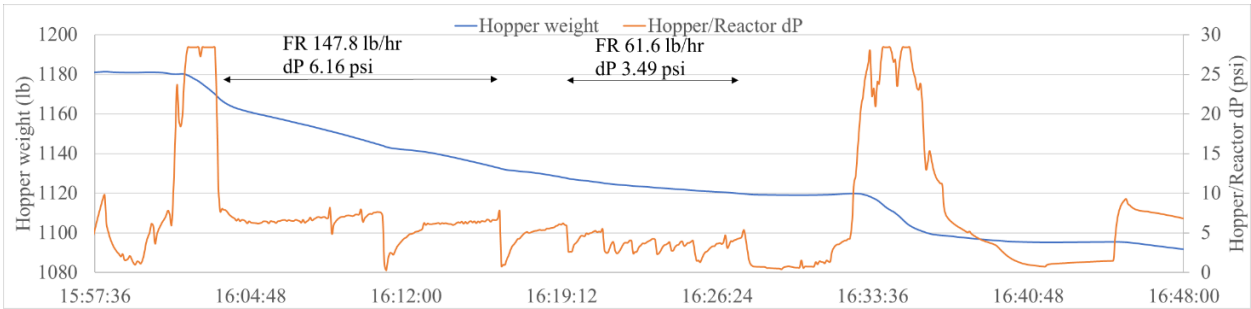

Figure 69. Test results at 230 psi reactor pressure

The coal feed rates are plotted with dP in Figure 70. In spite of the different conditions, these data show a linear relationship between the two variables; suggesting the feed rate is strongly dependent on the pressure difference between the hopper and reactor.

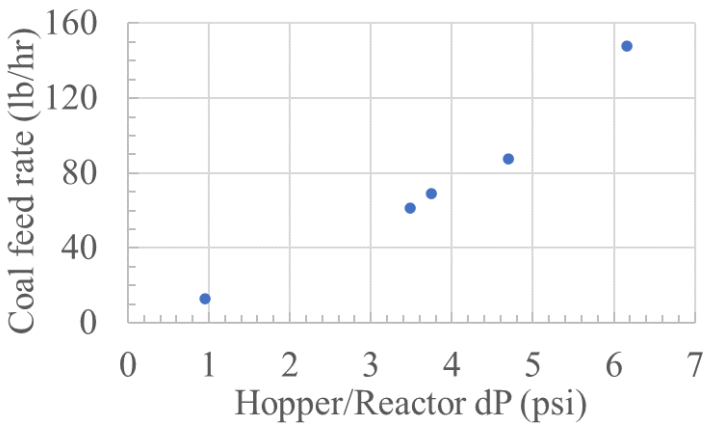

Figure 70. Coal feed rate versus dP

After adding the depressurizing needle valve, candle filter outlet control valve and replacing the coil tube, another test of reactor pressure at 215 psi was completed. Figure 71 shows an averaged feed rate at 72 lb/h over a time span of 26 minutes with corresponding flow rates for supplemental gas, pressurizing gas, and fluidization gas shown in Figure 72.

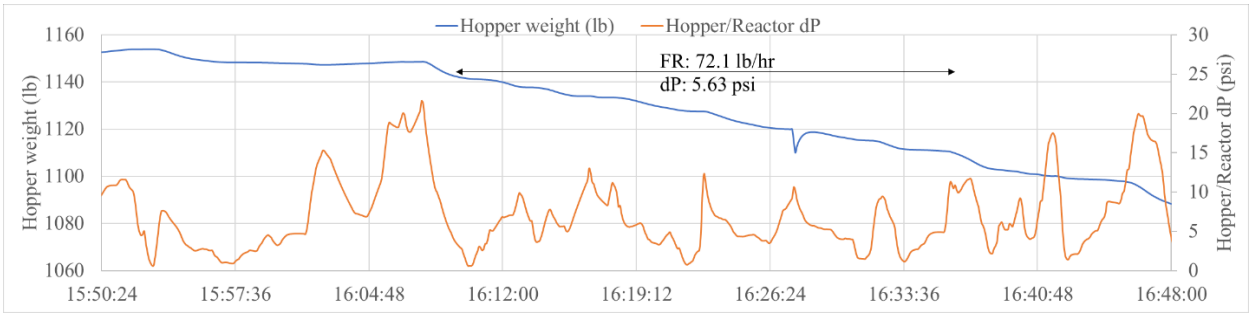

Figure 71. Coal feed rate and hopper to reactor dP at 215 psi reactor pressure after additional system modifications.

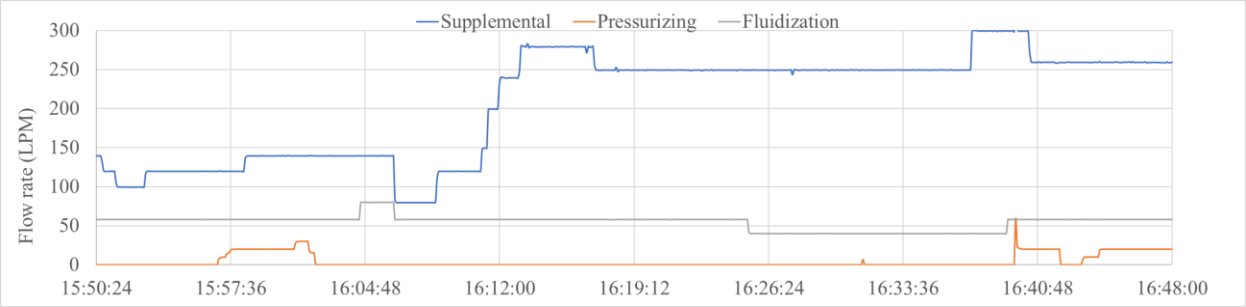

Figure 72. Flow rates for supplemental, pressurizing, and fluidization CO_2 at 215 psi reactor pressure after additional system modifications.

From the results above, it is clear that the coal feed rate is sensitive to the hopper to reactor pressure difference. A feed rate of 60 lb/h, corresponding to the target firing rate of 200 kW for Utah Sufco coal, can be produced when the dP is maintained around 3.5 psi under these test conditions. The tests also showed the coal feed stopping when dP is reduced below 0.5 psi.

With the improvements made to the system, it was shown to be able to achieve a coal feed rate within the target range for the testing campaigns. Although a feed rate of 60 lb/hr could be achieved when the pressure difference is reduced below 4 psi, it was subsequently learned that maintaining such a low dP was found to interfere with the operation of stabilizing the feeding process. The dP running at the lower end of the transducer range, 27.1 psi, limited the control capacity. And increased the risk of halted feeding in the event that the dP unexpectedly reduced to near zero. Therefore, an effort was made to increase the dP to an acceptable value while still yielding a desired coal feed rate under the 200kW firing condition.

The total length of the coil used to create pressure drop for coal feeding was extended to 90 feet although the two parts of the coil have different inner diameters. As shown in Figure 73, the original 50 feet of ⅜-inch coiled tube was connected to the existing 40 feet of ½-inch coil. This greatly increased the pressure difference between the hopper and the reactor (dP), without causing any clogging problems with the coal.

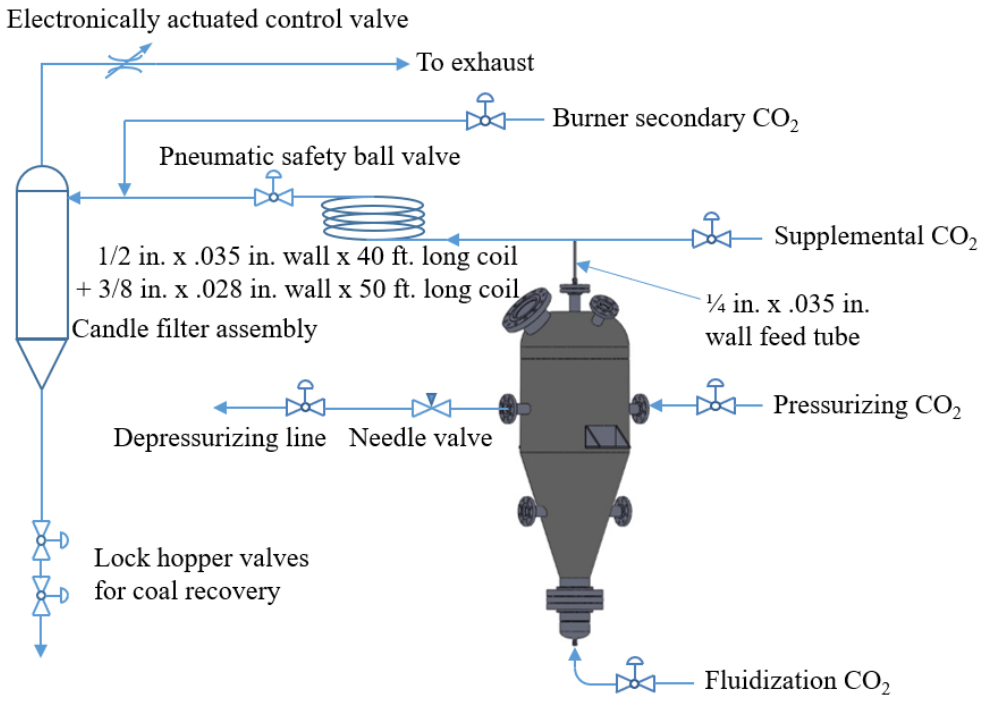

Figure 73. Demonstration of the dry feed coal delivery system

The welded sintered cup and flange assembly was tested and verified to provide improved fluidization at the bottom of the hopper. An alternative design shown in Figure 74 replaced the original distributor cup. The key component of this modified design is a sintered metal disk (the dark gray material in the figure) sandwich mounted between the hopper flanges and sealed

with multi-layer gaskets. The plenum assembly with the sintered disk was initially tested on a bench with CO_2 flowing through the disk, which was shown to create a uniform gas distribution for coal bed fluidization. Due to the consistency in the coal bed fluidization observed with the sintered disk approach, this configuration was maintained as the CO_2 fluidization method during subsequent tests. In addition to modifications to the fluidization apparatus, different insertion depths of the vertical feed tube were attempted. These modifications helped change the density of the coal stream uptake into the feed tube.

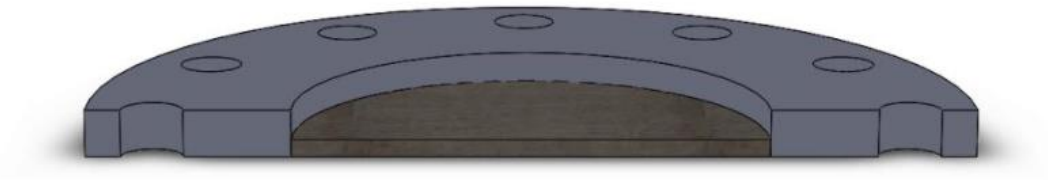

Figure 74. Sectional illustration of the sintered disk (not dimensioned).

Tests with the new fluidization apparatus and varying feed tube location followed the same procedure described for the preceding tests. The hopper and the candle filter representing the reactor were separately pressurized with CO_2, and then connected by opening the middle pneumatic valve to enable the coal feed process. Several test runs were completed, and the test described below provides a representative sample of those tests. Figure 75 shows the flow rates of the supplemental, pressurizing and fluidization CO_2 streams. The mass flow controllers provided stable flow rates up to 350 LPM under these backpressure conditions. During the test, the supplemental and fluidization rates were unchanged while the pressurizing gas was periodically adjusted to control the hopper pressure.

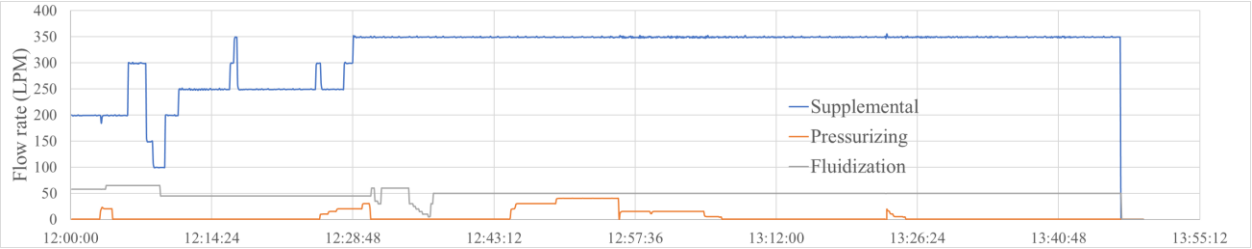

Figure 75. Flow rates of the three CO_2 streams.

The hopper weight and the hopper/reactor pressure drop (dP) are depicted in Figure 76. The feeding process is divided into several finer time periods labeled with respective FR (feed rate) and dP values that are averaged over the corresponding period. It is clear to see that the feed rate is dependent on the pressure difference. In the current system, a 60lb/hr coal feed rate is reached when dP is around 17 psi. Compared to previous tests, this gives more room for hopper pressure control, which will directly affect the coal feed rate during combustion.

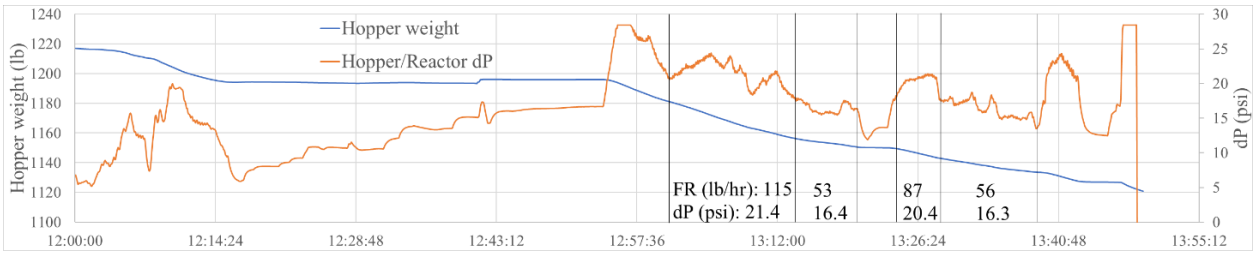

Figure 76. Hopper weight and pressure difference (dP) labeled with feed rate (FR)

Figure 77 shows the hopper and reactor pressures during the test. The operating pressure was set below 170 psi due to safety concerns on the sealing gaskets of the sintered metal disk. The reactor pressure was 145±5 psi during the coal feeding process. In these tests, efforts were made to maintain the reactor (downstream candle filter) pressure, followed by the hopper pressure. The objective was to stabilize the two pressures while maintaining a constant pressure difference, which would consequently keep the coal feed rate stable at the target firing rate. This objective had to be achieved for us to confidently begin combustion tests with a stable flame. As it became apparent that the problems encountered with unstable coal flow would not be solved under the program's time and budget constraints, REI invoked its risk management strategy and sought alternatives for performing pressurized oxy-coal experiments. This resulted in a collaboration between REI and Brigham Young University (BYU) who had developed a pressurized dry coal feed system of their own in a separate DOE-funded project. The outcomes of those tests are described in the following section entitled Task 5 – Pressurized Testing with Minimal CO_2 for Coal Transport.

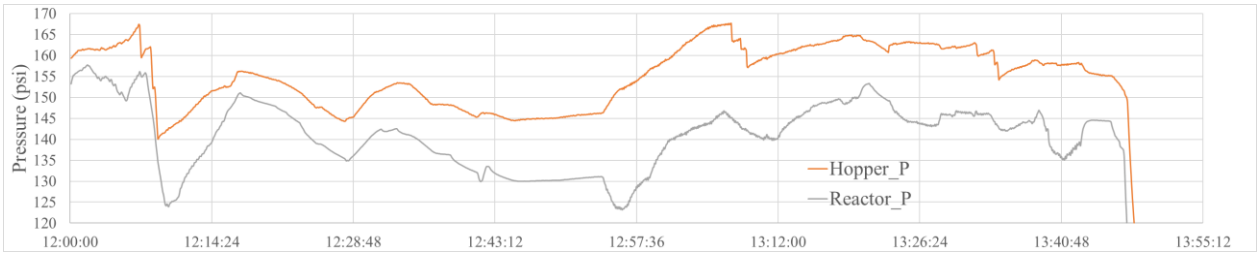

Figure 77. Hopper and reactor pressures during the test

Task 2 Summary and Conclusions

Project partner Southeast University developed a design for a pulverized coal dry feed system based on design specifications from the University of Utah. Although SEU had demonstrated controlled feed of coal powder under pressurized conditions for gasification applications using a similar design, this would be the first time that this design would be used for oxy-coal combustion. The design centered on a cone-shaped pressure vessel approximately 5 feet high and 2 feet diameter. The vessel serves both as the fuel hopper and as an integral part of the feed system. Three pressurized gas lines carrying CO_2 are used to pneumatically convey the pulverized fuel and balance the pressure around the system. REI and the University of Utah carried out both physical model and CFD-based assessments to gain a detailed understanding of

behavior of coal particles in the fluidization zone and within the hopper overall. Prior to combustion tests in the UofU entrained flow pressurized reactor (EFPR), non-reacting or "cold" tests were conducted in order to obtain operational experience with coal transport using the pressurized system. A relationship between pressure drop between the coal hopper and the reactor, and coal flow rate was developed from the cold tests. Over the course of many experiments attempting to stabilize a coal flow rate appropriate for the combustor, it became clear that a system pressure drop of 4 psi would produce the target coal flow rate near 60 lb/h (approximately 200 kW firing rate with the Utah bituminous coal. Although the target coal feed could be achieved with this dP, it was observed that maintaining such a low dP corresponded to unstable coal transport. Instability and unpredictable coal flows would conflict with achieving the stated objectives for pressurized oxy-coal experiments. As it became apparent that the problems encountered with unstable coal flow at the University of Utah facility would not be solved under the program's time and budget constraints, REI invoked its risk management strategy and sought alternatives for performing pressurized oxy-coal experiments. This resulted in a collaboration between REI and Brigham Young University who had developed a pressurized dry coal feed system of their own in a separate DOE-funded project.

Task 3 – Pressurized Reactor Preparation

Objective: Modify, as necessary, the instrumentation and flue gas handling equipment for use in the proposed high pressure oxy-coal combustion conditions.

Prior to operation of the Pressurized Oxy-Coal Combustor (POC) for this program, there were many maintenance and upgrade activities that were required. The furnace had previously been used for a DOE -funded project (DE-FE0029157). The POC was left with deposited ash build up in the region of the quench spray, and in the pressure relief nozzle in the converging cone at the bottom of the reactor. Additionally, there was slag build up in the slag tank and fouling of the pressurized heat exchanger by ash. Portions of the reactor were disassembled or removed to clean each of these components. During the last phase of testing for the preceding program, it was determined that the coal feed rate was most impacted by the pressure differential between the pressurized fluidized bed feeder and the POC. This pressure differential proved to be difficult to maintain within the desired threshold when the operating pressure of the POC was not steady. To rectify this problem, the PID control on reactor pressure was tuned using the throttling valve. This proved to be a critical fix for operating at steady fuel feed rates.

Modifications to the furnace and ancillary equipment were necessary to install the REI corrosion/deposition probe on the POC. The probe was to be installed on the fifth port level from the burner. Although the nozzle and flange were available for this purpose, the refractory had not yet been cut to allow access through this port. We used a diamond core bit to core out the refractor in line with the desired port. The REI probe was cooled using CO_2 from the BYU microbulk tank. The plumbing on the CO_2 delivery system was reconfigured to provide a CO_2 stream with its own pressure regulator for the probe. Plumbing was also installed to direct the CO_2 exhaust from the probe into the reactor ventilation system. The CO_2 cooling system inlet and outlet posed a safety risk to operation of the system. If the pressure seals on the corrosion element were to fail, the flue gas from the reactor would have had a direct path out of the system through these access points. Therefore, a check valve was installed on the inlet and an automatic (normally closed) ball valve was installed on the outlet. Downstream of the ball valve a thermocouple was inserted into the exhaust stream. The ball valve and thermocouple were incorporated into the OPTO 22 control system. The temperature measured by the thermocouple was continually monitored and if it registered above a threshold, indicating a flue gas breach, the ball valve would immediately be closed. Once the corrosion probe monitoring and safety systems were integrated into the OPTO 22 controls system, they were tested.

Additional routine maintenance was performed to prepare the POC for operation. The fluidized bed section of the dry feed system was disassembled. The distributor screen was inspected and residual large particles that had accumulated during the previous operation were cleaned out. The pressurized shell and tube heat exchanger was disassembled, and ash deposits were cleaned off the tubes. The lock hopper and valves were also cleaned out. The optical access windows were cleaned and reinstalled. After the furnace was fully reassembled it was pressure tested. The gas analyzers were also calibrated.

Task 3 Summary and Conclusions

Prior to operation of the Pressurized Oxy-Coal Combustor (POC) for this program, there were several repairs and upgrades to the system were required. A notable upgrade addressed instability on system pressure and coal feed through an improved approach on the reactor pressure control using the throttling valve.

Modifications to the furnace and ancillary equipment were necessary to install the REI corrosion/deposition probe on the POC and provide CO_2 to cool the probe. Additional maintenance was performed to prepare the POC for operation, including:

1. The fluidized bed section of the dry feed system was disassembled to inspect the distributor screen and remove residual large particles that had accumulated during previous operation.
2. The pressurized shell and tube heat exchanger was disassembled and cleaned.
3. The lock hopper and valves were cleaned.
4. Optical access windows were cleaned and reinstalled.
5. The reassembled furnace was pressure tested.
6. Gas analyzers were calibrated.

Task 4 – Design, Installation, and Shakedown of EFPR Burner

Objective: Design, construct and successfully operate a new dry feed EFPR firing system.

Potential burner design concepts for dry pulverized coal-fed pressurized combustion were initiated with a survey of the literature on firing systems for pressurized combustors. Commercial experience with dry feed burner concepts for high pressure combustion of pulverized coal is limited, but the team applied its experience with atmospheric pressure commercial dry feed systems and with high pressure gasifiers to develop preliminary burner design concepts. Conceptual designs were focused on producing stable flames and a heat flux profile suitable for the tolerances of the combustion equipment.

In a parallel path, models developed and experimental data gathered from the EFPR with a slurry-fed burner in a separate DOE-funded program (DE-FE0025168) provided valuable operational experience for pressurized oxy combustion. Lessons learned from the slurry-fed combustion studies were then applied to further refine the conceptual designs. REI leveraged the existing model of the EFPR with a slurry-fed burner to gain insight into high pressure oxy-coal operational conditions. The numerous operational challenges associated with slurry-fed oxy-coal combustion at high pressure provided valuable guidelines for determining conceptual designs of the dry feed burner.

CFD Modeling of the EFPR

REI's proprietary CFD code, *GLACIER*, was used in this task. *GLACIER* simulates reacting and non-reacting flow of gases and particles, including gaseous diffusion flames, pulverized-coal flames, liquid sprays, coal slurries, isothermal and reacting two-phase flows, injected sorbents, and other oxidation/reduction systems. *GLACIER* has been applied to a wide variety of industrial and utility systems encompassing utility boilers, pyrolysis furnaces, gas turbine combustors, rotary kilns, waste incinerators, smelting cyclones and others. These applications have been used for basic design, problem solving, pollution control, etc. using many different fuels including natural gas, coal, oil, biomass and waste.

REI leveraged its existing *GLACIER* model of the EFPR to guide the design of the new firing system in the reactor. While carrying out new simulations to investigate the characteristics of new firing system designs, REI carefully reviewed CFD-based studies that were previously completed in support of REI's DOE-funded efforts in DOE Cooperative Agreement No: DE-FE0025168, "Characterizing Impacts of High Temperatures and Pressures in Oxy-Coal Combustion Systems."

The reactor is a modified gasifier that was converted into a combustor. Coal combustion in the reactor was, to that point using a slurry feed. Slurry feeding presents many challenges, namely maintaining adequate atomization of the coal/water mixture to achieve desirable conversion; as well as challenges in operation to maintain steady conditions and control temperatures within the reactor.

The overall reactor geometry shown in Figure 78 and Figure 79 describes the model domain representing the reactor interior from the burner nozzle plane at the top to the model exit at the cooling ring inlet. This domain also includes a series of channels terminating at water

cooled flange targets opposite of channels where the radiometers are located. The CFD model's representation of the geometry is shown in Figure 80.

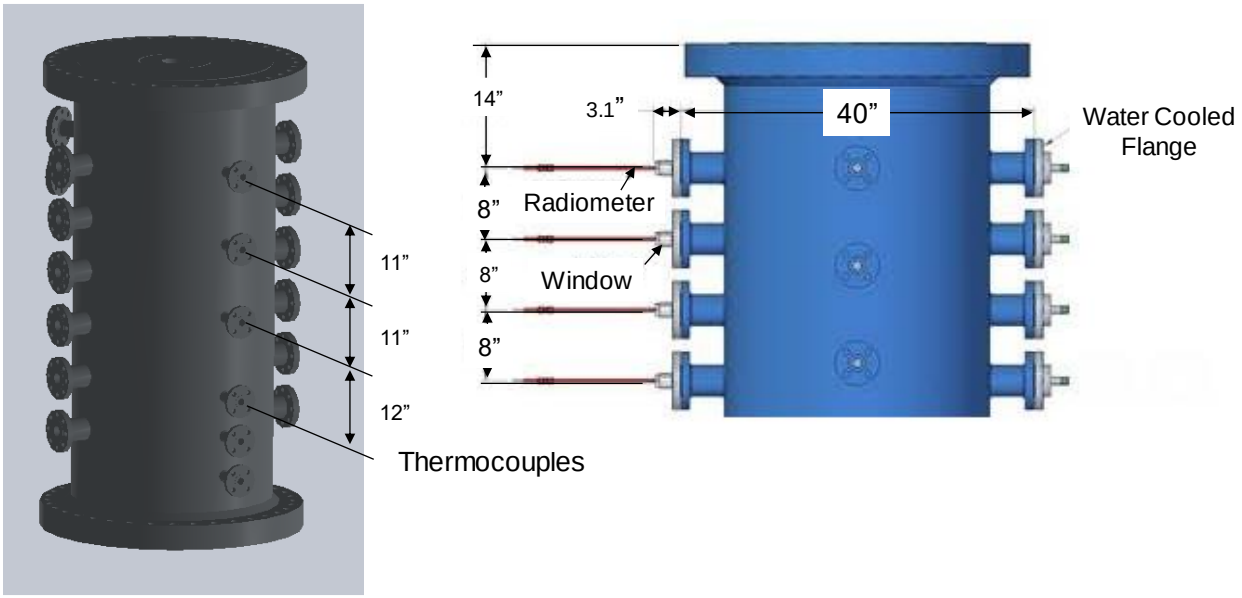

Figure 78. Overall EFG reactor geometry

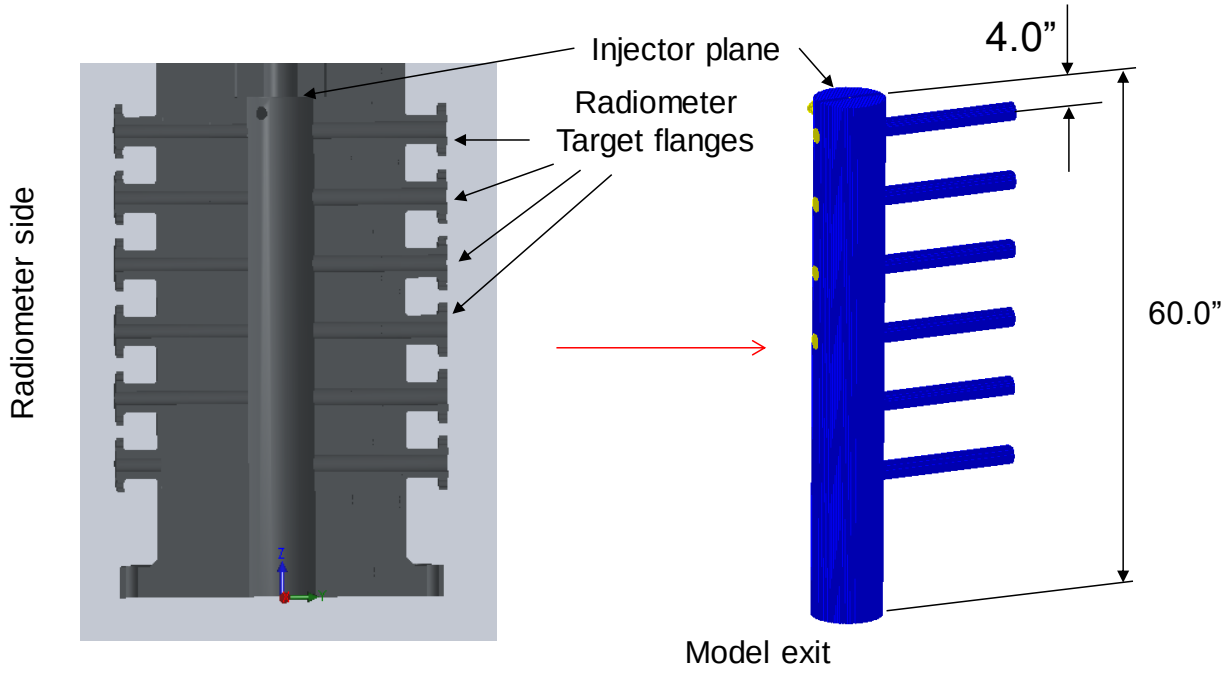

Figure 79. CFD domain representing interior of the EFG reactor

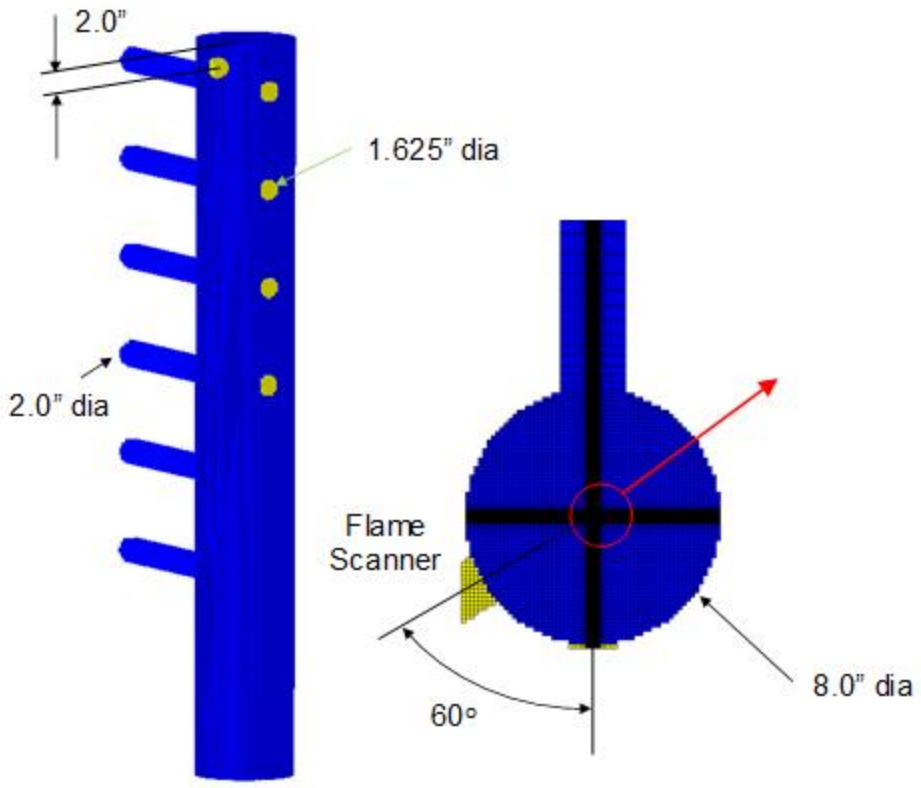

Figure 80. Reactor model geometry

A focal point of the initial simulations was a burner design that distributed the heat release axially to avoid excessive local heat fluxes and wall temperatures above the rating of the refractory lining. CFD modeling suggests it is possible to produce an elongated flame with mixing rates high enough to produce the locally high peak temperatures of interest. Simulations are currently being carried out to investigate 2 burner arrangements and associated near field burner aerodynamics. The burner designs are all capable of producing an unswirled axial jet and may be modified to produce more mixed combustion environments. As shown in Figure 81, the Design1 simulation involves a center tube carrying a pure stream of O_2. This tube is encircled by an annulus delivering fuel carried by CO_2, followed by an outer annulus with an O_2/CO_2 mixture.

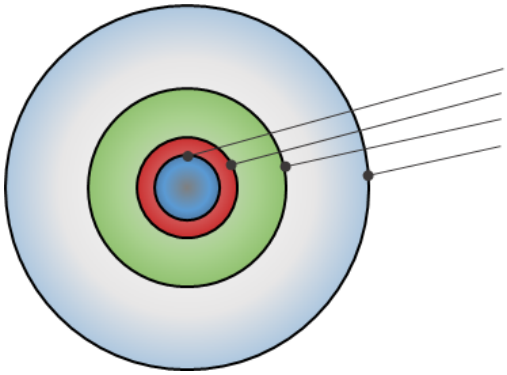

Tube Identifier	Tube Specs	OD (in)	ID (in)
Primary O2 (100% O2)	5/8" OD Tube	0.625	0.527
Fuel + CO2	1 1/16" OD Tube	1.0625	0.9645
O2+CO2	2" OD Tube	2.0	1.902
Water Jacket	3.5" OD Tube	3.5	

Figure 81. Burner geometry for the Design1 simulation.

Model Conditions

The furnace operating conditions are shown in Table 10 and Table 11. Table 10 displays the inlet boundary conditions while Table 11 shows the coal properties including the ultimate analysis of the Utah Sufco coal. The coal flow rate is relatively low compared to the firing capacity of the reactor. The 72-kW firing rate is an initial starting point chosen out of a desire to avoid slagging conditions in the reactor, which would interfere with ash particle sampling and analysis. The 72-kW heat input is low compared to the 300-kW firing capacity of the reactor, and a low thermal input includes the following challenges:

- Difficulties keeping the reactor sufficiently hot or maintaining a flame
- Fabrication of burner components for small burner geometries
- Sustainable operation of the dry feed system with carrier gas velocities lower than design specifications

The composition of the O_2/CO_2 stream is 26.7% O_2, which is close to the O_2 concentration typically targeted in the inlets of first generation oxy-coal technologies. Each stream is assumed to be entering the reactor at 100°F – 150°F and 260 psi. Flow rates of the pure O_2 stream and the O_2/CO_2 mixture were set to achieve theoretical excess O_2 of 3.0% on a dry basis. Each register was sized to achieve a relatively low velocity of about 5 ft/s.

Table 10. Inlet boundary conditions for the initial 300 kW EFPR burner design cases

Case	Design 1, Design 2
Firing Rate (MBtu/h) [kW]	0.25 [72]
Coal Flow Rate (lb/h)	22.1
Coal Carrier CO_2 Flow Rate (lb/h)	30.6
Coal Carrier CO_2 Temperature (°F)	150
Coal Carrier CO_2 Pressure (psi)	260
Coal Carrier CO_2 Density (lb/ft^3) [kg/m^3]	1.75 [28.0]
Primary O_2 Flow Rate (lb/h)	13.9

Case	Design 1, Design 2
Secondary O_2 Flow Rate (lb/h)	33.4
Secondary CO_2 Flow Rate (lb/h)	126.1
O_2 in CO_2/O_2 Inlet Mixture (vol%, wet)	26.7%
Primary O_2 Temperature (°F)	100
Secondary Mixture Temperature (°F)	100
Theoretical Excess O_2 (vol%, dry)	3.0%

Table 11. Ultimate analysis of the Sufco coal used in the EFPR

	Sufco Coal
C (wt%)	62.97
H (wt%)	4.55
O (wt%)	11.21
N (wt%)	1.11
S (wt%)	0.46
H_2O (wt%)	6.08
Ash (wt%)	13.63
HHV (Btu/lb)	11148

A practical concern for the Design1 configuration is the delivery of the fuel through a relatively narrow annulus. This could be problematic from an operational standpoint, so an alternative design was developed with fuel delivered through a center tube. As shown in Figure 82, Design 2 entails a center tube that is encircled by an annulus carrying pure O_2, which is inside an outer annulus delivering an O_2/CO_2 mixture. As was the case in the Design1 configuration, the O_2/CO_2 mixture is 26.7% O_2 by volume. The flow rates were set to achieve a theoretical O_2 concentration of 3.0%, dry and registers were sized to have similar velocities as in Design1. Specifications for the tubes used for each of the burner registers along with the corresponding inlet gas velocities are shown Table 12 for Design 1 and Design 2.

Both burners would be equipped with a water jacket for cooling of the burner components. The use of CO_2 reflects how we intended to operate the reactor in the experimental campaigns. At larger scales, CO_2 would be replaced with flue gas recycle (FGR) pulled from the effluent of the furnace.

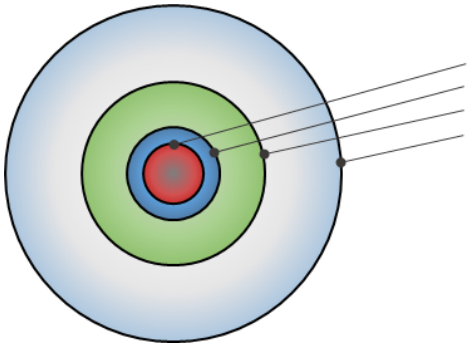

Tube Identifier	Tube Specs	OD (in)	ID (in)
Fuel + CO2	13/16" OD Tube	0.8125	0.7145
Primary O2 (100% O2)	1 1/16" OD Tube	1.0625	0.9645
O2+CO2	2" OD Tube	2.0	1.902
Water Jacket	3.5" OD Tube	3.5	

Figure 82. Burner geometry for the Design2 simulation.

Table 12. Tube sizes and corresponding inlet velocities for variants of the dry feed burner design

Case	Register	Tube Specs	OD (in)	ID (in)	Velocity (ft/s)
Design 1	Primary O_2 (100% O_2)	5/8" OD Tube	0.625	0.527	5.12
	Fuel + CO_2	1 1/16" OD Tube	1.0625	0.9645	4.59
	O_2+CO_2	2" OD Tube	2.0	1.902	5.13
Design 2	Fuel + CO_2	13/16" OD Tube	0.8125	0.7145	4.86
	Primary O_2 (100% O_2)	1 1/16" OD Tube	1.0625	0.9645	5.27
	O_2+CO_2	2" OD Tube	2.0	1.902	5.13

CFD Model Predictions

The CFD model shows that the interface between the fuel and pure O_2 streams produces high temperature conditions locally. Mixing tends to occur more rapidly with the Design 1 configuration where fuel is transported through an annular opening. Two indicators are used to determine this. First, the peak gas temperature predicted within the flame in Design 1 is nearly 500°F hotter than that of Design 2. The gas temperature contours shown in Figure 83 and Figure 84 show the development of a high temperature ring directly downstream of the burner tip with both designs. The ring is indicative of the envelope of high heat release where the coal and O_2 are mixing. The annular delivery of the fuel with Design 1 produces a high velocity jet of hot gases in the center of the furnace as the fuel-rich annulus quickly mixes with the pure O_2 at the center of the furnace. Stratification at the center of the flame rapidly mixes out between the first and second observation port at the top of the furnace. In addition to the mixing between the coal and pure O_2 at the center, there is also heat release occurring at the outer edge of the coal stream as the fuel mixes with the O_2 in the O_2/CO_2 mixture.

Reactions in Design 2 are elongated, and the associated heat release creates a ring of high temperature gas that stretches approximately 1/3 of the length of the reactor. The relatively cool and fuel-rich core of the flame mixes more slowly with the annulus of pure O_2. The spread of the fuel from the center of the flame limits the shape of the high temperature region to a narrow band of gases that gradually expands to larger radii upstream of the third observation

port. The limitations on mixing and corresponding heat release in Design 2 is an attractive feature compared to that of Design 1 since the development of the extreme conditions shown here must be controlled to protect the burner and the inside surfaces of the furnace.

As noted in Figure 83, the peak temperature for both cases are above 4500°F, which is a threshold commonly referenced in high temperature oxy-coal combustion. These locally hot conditions are to be expected under the operating conditions prescribed in these cases. Additional CO_2 (or FGR) can be added to further dilute the flue gas to control gas temperatures.

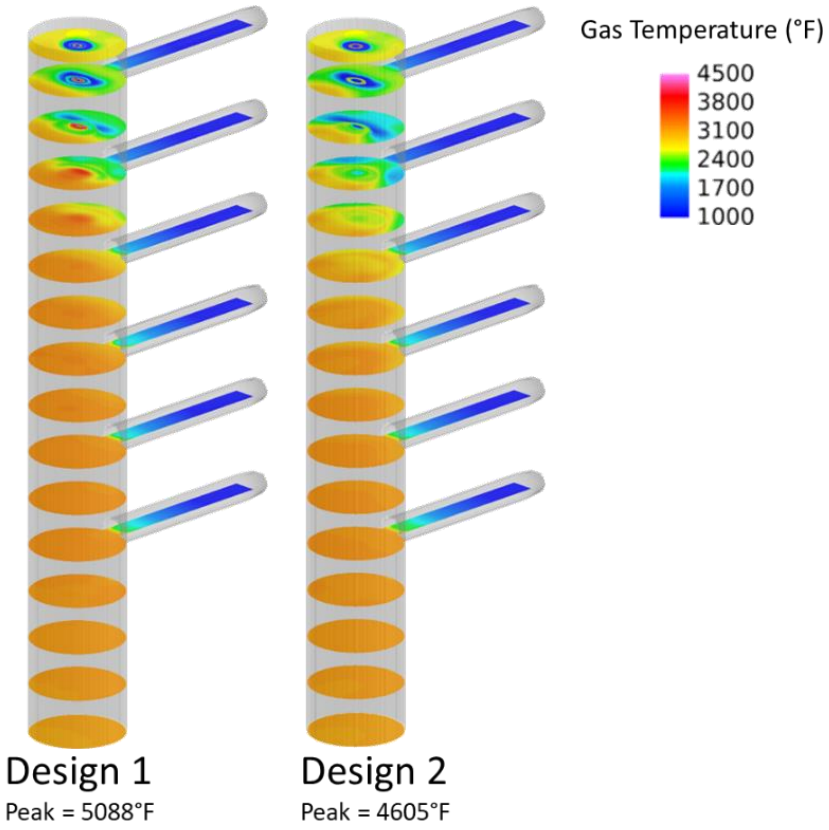

Figure 83. Cross sectional gas temperature profiles for burner Design 1 and Design 2 in the EFPR showing evolution of high temperature regions in the flame within cross-sectional planes along the length of the reactor

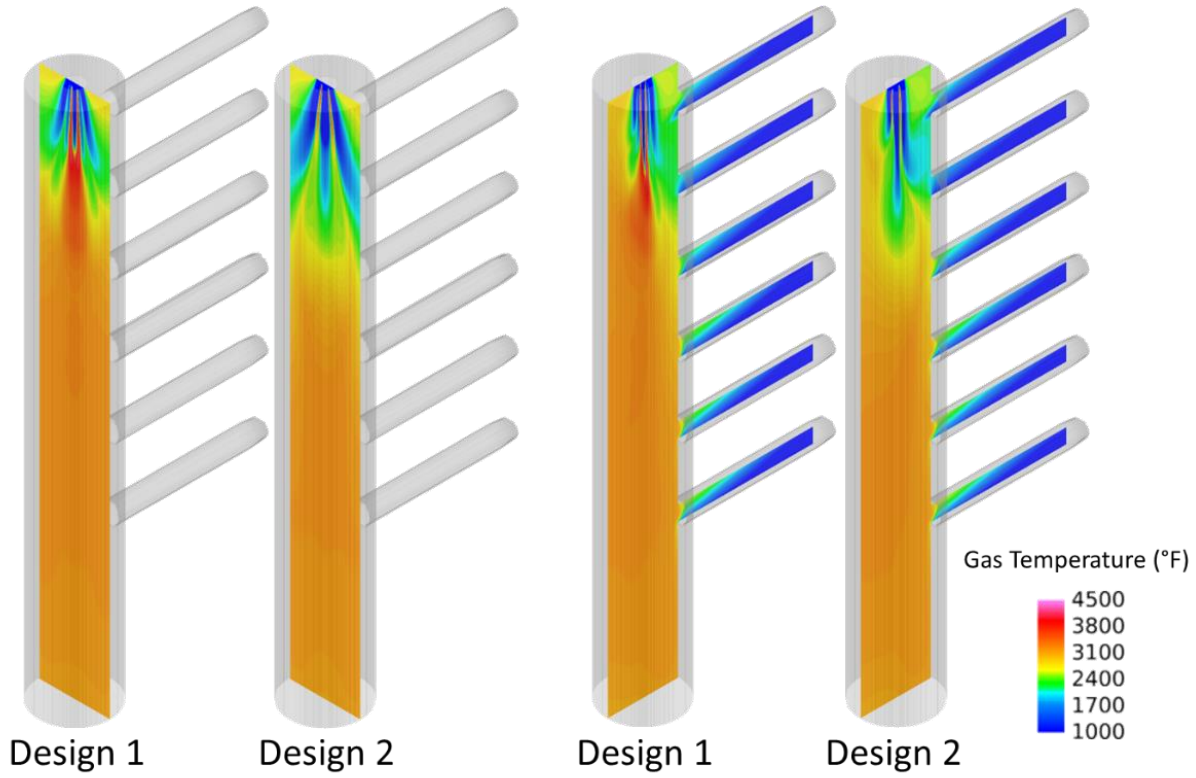

Figure 84. Gas temperature profiles for burner Design 1 and Design 2 in the EFPR

CO_2 can be used as a proxy for heat released, so the second indicator used to determine the rate of mixing and heat release is CO_2 evolved along the length of the reactor. The quantity of CO_2 produced from complete combustion can be directly linked to the extent of heat released in the furnace. Curves of CO_2 evolved from the combustion process were obtained from the model and normalized based on the ultimate quantity of CO_2 produced for each specific case. In other words, at the model exit, the curves for each case reach 100% of the ultimate CO_2 evolved in the furnace. The normalization includes an adjustment that eliminates the impact of CO_2 in the inlets so that curves are purely the CO_2 evolved from combustion. A plot of CO_2 evolved as a function of axial length (Figure 85) indicates that CO_2 is produced at a much faster rate in Design 1 compared to Design 2. The interesting behavior in the first 5" of the reactor where the percentage drops is due to dissociation of CO_2 to CO and O_2. Discontinuities observed further downstream are due to the influence of the observation ports on the flow field along the reactor length.

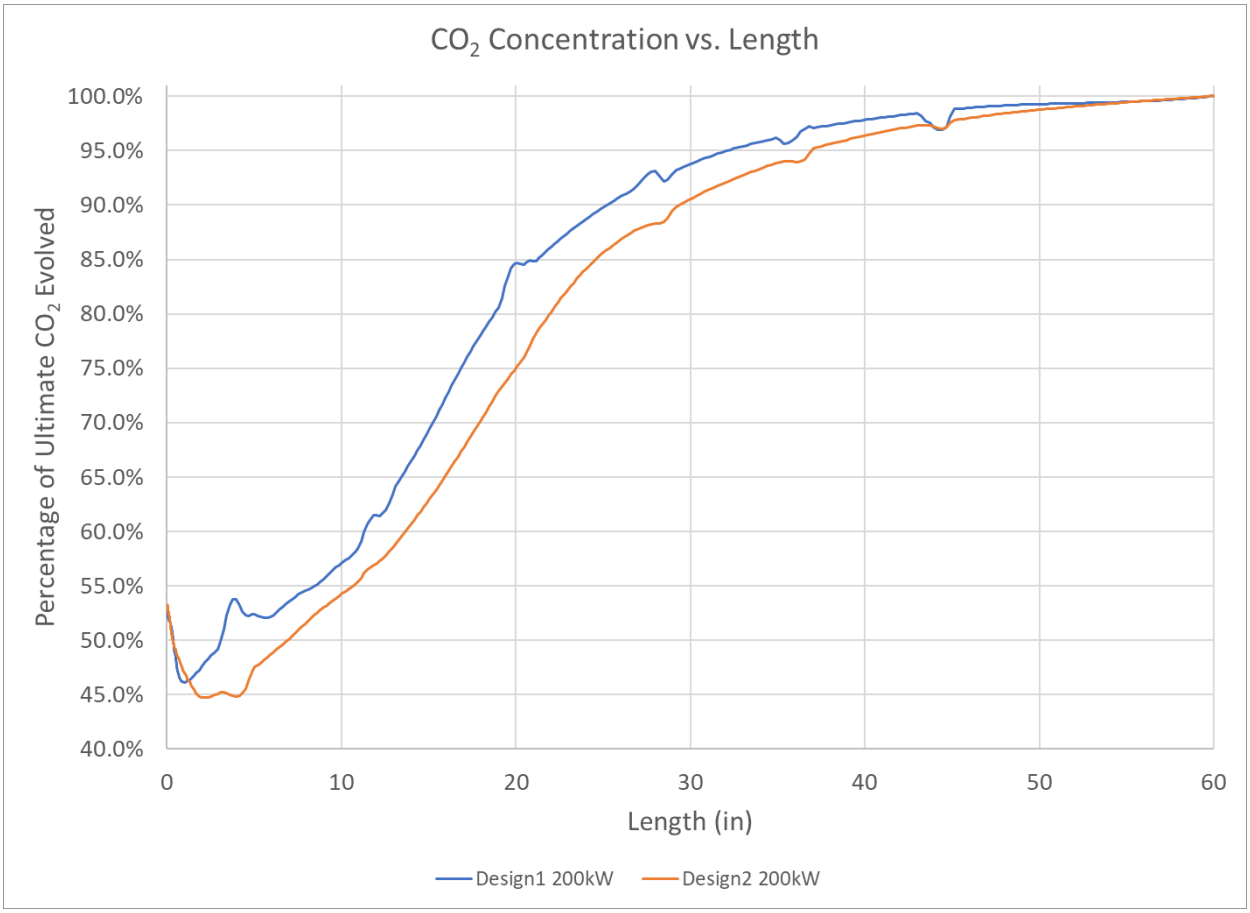

Figure 85. CO_2 evolved versus axial distance for burner Design 1 and Design 2. CO_2 evolved is used as a proxy for heat release in the furnace and is used to compare the heat release profile for different burner designs.

In both cases, the region of cooler gases at larger radii near the top portion of the furnace is a recirculation zone that develops as flow separates off the high velocity jet at the center of the furnace as shown in Figure 86. The narrower axial jet produced from Design 1 penetrates deeper into the reactor and leads to the development of larger volumes of recirculating gases along the walls of the reactor, especially in the upper 1/3 where reactions are occurring rapidly, and gas temperatures are rising quickly.

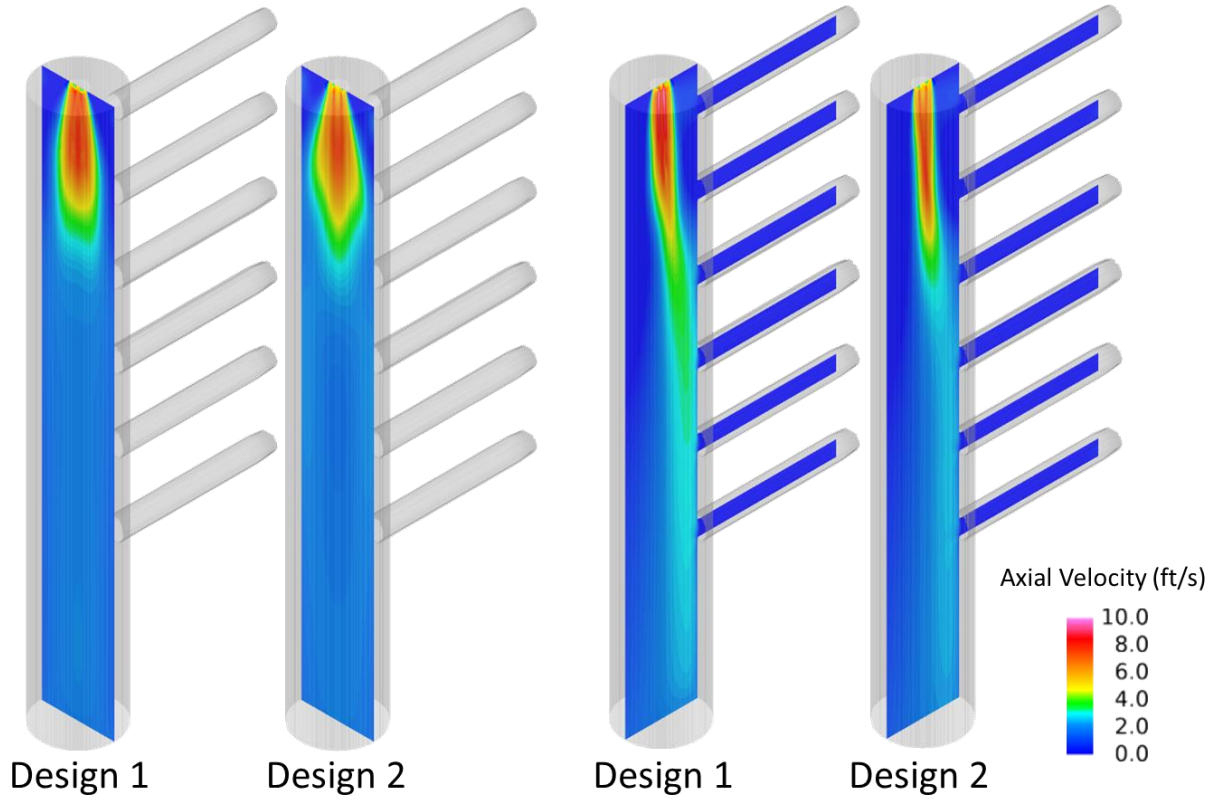

Figure 86. Axial velocity profile in the EFPR for burner Design 1 and Design 2.

Plots of CO in the reactor point to the delayed reaction profile with Design 2. CO production occurs at a faster rate in Design 1 as shown in Figure 87. The region over which the fuel and O_2 mix is visibly larger in Design 1 as the annular reaction envelope expands quickly and spreads combustion products across the reactor's cross section. Design 2 limits the mixing initially as the narrow band of CO that stretches to the second observation port indicates. Coal combustion occurs rapidly beyond the second port, producing a region of high CO that penetrates much further axially than the fuel rich zone in Design 1. A plot of CO mass flow in Figure 88 further illustrates the differences in mixing as production of CO in Design 2 lags behind that of Design 1 in the first 15" of the reactor. The mixing rates in Design 2, limited by the burner's design increase steeply with peak CO levels exceeding that of Design 1.

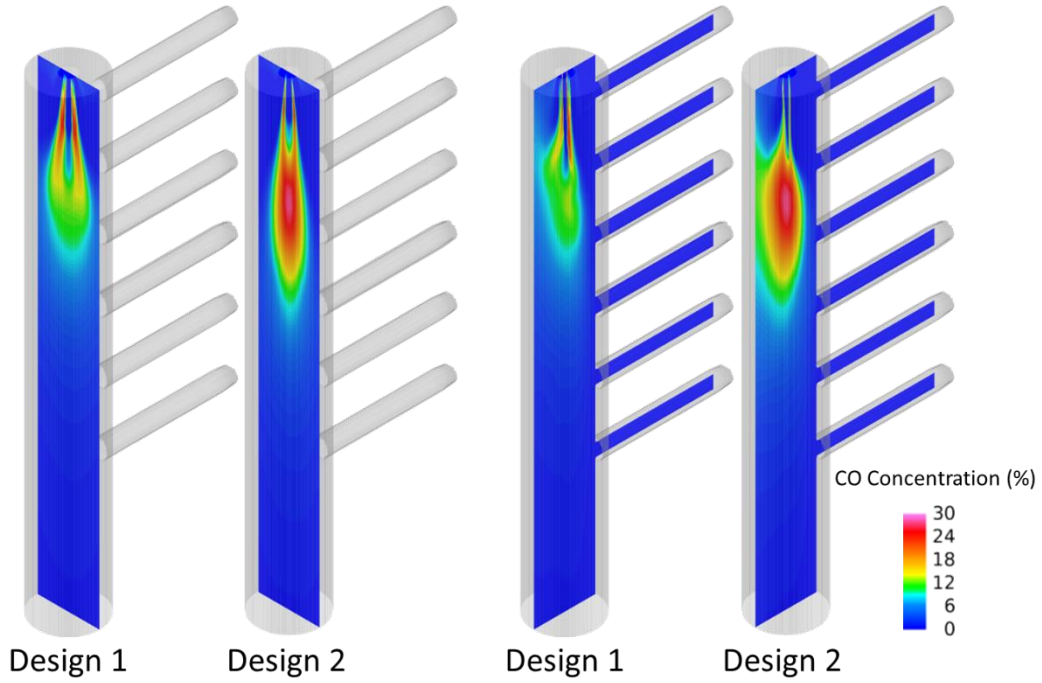

Figure 87. CO concentration profile in the EFPR for burner Design 1 and Design 2

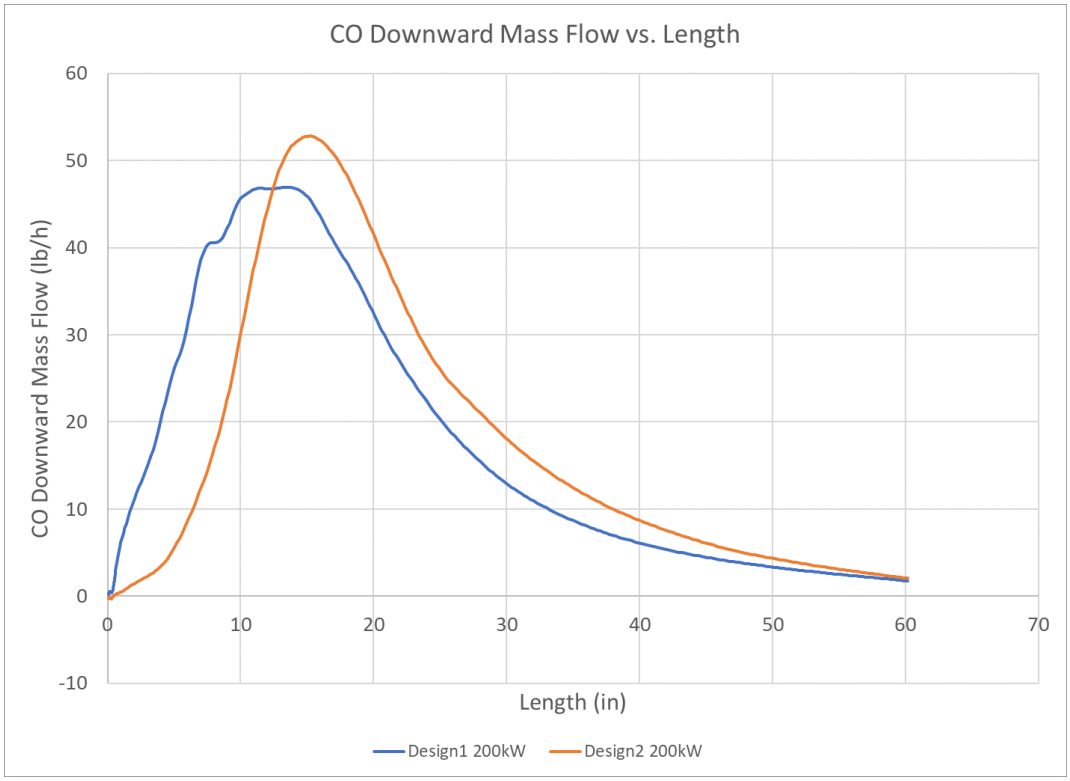

Figure 88. CO downward mass flow profile in the EFPR for burner Design 1 and Design 2

The delayed mixing in Design 2 spreads the region of high heat fluxes over a larger surface area and pushes peak incident fluxes deeper into the furnace as shown in Figure 89. This is a desirable characteristic for Design 2 since spreading the heat release over a larger area and avoidance of excessive heat flux near the burner zone will help protect the burner components and the furnace surfaces at the top of the reactor.

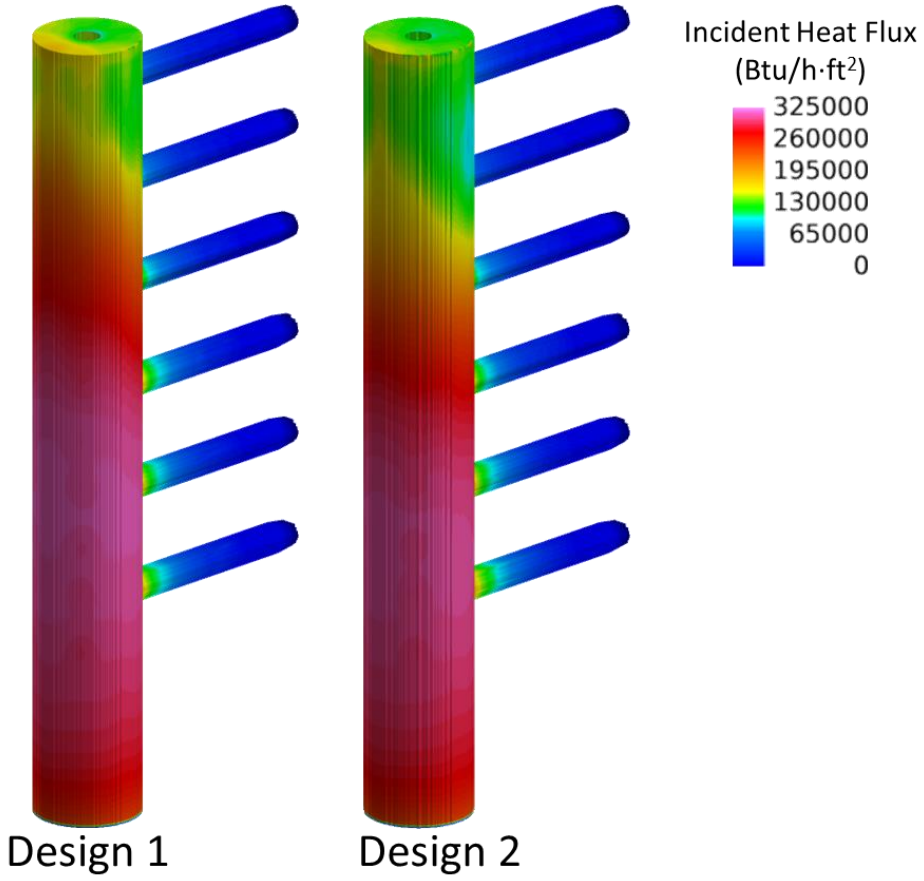

Figure 89. Incident heat flux profile in the EFPR for burner Design 1 and Design 2

The impact of inlet velocity on flame stability, flame shape, and axial heat release in the reactor were then considered for the 2 design concepts. Design 1a and Design 2a are modified versions of the original designs with increased register sizes to explore the impacts of lower inlet velocities. Specifications for the tubes used for each of the burner registers along with the corresponding inlet gas velocities are shown in Table 13 for each of the burner variants explored.

Table 13. Tube sizes and corresponding inlet velocities for variants of the dry feed burner design

Case	Register	Tube Specs	OD (in)	ID (in)	Velocity (ft/s)
Design 1	Primary O_2 (100% O_2)	5/8" OD Tube	0.625	0.527	5.12
	Fuel + CO_2	1 1/16" OD Tube	1.0625	0.9645	4.59
	O_2+CO_2	2" OD Tube	2.0	1.902	5.13
Design 1a	Primary O_2 (100% O_2)	3/4" OD Tube	0.750	0.652	3.35
	Fuel + CO_2	1 ¼" OD Tube	1.250	1.152	3.24
	O_2+CO_2	2 7/16" OD Tube	2.438	2.340	3.27
Design 2	Fuel + CO_2	13/16" OD Tube	0.8125	0.7145	4.86
	Primary O_2 (100% O_2)	1 1/16" OD Tube	1.0625	0.9645	5.27
	O_2+CO_2	2" OD Tube	2.0	1.902	5.13
Design 2a	Fuel + CO_2	1" OD Tube	1.000	0.9020	3.00
	Primary O_2 (100% O_2)	1 1/16" OD Tube	1.0625	0.9645	3.05
	O_2+CO_2	2" OD Tube	2.0	1.902	3.16

Evaluation of the 1a design with lower velocities showed that the burner did exhibit some degree of delayed mixing, but the short jet penetration evident in the gas temperature profiles in Figure 90, promoted the formation of a region with concentrated heat fluxes in the vicinity of the 3rd port from the top of the reactor. This is visible in the incident heat flux profiles shown in Figure 91 where the Design 1 case shows lower peaks and a more gradual increase in incident fluxes to the furnace walls along the length of the reactor. In addition, Design1a led to the formation of a recirculation zone in the near-burner region where relatively cool gases occupy the majority of the volume surrounding the axial jet. This led to concerns regarding operational stability and difficulties in maintaining a steady flame should conditions in the upper furnace become too cool resulting in problems igniting the fuel.

The Design 2a case showed similar characteristics as that of Design 2, and did not show a significant advantage over the design with higher inlet velocities. The overall carbon conversion with Design 2a was lower than in Design 2 and the heat release was delayed more than what was desired. This is evident in the incident flux profiles shown in Figure 92 where the delayed heat release in Design 2a corresponds to lower radiant fluxes in the upper furnace, and the reduction in carbon conversion is reflected in the lower heat fluxes near the 4th and 5th port upstream of the model exit.

Due to the undesirable conditions produced from Design 1a and the lack of significant improvement with Design 2a, these designs were not pursued further. The delayed mixing in Design 2 spreads the region of high heat fluxes over a larger surface area and pushes peak incident fluxes deeper into the furnace as shown in Figure 92. This desirable characteristic for distribution of heat release over a larger area led the selection of Design 2 as the burner design concept of choice for the combustion test campaigns in the EFPR.

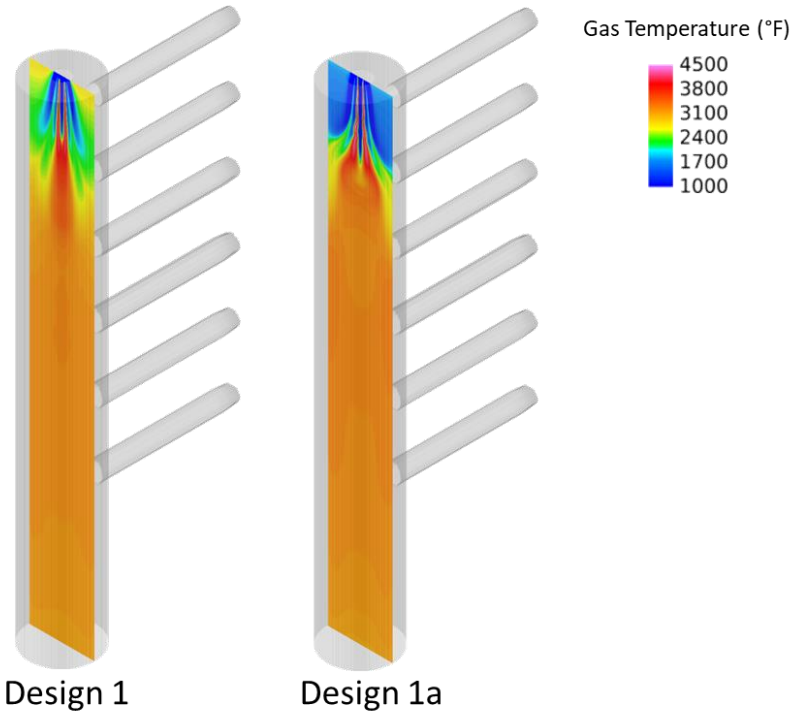

Figure 90. Impact of inlet stream velocity on gas temperature comparing burner Design 1 and Design 1a

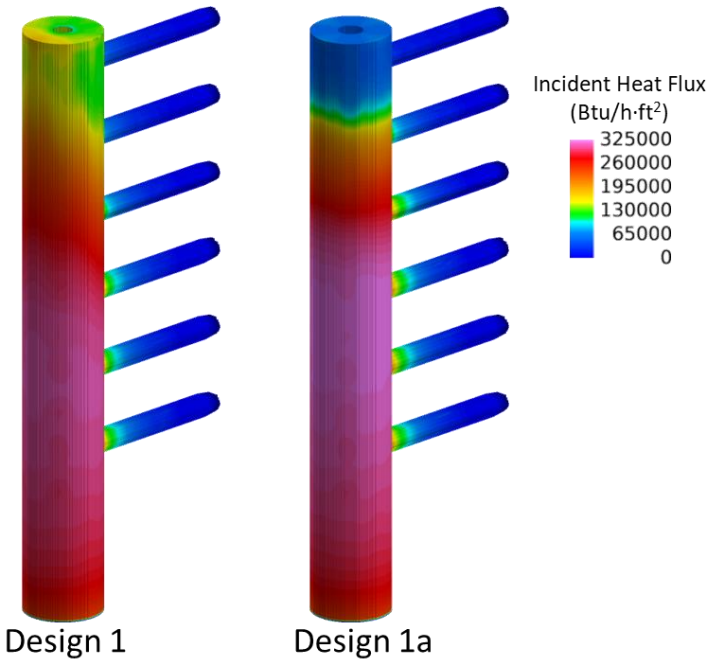

Figure 91. Impact of inlet stream velocity on incident heat flux comparing burner Design 1 and Design 1a

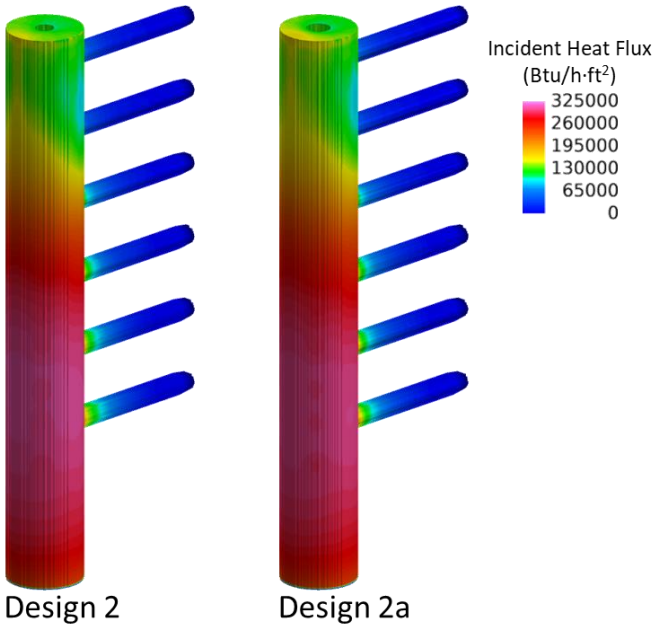

Figure 92. Impact of inlet stream velocity on incident heat flux comparing burner Design 2 and Design 2a

Burner Fabrication

When the Design 2 configuration was confirmed as the burner of choice, refinements were necessary to ensure a proper fit for the burner. With the size of the burner port opening as a limiting factor, the water jacket was designed to consist of a single annulus with opposing fins to channel the water down one side and up the other. The fuel carried by CO_2 enters the top of the burner through a ½-inch tube. The secondary O_2 and CO_2 are mixed upstream prior to entering the burner through a common port. The burner was designed such that the tip would be flush with the ceiling of the reactor. All materials for the burner shown in Figure 93 are of 316 stainless steel.

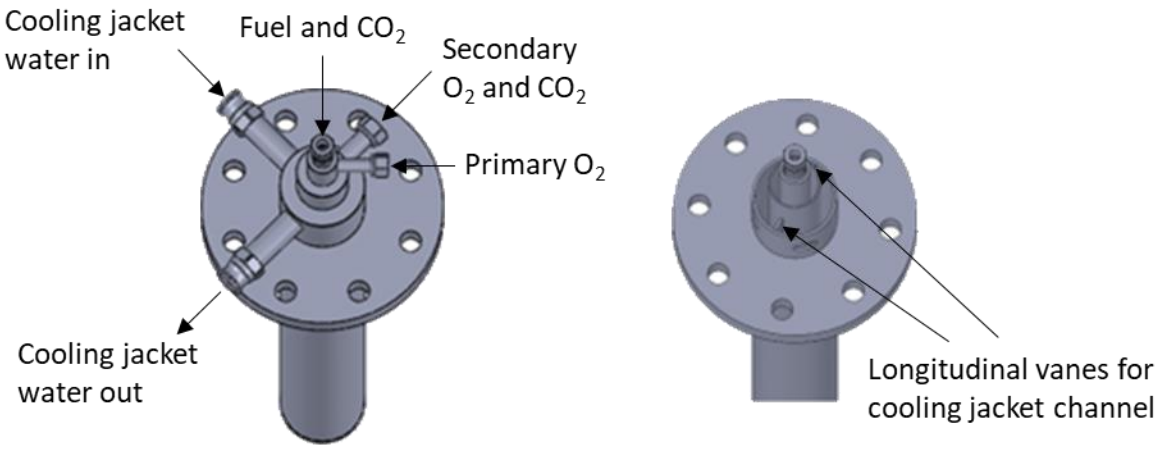

Figure 93. Burner ports and water jacket design

In addition to burning dry feedstock, burner design elements were incorporated that would allow the burner to be used to idle the reactor at temperature between individual tests using the center two registers for natural gas and air. The objective was to have the flexibility to operate such that once a day's testing was completed, and the reactor depressurized, three-way valves would switch to route natural gas through the inner annulus while air would be transported through the center pipe and outer annulus. This design provided an efficient and convenient approach to switching from system idle to solid fuel testing by eliminating the need to remove the burner used for pulverized coal combustion and installing a dedicated natural gas burner to keep the reactor hot during idle periods. This would be particularly important at startup since exchanging burners safely can take long enough that the reactor cools too much to ignite the fuel.

Experience with this reactor during slurry-fed pressurized oxy-combustion indicated that when the reactor hot face cools to below 1800°F, igniting the coal stream was problematic. Previous oxy-combustion campaigns with this reactor utilizing a coal slurry feed involved separate natural gas burners and coal injectors. The natural gas burner was pulled from the reactor after heating or overnight idling and the coal slurry injector was installed. The reactor would cool significantly as the burners were exchanged, so immediately after the slurry injector was installed, isopropyl alcohol (IPA) was fed to bring the reactor back up to temperature and attain a nominal pressure. Feed was switched from IPA to slurry, operating pressures were raised and tests were conducted. However, the dry feed system cannot employ IPA so it was necessary to have a burner capable of burning natural gas to keep the system warm while idling. This integrated burner concept is more efficient and eliminates reactor cool down caused by exchanging burners.

Figure 94 shows the final burner design and dimensions. To guard against nonconcentric annular registers, centering pins were located in each annulus at 4 inches and 15 inches up from the burner nozzle. The Figure 95 photograph shows the completed fabrication of the burner with center and annular registers along with the water jacket.

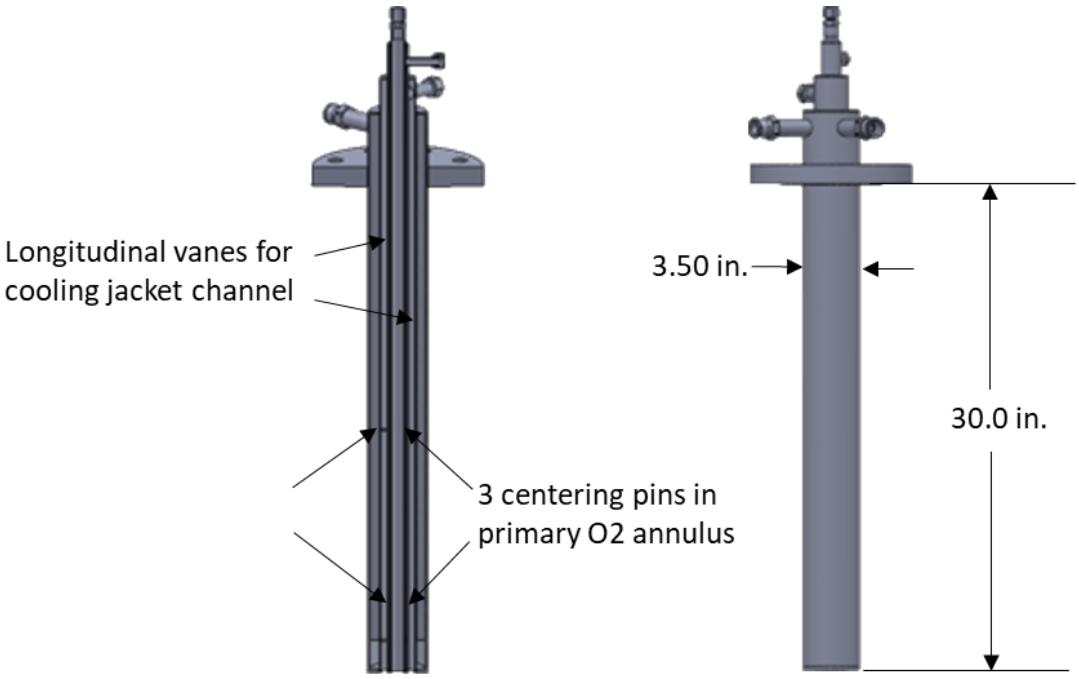

Figure 94. Burner features and key overall dimensions

Figure 95. Photograph of the burner registers and water jacket

As shown in the burner sketch in Figure 82, the fuel is transported through a center pipe encircled by a stream of pure O_2, followed by an outer annulus of an O_2/CO_2 mixture. When firing with natural gas, air is routed through the center tube and the outer annulus; and natural gas is routed through the inner annulus. This arrangement provides cooling of the two inner tubes that do not come in contact with the burner's water jacket. Additional switching solenoid valves in such a system also allows for purging the reactor with nitrogen as a precautionary safety measure. The design and geometry of the burner was chosen specifically to accommodate both modes of operation. A system of manual high-pressure ball valves was

developed to switch between firing on natural gas at low pressures and carbon dioxide, oxygen and coal at higher pressures.

The ability of the natural gas burner to sustain a flame in the closed reactor and to heat the reactor to the coal light-off temperatures was confirmed. Ignition and development of a stable flame involved light-off at low flow rates and then a steady increase of both natural gas and air flows. Flame stability was first evaluated visually outside of the reactor and mass flow rates and ramps thereof were noted. The burner with a stable flame is shown in Figure 96.

Figure 96. Ex situ burner flame calibration on natural gas

The burner was then installed in the reactor, and then sealed. With the burner in the reactor, a heat up cycle was performed. The results of this cycle are shown in Figure 97. The levels referred to in the figure are numbered from 1 through 4, 1 being at the top of the reactor and 4 at the bottom. Level 1 is at the top of the reactor at the height of the burner tip. Level 2 is 11 inches below level 1, with subsequent levels spaced 11 inches apart. Two type-B thermocouples are embedded in the refractory at each level at depths of 13 mm (shallow) and 77 mm (deep) from the inside reactor surface. The refractory surface temperature is estimated by extrapolation from these two temperature readings.

The upper part of the reactor was heated to 2000°F and could have reached even higher temperatures, but the test was terminated because it had demonstrated what was desired. The heat-up test was successful and showed that the multi-purpose burner is capable of operation on natural gas. This was important since it would allow the change-over from natural gas heating to oxy-coal combustion to occur in a very short period (1-2 minutes). The reactor

walls would retain heat during this period so that the coal would quickly ignite. Had it been necessary to exchange the burner used for heating with the oxy-coal burner as was necessary in previous tests with coal slurry feed, the process would have taken 30-40 minutes, the reactor would have been open for a significant amount of time and the walls would have cooled several hundred degrees. Additionally, the use of one multi-purpose burner provides an additional degree of safety since the reactor is not being opened to switch single-purpose burners.

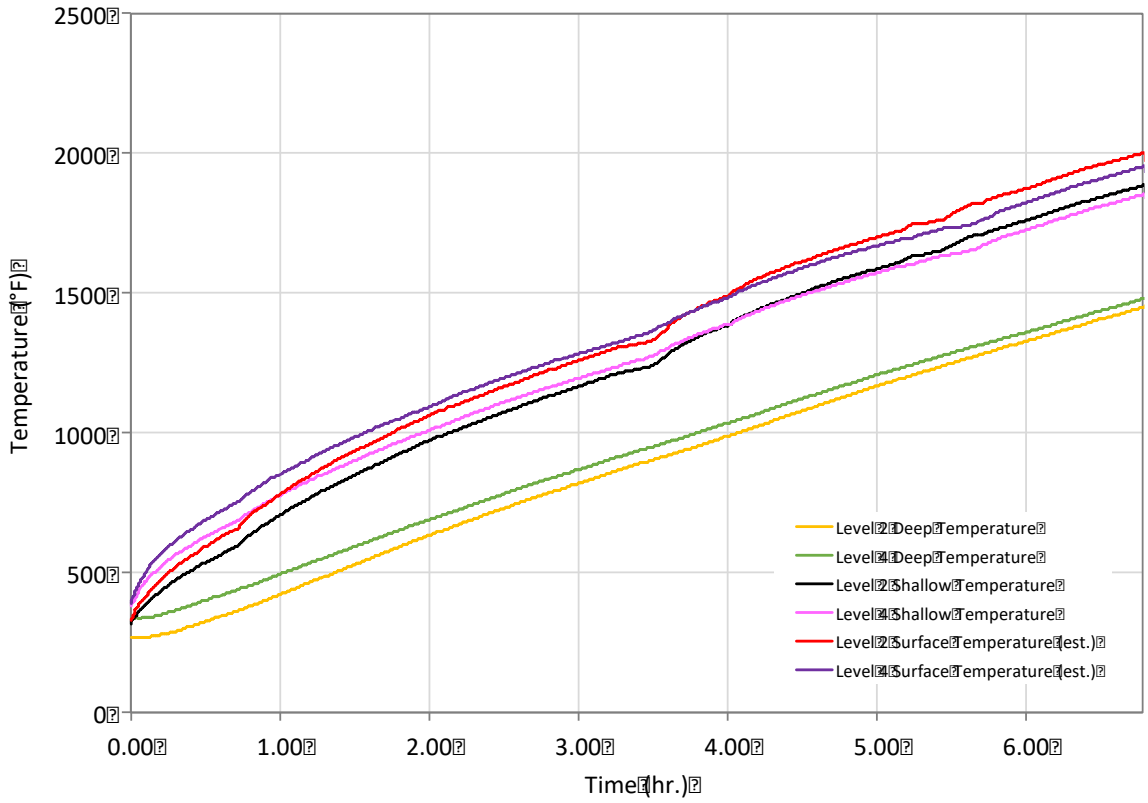

Figure 97. Reactor temperatures during controlled heat-up

Local heat flux to the reactor wall can be estimated from the thermocouple readings and knowledge of the thermal conductivity of the refractory material. Measured heat flux is shown in Figure 98. Heat flux is sensitive to fuel and air flow, especially at high temperature when radiation is the primary mode of heat transfer.

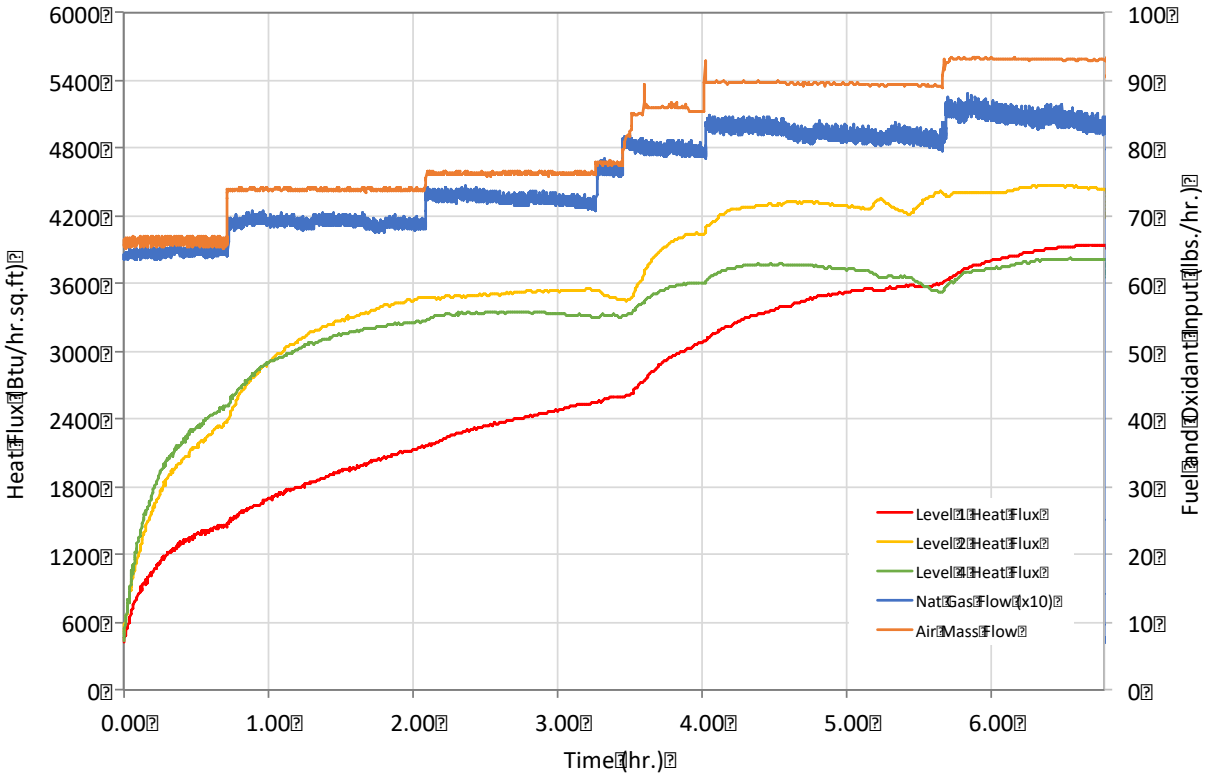

Figure 98. Measured heat flux and fuel input during heat-up. Natural gas flow rate is multiplied by 10 to better show changes

In addition, a larger pressure-building heat exchanger on the CO_2 supply system was installed to better ensure that the supply pressure would be able to be maintained during long-term operation of the system. With all flow meters and sensors installed and confirmed as functional, the next step was to perform initial testing of coal feed into the reactor, thus expanding on cold testing described earlier and confirming that the dry feed system is operational.

Initial testing were to be into the cold reactor with shakedown tests of oxy-coal combustion with co-feed of coal, O_2 and CO_2 performed thereafter. However, although periods of acceptable coal flow rates appropriate for the capacity of the reactor were recorded, achieving a stable flow rate for a suitable length of time ultimately proved to be unattainable. As part of REI's risk management strategy, an alternative approach to gathering relevant experimental data were sought. This process required careful considerations of risks to the program including the recognition that the as-built burner that was designed specifically for the University of Utah's reactor would not be utilized in different system. It was determined that the best path forward involved REI engaging BYU who had been developing their own dry feed system for a pressurized oxy-coal combustion facility in a separate DOE-funded project. REI's collaboration with BYU resulted in a successful experimental campaign for pressurized oxy-coal

combustion. The outcomes of those tests are described in the following section entitled Task 5 – Pressurized Testing with Minimal CO_2 for Coal Transport.

Task 4 Summary and Conclusions

Burner design concepts for dry pulverized coal-fed pressurized combustion were initiated with a survey of the literature on firing systems for pressurized combustors. Commercial experience with dry feed burner concepts for high pressure combustion of pulverized coal is limited, but REI applied its experience with atmospheric pressure commercial dry feed systems and with high pressure gasifiers to develop burner design concepts. Conceptual designs were focused on producing stable flames and a heat flux profile suitable for the tolerances of the combustion equipment. The impact of burner design features (including fuel/oxidant mixing related to velocities and velocity differentials) on behaviors including recirculation patterns and flame locations/shapes heat release profiles, flame stability, flame temperatures, peak burner and wall temperatures was evaluated. A CFD modeling approach was developed to evaluate the impact of specific design features. For example, the impact of a burner register layout with pure O_2 in the center and fuel introduced through a concentric annular opening was determined to release too much heat close to burner, while the utilization of lower velocity inlets from larger pipe diameters resulted in delayed heat release and high heat fluxes in a small volume near the midpoint of the furnace's axial length. A specific burner configuration/operation was identified for further testing. It was also noted that fuel conversion indicators, such as CO and unburned carbon, near completion for all designs. In the final design that was fabricated for testing, the fuel is transported through a center pipe encircled by a stream of pure O_2, followed by an outer annulus of an O_2/CO_2 mixture. When firing with natural gas, air is routed through the center tube and the outer annulus; and natural gas is routed through the inner annulus. This arrangement provides cooling of the two inner tubes that do not come in contact with the burner's water jacket. The design and geometry of the burner was chosen specifically to accommodate both modes of operation and improved the efficiency in switching between reactor idle during standby mode and pressurized oxy-coal combustion experiments. Upon determining that stable coal flow would be unatainabkle using the dry feed system at the UofU, REI began collaboration with BYU to leverage their dry-fed pressurized oxy-coal facility for experiments. This process required careful considerations of risks to the program including the recognition that the as-built burner that was designed specifically for the University of Utah's reactor would not be utilized in different system. It was ultimately determined that the best path forward for the program involved REI moving forward with experiments in the BYU facility.

Task 5 – Pressurized Testing with Minimal CO_2 for Coal Transport

Objective: Perform pilot-scale tests and experiments to provide a comprehensive data set describing heat release profile, material temperatures and mineral matter behavior in high temperature, high pressure flames generated by oxygen combustion of coal with zero or minimum flue gas recycle

Dry-Fed Pressurized Oxy-Coal Combustion Testing

Project execution as described in the preceding sections focused on design construction and operation of a pressurized dry-fed pulverized coal oxy-combustion system at the University of Utah. This was the case until the middle of the 2021 calendar year when it became apparent that the dry feed system at the University of Utah would require additional time and effort to achieve stable and reliable pulverized coal flow rates required for the pressurized oxy-coal experiments described in the project objectives. As stated above, the dry feed system provided by project partner Southeast University in Nanjing, China was connected to a pressurized candle filter assembly for tests on the functionality of the system to deliver steady and reliable flow rates at values appropriate for the combustor to be used in proposed high pressure oxy-combustion experiments. Although periods of acceptable coal flow rates appropriate for the capacity of the reactor were recorded, achieving a stable flow rate for a suitable length of time proved to be unattainable.

As part of REI's risk management strategy, an alternative approach to gathering relevant experimental data were sought. REI engaged BYU who were developing their own dry feed system for a pressurized oxy-coal combustion facility and had seen reasonable success in achieving consistent coal flow rates with their facility. A plan was established where REI would install its real-time corrosion monitoring probe in the BYU reactor. In addition, UofU would leverage the BYU system by employing their ash aerosol sampling system in the BYU test rig. The BYU facility came equipped with instrumentation providing temperature, heat flux, radiation intensity, gas and particle temperature, and flue gas properties.

Upon authorization from DOE on the shift in approach and facilities used for the pressurized oxy-coal experiments, REI and BYU worked quickly to make preparations for testing using the Pressurized Oxy Combustor (POC) at BYU. The POC is a 100kW refractory lined furnace designed for the investigation of combustion of pulverized solid fuels at elevated pressure. The configuration of the POC is presented in Figure 99 with a photograph of the reactor shown in Figure 100. The reactor is a vertically oriented down-fired combustion chamber with an inside diameter of 203 mm (8 inches) and 1.8 meters long (72 inches). In the main combustion chamber, there are five levels of access ports in each of the four quadrants, separated by 305 mm (12 inches) axially. Two opposing ports at each level are fit with sapphire optical access ports. The reactor can be fired at pressures up to 27.6 bars (400 psi) and the inside refractory can withstand temperatures up to 1760 °C (3200 °F).

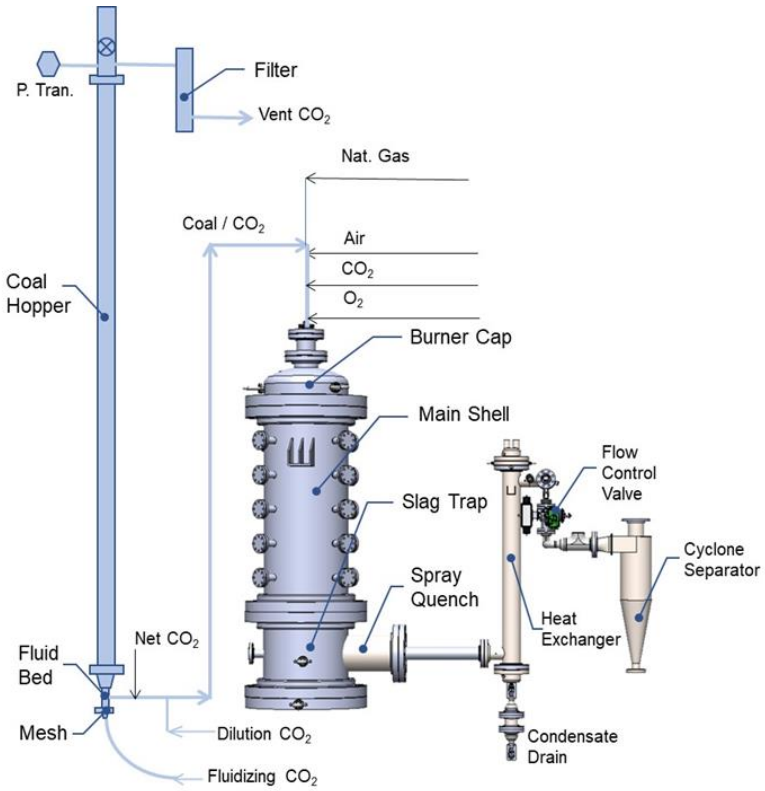

Figure 99. Pressurized Oxy Combustor (POC) at Brigham Young University

Figure 100. The current location for gathering pressurized oxy-coal corrosion measurements

The burner currently configured on the POC consists of four annular tubes (resulting in one injector and two annuluses) surrounded by 8 additional injection ports. The configuration of the burner is presented in Figure 101 along with port and annulus dimensions shown in Table 14. Pulverized coal is delivered through the centermost port from a pressurized fluidized bed feeder. A mixture of O_2 and CO_2 is introduced through the outermost annulus and a separate mixture of O_2 and CO_2 is introduced through the 8 outer ports. Air and natural gas can also be introduced through the annuluses and are used to heat the refractory in preparation to fire coal. The overall coal feed rate and the fuel to oxidizer ratio were selected in order to keep the reactor refractory walls above the slagging temperature of the coal ash. Combustion occurs as the fuel / oxidizer mixture moves down the reactor.

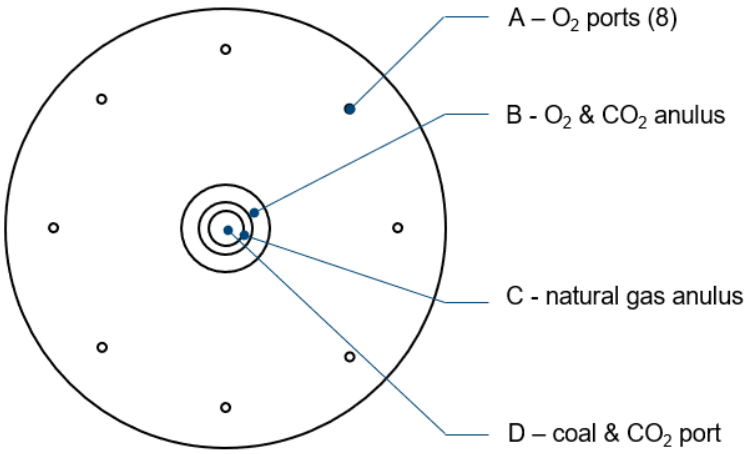

Figure 101. Burner configuration mounted on the POC

Table 14. Burner dimensions

Label	Port or Anulus	Inner (mm)	Outer (mm)	Coal (kg/h)	CO_2 (kg/h)	O_2 (kg/h)
A	O_2 ports	NA	3.86	0	37.2	0
B	O_2 & CO_2 anulus	9.53	28.45	0	55	27
C	natural gas anulus	6.35	8.51	NA	NA	NA
D	Coal & CO_2 port	NA	4.93	13.6	0	0

Combustion products and fly ash exit the reactor through a refractory lined exit port. The exit port contains a water spray quench to reduce the reactor exit gas temperature. The temperature is lowered to enable a stainless-steel pipe without refractory to be used to convey the products beyond the reactor.

Ash that deposits on reactor walls will melts and become slag. The slag flows down the reactor walls and falls into the reactor slag trap at the bottom of the reactor. The slag trap can be removed periodically to remove the collected slag.

The product gas, fly ash and spray water then enter a shell and tube heat exchanger that reduces their temperature to below near room temperature. The products in the heat exchanger are still at the same pressure as the reactor. The gas temperature is reduced in the heat exchanger in order to allow a low temperature valve to be used for flow and pressure control. Downstream of the flow control valve the gases enter a cyclone separator where any remaining liquid water and ash are removed.

Dry Feed System for the POC

The dry feed system transports the pulverized coal from the fluid bed to the reactor using carbon dioxide. A drawing of the lower portion of the coal feed system is shown in Figure 104. The system for this reactor was built using the same dimensions for the key components as were used by Tuia[2] and therefore the coal flow results obtained were expected to be similar. The figure shows where the 325 mesh, stainless steel screen is sandwiched between two 300# flanges with Garlock gaskets allowing CO_2 flow from below to create a fluidized bed within the 2 in. schedule 80 steel pipe. A reducer transitions the diameter from 49.25 mm on the 2 inch pipe to 146.3 mm on the 6 inch pipe. The inside surface of the reducer and the welds were ground and polished to reduce coal from sticking to the inner walls of the pipe and allow coal to fall freely from the hopper into the fluid bed region. The exit for the mixture of pulverized coal and CO_2 flowing toward the burner was located 222.25 mm above the wire screen through the threadolet indicated in Figure 104.

Commonly acknowledged regimes for are fluidized bed with increasing flow velocity are: 1) minimum fluidization, 2) bubbling bed, 3) slugging bed 4) turbulent bed, 5) fast fluidization, and 6) pneumatic transport. The work of Tuia suggests that fluidization CO_2 flow rates between 1 and 3 kg/hr produce a minimum fluidization regime in the 2 inch pipe and pneumatic transport in the 9.525 mm tubing that transports the coal / CO_2 to the burner. It is also possible that the bed transitions between the minimum fluidization and the bubbling bed regimes during operation.

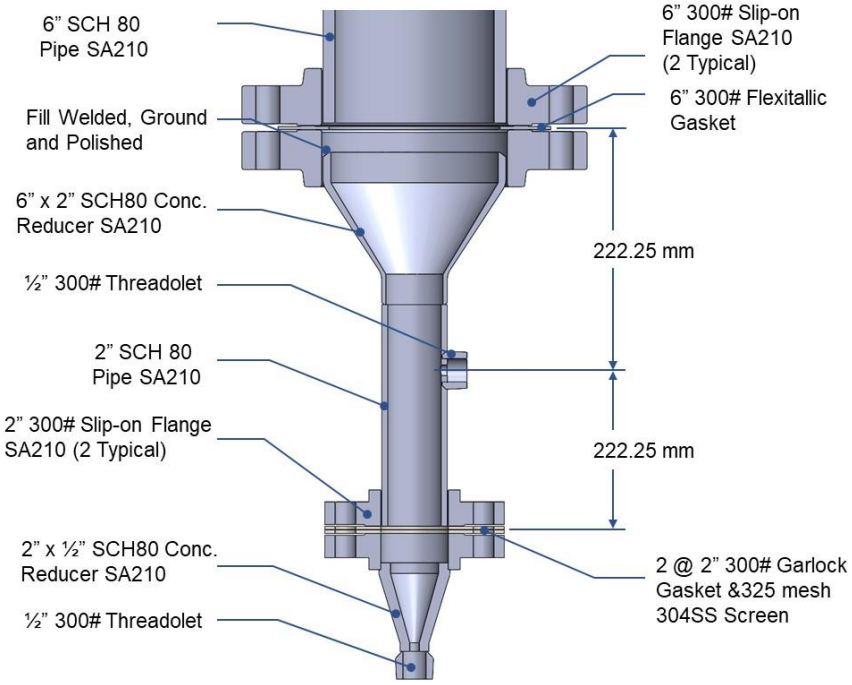

Figure 102. Cross section of the bottom of the coal feeder showing the geometry of the fluidizing region.

Reactor Core or Pressurized Reactor Vessel

A side view cross section of the burner cap, main shell, slag trap and quench port is shown in Figure 103. The figure contains key dimensions for the location of access ports, the materials and dimensions of the refractory, and the dimensions of the path for reactants and products through the reactor. The burner cap is made from a 30 in pipe cap with a 30 in flange welded on the bottom and an 8 in pipe connecting the cap to an 8 inch flange on top. The cylindrical refractory for the burner slides though the top flange of the burner cap.

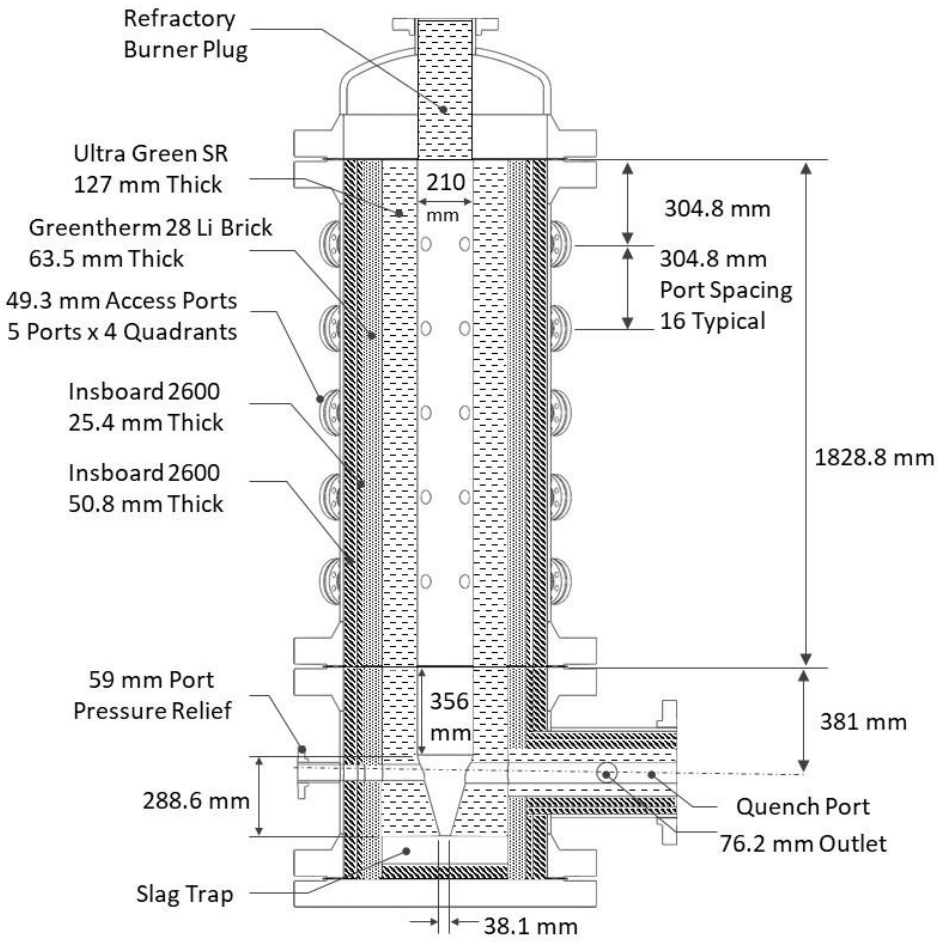

Figure 103. Cross section of the burner cap, main reactor and slag trap. All dimensions are in mm.

The main reactor core is 1,829 mm (6 ft) in length and 210.2 mm (8.25 in) in diameter with the outer shell diameter of 0.813 m (32 in). The main reactor contains five access ports distributed axially 304.8 mm (1 ft) apart along each of the four sides of the reactor for a total of 20 access ports. Currently, the northeast and southwest ports are optical access ports containing quartz windows. Each optical access port contains a fitting where a purge gas can be added to eliminate condensation and deposition on the windows. The ports along the northwest side of the reactor contain embedded B-type thermocouple pairs. One thermocouple is 114.3 mm from the reactor centerline while the second is 165. 1 mm from the centerline. Because the thermocouples were embedded when the refractory was poured, the thermal resistance to heat transfer is relatively undisturbed and can therefore provide a more accurate means of measuring heat flux. From these two thermocouples, the surface temperature can also be estimated.

The insulation between the reactor core and shell consists of four separate refractory layers. The outer most layer next to the metal shell is Insboard 2600 and is 50.8 mm thick. The second layer is the same material only 25.4 mm thick. The third layer is Greentherm 28 Li brick with a

thickness of 63.5 mm. The inner most layer is 127 mm (5 in) thick Ultra Green SR, which is a castable material.

In the bottom section, the refractory narrows in a cone shape from 203.2 mm to 38.1 mm and then expands abruptly into the slag trap. This design allows the slag to flow down the reactor surface and then fall off the tip of the cone into the trap. Two ports are drilled through the refractory: one for the exit exhaust gas and a second which contains an exit nozzle for a rupture diaphragm for safety pressure relief. The exhaust exit passage is a 76.2 mm (3 inch) diameter hole cast into the refractory and a 76.2 mm hole cast into a 12 inch pipe ending with a 12 inch flange. An access port perpendicular to the exhaust port is a 76.2 mm hole and 6 inch flange used to mount a spray atomizer to quench the exhaust gases.

Atmospheric Pressure Testing in the POC

Prior to the experiments conducted for this program, the reactor had been operated only at a pressure of 13.8 bar (200 psi) while firing a Utah Bituminous Coal. The feeding system was specifically designed to operate at pressure. Its efficacy has not been demonstrated at near atmospheric pressures, but REI and BYU attempted to operate at near atmospheric conditions during the test campaign.

The POC was designed for the investigation of combustion of pulverized solid fuels at elevated pressure. A desired outcome of this project was to gather deposition and corrosion data at near atmospheric pressures. However, the POC had only been operated at pressures at or near 200 psig. Moreover, the fluidized bed coal feed system was designed to operate in the range of 200 to 400 psig and the bench scale testing was performed at those pressure conditions. As a preparatory step for atmospheric tests, BYU performed scoping tests on the POC to evaluate the coal feed behavior at near atmospheric conditions. The furnace was heated overnight to wall temperatures necessary for coal flame ignition. Previous bench and pilot-scale testing suggests that to achieve a Utah bituminous coal flow rate of approximately 13 kg/hr (100 kW) a CO_2 fluidization flow rate of between 3 and 4 kg/hr is necessary. With no other information available, tests were initiated at a fluidization flow rate of about 1 kg/hr. The result was near-zero coal flow. The fluidization CO_2 flow rate was then increased to 3 kg/hr and the coal flow rate spiked up to 90 kg/hr filling the reactor with unburned material. In response to that, the fluidization CO_2 flow rate was reduced back to 1 kg/hr, which did slow the coal flow rate. However, the change was not drastic enough, so the fluidization flow was stopped altogether and the tests were discontinued. A summary plot of the data representing this behavior is provided in Figure 104.

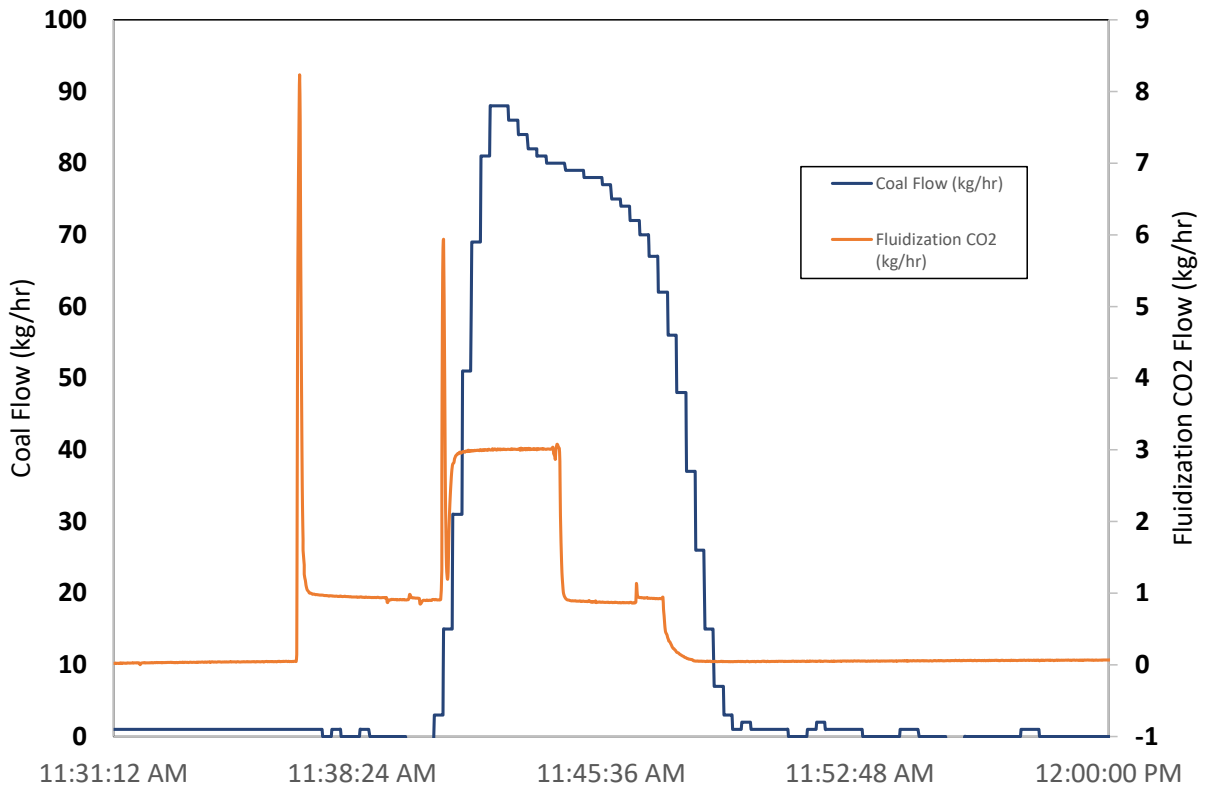

Figure 104. Coal flow rate as motivated by CO_2 fluidization in a pressurized dry coal feed system attached to the POC at BYU

The data presented in Figure 104 indicate that it is certainly possible to flow coal into the POC at atmospheric pressure. It is also apparent that the window of fluidization flow necessary to control the coal flow rate is very small. This is not necessarily concerning because there are other parameters that can be tuned to reduce the sensitivity of flow rate to the fluidization flow rate, such as the amount of CO_2 that is vented at the top of the column. Finding the right combination of settings for atmospheric operation could be very time consuming.

As BYU performed these tests at atmospheric pressure, REI and University of Utah worked on making necessary changes to hardware configurations that would facilitate integration of their respective instrumentation into the POC system. This included the REI real-time corrosion monitoring system and the University of Utah ash aerosol sampling system.

Coal is fed to the POC using a high pressure fluidized bed feeder, represented by the leftmost object in Figure 99. The feeder consists of a 6" SCH 80 carbon steel hopper approximately 18' in height and a 2" SCH 80 fluidization section that is approximately 8" in height. The hopper is filled with coal prior to a test campaign. A completely full hopper would provide approximately 6 hours of operation, depending on the firing rate. There are three CO_2 flows associated with operation of the high-pressure solids feeder. A flow of CO_2 is introduced into the bottom of the fluidization section to fluidize the coal in the bottom of the feeder and to motivate a dense

phase stream of coal and CO_2 out of the feeder and into the coal feed line. This CO_2 flow is referred to as fluidization CO_2. Additional CO_2 is introduced into the coal feed line immediately after the dense phase coal flow leaves the pressurized feeder to speed up the coal flow well above saltation velocities. This CO_2 flow is referred to as dilution CO_2. A small stream of CO_2 is also vented from the top of the pressurized coal feeder to lightly fluidize the coal in the hopper. This stream is referred to as the vent CO_2.

The coal fired in these experiments was a Utah Bituminous Coal from Skyline Mine. It was pulverized using a 1 ton per hour CE 312 Raymond Bowl Mill. The ultimate and proximate analysis of the coal is presented in Table 15 and the mineral matter composition is presented in Table 16. The particle size distribution was measured using a sieve shaker. The collected data representing the percentage of coal retained on each screen in that analysis is provided in Table 17.

Table 15. Skyline coal Ultimate and Proximate analysis.

	Ash	C	H	N	S	O	H_2O	Vol.	FC	HHV (Btu/lb)
Skyline	10.50	67.47	4.89	1.39	0.48	12.67	2.60	40.27	46.63	12212

Table 16. Skyline coal mineral matter composition.

	SiO_2	Al_2O_3	TiO_2	CaO	Fe_2O_3	K_2O	MgO	Na_2O	SO_3	P_2O_5	BaO	MnO_2	SrO
Skyline	65.34	15.32	0.76	5.24	3.57	0.74	1.27	1.35	5.11	0.63	0.08	0.01	0.12

Table 17. Particle Size Distribution of the Skyline Coal

Screen Mesh Size	% Mass Retained on Screen
30	0.00
50	0.96
80	3.86
100	4.82
200	55.63
325	31.19
400	0.96
Pan	2.57

Dry Feed System and Combustor Performance

The target operating conditions were to feed coal at a stable rate (more important that actual firing rate) at atmospheric pressure, 6.9 Bar (100 psig) and 14.5 Bar (210 psig). It should be appreciated that the POC was never intended for operation at atmospheric conditions. During design and preliminary testing of the feed system atmospheric conditions were never considered and the reactor dimensions were tailored for pressurized combustion when

considering residence time and velocity. The operating conditions for the firing rate and the oxygen and CO_2 flows were constrained by reactor behavior in the following ways: 1) The refractory temperature in the bottom of the reactor must remain above the melting temperature of the ash to allow the ash to flow as slag out of the bottom of the reactor. 2) The burner was designed to produce a long flame to distribute the heat release and avoid hot spots on the refractory. After operating, it was found that high O_2 concentrations are necessary to avoid production of CO, especially at lower firing rates where low velocities inhibit mixing.

The 6.9 Bar tests were run at two different coal flow rates on 03/10/22 and repeated at a third and higher coal flow rate on 03/29/22. The 14.5 Bar test was performed on 03/22/22 and the atmospheric tests were performed on 04/19/22. A summary of the average measured flows and other operating conditions for each of these tests is provided in Table 18. The calculated stoichiometric oxygen and stoichiometric ratios for various regions are also presented.

Table 18. Summary of average measured flows and other reactor conditions for the five tests. Stoichiometric oxygen and SRs are calculated values.

Date	Units	3/10/2022	3/10/2022	3/22/2022	3/29/2022	4/19/2022
Start Time		13:04:30	15:02:38	9:59:57	10:36:55	14:02:12
End Time		15:00:38	16:23:42	11:04:01	11:52:00	14:31:14
Reactor Pressure P3	psig	100.09	100.05	210.04	100.15	0.13
Coal Hopper	kg	31.37	19.80	24.64	29.39	28.63
CO_2 Fluidization	kg/hr	3.01	3.31	4.01	2.60	1.16
CO_2 Dilution	kg/hr	6.01	6.00	7.70	6.01	2.33
CO_2 Vent	kg/hr	1.5	1.5	1.5	1.5	0.5
Coal Flow (5 min ave)	kg/hr	5.34	9.29	6.97	12.84	7.59
CO_2 Annulus	kg/hr	12.65	12.65	12.65	12.65	12.65
CO_2 Tertiary	kg/hr	27.13	27.12	26.76	27.10	27.11
O_2 Annulus	kg/hr	3.21	3.17	3.21	3.16	3.21
O_2 Tertiary	kg/hr	26.96	35.06	26.91	31.77	26.91
Flue Gas O_2	% Vol, Dry	25.79	24.91	22.70	10.49	22.24
Flue Gas CO_2	% Vol, Dry	60.12	62.71	60.66	71.27	70.73
Clue Gas CO	% Vol, Dry	-0.02	-0.01	-0.02	-0.02	-0.46
Flue Gas SO_2	% Vol, Dry	-0.02	-0.01	-0.02	-0.02	-0.21
Flue Gas NOx	PPMV, Dry	-0.08	-0.01	-0.24	2.31	-100.78
B Thermocouple S1	°F	1122.41	1879.28	1655.64	1849.43	1590.65
B Thermocouple S3	°F	2100.71	2295.02	2053.26	2430.71	2082.96
B Thermocouple S5	°F	2081.52	2244.18	1967.82	2513.31	2118.90
Stoichiometric O_2	kg/hr	11.16	19.41	14.56	26.83	15.86
Overall SR		2.70	1.97	2.07	1.30	1.90
Inner Annulus SR		0.29	0.16	0.22	0.12	0.20

The measured coal flow and coal retained in the hopper for each of the tests are presented in Figure 105 through Figure 108.

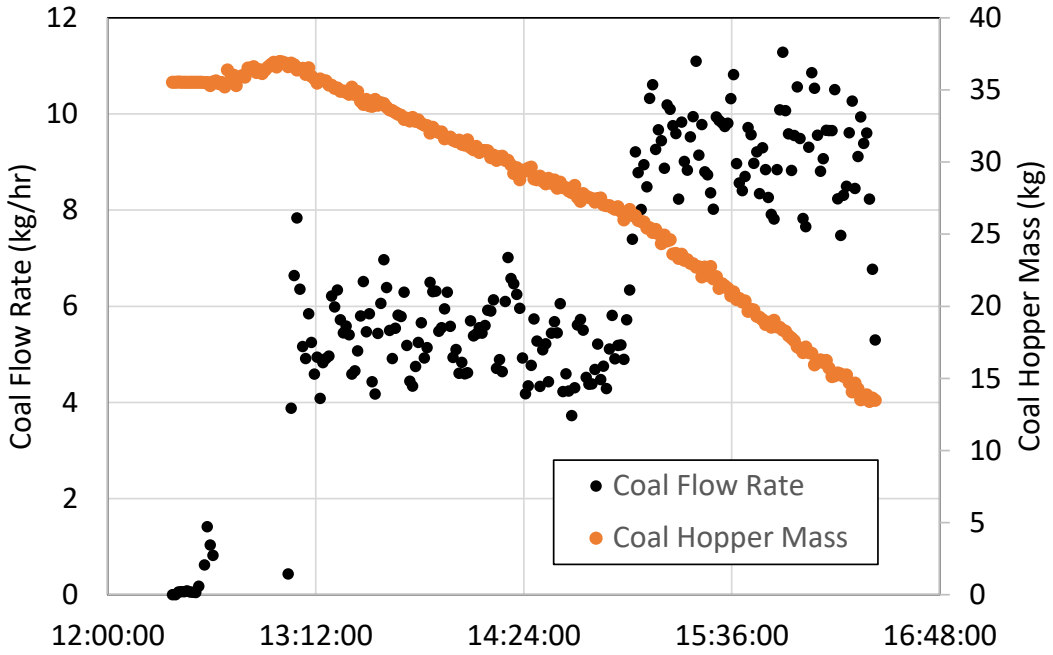

Figure 105. Coal flow rate and coal retained in the hopper for the testing on 03/10/22 (6.9 Bar conditions)

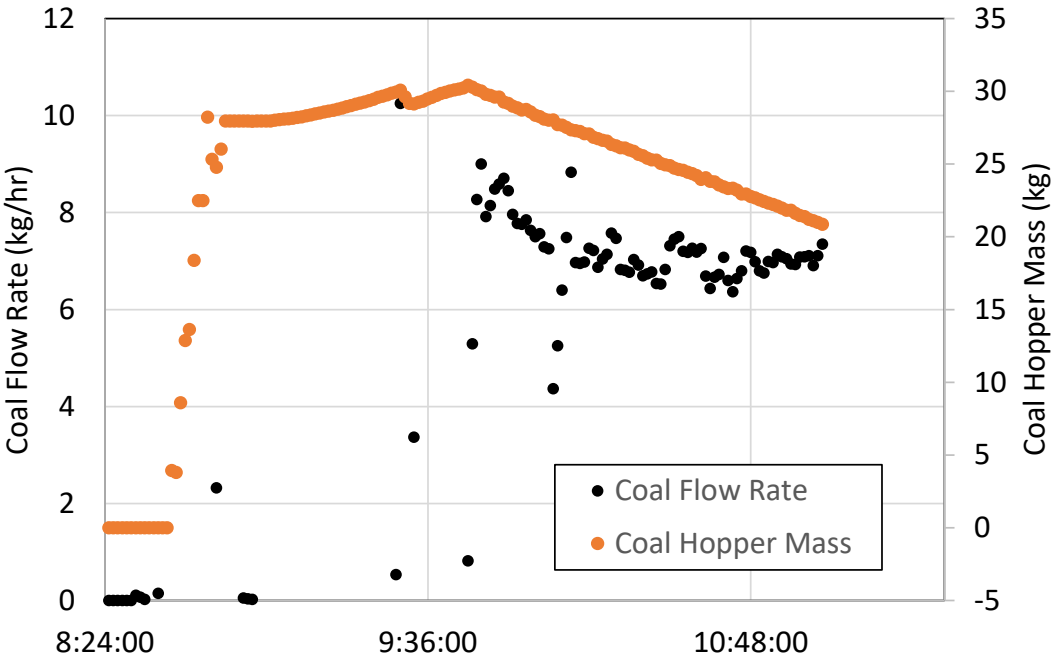

Figure 106. Coal flow rate and coal retained in the hopper for the testing on 03/22/22 (14.5 Bar conditions)

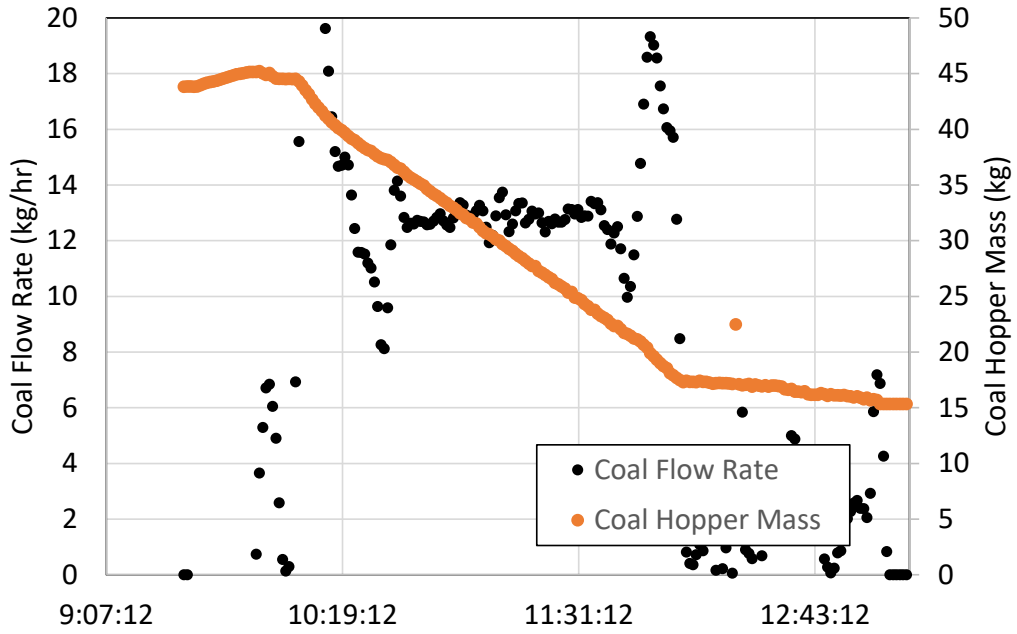

Figure 107. Coal flow rate and coal retained in the hopper for the testing on 03/29/22 (6.9 Bar conditions and high firing rate)

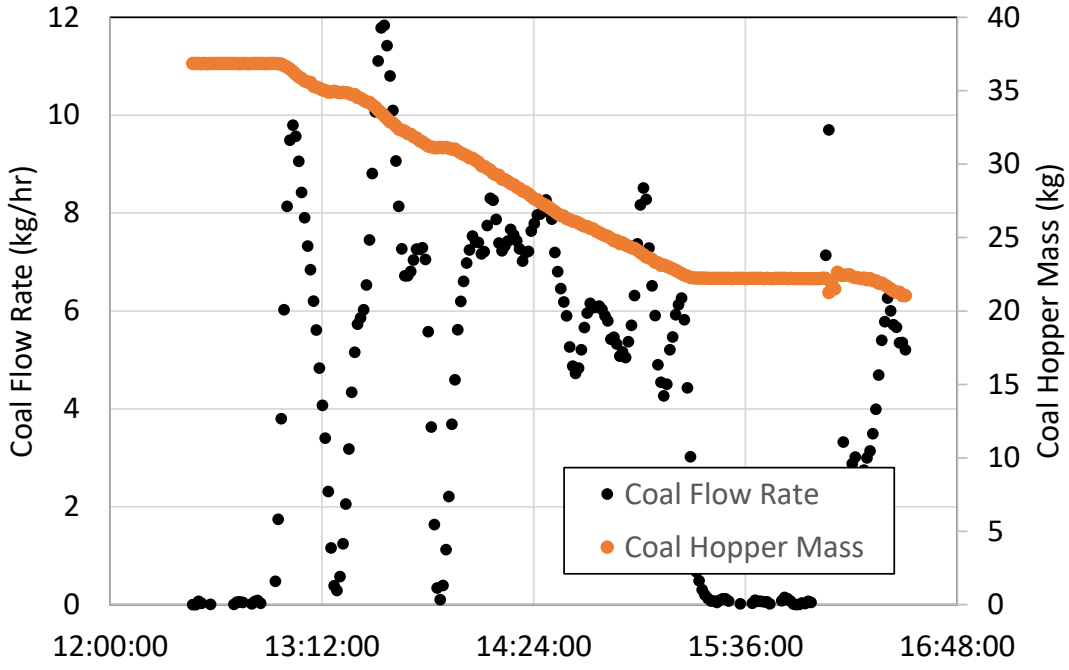

Figure 108. Coal flow rate and coal retained in the hopper for the testing on 04/19/22 (atmospheric conditions)

The coal flow data presented in Figure 105 through Figure 108 show the measured coal remaining in the hopper using load cells. In some cases, process of loading coal into the hopper prior to the test is also apparent. The coal flow rate is a calculated value, which is the slope of the measured hopper mass using 5 minutes of data, centered on the time where the flow is presented. These data show that reasonably steady coal flow rates can be achieved for the pressurized conditions, as the system was designed. However, a steady coal flow rate was difficult to achieve at the atmospheric conditions. For the purposes of data analysis, the data were averaged during the period when the coal flow was most steady. These time periods are indicated in Table 18.

The reactor pressure was stable for each of the tests at the provided set point. This is described by the plot of reactor pressure for the tests performed on 03/10/22 provided in Figure 109.

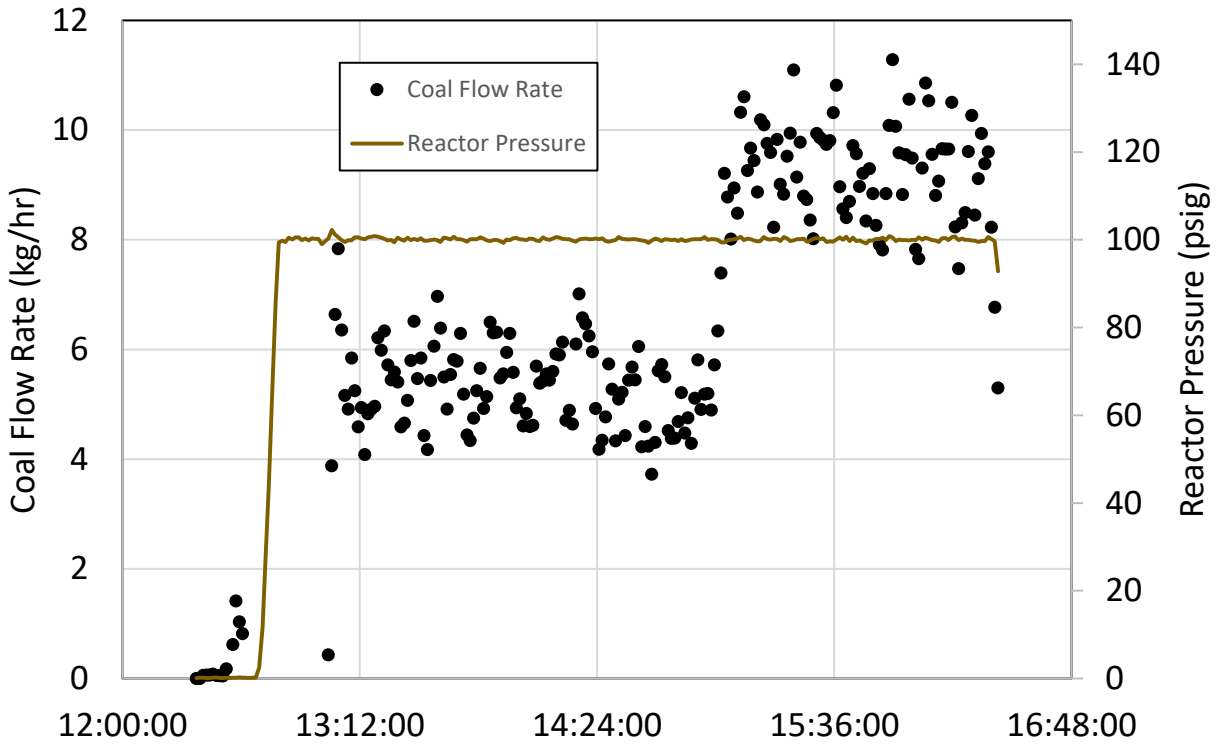

Figure 109. Coal flow rate and reactor pressure during the testing on 03/10/22

The measured flue gas O_2 and CO_2 concentrations are presented in Figure 110 through Figure 113. For these measurements, an extractive sample was taken from the reactor after the flue gas depressurizes through the pressure control valve and sent through a chiller to a California Analytical Analyzer. The O_2 measurement is paramagnetic and the CO_2 measurement is nondispersive infrared (NDIR). The O_2 and CO_2 are the dominant constituents in the dry flue gas. There was negligible CO and SO_2 for these tests. However, the sum of the O_2 and CO_2 do not quite equal 100%. This is because all of the optical access windows and the burst disc are all purged using N_2 for these tests.

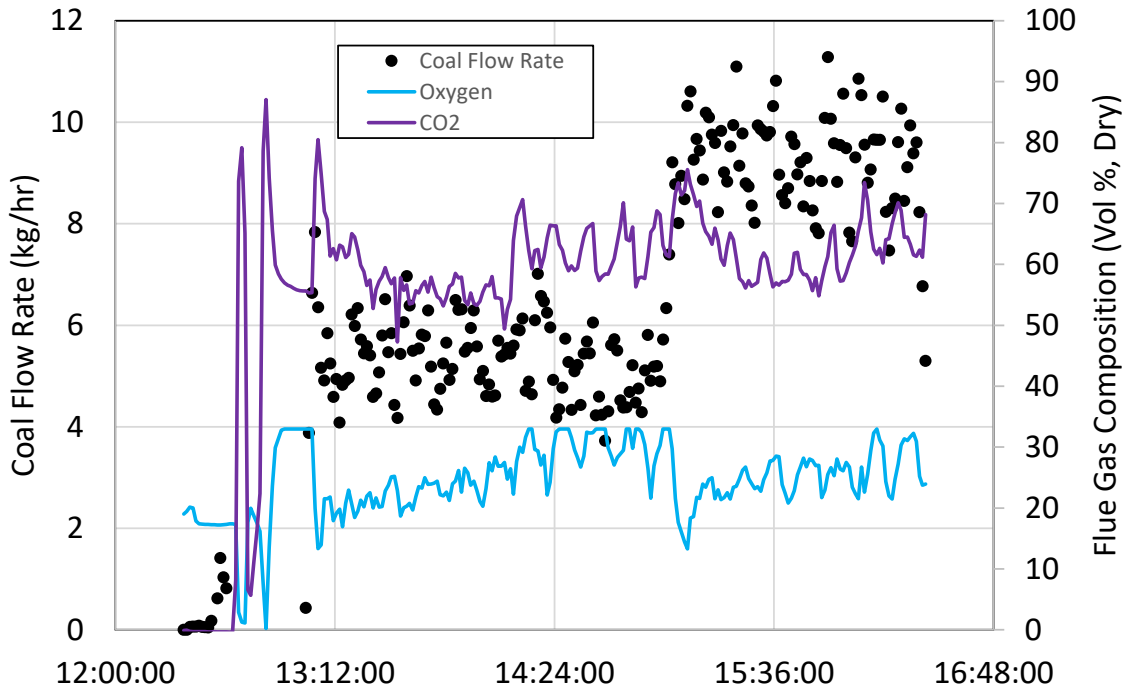

Figure 110. Measured O_2 and CO_2 concentrations in the flue gas along with coal flow rate for the tests on 03/10/22

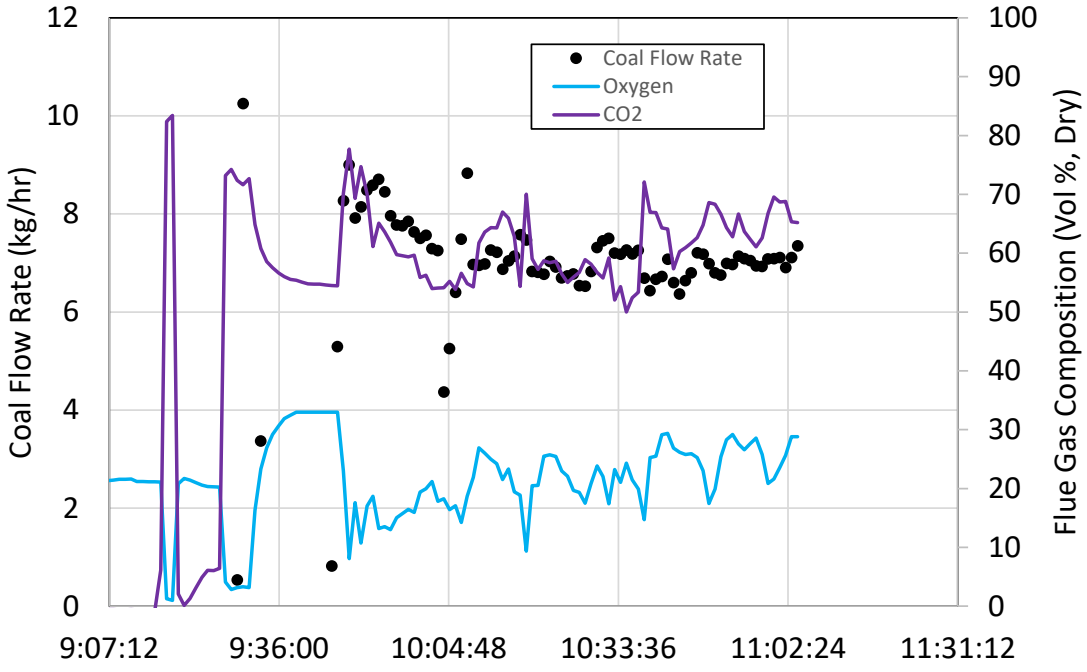

Figure 111. Measured O_2 and CO_2 concentrations in the flue gas along with coal flow rate for the test on 03/22/22

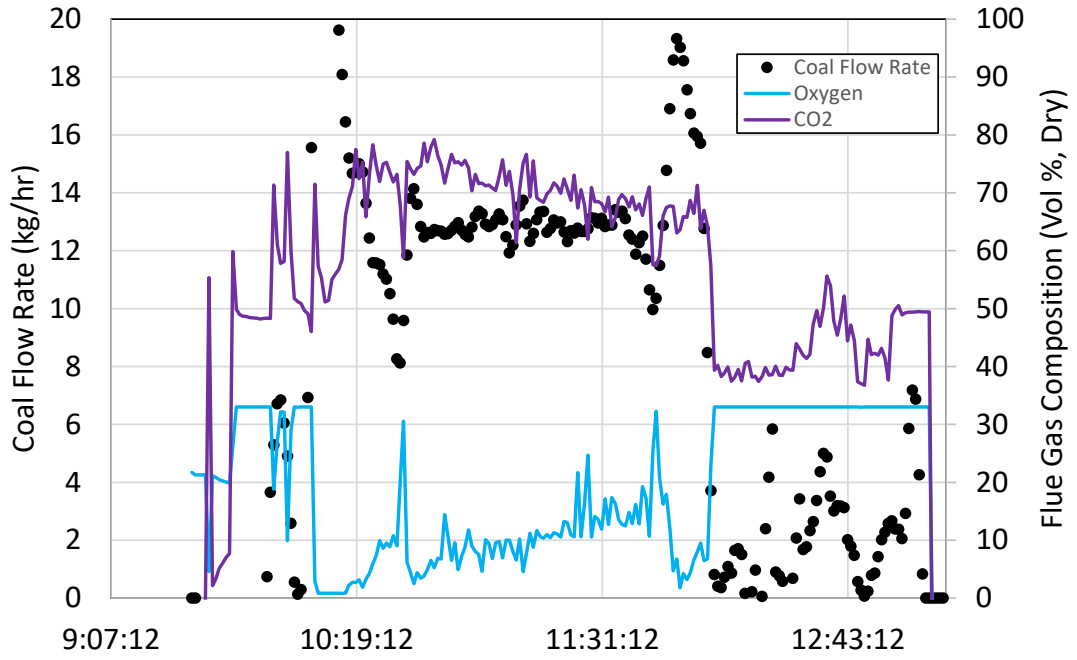

Figure 112. Measured O_2 and CO_2 concentrations in the flue gas along with coal flow rate for the test on 03/29/22

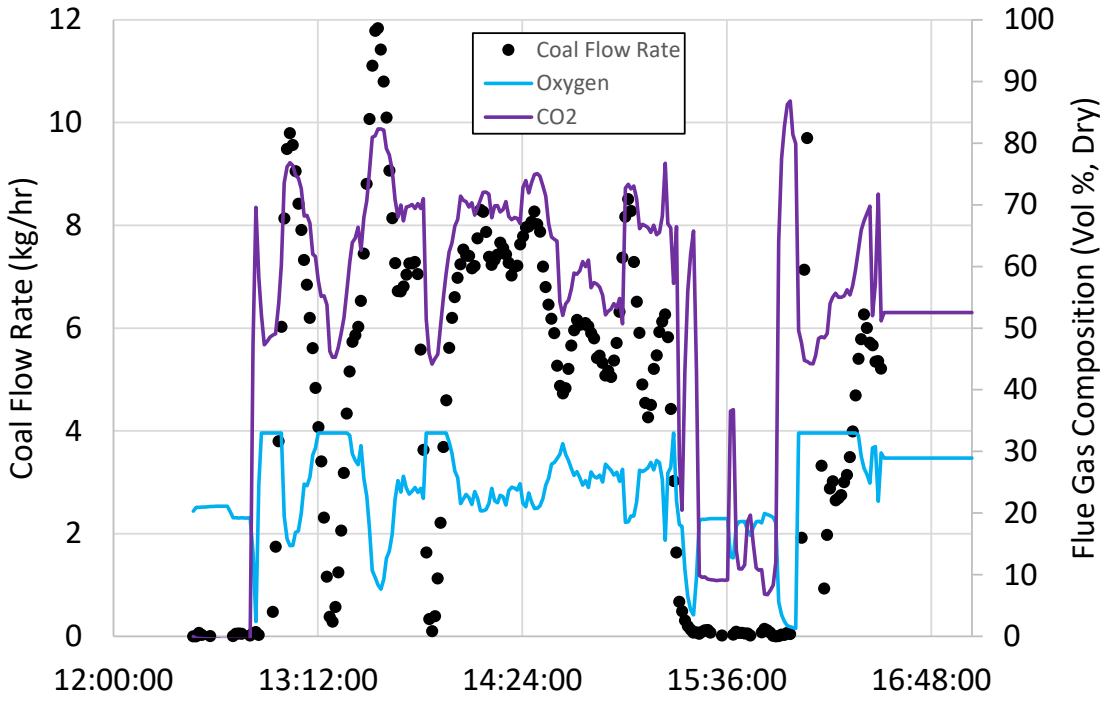

Figure 113. Measured O_2 and CO_2 concentrations in the flue gas along with coal flow rate for the test on 04/19/22

Subtask 5.1 – Heat Flux Characterization

The wall temperatures for these tests were measured using B-Thermocouples that were installed into ½" holes drilled into the refractory from outside of the reactor. The holes extended to within ½" of the inside surface of the refractory and the bead was placed next to the end of the hole. These thermocouples were installed in port 1 (Top), port 3 (middle) and port 5 (bottom). The data collected using these thermocouples is presented in Figure 114 through Figure 117.

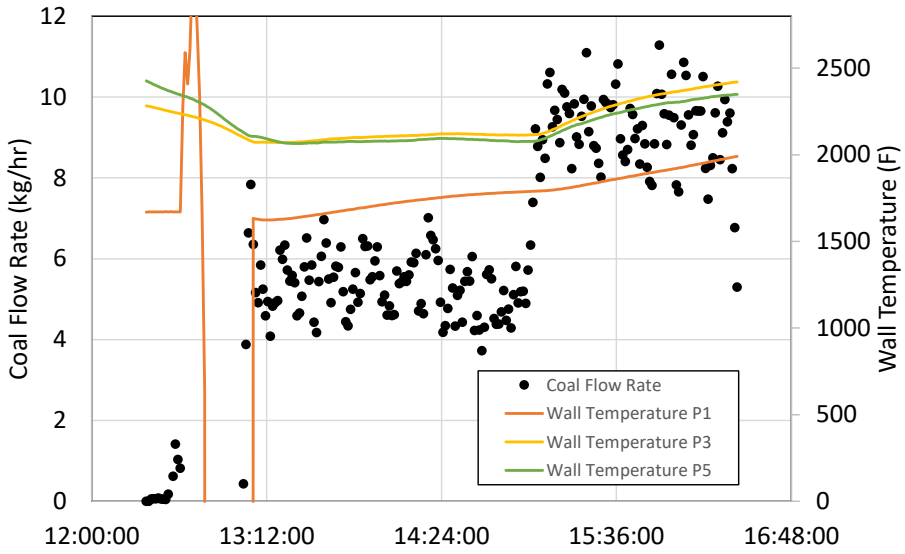

Figure 114. Wall surface thermocouple data along with coal flow rate for the tests performed on 03/10/22

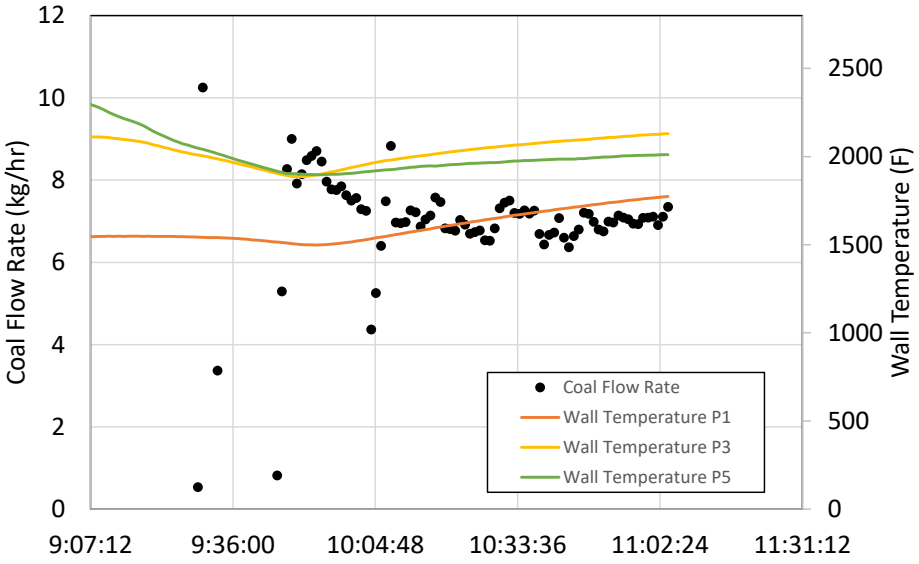

Figure 115. Wall surface thermocouple data along with coal flow rate for the tests performed on 03/22/22

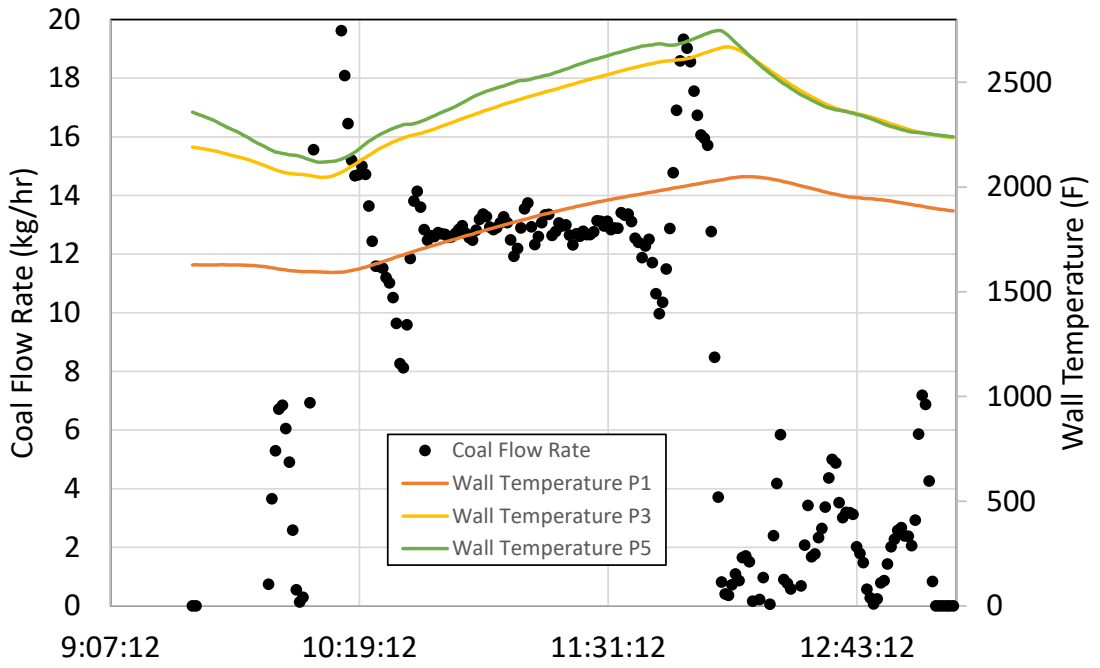

Figure 116. Wall surface thermocouple data along with coal flow rate for the tests performed on 03/29/22

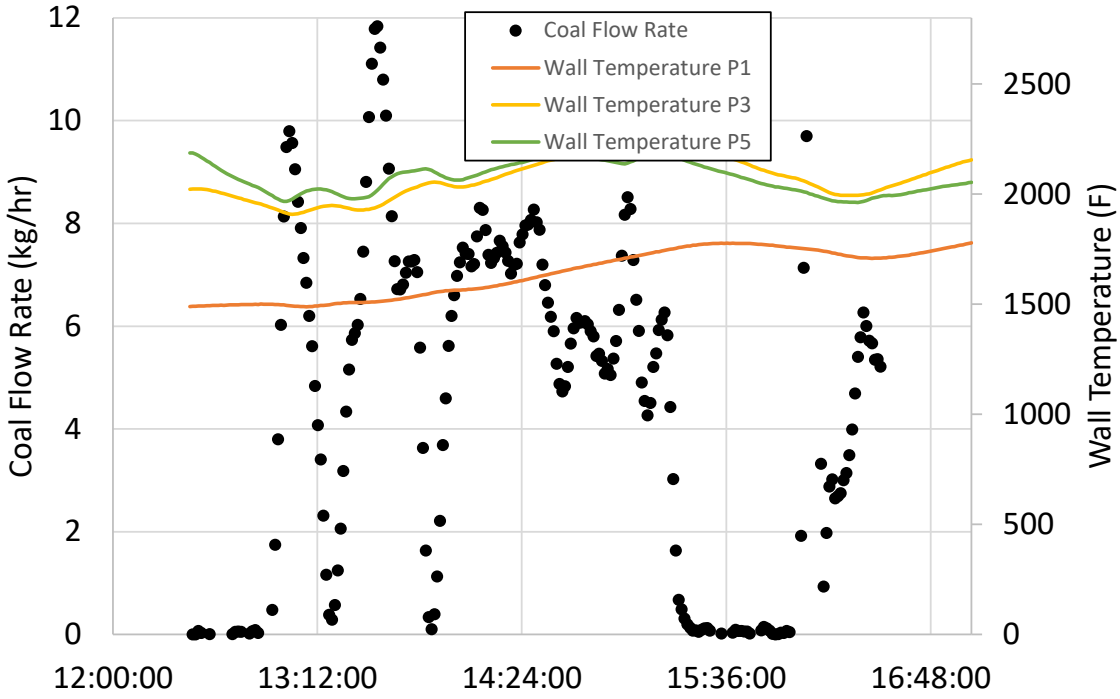

Figure 117. Wall surface thermocouple data along with coal flow rate for the tests performed on 04/19/22

The thermocouple data presented for the first two days of testing presented in Figure 114 and Figure 115 suggest two things. First, the overnight firing rate on natural gas is appropriate for coal flow rates of about 6 kg/hr. Second, the temperature profile of the refractory also supports the supposition that the flame is long and the heat release is delayed. This conclusion comes from the observation that the wall temperatures in the 3rd and 5th port are much higher than in the first port. When firing coal at 10-12 kg/hr as shown in Figure 109 and Figure 116, the surface temperatures of the reactor climb through the duration of the test. The temperature data presented in Figure 117 also support the observation that the coal flow rate is not very stable at the atmospheric condition.

Subtask 5.2 – EFPR Particle/Deposition Characterization

Initial calculations pertinent to the 300kW 17 bar high pressure tests in the EFPR were performed with a focus on the effects of water content in the feed on the adiabatic flame temperature of a PRB coal fired under various inlet oxidant conditions as well as pressure on the equilibrium ash speciation. The equilibrium calculations were performed using Outotec's Chemical Reaction and Equilibrium Software, HSC Chemistry. The effect of water content in the feed was an area of focus in the program as we were leveraging lessons learned in pressurized combustion experiments with a coal slurry feed to lay the foundation for pressurized tests with a dry feed. Previous work with slurry feeds in this reactor had a slurry feeding rate around 10 gallons per hour, with a coal weight fraction in the slurry between 50% and 55%.

Calculations of Adiabatic flame temperature (AFT)

Powder River Basin (PRB) coal in the slurry is combusted with pure oxygen (OXY100). The coal fraction of slurry is the parameter that changes AFT. The PRB coal analysis and its heating value are shown in Table 19.

Table 19: PRB coal analysis and heating value

C (%)	H (%)	S (%)	O (diff, %)	N (%)	A (%)	HHV (BTU/lb)
53.72	6.22	0.23	34.11	0.78	4.94	9078

Figure 118 reflects the adiabatic flame temperature with respect to the coal weight fraction of the slurry. Calculated results for a dry feed of PRB coal and Utah Sufco coal, with CO_2 as the diluent (as opposed to H_2O) are also plotted as comparison. At the same coal fraction, the PRB coal slurry has lower AFT than dry-fed PRB coal, resulting from heat absorption of water content. The Sufco coal dry feed has a relatively higher AFT than PRB due to its larger heating value. However, PRB coal has more interesting deposition behavior, since it is a high fouling coal.

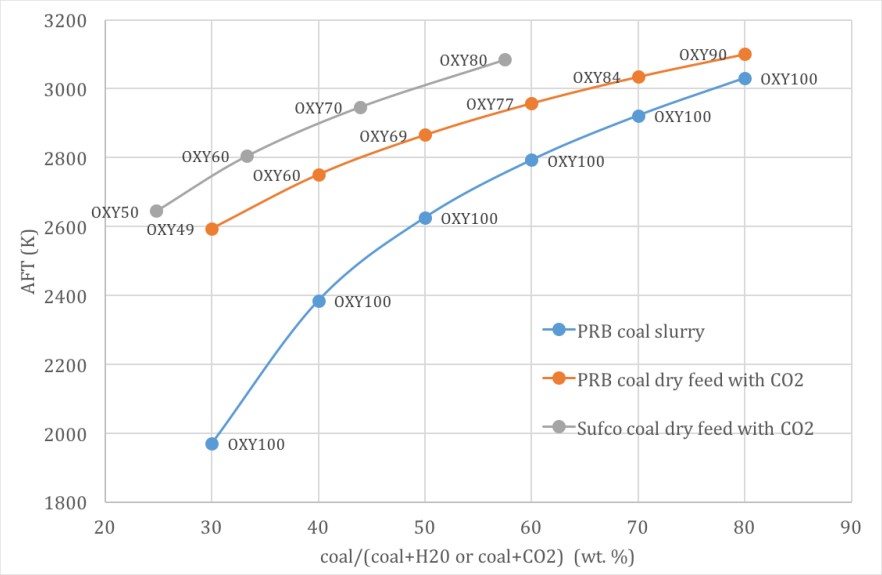

Figure 118: Adiabatic flame temperature with coal fraction in slurry or dry feed

Multicomponent mineral equilibrium

To investigate the influence of high pressure on mineral components of ash fume, an equilibrium calculation was performed using the HSC Chemistry software. Table 20 shows the ash analysis of PRB coal.

Table 20: PRB coal ash analysis

Al_2O_3 (%)	CaO (%)	Fe_2O_3 (%)	MgO (%)	MnO (%)	P_2O_5 (%)	K_2O (%)	SiO_2 (%)	Na_2O (%)	SO_3 (%)	TiO_2 (%)
14.78	22.19	5.2	5.17	0.01	1.07	0.35	30.46	1.94	8.83	1.3

The flue gas composition was calculated for a condition of 50 wt. % PRB coal and pure oxygen in slurry combustion. Table 21 provides the input species, in which aluminum, calcium, silicon, sodium and sulfur compounds were selected as major components in the original ash. Possible gaseous and solid phase species of the system are reported in Figure 119 and Figure 120, respectively. In this case, the corresponding AFT is 2626K and calculation temperatures are between 2000 and 2500K. Figure 121 shows significant species variation as pressure increased from 1 to 40 bar.

Table 21: Input species of HSC (kmol/kg coal)

CO_2	H_2O (g)	O_2	SiO_2	Al_2O_3	Na_2O	CaO	SO_3
0.04477	0.08665	0.00149	2.50E-04	7.16E-05	1.55E-05	1.95E-04	5.45E-05

Al(g)	AlS(g)	C2O(g)	H2O(g)	OAlH(g)	SiH(g)
Al2(g)	AlS2(g)	C3O2(g)	H2O2(g)	OAlOH(g)	SiH2(g)
AlC(g)	Al2S(g)	COOH(g)	HS(g)	OH(g)	SiH3(g)
AlC2(g)	(AlS)2(g)	COS(g)	H2S(g)	S(g)	SiH4(g)
Al2C2(g)	C(g)	CS(g)	H2S2(g)	S2(g)	Si2H4(g)
AlC3H9(g)	C2(g)	CS2(g)	H2SO4	SO(g)	Si2H6(g)
AlH(g)	CH(g)	Ca(g)	H2SiO3(g)	SO2(g)	SiH2(CH3)2(g)
AlH2(g)	CH2(g)	Ca2(g)	Na(g)	SO3(g)	SiO(g)
AlH3(g)	CH3(g)	CaH(g)	Na2(g)	S2O(g)	SiO2(g)
AlO(g)	CH4(g)	CaO(g)	NaH(g)	Si(g)	Si2O2(g)
AlO2(g)	C2H(g)	CaOH(g)	NaO(g)	Si2(g)	SiOOH(g)
Al2O(g)	C2H2(g)	Ca(OH)2(g)	Na2O(g)	Si3(g)	SiS(g)
Al2O2(g)	C2H3(g)	CaS(g)	Na2O2(g)	Si4(g)	SiS2(g)
Al2O3(g)	C2H4(g)	H(g)	NaOH(g)	SiC(g)	
AlOH(g)	C2H5(g)	H2(g)	Na2O2H2(g)	SiC2(g)	
Al(OH)2(g)	C2H6(g)	HCO(g)	Na2SO4(g)	Si2C(g)	
Al(OH)3(g)	CO(g)	HCOOH(g)	O(g)	Si(CH3)4(g)	
AlO(OH)(g)	CO2(g)	HO2(g)	O2(g)	Si(CH3)2O(g)	amount: 103

Figure 119: Possible gaseous phase species of the system

Al2CO	CaAl2Si4O12*4H2O	*4CaO*Al2O3*13H2O	CaSiO3	NaAlSi3O8	NaH2SiO4*8H2O	Na2SiO3*9H2O	Si(CH3)4
Al4CO4	CaAl2Si7O18*6H2O	CaO*Al2O3*SiO2	Ca2SiO4	Na2Al2Si4O12	NaO2	SO3	Si(C2H5)4
AlO	CaAl2Si7O18*7H2O	CaO*Al2O3*2SiO2	Ca3SiO5	Na2Al2Si6O16	NaO3	SiO2	Al
Al2O3	Ca2Al4Si14O36*14H2O	*2CaO*Al2O3*SiO2	Ca3Si2O7	*3NaAlSi3O8*CaCO3	Na2O	SiO2*H2O	Al2Ca
Al(OH)3	CaAl2Si3O10(OH)2	*3CaO*Al2O3*3SiO2	Ca3Si2O7*2CaCO3	NaAlSi2O6*H2O	Na2O2	Al2S3	Al4Ca
Al2O3*H2O	CaAl4Si2O10(OH)2	Ca(OH)2	*2Ca2SiO4*CaCO3	NaAl3Si3O10(OH)2	Na2O*Al2O3	CaS	AlH3
Al2O3*3H2O	Ca2Al2SiO6(OH)2	*2CaO*SiO2	HNaO4S	NaCH3COO*3H2O	NaOH	NaS	C
Al2O3*SiO2(D)	Ca2Al2Si3O10(OH)2	*3CaO*SiO2	H4O4Si	NaCHO2	Na2O*2SiO2	NaS2	Ca
Al2O3*2SiO2	Ca2Al3Si3O12*OH	*3CaO*2SiO2	H2SO4	NaC2H3O2	Na2O*3SiO2	Na2S	CaAl2
*3Al2O3*2SiO2	CaAl2Si2O7(OH)2*H2O	CaO*2SiO2*2H2O	H2SO4*H2O	NaCHOO*2H2O	*2Na2O*SiO2	Na2S2	CaAl4
Al2O3*2SiO2*2H2O	CaCO3	*2CaO*3SiO2*2.5H2O	H2SO4*2H2O	NaCHOO*3H2O	*3Na2O*2SiO2	Na2S3	CaH2
Al2(SO4)3	CaC2O4	*3CaO*2SiO2*3H2O	H2SO4*3H2O	Na2CO3	Na2SO3	Na2S4	CaSi
Al2(SO4)3*6H2O	CaC2O4*H2O	*4CaO*3SiO2*1.5H2O	H2SO4*4H2O	Na2C2O4	Na2SO4	SiS	CaSi2
Al2(SO4)3*6H2O(B)	Ca2NaAl5Si13O36*16H2	*5CaO*6SiO2*3H2O	H2SO4*6.5H2O	Na2CO3*H2O	Na2S2O3	SiS2	Ca2Si
Al2SiO5	CaO	*5CaO*6SiO2*5.5H2O	H2SiO3	Na2CO3*7H2O	Na2S2O7	Al4C3	Na
Al2Si2O7*2H2O	CaO2	*5CaO*6SiO2*10.5H2O	H2Si2O5	Na2CO3*10H2O	Na2SO3*7H2O	AlC3H9	NaAlH4
Al2Si2O5(OH)4	CaO*Al2O3	*6CaO*6SiO2*H2O	NaAl2(AlSi3O10)(OH)2	Na2CO3*3NaHCO3	Na2SO4*7H2O	AlC6H15	Na3AlH6
Al2Si4O10(OH)2	CaO*2Al2O3	CaSO3	NaAlCO3(OH)2	Na2CO3*NaHCO3*2H2(	Na2SO4*10H2O	AlC8H19	NaH
(COOH)2	CaO*6Al2O3	CaSO4	NaAlO2	NaCa3Al5Si7O24CO3	Na2S2O3*5H2O	AlC9H21	S
Ca2Al4Si8H14O31(L)	*2CaO*Al2O3	CaSO3*0.5H2O	NaAl(OH)4	NaHCO3	Na2SiO3	Al4SiC4	Si2H6
CaAl2SiO6	*3CaO*Al2O3	CaSO3*2H2O	NaAl3(SO4)2(OH)6	NaHSO4	Na2SiO3*5H2O	CaC2	
Ca3(Al2Si2O8)3*CaCO3	*12CaO*7Al2O3	CaSO4*0.5H2O	NaAlSiO4	NaHSO4*H2O	Na2SiO3*6H2O	Na2C2	
CaAl2Si4O12*2H2O	*3CaO*Al2O3*6H2O	CaSO4*2H2O	NaAlSi2O6	NaH2SiO4*7H2O	Na2SiO3*8H2O	SiC	amount: 181

Figure 120: Possible solid phase species of the system

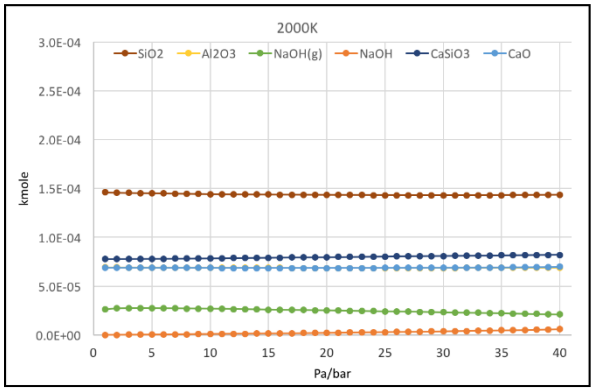

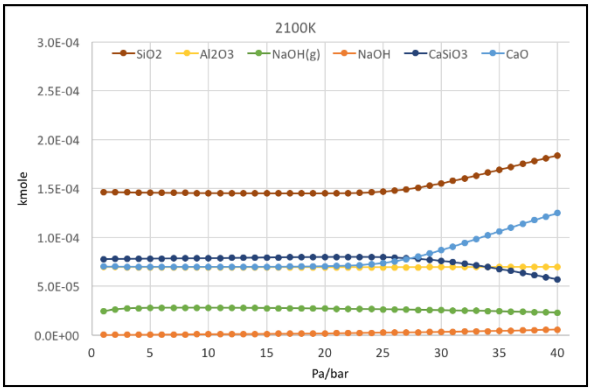

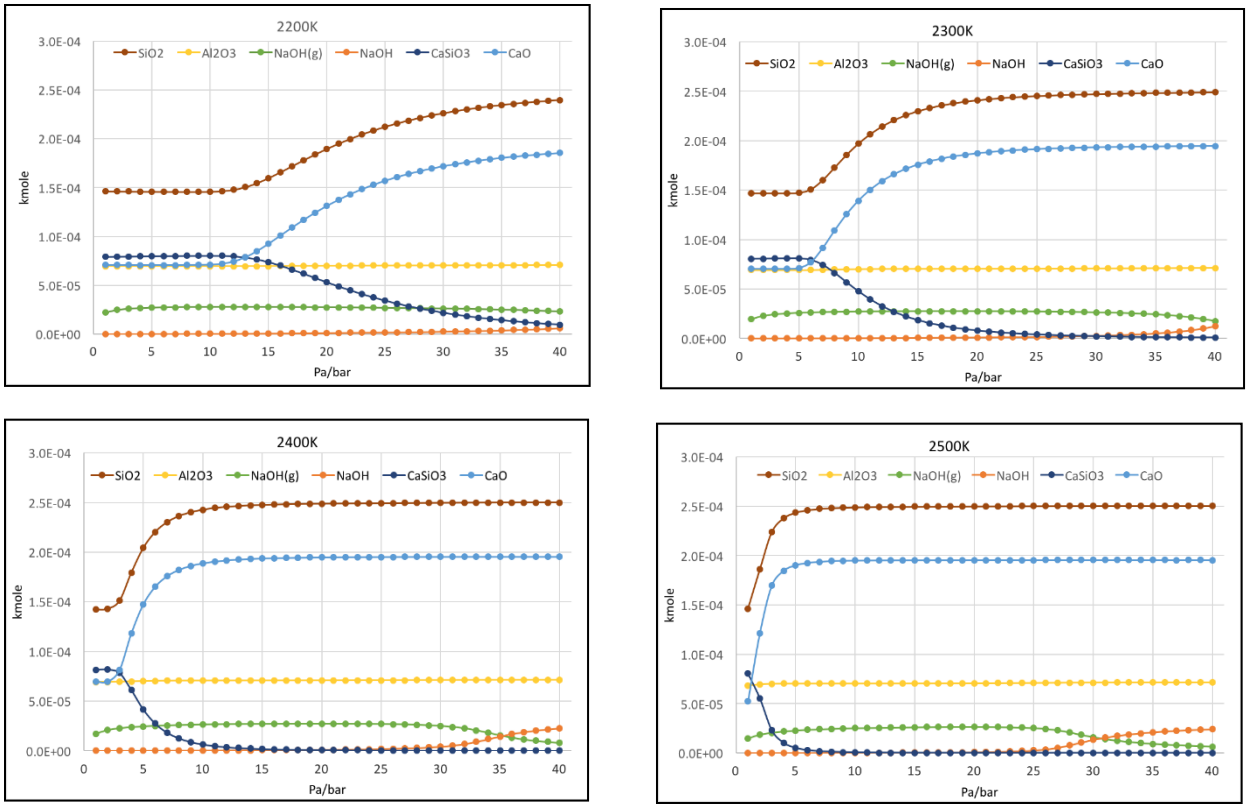

Figure 121: Mineral equilibrium calculation results

Pressure Effects on Coagulation Rates and the Accumulation Mode of Vaporized Ash Aerosol Particle Size Distribution

If assumed that at a given temperature the vaporized mass of mineral matter does not change, one can calculate the effect of pressure on the ensuing ash aerosol particle size distribution. To this end, we have employed the program MAEROS that uses a sectional model to integrate the General Dynamic Equation, considering only that portion of the aerosol particle size distribution that results from ash vaporization and subsequent nucleation, condensation and coagulation. This can be justified since it can be shown that there is no interaction between the much larger fragmentation modes (>1 µm) and the accumulation mode that results from coagulation of mineral matter that had been vaporized and nucleated.

In Figure 122 and Figure 123, we consider a prototype problem in which the temporal evolution of the (once vaporized) aerosol is assumed to and allowed to coagulate at a constant temperature (in this case set to 2000K). We have since completed similar calculations with a temperature quench and this did not alter the results significantly. Since the coagulation rate depends on the square of the number concentration of the aerosol, one might expect that the aerosol at 17 bar would coagulate to form much larger particle sizes than it would at 1 bar, for the same mass of nuclei input. We calculated the initial mass of the vaporized mineral matter from previous data taken at high temperatures and one atmosphere from the University of Utah's 100 kW Oxy-Fuel Combustor (OFC). All the nuclei were placed in the smallest 'bin,'

namely that of size 0.01-0.02µm. There are 20 logarithmically spaced 'bins' in all, from 0 to 100µm.

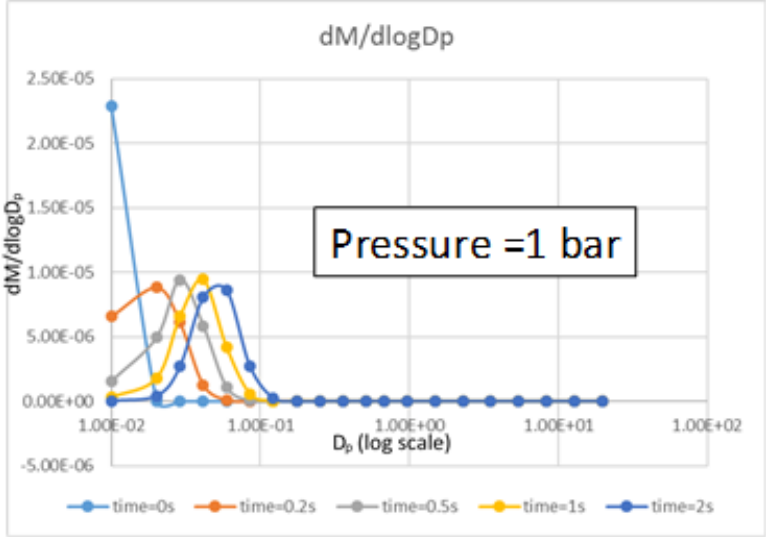

Figure 122: Temporal evolution of the PSD of ash nuclei resulting from mineral matter vaporization at 1 bar, constant temperature, 2000K

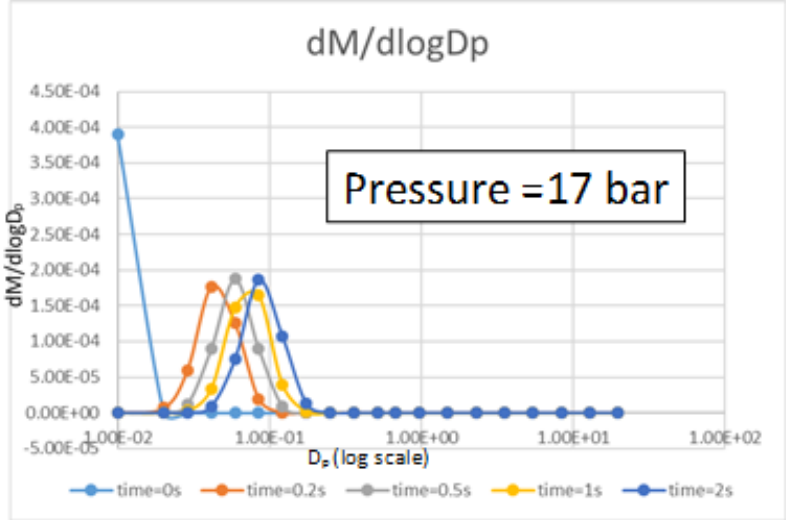

Figure 123: Temporal evolution of the PSD of ash nuclei resulting from mineral matter vaporization at 17 bar, 2000K

The results are surprising because they show that even though the initial mass concentration of nuclei varies by a factor of 17, the asymptotic value of the mean particle diameter at the accumulation (vaporization) mode at long times (2s) increases only modestly, although it does increase as expected. This shows again that it is extremely difficult to coagulate nuclei into much larger particles, because the number concentration falls so rapidly no matter what the initial concentration might be.

Work on the development and design of a probe system that would allow ash aerosols to be sampled iso-kinetically from the 17-bar oxy-combustion environment entailed the following system requirements:

1. The pressurized integrity of the EFPR cannot be compromised, and safety features to shut down the sample system should high temperatures spread beyond the probe tip, should be in place.
2. Water condensation must be avoided throughout the sample system. This is a special issue at the high pressures and large amounts of water to be expected in the slurry fed system, which represents the worst-case analysis.
3. The aerosol sample must be quenched at the probe tip in order to:
    a. Quench further reactions
    b. Minimize subsequent aerosol coagulation in the probe, so that the particle size distributions measured downstream in the sample line, correctly represent the particle size distributions in the EFPR
    c. Allow the sample rate at the probe tip to be such that the flue gas sample is extracted into the probe isokinetically, that is, without any bending or curvature of the fluid streamlines entering the probe tip. The mass flux $(\rho v)_{av,probe}$ of the sample entering the probe must equal the mass flux $(\rho v)_{av,EFPR}$ of the flue gas in the furnace.

Water condensation in the probe

We consider the most extreme case first, namely potential condensation of water in the probe, for a high moisture (slurry) coal feed into the EFPR. The dry feed conditions would be less severe, with lower water dew points. The more extreme case is used as the basis because we wished to use the same system for sampling particles for both slurry fed and dry fed EFPR conditions.

We wish to calculate the dew point in the sample probe over a range of dilution ratios injected at the probe tip. It is known that at atmospheric pressure, the dew point is never exceeded when dilution is sufficient to bring the sample to room temperature. This has been the basis of all of our particle sampling work heretofore. It is not clear whether this would still be valid at 17 bar. Note that it is not reasonable to have a critical orifice as the sampling entrance to bring the pressure to ~1 bar at the probe tip because then the sampling rate would not be isokinetic and would lead to distorted particle size distributions for dp > 5 µm.

Basis for the calculations:

Combustion conditions (worst case – slurry feed)

- Sufco coal slurry (OXY100)
- 40 wt. % coal, 60% H_2O (AFT of 2520K corresponding to OXY42 Sufco coal with dry feed)
- 55lb/hr coal
- Operation pressure: 17 bar

Flue gas parameters

- Flow rate: 31.0m^3/hr (at 1500K)

- Velocity: 0.27m/s (at 1500K)
- Composition (Table 22)

Table 22. Flue gas composition at given conditions for slurry fed oxy-coal combustion

Species vol. %				
CO_2	**H_2O**	**SO_2**	**O_2**	**NOx**
33.4	65.3	0.07	1.15	0.08

According to compressibility factors in Table 23, water vapor in flue gas is expected to behave ideally. So, Dalton's law was adopted to calculate its partial pressure p_w:

$$p_w = y_w p_t$$

where y_w is the molar fraction of water in gas mixture and p_t is the total pressure.

Table 23. Compressibility factors for water vapor[3]

TABLE 2-185 Compressibility Factors for Water Substance (fps units)*

Pressure, lb/in² abs.	Temp., °F																		
	400	600	800	1000	1200	1400	1600	1800	2000	2200	2400	2600	2800	3000	3200	3400	3600	3800	4000
10	0.9965	0.9989	0.9992	0.9995	0.9999	0.9999	0.9999	1.0000	1.0000	1.0000	1.0001	1.0006	1.0012	1.0024	1.0053	1.0084	1.0145	1.0211	1.0332
15	0.9943	0.9972	0.9986	0.9993	0.9997	0.9998	0.9999	0.9999	1.0000	1.0000	1.0001	1.0004	1.0012	1.0022	1.0042	1.0072	1.0124	1.0188	1.0295
20	0.9930	0.9970	0.9981	0.9991	0.9995	0.9996	0.9998	0.9999	1.0000	1.0000	1.0001	1.0003	1.0011	1.0020	1.0036	1.0065	1.0112	1.0173	1.0269
40	0.9861	0.9940	0.9967	0.9981	0.9990	0.9994	0.9996	0.9998	0.9999	0.9999	1.0001	1.0003	1.0010	1.0018	1.0028	1.0054	1.0090	1.0139	1.0214
60	0.9788	0.9910	0.9951	0.9973	0.9984	0.9991	0.9994	0.9997	0.9999	0.9999	1.0001	1.0003	1.0009	1.0018	1.0024	1.0048	1.0080	1.0120	1.0186
80	0.9714	0.9878	0.9935	0.9963	0.9979	0.9987	0.9992	0.9996	0.9998	0.9999	1.0001	1.0003	1.0008	1.0016	1.0023	1.0044	1.0073	1.0108	1.0170
100	0.9469	0.9848	0.9919	0.9954	0.9974	0.9985	0.9990	0.9995	0.9998	0.9999	1.0001	1.0004	1.0007	1.0015	1.0022	1.0042	1.0067	1.0099	1.0157
150	0.9435	0.9770	0.9879	0.9931	0.9960	9.9976	0.9985	0.9993	0.9997	0.9998	1.0001	1.0004	1.0006	1.0014	1.0021	1.0039	1.0059	1.0087	1.0137
200	0.9216	0.9690	0.9839	0.9908	0.9947	0.9968	0.9980	0.9991	0.9996	0.9998	1.0001	1.0005	1.0007	1.0015	1.0021	1.0037	1.0055	1.0080	1.0126
400		0.9356	0.9675	0.9817	0.9893	0.9935	0.9960	0.9982	0.9992	0.9998	1.0002	1.0007	1.0011	1.0017	1.0023	1.0033	1.0049	1.0070	1.0105
600		0.8989	0.9509	0.9725	0.9839	0.9904	0.9942	0.9973	0.9988	0.9997	1.0002	1.0008	1.0014	1.0019	1.0026	1.0034	1.0048	1.0066	1.0097
800		0.8586	0.9336	0.9633	0.9790	0.9872	0.9925	0.9964	0.9985	0.9996	1.0003	1.0010	1.0016	1.0022	1.0029	1.0036	1.0049	1.0065	1.0094
1,000		0.8138	0.9162	0.9540	0.9733	0.9841	0.9905	0.9955	0.9981	0.9994	1.0004	1.0012	1.0019	1.0025	1.0032	1.0039	1.0052	1.0066	1.0092
1,500		0.6702	0.8695	0.9305	0.9600	0.9764	0.9859	0.9932	0.9971	0.9992	1.0007	1.0017	1.0026	1.0033	1.0040	1.0048	1.0059	1.0072	1.0096
2,000			0.8188	0.9067	0.9468	0.9687	0.9813	0.9900	0.9958	0.9990	1.0010	1.0023	1.0034	1.0042	1.0049	1.0058	1.0068	1.0082	1.0104
4,000			0.5608	0.8060	0.8942	0.9392	0.9647	0.9836	0.9930	0.9989	1.0024	1.0050	1.0069	1.0082	1.0093	1.0106	1.0118	1.0132	1.0149
6,000				0.7042	0.8442	0.9121	0.9497	0.9771	0.9907	0.9991	1.0048	1.0081	1.0110	1.0128	1.0139	1.0152	1.0165	1.0179	1.0195
8,000				0.6185	0.8003	0.8883	0.9371	0.9714	0.9895	1.0004	1.0075	1.0118	1.0152	1.0172	1.0188	1.0204	1.0216	1.0229	1.0242
10,000				0.5699	0.7657	0.8693	0.9274	0.9668	0.9890	1.0025	1.0105	1.0158	1.0196	1.0220	1.0240	1.0258	1.0271	1.0284	1.0298

*Calculated by P. E. Liley from various steam tables for the lower temperatures and from Paper B-11 by P. H. Kesselman and Yu. I. Blank, 7th. Int. Conf. Properties of Steam, Tokyo, 1968, for the higher temperatures.

When the partial pressure of water vapor in gas mixture equals the vapor pressure of pure saturated liquid water:

$$p_w = p_w^{sat} \quad \textbf{3}$$

the temperature of the liquid water in equilibrium with water vapor is taken as an (approximate[1]) dew point

[1] This assumes that since the permanent gases are only slightly soluble in liquid water, which can be taken as pure water, the dew point and the bubble point are very close.

$$T_d = T^{sat} \quad (4)$$

The partial pressure p_w of water vapor was calculated for various dilution ratios from 0 up to 200, for total pressures ranging from 13 to 21 bar. Then by checking water saturation properties in the NIST database (similar to a saturated steam table), T_d is obtained by reading the corresponding T^{sat} for that partial pressure. Results are shown in Figure 124.

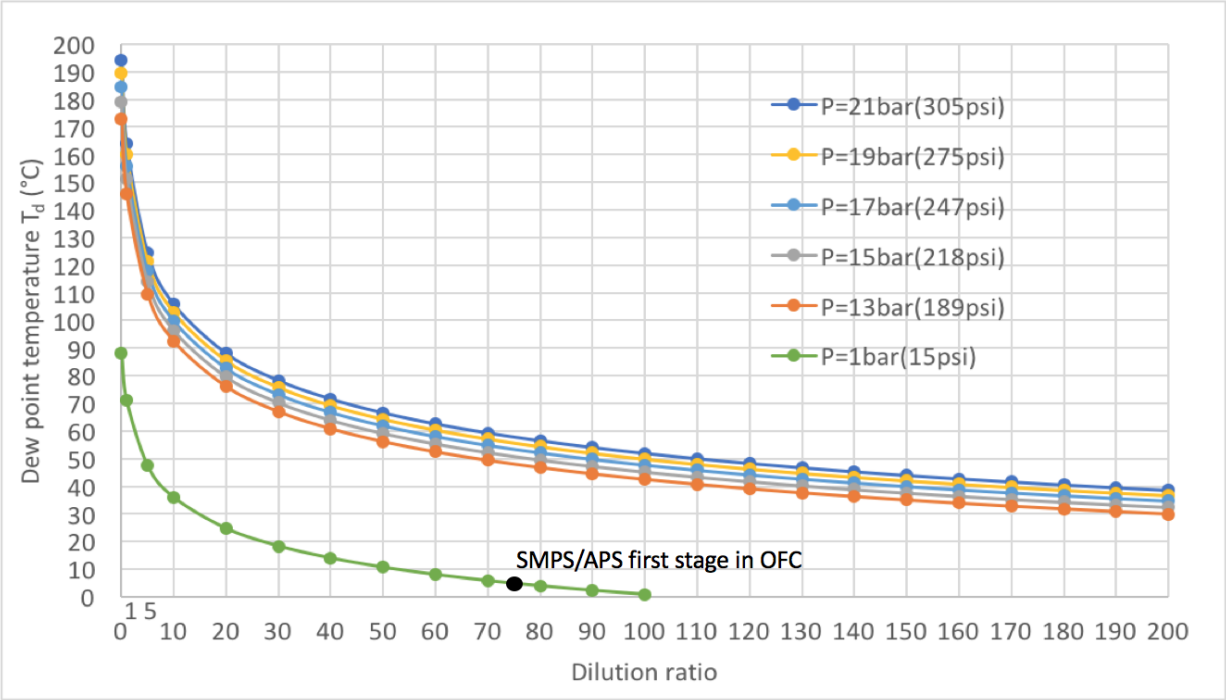

Figure 124. Dew point calculated for different dilution ratios at the sample probe tip. The lowest (green) curve is that for atmospheric pressure, and is applicable to the existing successful techniques for extracting aerosol samples at atmospheric pressure. The flue gas is that for the Sufco coal slurry feed shown above for all cases.

Figure 124 shows that whereas at atmospheric pressure, dilution alone easily lowered dew points to below atmospheric temperature, this is not the case at the higher pressures. There, heating must be applied to be well above the condensation point for the water.

Figure 124 does not show the results of a heat balance caused by dilution, and so does not show the actual temperatures of the mixtures. Rather, it calculates the temperature at which condensation occurs by virtue of dilution alone, not how that temperature might be reached.

For the first stage, complete mixing of flue gas (1500K) and dilution N_2 (303K) at the probe tip is assumed. The mixture temperature T_m is calculated from the following equations, where the left and right sides stand for heat loss of flue gas components and heat gain of N_2.

$$-\sum M_i \int_{1500}^{T_m} c_{pi}\, dT = M_{N_2} \int_{303}^{T_m} c_{pN_2}\, dT \qquad 5$$

$$c_{pi} = a_i + b_i T + c_i T^2 + d_i T^3 \qquad 6$$

A comparison of the mixture temperature T_m and the condensation temperature (dew point) is shown on Figure 125.

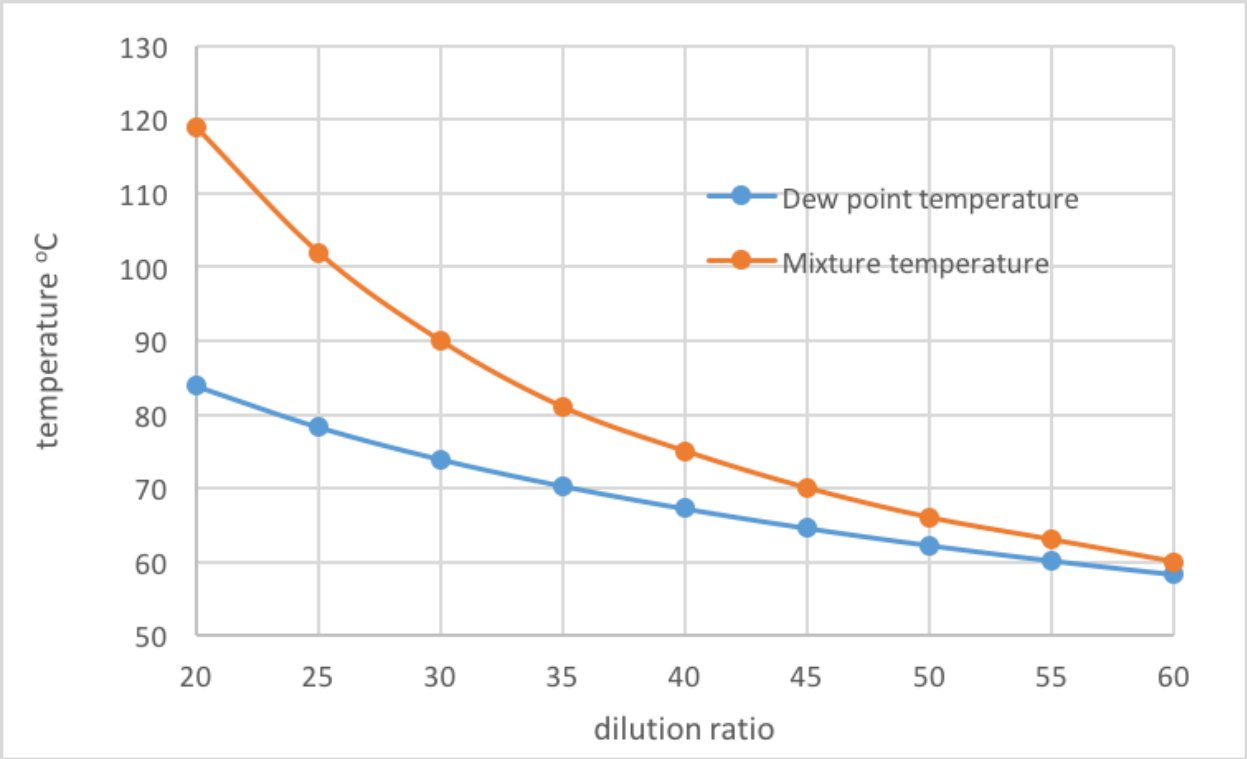

Figure 125. Comparison of sampled mixture temperature, T_m and condensation temperature (dew point) T_d at 17 bar, for the flue gas compositions above, as a function of dilution ratio at the probe tip. This assumes adiabatic mixing with no external heating or cooling.

Figure 125 shows that the mixture temperature closely approaches the condensation temperature at a dilution ratio of 60, which is less than we anticipate using here. Since this result is for an adiabatic system, additional work is required to incorporate the effects of heating for that section of the probe inside the EFPR and cooling outside the EFPR. After passing through the critical orifice to step down to atmospheric pressure there should be no condensation (see Figure 124).

The condensation temperature (water dew point) is elevated under high pressure conditions. The dew point in the flue gas, at 17 bar, for a coal slurry feed condition (worst case) has been calculated and presented in the preceding Q3 2017 progress report. Here, a solution to the same problem for a dry feed to the EFPR is presented.

Basis for the calculations for dry fed oxy-coal combustion include:

- Utah Sufco pulverized coal
- OXY50 (50 vol. % inlet O_2, 50 vol. % CO_2) as an initial condition for analysis
- 2645K adiabatic flame temperature
- Operation pressure: 17bar

Flue gas parameters

- Flow rate: 29.9m3/hr (at 1600K)
- Velocity: 0.26m/s (at 1600K)
- Composition (Table 24)

Table 24. Flue gas composition at given conditions dry fed oxy-coal combustion

Species vol. %				
CO_2	**H_2O**	**SO_2**	**O_2**	**NOx**
80.71	17.82	0.07	1.27	0.13

Although the pressure is maintained at 17 bar, the water content in the flue gas for dry fed coal is much lower than for slurry fed coal. Figure 126 displays the comparison of dew point temperatures in these two cases.

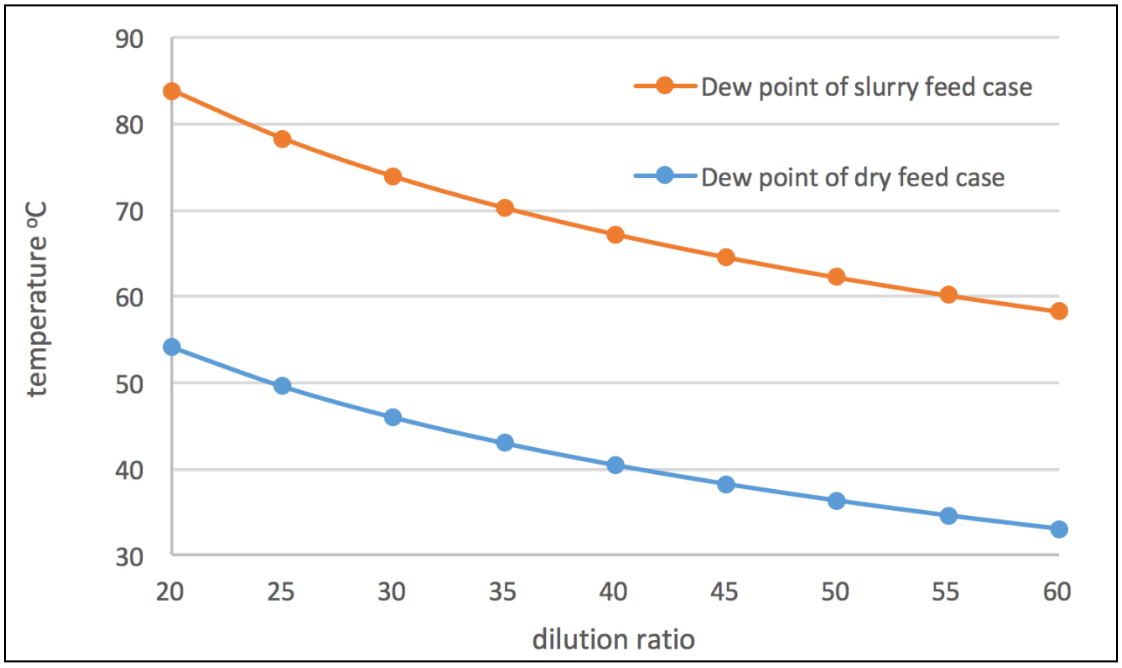

Figure 126. Comparison of condensation temperature (dew point) T_d at 17 bar in dry and slurry feed cases, as a function of dilution ratio at the probe tip.

The first stage dilution ratio at the probe tip is commonly chosen to be between 20 and 50. The dew point temperature at a dilution ratio of 50 is 36.3°C (309.5K). From Figure 126, the dry

feed leads to a dew point that is 30°C lower than that for a slurry feed. Therefore, there is a much lower potential for condensation in the dry feed case than in the slurry feed case.

A simulation of coupled fluid flow and heat transfer within the sample probe was conducted to determine probable sample temperatures before the pressure drops to 1 bar at the critical orifice in the sample line. Figure 127 is the schematic of the isokinetic probe designed for solid sampling from the EFPR. The boundaries of the model included the section of the probe that is inserted into the reactor (from the sampling tip to the connection flange). Beyond the flange, samples will lose heat to the environment as flow travels to the critical orifice.

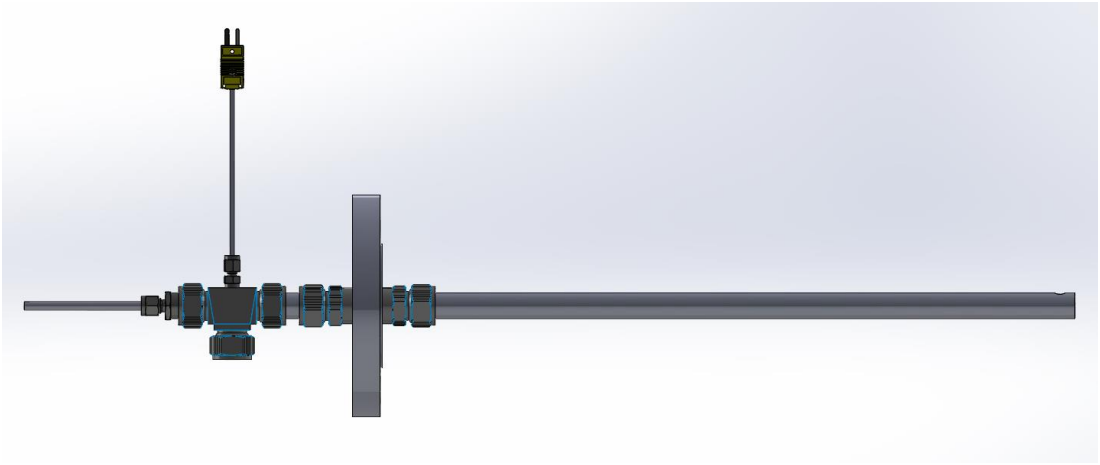

Figure 127. Schematic diagram of the high-pressure isokinetic probe

The simulation model is shown in Figure 128. It is a simplified geometric model consisting of a section of the EFPR, a sample port and the probe itself. Inswool insulation inserted between the port pipe and the probe outer tube will be used during initial tests to protect the probe from the high temperatures produced in the oxy-coal environment.

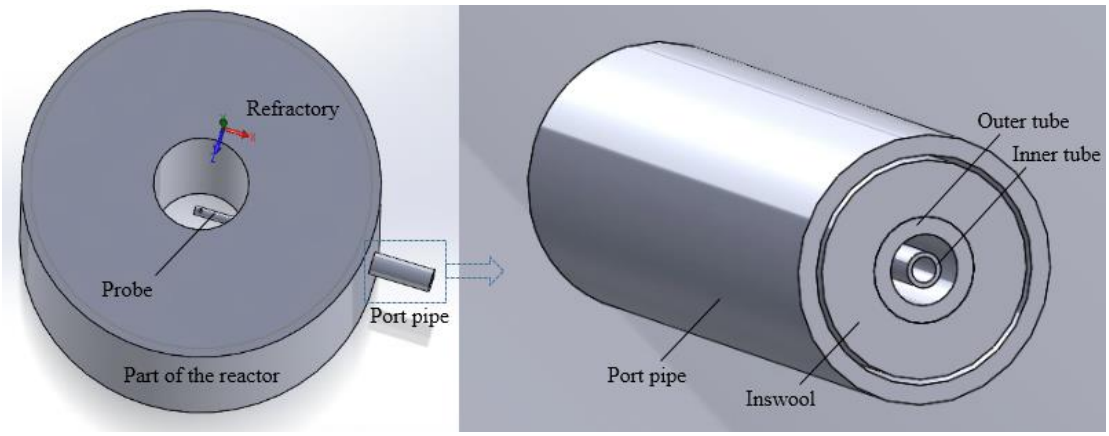

Figure 128. Simplified geometric model in the simulation

Simulation results in Figure 129 show the temperature profile at the cross-section of the model. The average temperature of the sample at the port exit is 477.3K, which is safely above the

calculated dew point of 309.5K. In addition, the predicted maximum temperature on the shell of 396.4°F is below the 500°F maximum allowed for the metal to maintain structural integrity. Model predictions indicate that the dilution nitrogen has a notable cooling effect on the sampled flue gas, although water condensation in the diluted sample is not likely to happen. The considerations cited above meet the requirements of solid sampling in the EFPR. Similar calculations were performed for the worst-case scenario with a slurry feed and similar results were found there as well.

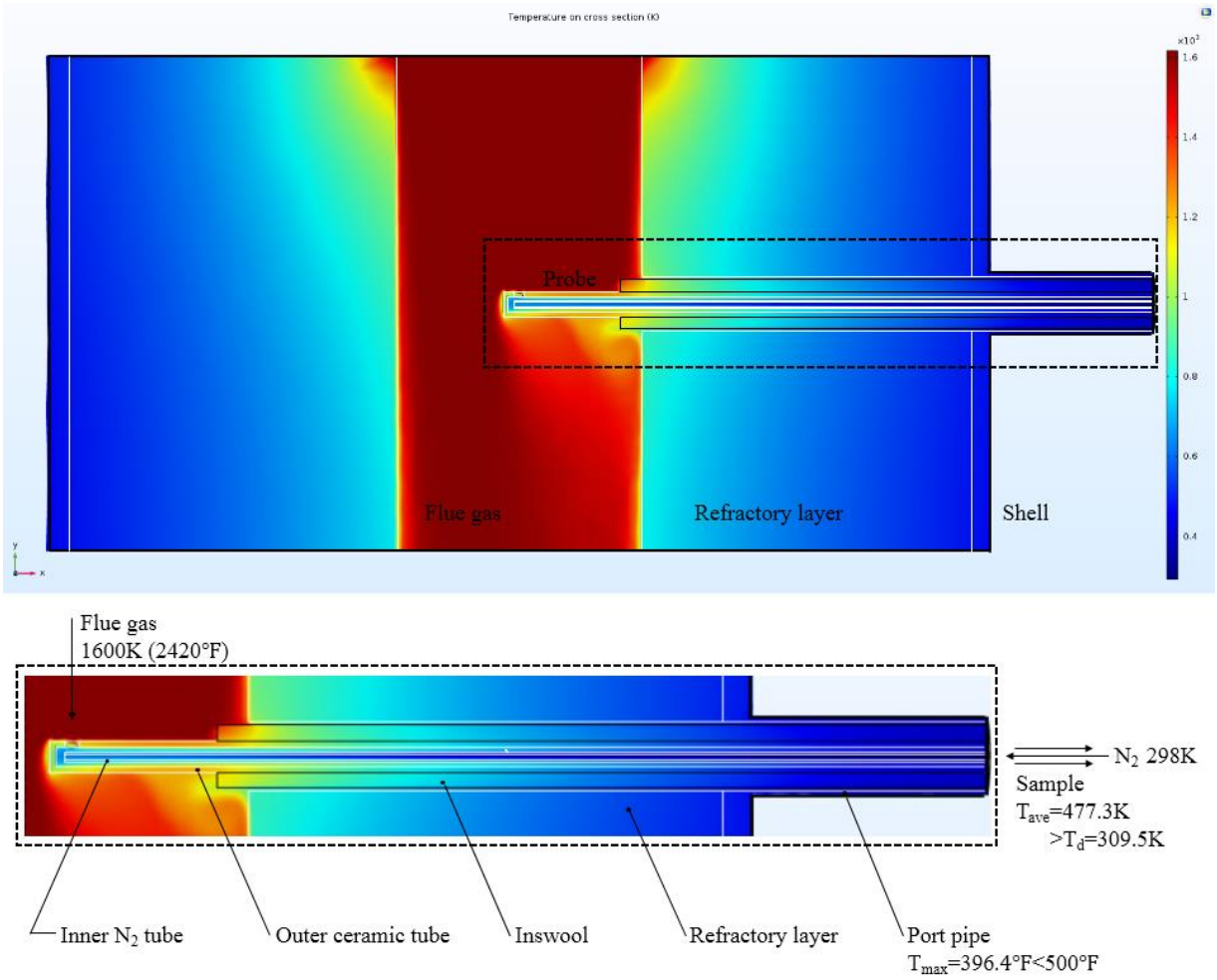

Figure 129. Temperature profile on the cross-section

Isokinetic probe design

The probe was designed for the combustion conditions following combustion conditions shown above and for the flue gas compositions depicted in Table 22, and with flue gas volumetric flow rate of 31.0 m^3/h (at 1500K), velocity of 0.27 m/s (at 1500K), Re = 2540.

The high-pressure particle probe is different from that used at atmospheric pressure because it is not cooled by a water jacket. Rather it is constructed of ceramic, without cooling, and with dilution N_2 injected at the probe tip. The ceramic tube envisioned has a maximum working temperature as high as 1750°C, making direct aerosol sampling in the combustor possible.

Figure 130 shows the design of the isokinetic probe. As shown in Figure 130, the probe, as an initial concept, has an outer ceramic sample tube and an inner steel tube for the dilution. The diameter of the tip inlet is 8mm and the (calculated) isokinetic sample flow rate is 0.8L/min N_2.

The ceramic tube is connected by tube fitting with graphite ferrules.

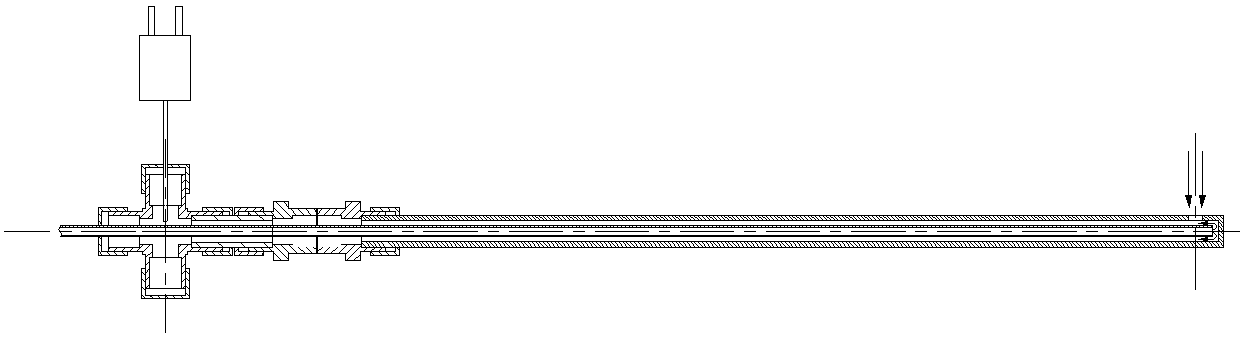

Figure 130. Design of the ceramic isokinetic probe

As shown in Figure 131, the dilution N_2 is supplied after passing through the check valve and the diluted sample is directed to the critical orifice to reduce pressure and control flow rate. The thermocouple inserted into the cross union monitors local temperature, providing a feedback signal for the safety valve, which will shut down the system once the temperature there exceeds a warning value. In the figure, key components are numbered:

1. 3/4'' OD ceramic tube 2. 1/4'' OD N_2 dilution tube 3. 3/4'' tube socket weld

4. 2'' 300lb blind flange 5. thermocouple 6. 3/4'' union cross

7. check valve 8. mass flow controller 9. N_2 cylinder 10. safety valve

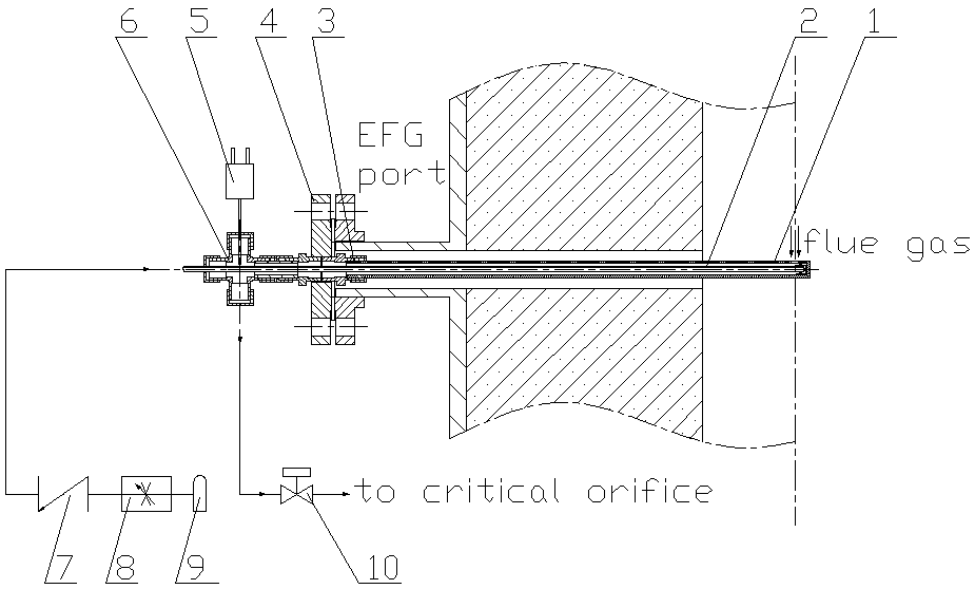

Figure 131. Schematic diagram of the high-pressure particle probe system

The flue gas sampled in the probe will remain high pressure before reaching the critical orifice. Water dew point temperature, T_d in this condition is higher than in an atmospheric condition, which makes condensation more likely to happen. Condensation will impair particle sampling, so the gas temperature must be kept higher than dew point.

Sampling system using SMPS/APS – two stage dilution is required

The critical orifice drops the pressure to atmospheric at which point condensation of water is no longer an issue. In order to use the scanning mobility particle sizer (SMPS) coupled with the aerodynamic particle sizer (APS) for on-line measurements of particle size distributions less than 20 µm, a two-stage dilution is required, as shown on Figure 132. The first stage dilution occurs at 17 bar at the probe tip. The second stage dilution occurs after the critical orifice at 1 bar. The issue is to avoid condensation upstream of the critical orifice.

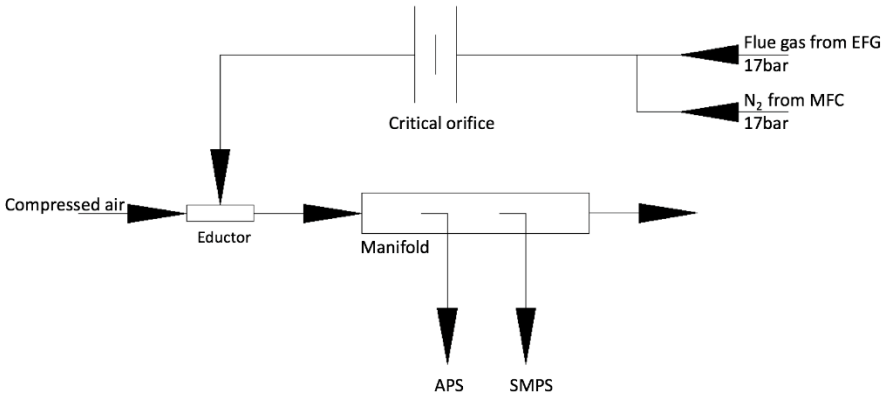

Figure 132. Schematic diagram of sample system for SMPS/APS measurement

Berner Low Pressure Impactor samples require only the single stage dilution at the probe tip, and so the sample system then is as shown on Figure 133.

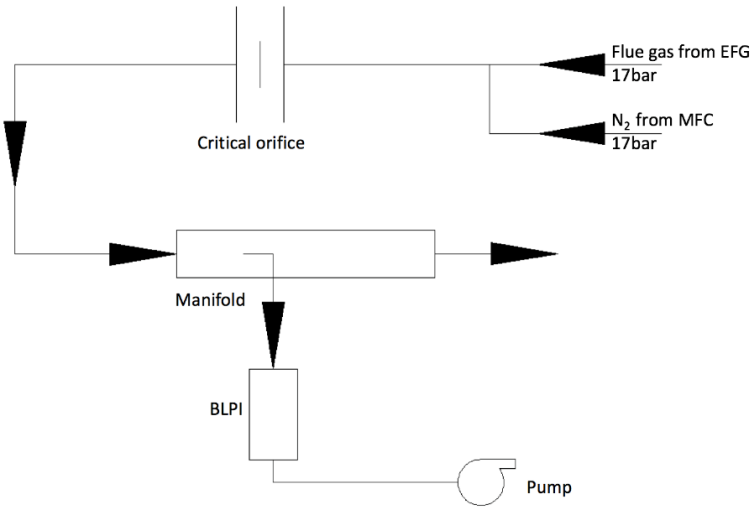

Figure 133. Schematic of sampling system using BLPI – single stage dilution is sufficient

Still unresolved at this point was whether the sample line must be heated externally up to the critical orifice at which point the pressure is dropped to atmospheric. Calculations were needed to show whether heat transfer into the probe within the EFPR is sufficient to keep the sample above the condensation point, and whether the heat transfer out of the sample is sufficiently slow outside the EFPR upstream of the critical orifice to prevent condensation.

Upon acquisition of all the components necessary in the sampling system, assembly of the probe commenced. The probe system is depicted in Figure 134.

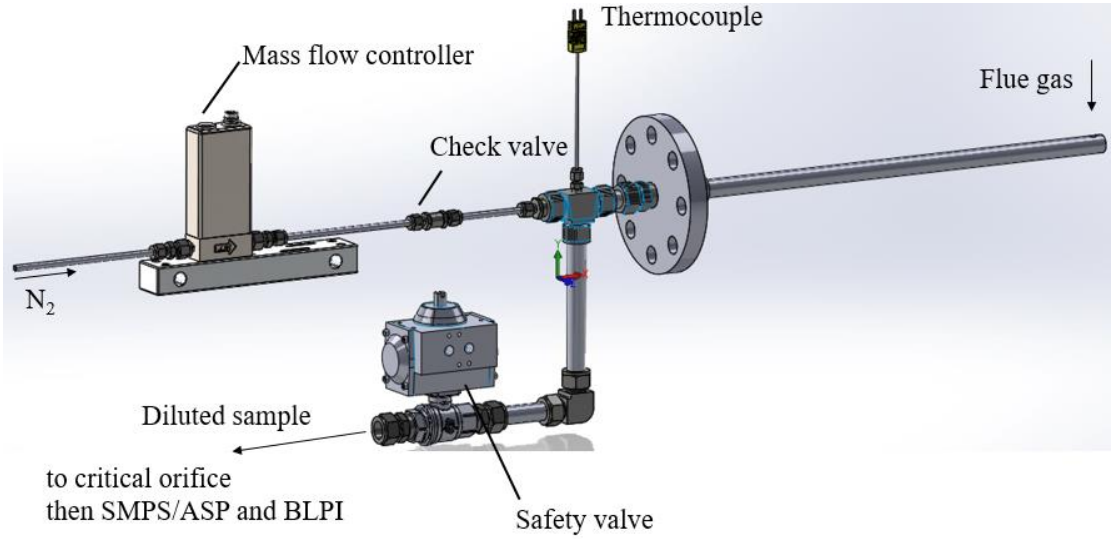

Figure 134. Depiction of the probe system

Safety is the primary issue in the design of this system. After the sampling system was completed, preliminary work (e.g., cold-state leak test, flow rate calibration, tentative particle sampling and measurement, etc.) was carried out to ensure its reliability. The system was fully validated before being used for sampling under high temperature and high-pressure conditions in the EFPR.

The focus of the work then shifted to the following:

- Building and testing the high-pressure ash aerosol sampling system under pressurized combustion conditions,
- Obtaining the first data ever on the size segregated composition of the ash aerosol at high pressures, and
- Comparing those data to data from the identical coal burned under roughly similar temperatures but at atmospheric pressure.

Although the data obtained were for a Utah SUFCO coal slurry feed, they have relevance to a dry feed since they comprised a prerequisite for the subsequent dry feed experiments. The data obtained from the slurry feed experiments are intrinsically useful in and of themselves because they relate for the first time, to ash formation mechanisms at high pressures, and can identify differences in these mechanisms due to pressurized conditions.

Figure 135 is the schematic of the probe designed for high-pressure ash aerosol sampling. The outer ceramic tube is exposed to the gas environment inside the combustor. Ash aerosol in the flue gas is sampled through the sampling hole at the probe tip. The dilution N_2 is injected via the inner N_2 tube to the tip to dilute and quench the sampled flue gas. The diluted sample then flows between the outer and inner tubes and is directed to the critical orifice for pressure reduction.

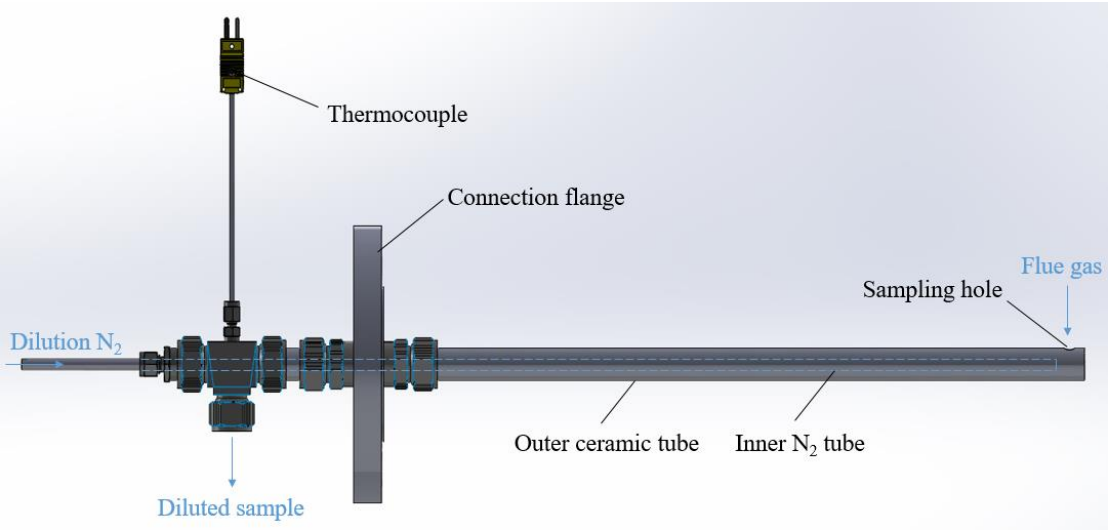

Figure 135. Schematic of the high-pressure sampling probe

The N_2 flow rate is controlled by a mass flow controller. Between the probe and critical orifice, a safety valve is installed to cut off the sample line if the measured temperature were to exceed the threshold value. The final physical realization of the aerosol sampling probe is demonstrated in Figure 136. As designed, the probe contains an outer ceramic tube and an inner N_2 tube. The probe is installed by a flange connection on the sample port of the combustor, as shown in Figure 137. Figure 138 is a top view of the reaction zone of the combustor, where the probe tip is located at the centerline.

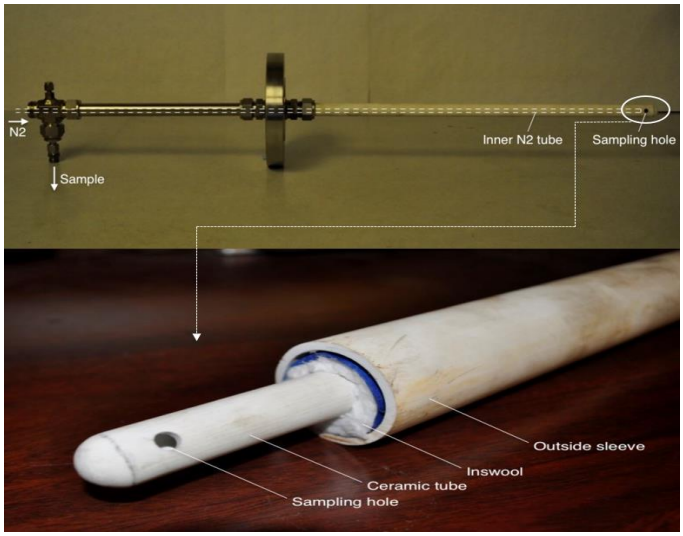

Figure 136. High-pressure sampling probe

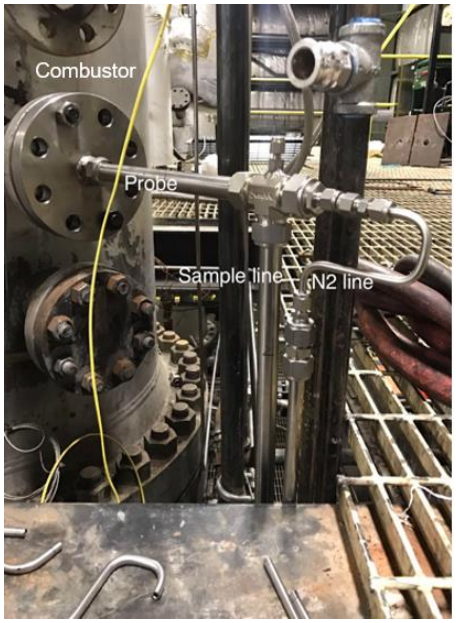

Figure 137. Sampling probe built on the combustor

Figure 138. Probe tip at the combustor centerline

After pressure reduction, the diluted sample enters the measurement part of the system. Figure 139 shows the measurement bench. After a second stage dilution in the manifold, the sample concurrently enters the SMPS and APS (Scanning Mobility Particle Sizer and Aerodynamic Particle Sizer), which provide online particle size distribution (PSD) measurements in an integrated size range of aerodynamic diameter from 0.014 to 20 μm. A BLPI (Berner Low Pressure Impactor) is also used to measure the PSD and collect size-segregated ash samples, but without the second stage dilution.

Figure 139. Measurement bench in the system

Ash aerosol characterization in EFPR (slurry feed) and comparison to analogous data with a dry feed

Aerosol sampling was conducted during Utah Sufco coal slurry combustion at a pressure of 7.9 bar (114.6 psia). Combustion conditions are given in Table 25 (with more details included in Table 27), and the coal analysis is listed in Table 26.

Table 25. Combustion conditions in EFG slurry test

Coal type	Utah Sufco
Slurry feeding rate (gal/min)	0.0962
Coal feeding rate (lb/hr)	18.5
Energy input (kW)	65
Coal wt. % in slurry	35
Coal wt. % with additional injected water	23.8
Excess O_2 wt. %	45.6
Pressure (psi)	114.6

Table 26. Coal analysis

	ASH (%)	C (%)	H (%)	N (%)	S (%)	O (diff) (%)	LOD (%)	V (%)	FC (%)	HHV (BTU/lb)
Sufco	8.36	67.87	5.45	1.09	0.36	16.87	6.11	38.49	47.04	11899

The temperature and pressure profiles are shown in Figure 140 and Figure 141, respectively. Note that the temperatures at port 1 to port 4 are the wall surface values but at port 5, a B-type thermocouple is used to gather gas temperature measurements. During sampling, the temperature and pressure profiles were stable.

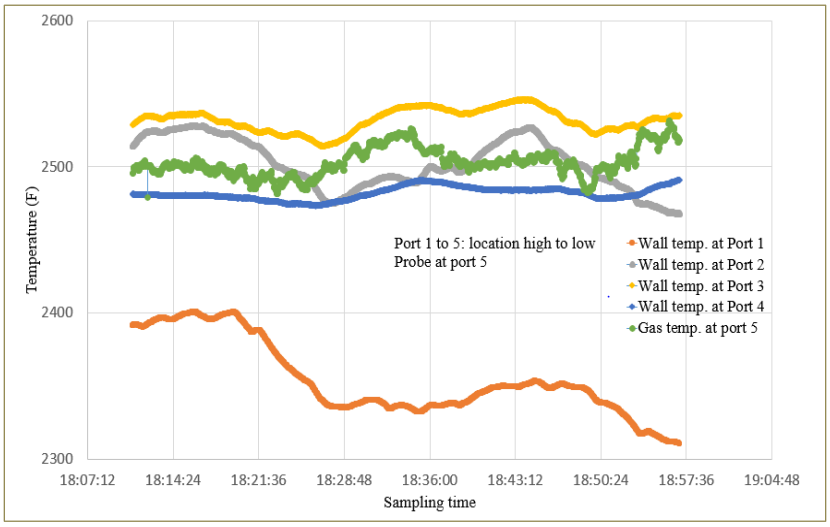

Figure 140. Temperature profile during sampling

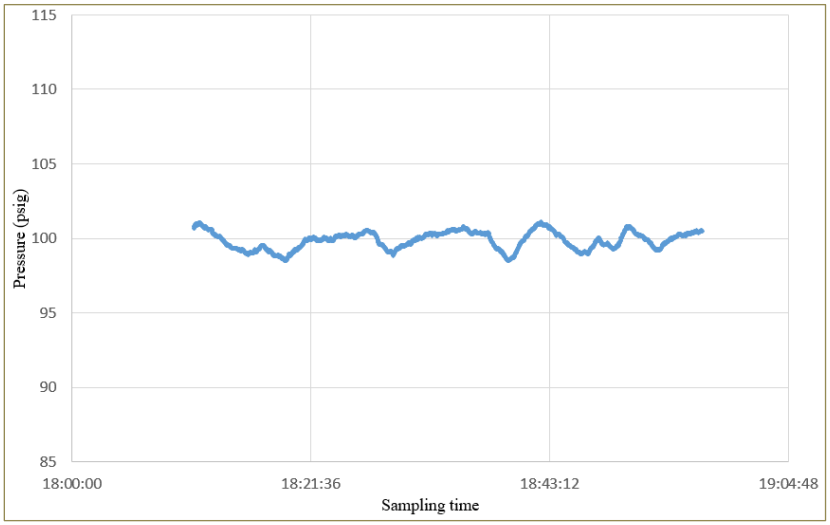

Figure 141. Pressure profile during sampling

Table 27 is a comparison of the 7.9 bar (114.6 psia) test conditions and the analogous 1 bar (14.7 psia) test conditions for the high temperature (OXY70) and low temperature (OXY27) tests in the 100 kW Oxy Fuel Combustor (OFC). There are profound differences in these conditions, and these must be considered when interpreting the high-pressure data. Note that the EFPR is much better insulated than the OFC, which, combined with the higher load, led to much higher temperatures, as shown on Table 27 and on Figure 142 and Figure 143 below. Especially

noteworthy is the high flue gas temperature at the ash aerosol sampling point for the EFPR (2503°F) compared to the OFC (1409°F for OXY27 and 1268°F for OXY70).

Table 27. Comparisons between EFPR (7.9 bar) and OFC (1 bar) tests on Sufco coal

		EFPR test 7.9 bar	OFC test 1 bar OXY70	OFC test 1 bar OXY27
Combustion conditions	Coal type	Sufco slurry	Sufco dry	Sufco dry
	Coal feed rate (kg/hr)	8.42	3.46	3.46
	Energy input (kW)	65	26	26
	O_2 (mol/hr)	795.64	233.89	251.75
	H_2O or CO_2 (mol/hr)	1501.24 (H_2O)	100.20 (CO_2)	680.50 (CO_2)
	OXY condition	OXY30	OXY70	OXY27
	Pressure (psia)	114.6	14.7	14.7
	Ash formation (g/hr)	703.68	289.25	289.25
	Vaporization rate	0.325%	0.160%	0.024%
Standard condition (293.15 K, 14.7 psi)	Gas flow (standard_m^3/hr)	66.88	8.96	22.41
	Ash concentration (g/standard_m^3)	10.52	32.27	12.91
Peak temperature condition	Peak temperature (F)	>2530 (wall) (2800 estimated) (Port 3)	2381 (Port 2)	2086 (Port 2)
	Gas flow rate (actual_m^3/hr)	53.00	48.24	108.11
	Ash concentration (g/actual_m^3)	13.28	6.01	2.68
Aerosol sample port condition	Temperature (ºF)	2503 (Port 5)	1268 (Port 9)	1409 (Port 9)
	Ash concentration (g/actual_m^3)	14.61	9.86	3.64
	Gas flow (actual_m^3/hr)	48.2	29.3	79.4
	Cross sectional surface area (m^2)	0.0324	0.0558	0.0558
	Ash mass flux (g/(m^2*hr))	21719	5184	5184

Table 27 (Continued). Comparisons between EFPR (7.9 bar) and OFC (1 bar) tests on Sufco coal

		EFPR test 7.9 bar	OFC test 1 bar OXY70	OFC test 1 bar OXY27
	Coal type	Sufco slurry	Sufco dry	Sufco dry
Gas temperature (ºF)	Port 1	2570 (estimated)	2275	1906
	Port 2	2753 (estimated)	2381 (peak)	2086 (peak)
	Port 3	2800 (estimated) (peak)	2365	1954
	Port 4	2716 (estimated)	2242	1879
	Port 5	2503 (sample)	2041	1754
	Port 6	-	1785	1690
	Port 7	-	1513	1528
	Port 8	-	1412	1492
	Port 9	-	1268 (sample)	1409 (sample)
Gas residence time (s)	Port 1	0.17	1.80	0.86
	Port 2	0.62	3.96	1.86
	Port 3	1.07	6.13	2.90
	Port 4	1.53	7.39	3.49
	Port 5	2.02	8.89	4.19
	Port 6	-	10.50	4.88
	Port 7	-	12.34	5.62
	Port 8	-	14.34	6.41
	Port 9	-	16.47	7.33
Gas velocity (m/s)	Port 1	0.422	0.152	0.328
	Port 2	0.448	0.158	0.353
	Port 3	0.454	0.157	0.335
	Port 4	0.442	0.202	0.436
	Port 5	0.413	0.265	0.585
	Port 6	-	0.237	0.568
	Port 7	-	0.209	0.525
	Port 8	-	0.198	0.516
	Port 9	-	0.183	0.494

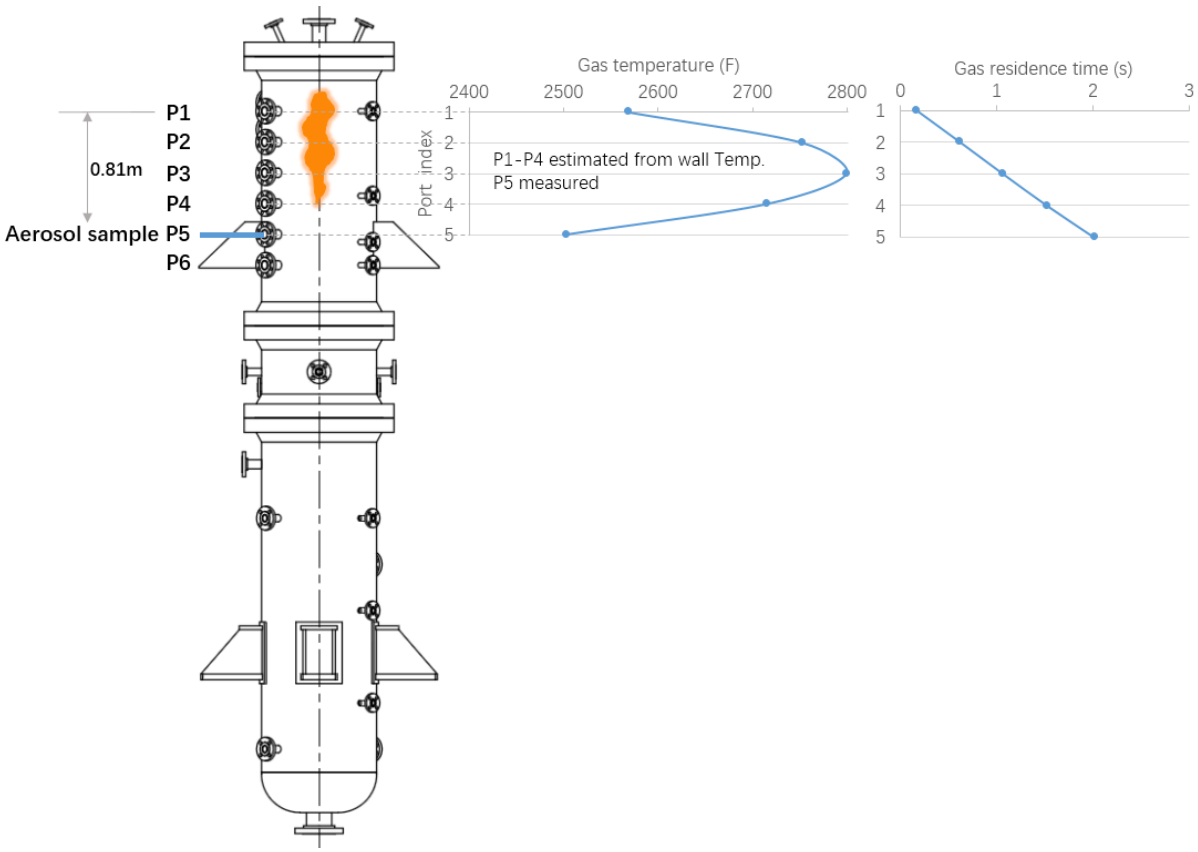

Figure 142. EFPR configuration, temperature profile and gas residence time profile.

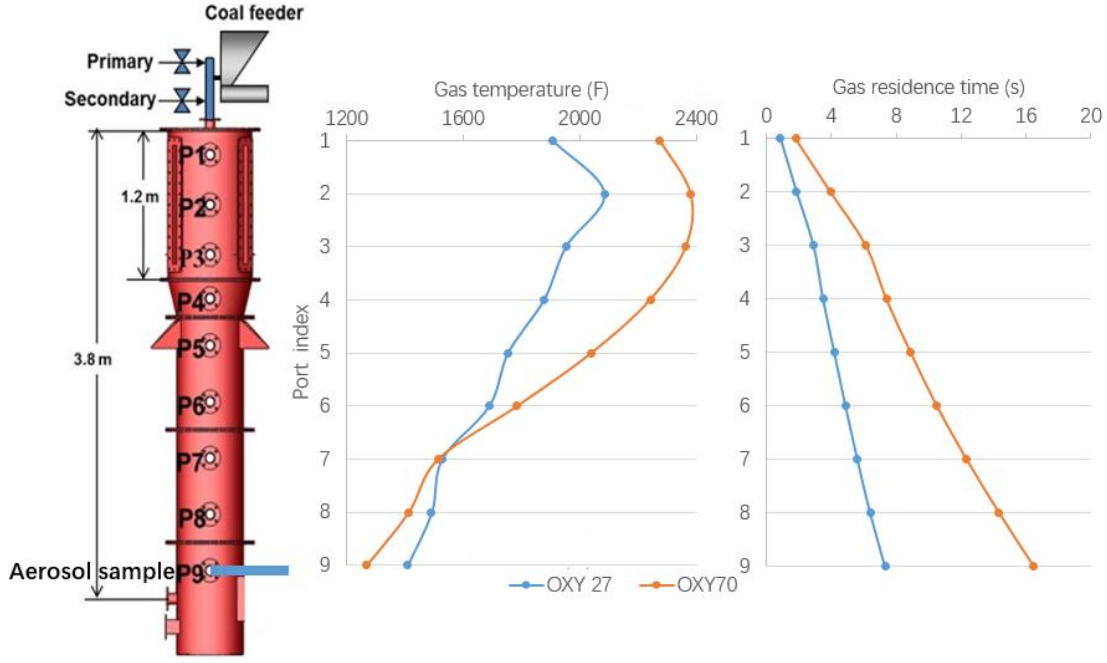

Figure 143. OFC configuration, temperature profiles (OXY27 and OXY70), and residence time profiles.

Water condensation was found in BLPI but not in the SMPS/APS line. This is because the BLPI, due to operational issues, used the first stage dilution, with a dilution ratio of only around 17 that was much lower than the design value of 50. This caused the dew point temperature in the sample to remain as high as 81.9°F as the sample entered the BLPI. The SMPS/APS used both the first and second stage dilutions to reach a total dilution ratio around 110, and so no water condensation occurred in this line. Future work will avoid this problem by taking the BLPI sample after the second stage dilution, since this is now feasible because of the increased ash aerosol concentrations sampled at high pressure.

The slagging problem was still severe. Figure 144 is the photo inside the combustor taken after the test. The slagging near the probe made it adhere to the wall. The heavy slagging was likely due to relatively long residence times.

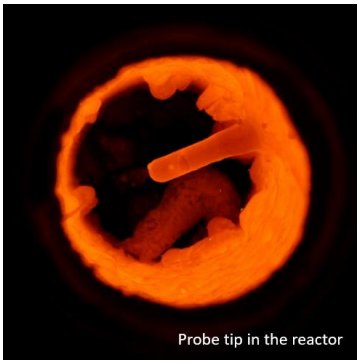

Figure 144. Probe with slagging

In this test, the combustor shell and the sampling probe worked within the safe temperature limits. The safety valve in the sample line was tested to efficiently respond to the temperature alarm thresholds. In the next test, the BLPI will sample after the second stage dilution to ensure no water condenses. The slurry combustion should be conducted in a proper timespan to alleviate slag accumulation inside the combustor.

Aerosol sampling results

In the section that follows, experimental results on ash characterization and size segregated composition at high pressure (17.9 bar) are presented, and as appropriate, are compared to atmospheric data from the same coal.

The EFPR (high pressure) PSD results obtained from the SMPS/APS and BLPI are reported on Figure 145. Previous data on Sufco coal combustion in the OFC (Oxy-fuel Combustor), namely the OXY27 and OXY70, are provided in Figure 146. The two combustor configurations are described in Figure 142 and Figure 143, and the detailed condition comparisons are listed in Table 27.

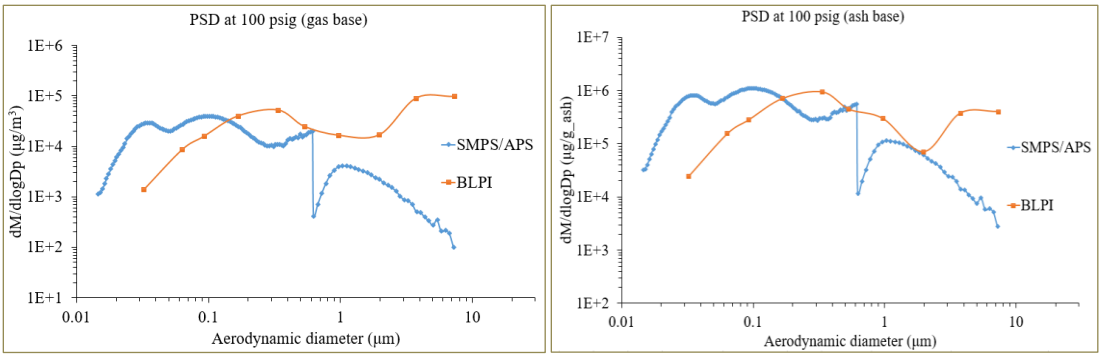

Figure 145. Sufco PSD data from EFPR test (left: gas base; right: ash base)

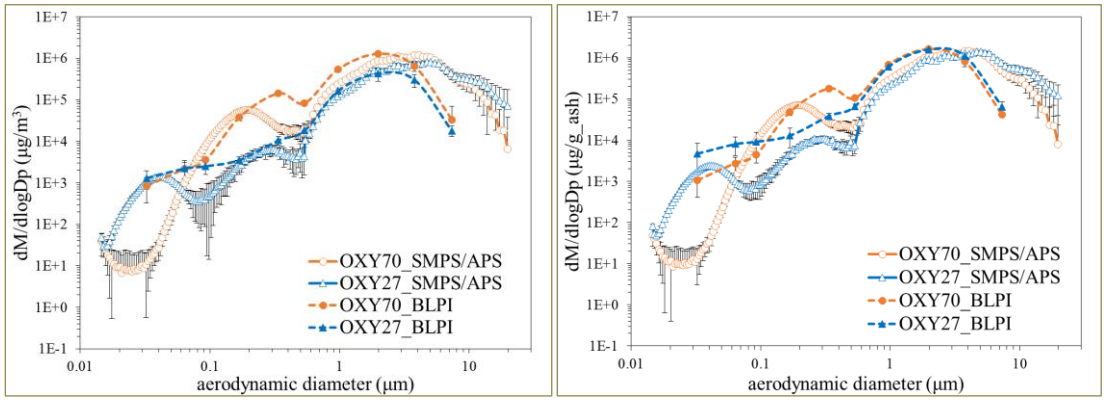

Figure 146. Sufco PSD data from OFC test (left: gas base; right: ash base)

Compared with the OXY27 and OXY70 OFC tests, the EFPR test produced more vaporized ash due to its higher peak temperature. The SMPS data indicates that two vaporization mode peaks exist at 33 nm and 98 nm in the EFPR test. The smaller one probably was produced by nucleation in the long cooling sample line. The peak of the larger coagulation mode moves to the left compared with OFC data. This contradicts the assumption that with higher peak temperature and higher ash concentration, ash vaporization, nucleation and subsequent coagulation should be enhanced.

The role of high pressure on this mode formation needs more careful consideration. In addition, dissolvable impurities and solid particles in tap water were found to produce sub-micron particles with peak number concentration up to 10^5 particles/cm^3, and higher values under pressurized air atomizing conditions[4]. Since complete water vaporization occurred in EFPR combustion, these particles may reach a concentration level comparable to the SMPS data (10^5-10^{10} particles/std_cm^3). A finer fragmentation mode was found in EFPR test. This may be explained as more porous char particles produced at higher pressure[5], resulting in improved fragmentation and reduced coalescence in coarse particle formation.

A distinct gap at the border of SMPS and APS data in EFPR test exists. However, the SMPS/APS instrument was tested in air before the sample was introduced, resulting in Figure 147, which shows the number and mass concentration of particles in the air. The small gap in this air test

suggests that the instruments worked properly. However, the EFPR test has a much lower APS number concentration (10^1-10^4 particles/std_cm^3) than that of OFC test (10^2-10^6 particles/std_cm^3), while it has a reasonably higher SMPS number concentration (10^5-10^{10} particles/std_cm^3) than that of OFC test (10^4-10^8 particles/std_cm^3). Therefore, the APS is believed to under-report the concentrations. The light absorption by black carbon in ash is not likely to account for this, since the samples of BLPI stage 7 to 10 (corresponding to APS data range) appear to contain little soot in Figure 148. The under-sampling effect at the probe tip may also contribute to the low concentration in APS data. It should be noted that the data gap exists, both in our instruments (~3 times in air test, ~10 times in above OFC test and ~50 times in EFG test) and also in experiments described in the literature (~10-100 times)[6].

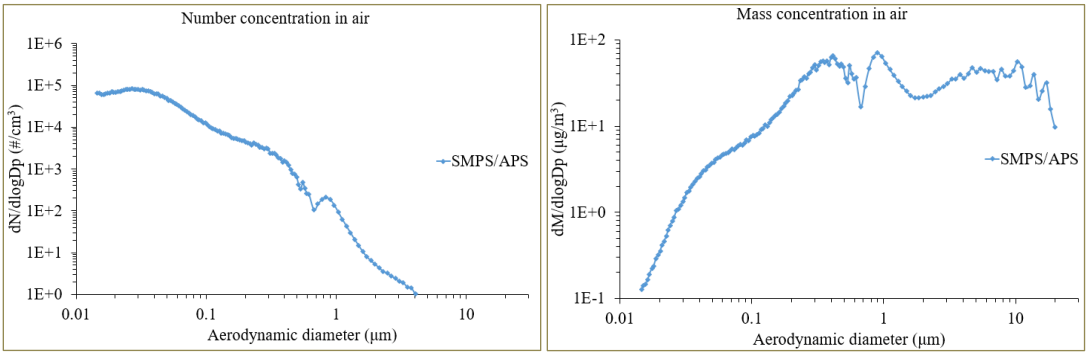

Figure 147. SMPS/APS data on air particles before combustion sampling. Left: number concentration; right: mass concentration.

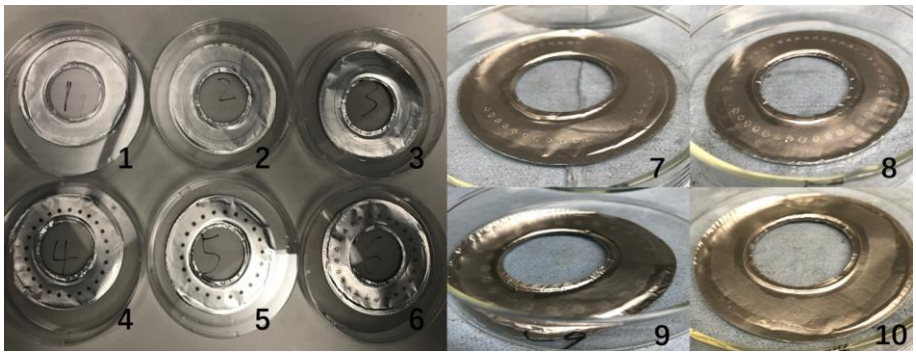

Figure 148. Ash samples collected on BLPI filters (1 to 10: bottom to top stage)

Size-segregated composition of ash aerosol in EFPR tests

Figure 149 below shows the size segregated composition for the composition set of Na, Si, Ca, Mg, S and Fe, on the stages 1-9 in BLPI, and compares the EFPR data (denoted as EFG in the figure) to the previous OFC data. Note that aluminum in ash could not be measured because of the aluminum filter substrates that was used in the EFPR instead of the previous acetate substrates that were used for the OFC tests. In Figure 149, all the elemental compositions (EFPR and OFC) have been reported on an aluminum free basis. Hence the OFC data may appear different from that previously reported, where aluminum was included.

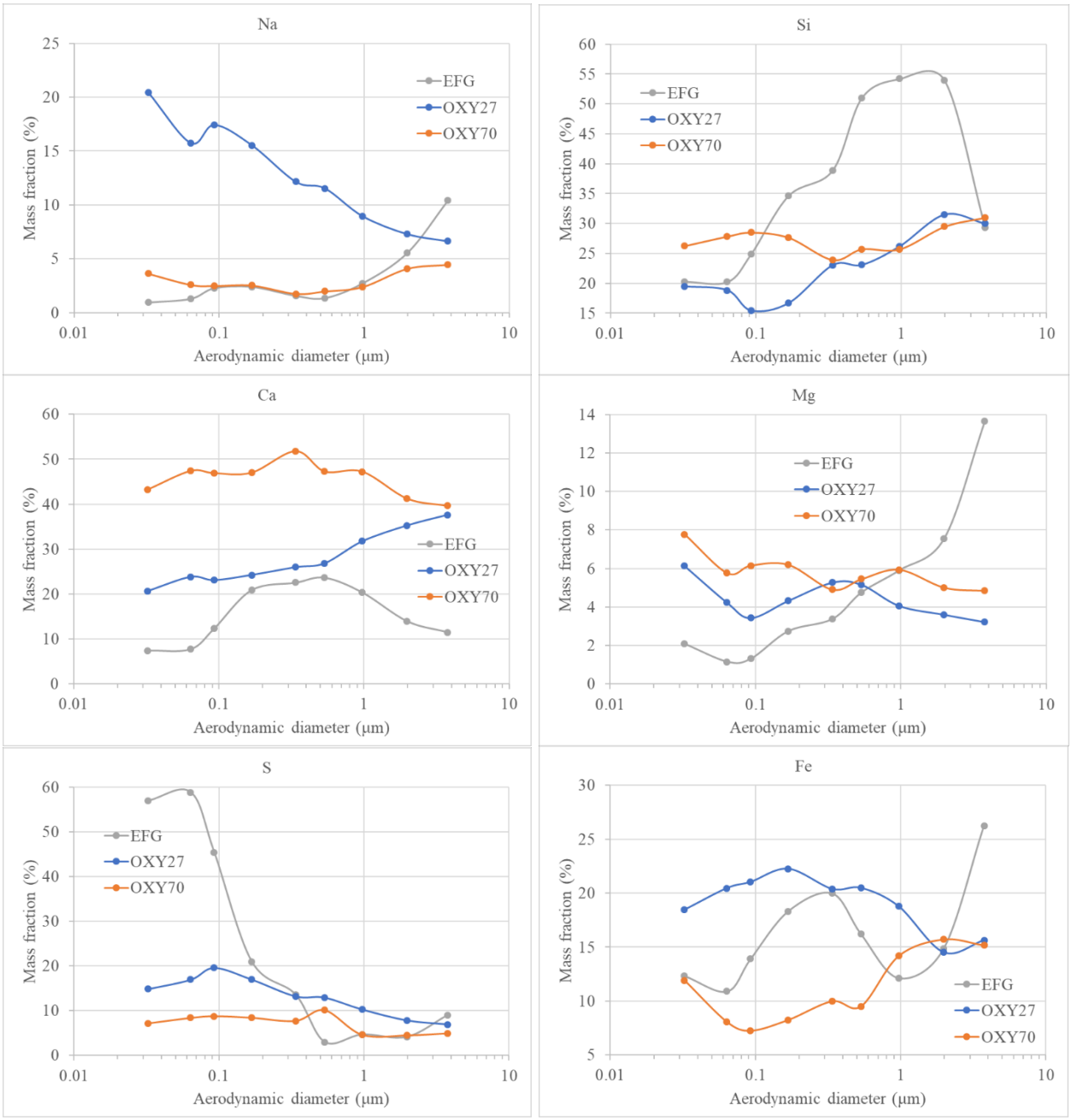

Figure 149. Composition of size-segregated ash aerosol in EFG and OFC tests (BLPI: 1-9 stages)

The coal mineral analysis is given in Table 28:

Table 28. Mineral analysis of Utah Sufco coal

Al_2O_3 (%)	CaO (%)	Fe_2O_3 (%)	MgO (%)	MnO (%)	P_2O_5 (%)	K_2O (%)	SiO_2 (%)	Na_2O (%)	SO_3 (%)	TiO_2 (%)
8.34	18.21	5.25	2.84	0.05	0.01	0.33	48.85	3.09	5.96	0.64

Increased scavenging effects at higher temperature still mainly contribute to the low sodium content in EFPR test result. Alkaline earth metals, Ca and Mg, are higher in OXY70 compared with OXY27 because of increased vaporization. But temperature alone cannot account for the EFPR data because it has lower Ca and Mg mass fractions but a higher peak temperature than the OFC. This may be explained as these metals vaporized more extensively in the EFPR test and were more readily scavenged by silicate and alumino-silicate particles (see the high Si fraction around 1 μm), which form a smaller mode (also around 1 μm) at higher pressure than the OFC data and thus have larger surface area in this gas-to-solid process. This is especially likely for magnesium, which shows an increasing mass fraction to the super-micron range.

The high sulfur content in ultrafine particles (stages 1-3) in the EFPR test likely comes from increased sulfur condensation in the lower BLPI stages. The measurement for iron in the EFPR may not be accurate because the aluminum filter also contains iron (Reynolds Wrap foil: 98.5 % Al with primary balance of Fe and Si).

The carbon mass fraction reported in Figure 150 was calculated based on the composition set of C, Na, Mg, Si, S, K, Ca and Fe. Note that C analysis was possible here because aluminum, rather than acetate substrates were used on the BLPI plates. Although the measurement may not be accurate due to the presence of Apiezon grease as an anti-bounce-off coating, it indicates that soot may have collected on the BLPI lower stages, as the collected black samples also show. This assumes that the Apiezon grease is obscured by the ultrafine particles. The Ash samples on stage 8 and 9 are few in quantity and sparsely distributed, and so the Apiezon grease contributes to apparently high (but probably erroneous) carbon fractions in super-micron particles.

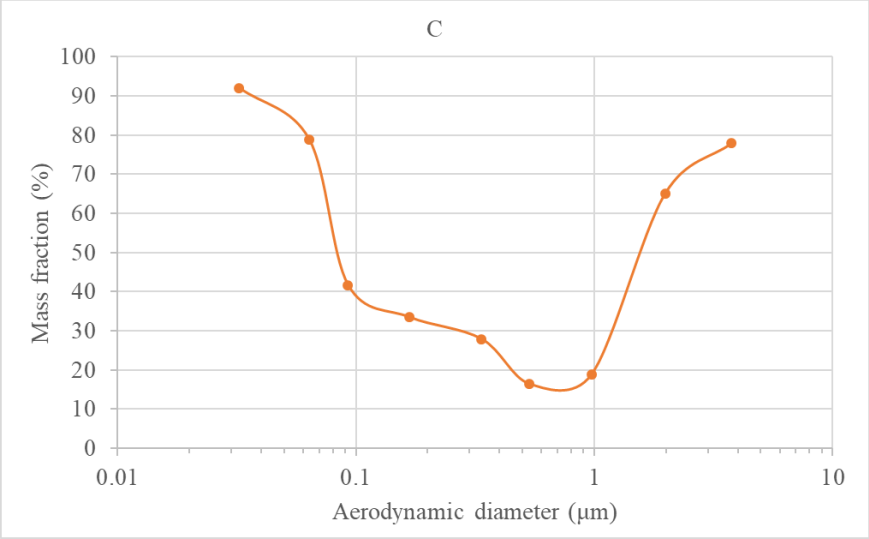

Figure 150. Carbon mass fraction of size-segregated ash aerosol in EFG test. Base: C, Na, Mg, Si, S, K, Ca and Fe

A second high-pressure test was conducted in the EFPR combustor. Although this test still used a coal-water slurry as fuel, the focus was on improving the performance of the high-pressure combustion ash aerosol sampling system, which is a critical component of the dry feed high pressure project.

A new batch of Utah Sufco coal was used for this test, rather than the one used in the last test. The two batches of coal have significantly different content and composition in ash, and therefore, need to be treated separately as two fuels. For convenience, the coal is denoted as *Sufco 1* and *Sufco 2* in the first and second test, respectively. Analyses of coal and ash are listed in Table 29 and Table 30.

Table 29. Coal analyses (as received)

	ASH (%)	C (%)	H (%)	N (%)	S (%)	O (%)	V M (%)	FC (%)	M (%)	HHV (BTU/lb)
Sufco 1	8.36	67.87	5.45	1.09	0.36	16.87	38.49	47.04	6.11	11899
Sufco 2	13.96	62.41	4.52	1.10	0.46	11.04	37.36	42.16	6.52	11745

Table 30. Coal ash analyses

Sufco 1	Al_2O_3 (%)	CaO (%)	Fe_2O_3 (%)	MgO (%)	MnO (%)	P_2O_5 (%)	K_2O (%)	SiO_2 (%)	Na_2O (%)	SO_3 (%)	TiO_2 (%)
	8.34	18.21	5.25	2.84	0.05	0.01	0.33	48.85	3.09	5.96	0.64
Sufco 2	Al_2O_3 (%)	CaO (%)	Fe_2O_3 (%)	MgO (%)	MnO_2 (%)	P_2O_5 (%)	K_2O (%)	SiO_2 (%)	Na_2O (%)	SO_3 (%)	TiO_2 (%)
	12.09	11.90	3.62	3.94	0.03	0.25	1.13	62.48	0.81	1.83	0.68

Ash aerosol sampling was realized through the high-pressure aerosol sampling system, which has been described in the preceding progress reports. The sampling was conducted in oxy-combustion of Sufco 2 slurry at a pressure of 7.9 bar. The combustion conditions during the sampling period are given in Table 31.

Table 31. Combustion conditions in Sufco 2 test

Coal type	Sufco 2 (Utah Sufco coal)
Slurry feeding rate (gal/min)	0.151
Coal feeding rate (kg/hr)	13.22
Energy input (kW)	100
Coal wt. % in slurry	35
Coal wt. % with additional injected water	27.6
Operation pressure (bar)	7.9

The furnace wall surface temperatures are reported in Figure 151. Note that the particle sampling process occurred during the 100-kW period. The B-thermocouple used for gas temperature measurement at the sampling point failed to work. However, on the temperature profile measured in the last test, the gas temperature is approximately 2450 °F (1616 K).

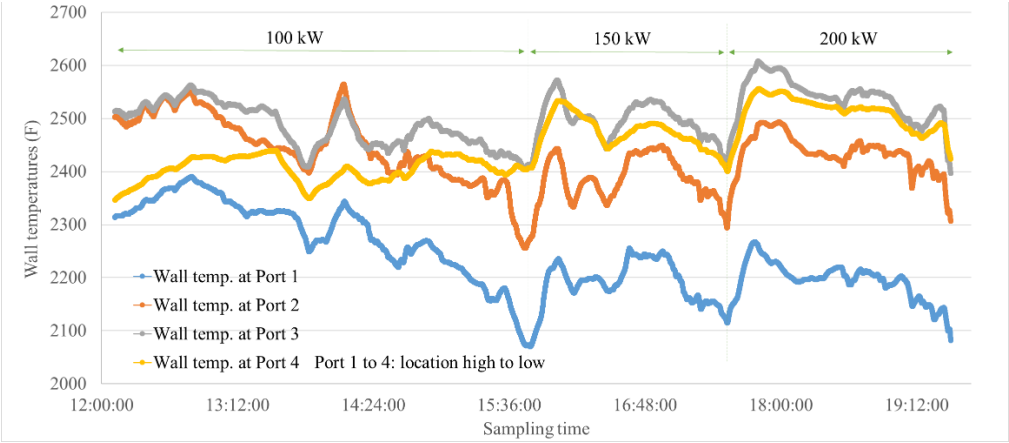

Figure 151. Wall temperatures in the second test (Sufco 2)

In this test, the Berner Low Pressure Impactor (BLPI) was connected after a two-stage-dilution, with the cooling N_2 at probe tip being the first one and compressed air in manifold being the second. In contrast to the previous experiment, the total dilution ratio reached 98.1 and no water condensation occurred in the BLPI sampling line, as it did before. The BLPI, together with the Scanning Mobility Particle Sizer (SMPS) and the Aerodynamic Particle Sizer (APS), measured ash aerosol PSDs within aerodynamic diameter range from 0.014 to 20 μm. Ash samples are also used in the Scanning Electron Microscope (SEM) and the Energy-dispersive X-ray Spectroscopy (EDS) to analyze size-segregated compositions. The drop in the PSD that occurred at the inception of the APS particle size range may be due to significant light absorption as well as light scattering caused by the presence of soot and is discussed further below.

Ash aerosol particle size distributions in EFPR test

PSD results of Sufco 2 test are shown in Figure 152. Aerosol mass concentrations on the right are based on the total ash mass in the coal fed into the combustor. The SMPS/APS and BLPI data show a good consistency in Sufco 2. Figure 153 is the comparison of PSDs of Sufco 2 in this test and Sufco 1 in the previous test. While a peak finer than 0.1 μm exists in the Sufco 1 test, it disappears with Sufco 2. This mode is likely to be formed by homogeneous nucleation of vaporized ash species in the sampling line.

As Table 30 indicates, ash in Sufco 2 contains much less sodium and sulfur than that in Sufco 1 does, possibly producing less alkali sulfate such as Na_2SO_4, which more readily nucleates to form ultra-fine particles (< 0.1 μm) as the temperature drops. Similar to the Sufco 1 test, the accumulation mode of sub-micron particles in the Sufco 2 test is also found to have a peak around 0.1 μm, as measured by the SMPS, suggesting the coagulation is not intensive as expected at the high temperature condition. Through theoretical and experimental methods, Liu et al.[7] concluded that the accumulation mode is formed by coagulation in a diffusion layer

very close to the coal or char particles during pulverized coal combustion. In slurry droplet combustion, however, it is possible that the evaporated moisture flux enhances the transport of volatile species away from the parent particles, resulting in a larger diffusion layer and lower concentration for the coagulation process. On the other hand, the water and its evaporation lead to formation of large-size agglomerate of coal particles[8,9], which may inhibit volatile vaporization in this process.

For super-micron particles, the APS still reports a relatively low concentration level as it did in the last test. Apart from the mode at 1 μm in Sufco 1, Sufco 2 produced a larger fragmentation mode around 5 μm. It is possibly formed by the influential weights of those large fragmentation particles but was somehow missed by the APS in the Sufco 1 test.

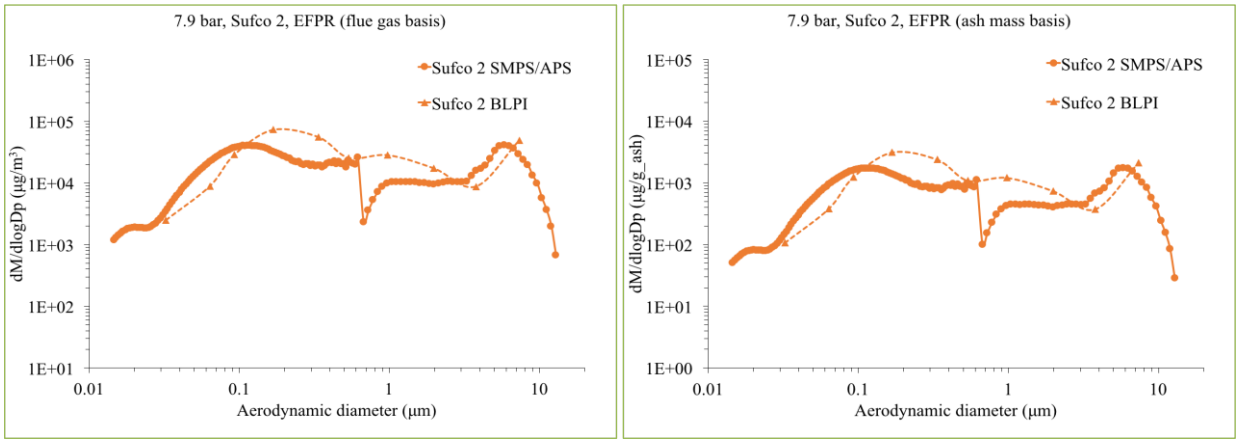

Figure 152. PSDs of Sufco 2 at 7.9 bar (left: flue gas basis; right: ash mass basis)

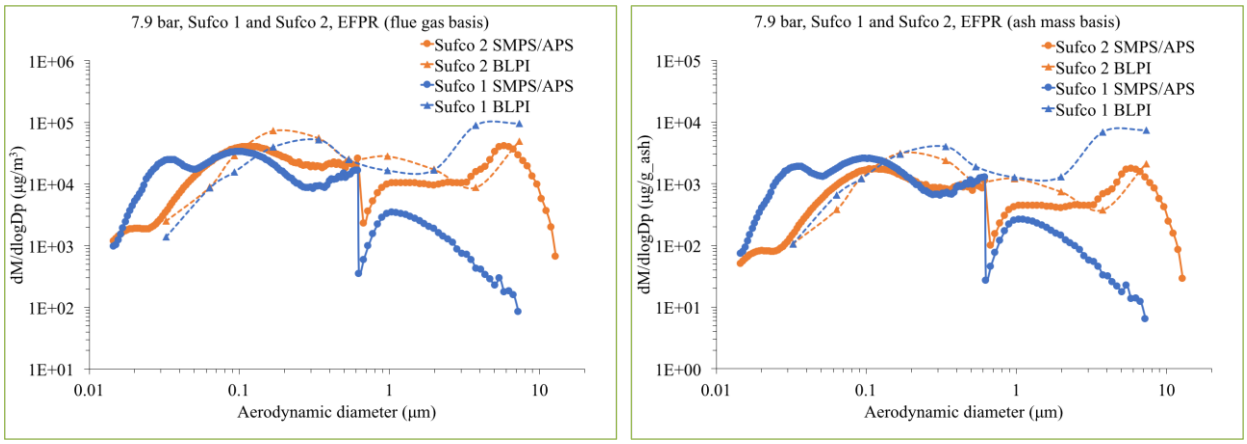

Figure 153. PSDs of Sufco 1 and Sufco 2 at 7.9 bar (left: flue gas basis; right: ash mass basis)

Size-segregated composition of ash aerosol in EFPR tests

Figure 154 shows the composition results based on an elemental set of Na, Mg, Si, S, Ca and Fe, in both Sufco 1 and Sufco 2 tests. Due to poor contrast caused by the enrichment of carbon in ash samples and background of cellulose acetate substrate, SEM/EDS analysis was conducted using samples on aluminum substrate, causing aluminum in the samples to be immeasurable. In Figure 154, the dashed horizontal lines correspond to the mass fractions in original total ash (calculated from Table 30), on a same elemental basis. The particle size range is up to 1 µm because larger particles on impactor stages 8 to 10 are hardly observed in the Sufco 2 test.

Figure 154. Composition of size-segregated ash aerosol in EFPR (BLPI: 1-7 stages)

Sufco 2 has less sodium and calcium in the original ash, but these compositions in sub-micron aerosol are always higher than those in Sufco 1, indicating vaporization of alkali and alkaline earth metals in Sufco 2 is increased at similar estimated peak temperatures and same pressure with Sufco 1 test. Figure 154 also shows that the scavenging effect of sodium is decreased in Sufco 2 with the molar ratio of Na/S being 0.75 while 0.03 in Sufco 1, for particles smaller than 0.1 μm. Because Sufco 2 contains more silicon in ash, it produces higher vaporized silicon fraction in sub-micron range. The high fraction of sulfur in Sufco 1 is likely to be contributed by the absorption of SO_2 in condensed water in the impactor during the first EFPR test. Without water condensation, the Sufco 2 result gives a reasonably low sulfur content.

It is interesting that for Sufco 1 and Sufco 2, mass fractions of the same element at 1 μm are close. If ash particles larger than 1 μm are assumed to be formed only by fragmentation, the measured mass fractions at 1 μm should be equal to those calculated values (dashed lines) in original coal. From Figure 154, the difference is more notable in Na, Si and Fe, suggesting that pressure may have some effects on partitioning of these elements during fragmentation. Table 32 is the comparison of combustion conditions in Sufco 1 and Sufco 2 EFPR tests.

Table 32. Comparison of combustion conditions in Sufco 1 and Sufco 2 tests

Coal	Sufco 1	Sufco 2
Slurry feeding rate (gal/min)	0.139	0.151
Coal feeding rate (kg/hr)	12.17	13.22
Coal wt. % in slurry	35	35
Coal wt. % with additional injected water	26.8	27.6
Energy input (kW)	94	100
Pressure (bar)	7.9	7.9
Peak temperature (K)	1711, estimated	1698, estimated
Aerosol sampling point temperature (K)	1646	1616, estimated
Flue gas at standard state (standard_m^3/hr)	77.91	78.82
Flue gas at peak temperature point (actual_m^3/hr)	57.56	57.79
Flue gas at aerosol sampling point (actual_m^3/hr)	55.37	55.00
Ash concentration at standard state (g/standard_m^3)	13.04	23.39
Ash concentration at peak temperature (g/actual_m^3)	17.65	31.90
Ash concentration at aerosol sampling point (g/actual_m^3)	18.35	33.52

Figure 155 is a photo of one sample set obtained on the cellulose acetate substrates of BLPI stages 1 to 10. It shows that stages 1 to 7 collected black particle samples, while almost nothing can be observed on stages 8 to 10 (although their weights did increase during sampling and were used for PSD measurement).

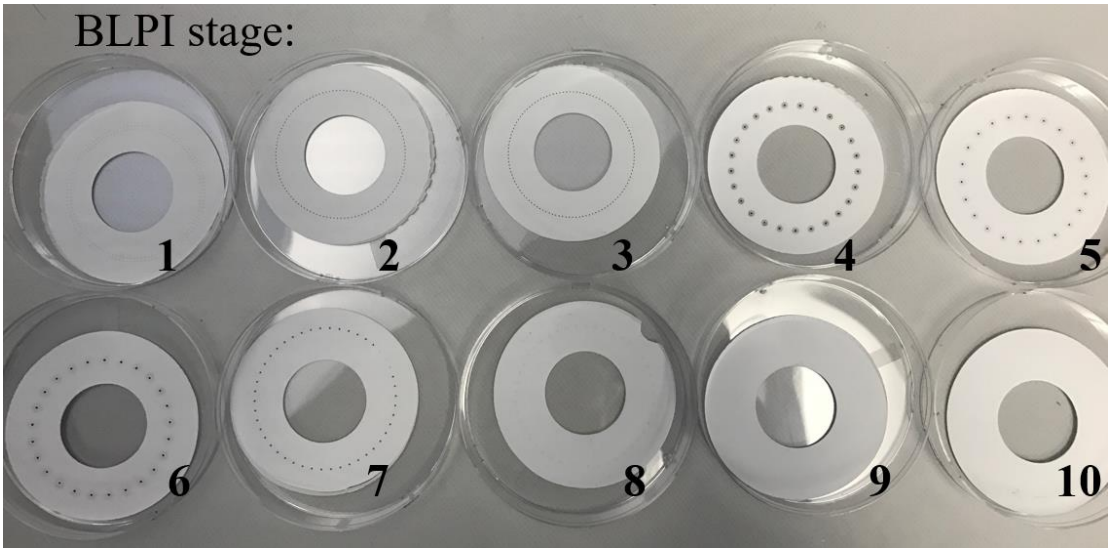

Figure 155. One set of samples on the impactor stages

The O_2 volume fraction in dry flue gas varied between 0 to 19% during the whole sampling process, while the CO remained nearly zero. This may not be evidence of complete combustion, due to the water-gas shift reaction: $CO + H_2O \rightleftharpoons CO_2 + H_2$, hence soot may still have been significantly formed in this test.

Figure 156 shows the N_2 tube which was taken out after the test. Particles inside the ceramic tube deposited on the N_2 tube surface, with most of them concentrating on the middle and back part where the temperature is lower, and thermophoresis is increased compared with the tip.

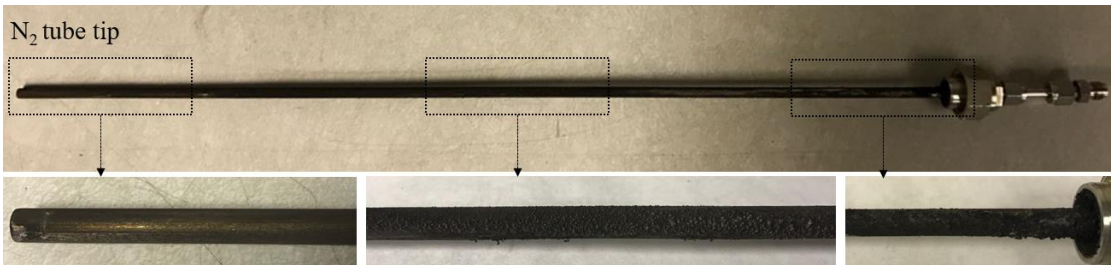

Figure 156. Deposition on N_2 tube surface

During succeeding tests, ash aerosol samples and their subsequent analysis were completed for the EFPR operated at close to a design load. This mode of operation allowed steady conditions to be achieved. As stated above, the coal was a new batch of Sufco coal (Sufco 2), which had an ash composition different from that of the original Sufco coal (Sufco 1) for which atmospheric pressure ash aerosol data was available. For this reason, additional tests were conducted using the 100 kW oxyfuel combustor (OFC) atmospheric test rig, so that we could make a comparison between high and low-pressure effects on the combustion ash aerosol.

A comparative analysis of results from the EFPR at high load (38 kg/h at 15 bar, OXY100) and from the OFC (6.8 kg/h, 1 bar, OXY70 and Air) was completed. As stated in previously, the numeric component of each case description is the amount of O_2 in the fully mixed gaseous inlet streams. For example, the OXY100 case in the EFPR was a coal slurry-fed condition that has pure O_2 as the only gaseous inlet stream. Thus, the gas inlet is 100% O_2. The OFC, on the other hand introduces both O_2 and CO_2 through the burner inlets. The OXY70 case has 70% O_2 in the fully mixed gas inlets. We attempted to achieve furnace temperatures as similar as possible for both the EFPR OXY100 15 bar test and the OFC OXY70 1 bar test. In this manner, the effect of pressure on ash partitioning mechanisms could be ascertained, without the complicating effects of large differences in flame temperature. Because the high load EFPR tests forced us to sample the ash aerosol after short residence times, the OFC 1 bar tests also included temporally resolved data on the evolution of the size segregated composition of the ash aerosol. This involved samples at several ports. For completeness, the previously reported EFPR results at a lower feeding rate are also included here.

Results: Effect of pressure on ash partitioning for Sufco 2 coal

The OFC (1 bar) and EFPR (8 bar and 15 bar) combustion conditions are compared in Table 33. The EFPR 15-bar case and OFC 1-bar case have similar peak and sampling temperatures. Figure 157 and Figure 158 show the gas temperature and residence time profiles in the EFPR and OFC, respectively.

Table 33. Comparison of Sufco 2 combustion conditions

Combustor	**EFPR**		**OFC**	
Coal	Sufco 2		Sufco 2	
Feeding	slurry	slurry	dry	
Coal feeding rate (kg/hr)	13.22	38.60	6.80	
Firing rate (kW)	100	293	52	
Feature	8 bar, OXY100	15 bar, OXY100	1 bar, OXY70	1 bar, Air
Peak temperature (K)	1698 estimated	1910 estimated	1866	1489
Aerosol sampling point temperature (K)	1616 estimated	1894 estimated	1833/1559/1183 (ports 3/6/9)	1474/1369/1203 (ports 3/6/9)
Flue gas at standard state (std_m^3/hr)	78.82	209.88	18.09	55.82
Flue gas at peak temperature (m^3/hr)	57.79	91.35	115.15	283.53
Flue gas at sampling point	55.00	91.35	116.20/96.20/73.00	280.67/260.68/229.07

Combustor	EFPR		OFC	
(m^3/hr)				
Ash concentration at standard state (g/std_m^3)	23.39	25.65	52.50	17.02
Ash concentration at peak temperature (g/m^3)	31.90	58.93	8.25	3.35
Ash concentration at sampling point (g/m^3)	33.52	58.93	8.17/9.82/13.01	3.38/3.64/4.15
Aerosol sampling location	combustor centerline	combustor port	combustor centerline	combustor centerline
Gas residence time at sampling port (s)	1.8	1.2	3.7/6.4/9.8	1.5/2.5/3.7

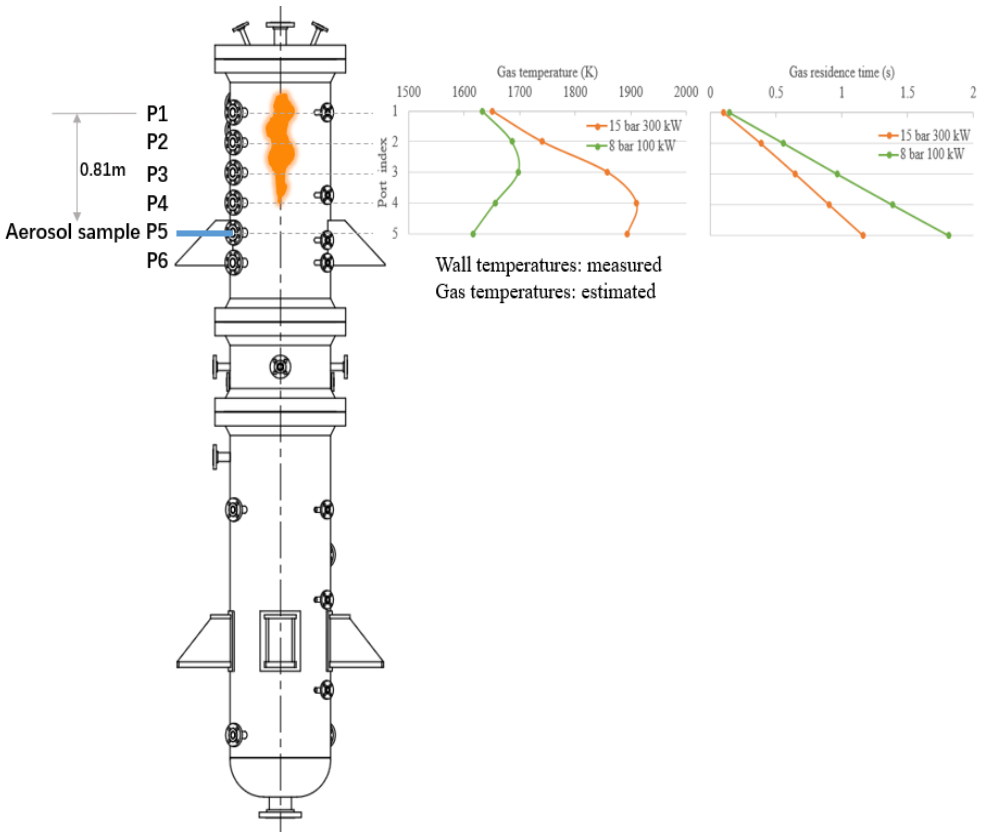

Figure 157. Gas temperature and residence time profiles in the EFPR

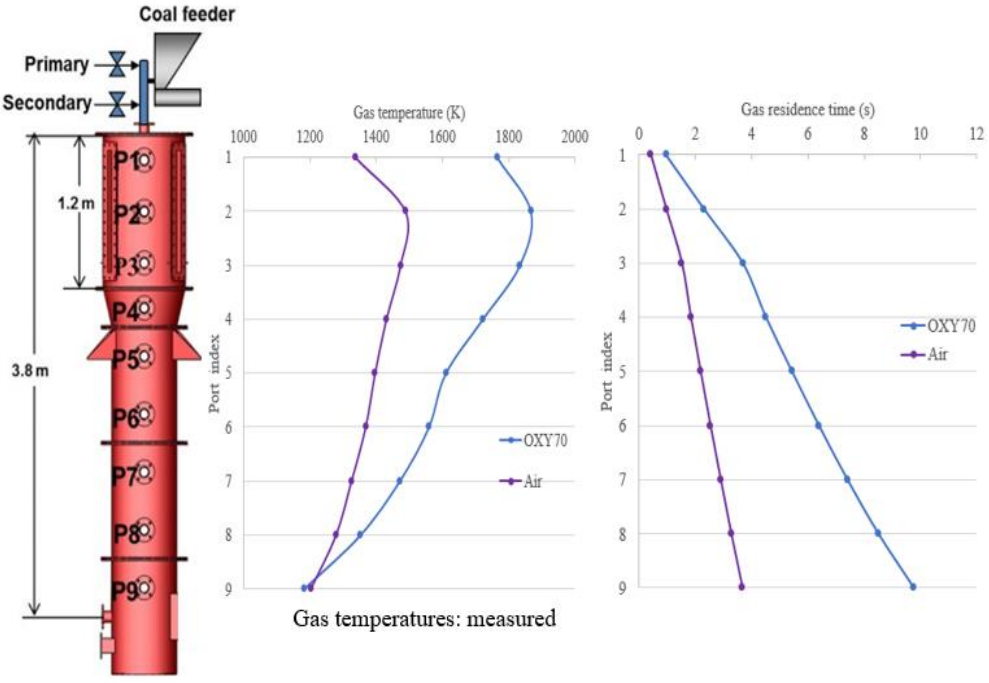

Figure 158. Gas temperature and residence time profiles in the OFC

Particle size distribution measurements: OFC and EFPR data

Figure 159 shows the PSDs in OFC 1 bar OXY70 test, with data being obtained from ports 3, 6 and 9. It suggests that sampling location (temperature and residence time) does not have a significant influence on the results, especially between port 3 and 6. The deposition probe is inserted in port 8 above the aerosol probe in port 9 and this may cause the smaller aerosol concentration at that location. As shown in the figure, the SMPS and APS data are in good agreement with the BLPI data.

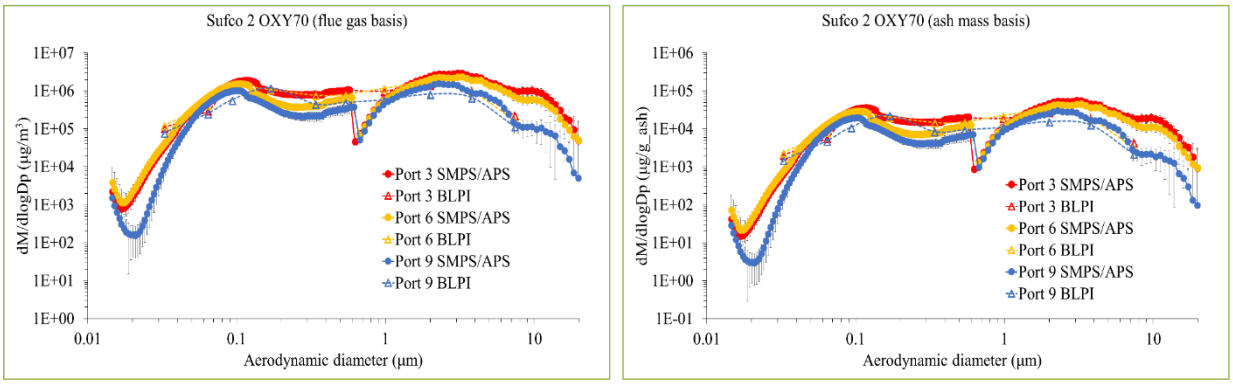

Figure 159. PSDs in OFC Sufco 2 OXY70 test (Sampling temperatures: Port 3: 1833 K; Port 6: 1559 K; Port 9: 1183 K)

Figure 160 compares the PSDs in OXY70 and Air cases, both being sampled at port 9. The OXY70 case produces a much higher concentration in the submicron vaporization range than the air case due to the higher combustion temperature under oxy-coal conditions. Data for the air case and OXY70 in the fragmentation size range show good agreement, which indicates temperature has a minor effect on fragmentation.

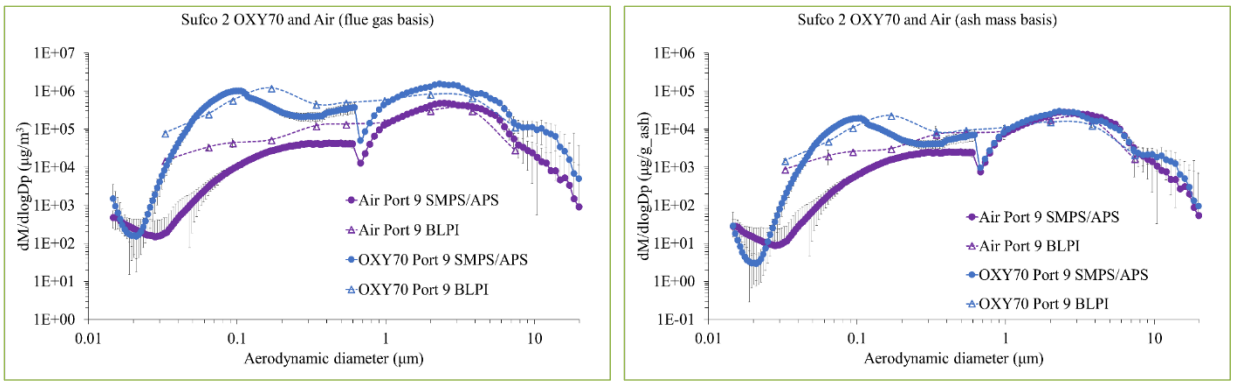

Figure 160. PSDs in OFC OXY70 and Air cases

Figure 161 compares the PSD in OFC OXY70 sampled at port 6 (close to PSD at port 3 in Figure 159) with PSDs of the second (8 bar) and third (15 bar) EFPR tests. It shows that at a peak temperature around 1900 K, the 15-bar case produces much lower quantities of submicron aerosols than the 1-bar case. The 8-bar case has a lower peak temperature around 1700 K, but its aerosol concentration is between the other two cases. One possibility is that the higher combustion pressure, which is harder for vapor pressures of ash volatile species to reach, may inhibit the sublimation (volatilization) process of these species. So even though the EFPR 15-bar case has a higher calculated ash concentration than the OFC cases at peak temperature, its total vaporized ash concentration may be lower, resulting in a lower condensed ash concentration. Its higher peak temperature may lead to the coarser accumulation mode during coagulation than in the 1-bar case. But aerosols in the super-micron range show a similar effect from pressure, which is not expected for the fragmentation mechanism.

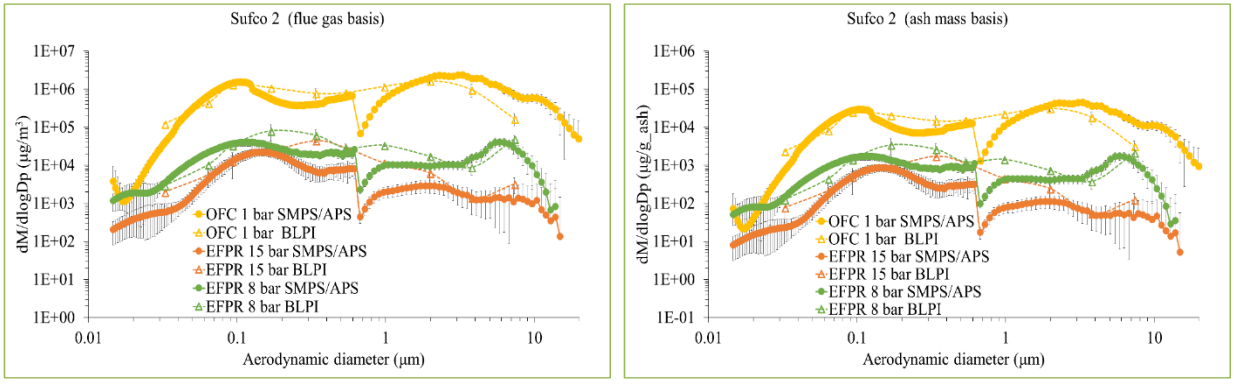

Figure 161. PSDs in OFC (1 bar) and EFPR (8 bar and 15 bar) tests

Temporally resolved Size segregated composition data at 1 bar, OXY70 aerosols from ports 3, 6 and 9

Figure 162 compares the EDS results of OXY70 aerosols from ports 3, 6 and 9, based on the elemental set of Na, K, Mg, Ca, S, Si and Fe. The black line represents the mass fraction of each coresponding element in the same set.

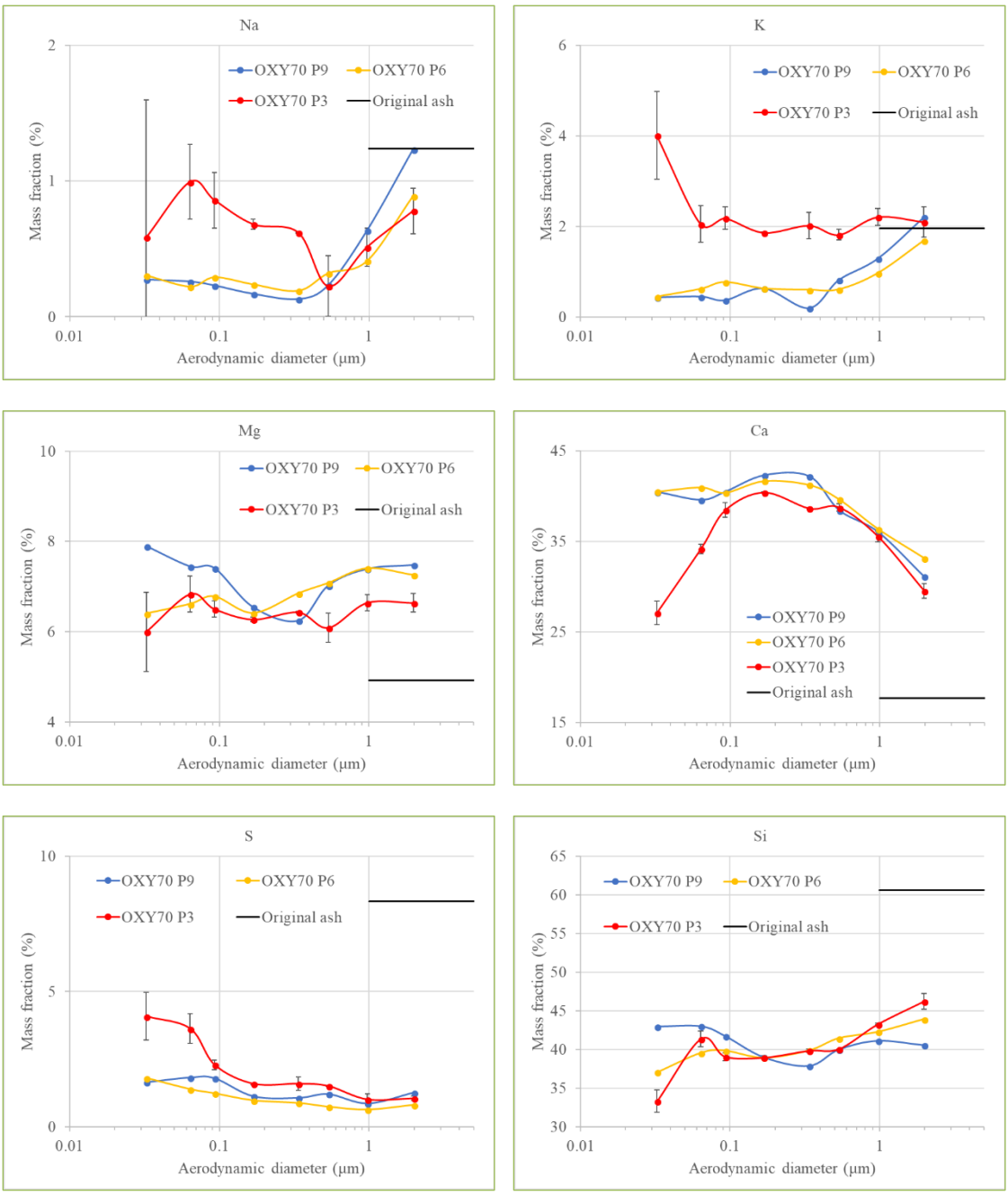

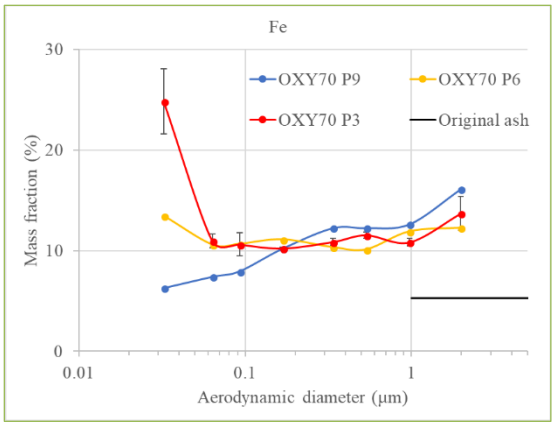

Figure 162. Size segregated aerosol compositions in 1 bar OXY70 tests (Port 3, 6 and 9)

An HSC equilibrium calculation has been conducted using the inputs of the OXY70 case at temperatures ranging from 500 K to 2500 K and at a constant pressure of 1 bar. Ash species include Na, Mg, Al, Si, S, K, Ca and Fe. Chloride is not considered due to its minor existence in Sufco 2. Table 34 and Table 35 show the species selected in the calculation and the initial inputs, respectively.

Table 34. Species selection in HSC calculation

CO2(g)	Al2O3(K)	SiO2(S)	MgO(g)	FeSiO3(M)	Si2O2(g)	CH4(g)
H2O(g)	Al2O3(D)	Al2SiO5(S)	MgO2	Na2O*Fe2O3	Fe(OH)2	Al2Si4O10(OH)2
CO(g)	Na2SO4	Al2SiO5(A)	H2O2(g)	FeO*SiO2	Na2O2	K2SO3
O2(g)	KFe3(FeSi3O10)(OH)2	(CaFe)0.5SiO3	NO2(g)	N2O(g)	FeCO3	H2SO4
H2(g)	Na2SiO3	NaAlSi3O8(G)	*3CaO*SiO2	Na2Al2Si6O16(HA)	Fe(OH)3	*4CaO*3SiO2*1.5H2O
SiO2(H)	(CaMg)0.5SiO3	Na2CO3	MgSiO3(PE)	*3CaO*Al2O3*3SiO2	Na2O2(g)	FeSO4*H2O
N2(g)	MgSiO3(L)	Na2O*3SiO2	Mg2SiO4(BF)	Na2O2H2(g)	NO3(g)	Na2SO3
H2SO4*4H2O	CaMgSi2O6	NaAlSi2O6(D)	FeSiO3	KHSO4	K2O2(g)	Al2O3*3H2O
CaAl2Si3O10(OH)2	*2CaO*SiO2	NaOH	COOH(g)	NaNO3	SO2(g)	Al2Si2O5(OH)4
CaSiO3(P)	MgSiO3(P)	Mg(OH)2(g)	AlO(OH)(B)	MgSO4	*3Na2O*2SiO2	Al2O3*2SiO2*2H2O
Al2O3*SiO2(D)	CaSO4(A)	CaO*Al2O3*SiO2	NaAlSi3O8(AN)	Al(OH)3	Al2O3(g)	Al2O3*3H2O(B)
SiO2	CaO(L)	KOH	Mg2SiO4(GF)	K2O2H2(g)	Al2O3*H2O	*7MgO*8SiO2*H2O
CaSO4	CaO*MgO*2SiO2	NaO(g)	Ca(OH)2	*2Na2O*SiO2	Ca2Al2Si3O10(OH)2	Al2Si2O7*2H2O(H)
SiO2(Q)	MgSiO3(HP)	*2CaO*MgO*2SiO2	MgCO3	Na2O(g)	H2SiO3(g)	Al2Si2O7*2H2O(D)
SiO2(V)	MgSiO3(HT)	Na0.96Al0.96Si2.04O6	Ca2MgSi2O7	K2(OH)2(g)	K2O	Ca(NO3)2
SiO2(CR)	CaO*MgO*SiO2	Al2SiO5(K)	FeAl2O4	K2CO3(g)	H2SO4(g)	*2CaO*3SiO2*2.5H2O
SiO2(G)	K2SO4	KAlO2	Na0.96Al0.96Si2.04O6(	Al(OH)3(G)	NaHSO4	SO3(G)
SiO2(T)	K2CO3	NaAlSi3O8(LA)	Na2O*Al2O3	*3MgO*4SiO2*H2O	K2SO4(g)	*6CaO*6SiO2*H2O
SiO2(B)	CaO	KAlSi3O8(G)	NaHCO3	NH3(g)	NaOH*H2O	Fe3Al2Si3O12
CaSiO3	Ca2SiO4(L)	Ca(OH)2(g)	*2CaO*Al2O3*SiO2(L	FeSiO3(I)	CaO*6Al2O3	SO3(B)
SiO2(CRS)	CaSO4(B)	KAlSi3O8(A)	NaH2SiO4*8H2O	Na2O	CaFeSiO4	N2O4(g)
NO(g)	SiO(g)	NaAlSi3O8(A)	CaO(g)	Ca2SiO4(B)	*2CaO*5MgO*8SiO2*H	Fe2Al4Si5O18
(CaMg)0.5SiO3(CL)	CaO*Al2O3*2SiO2	KAlSi3O8(K)	NaAlSiO4(K)	Ca2SiO4(AA)	N2O2(g)	N2O4
SiO2(C)	MgO*Al2O3	NaAlO2	CaO*Fe2O3	FeO(g)	Fe3O4(H)	N2O5(g)
MgSO4(A)	Ca2SiO4(O)	*2CaO*Al2O3*SiO2	Mg(OH)2	*2CaO*Fe2O3	KAl3Si3O10(OH)2	*3CaO*2SiO2*3H2O
NaH2SiO4*7H2O	CaCO3	Ca3SiO5	*2CaO*Al2O3	K2O(g)	KAl2(AlSi3O10)(OH)2	Mg(NO3)2
NaOH(g)	MgSiO3(G)	CaCO3(V)	K2SO4*2MgSO4	NaNO3(g)	K2O2	KAl(SO4)2
MgSiO3	CaCO3(A)	Fe2O3	CaFe(SiO3)2	*2FeO*SiO2	H2SO4(Dg)	N2O5
Fe2O3(G)	KAlSiO4	KFeO2	KHCO3	Fe2SiO4(F)	CaAl4Si2O10(OH)2	*5CaO*6SiO2*3H2O
KOH(g)	Na2O*2SiO2	CaO*MgO	O3(g)	Al2O3*H2O(B)	*4CaO*Al2O3*13H2O	Fe2(SO4)3
Al2O3(C)	KAlSi3O8	KAlSi3O8(X)	KNO3	Ca2SiO4(A)	*3MgO*2SiO2*2H2O	*4CaO*Al2O3*Fe2O3
Al2O3	KAlSi2O6	MgSiO3(M)	HCOOH(g)	FeO2(g)	Mg3Si2O5(OH)4	K3AlSi3O8
KAlSiO4(K)	CaO*Al2O3	NaFe(SiO3)2	Fe3O4	SiO2*H2O	FeSO4	K2S(g)
MgSO4(B)	CaMgSiO4	FeO	*3CaO*Al2O3	Na2Al2Si6O16(LA)	Ca2Al2SiO6(OH)2	Al2(SO4)3
Mg4Si6O21H12	Mg2SiO4	KAlSi3O8(M)	KNO3(g)	Na2Al2Si4O12(J)	HNO3	*3CaO*Al2O3*6H2O
MgO(M)	Ca3Si2O7	MgSiO3(I)	Mg3Al2Si3O12	FeSiO3(P)	CaO*2SiO2*2H2O	H2Si2O5
NaAlSiO4	NaAlSi3O8	Al(OH)3(g)	Fe2O3(H)	FeO*OH(g)	Na2SO4(g)	KAl3(OH)6(SO4)2
H2O	SiO2(g)	MgCO3(M)	CaMg(CO3)2	Fe2SiO4(G)	H2SO4*H2O	KAl3(SO4)2(OH)6
MgO	Mg2SiO4(F)	*3CaO*MgO*2SiO2	Al2O3*2SiO2	Fe2SiO4(B)	NaAl(OH)4	NaAl3(SO4)2(OH)6
CaSiO3(C)	*3CaO*2SiO2	NaAlSi2O6(J)	NaO2	SO3(g)	CaSO3	K2S
Al2O3(G)	H2SiO3	CaO*2Al2O3	Fe(OH)2(g)	HNO3(g)	N2O3(g)	

(g): gas phase; others: condensed phase

Table 35. Inputs in HSC calculation

Species	CO2(g)	H2O(g)	O2(g)	SO2(g)	N2(g)	Al2O3	CaO	Fe2O3	K2O	MgO	Na2O	SO3	SiO2
Input (kmole)	0.533234	0.178413	0.02835	0.000978	0.001336	0.001126	0.002015	0.000215	0.000114	0.000928	0.000123	0.000217	0.009875

Figure 163 shows the equilibrium amounts of Na and K abundant species. Note that (g) respresents gas phase while others are in the condensed phase. Figure 163 suggests that vaporized Na and K are likely to exist as hydroxides at higher temperature (but again, chlorine is not considered), so NaOH(g) and KOH(g) are likely to be reactants during the scavenging process. As temperature drops from 1833 K at port 3 to 1559 K at port 6, the residual vaporized alkali metals (mainly Na and K) become more stable in the form of solid -$AlSiO_4$.

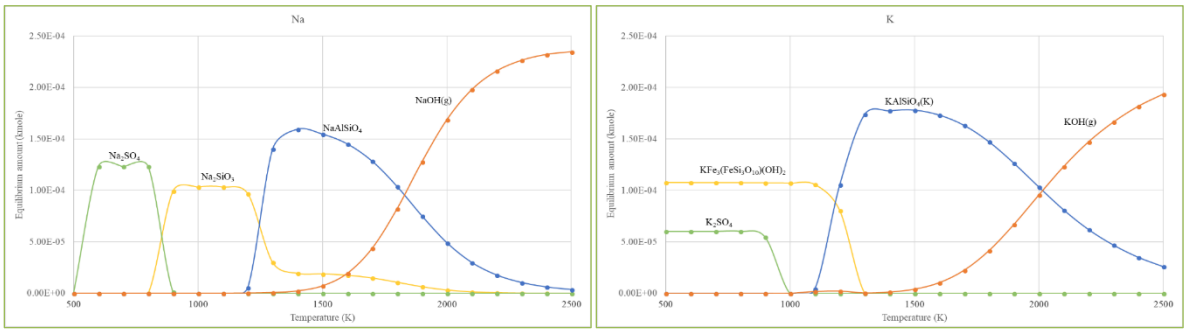

Figure 163. Equilibrium amounts in HSC calculation (P = 1 bar; T: 500 K to 2500 K)

Since the temperature at port 3 in the OXY70 case is 1833 K, it is possible that enriched NaOH(g) and KOH(g) react with SO_2 (or abundant H_2SO_4*$4H_2O$ as reported in HSC) and condense in the cooling probe to form small Na_2SO_4 and K_2SO_4 particles at temperatures below 1000 K (Figure 163), which explains why port 3 has higher Na, K and S mass fractions in submicron aerosols than ports 6 and 9 do (Figure 162).

Effect of pressure: OFC with OXY70 and Air and EFPR at 15 bar

Figure 164 shows the EDS results of OXY70 at 1 bar (port 6), air at 1 bar and EFPR at 15 bar, based on the elemental set of Na, K, Mg, Ca, S, Si, Al and Fe. Sufco 2 ash has very low sodium (oxide 0.8% in original ash) but high silicon (62.5%) contents, so efficient scavenging of sodium in submicron particles by larger silicate particles is observed in the plots. It also shows that temperature effects in this process is still clear at such a low sodium level with the OXY70 case having even lower sodium than the air case. Similar results are also observed for potassium (Figure 157), which has a higher concentration than sodium. OXY70 has more calcium and silicon in submicron aerosols than the air case does because it has a much higher combustion temperature and more Ca and Si are vaporized. Magnesium shows little difference in behavior between the air case and OXY70.

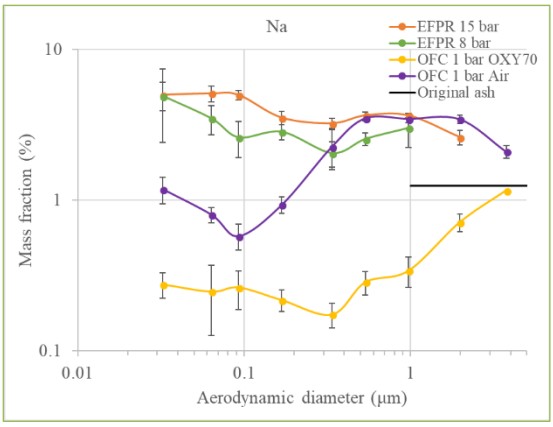
Na
EFPR 15 bar
EFPR 8 bar
OFC 1 bar OXY70
OFC 1 bar Air
Original ash
Mass fraction (%)
Aerodynamic diameter (µm)

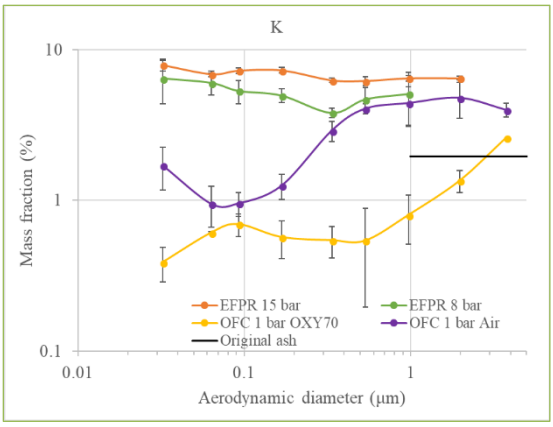
K
EFPR 15 bar
EFPR 8 bar
OFC 1 bar OXY70
OFC 1 bar Air
Original ash
Mass fraction (%)
Aerodynamic diameter (µm)

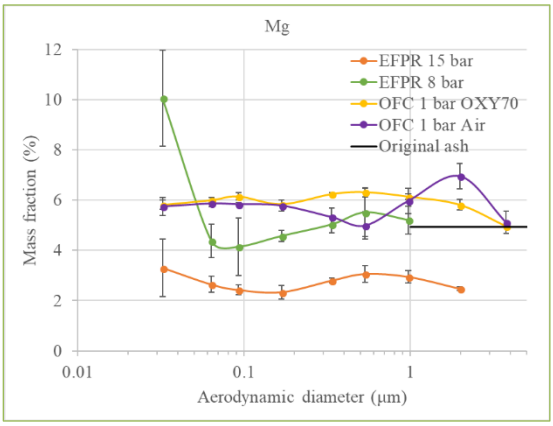
Mg
EFPR 15 bar
EFPR 8 bar
OFC 1 bar OXY70
OFC 1 bar Air
Original ash
Mass fraction (%)
Aerodynamic diameter (µm)

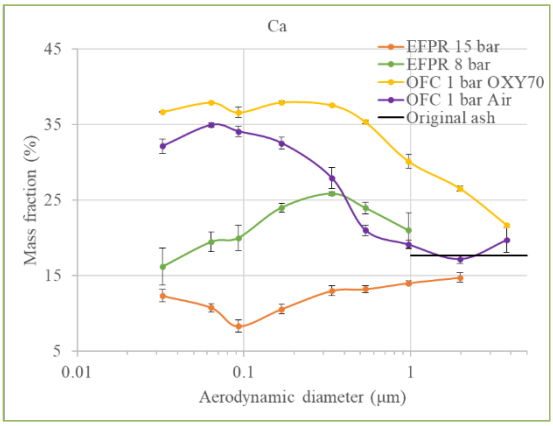
Ca
EFPR 15 bar
EFPR 8 bar
OFC 1 bar OXY70
OFC 1 bar Air
Original ash
Mass fraction (%)
Aerodynamic diameter (µm)

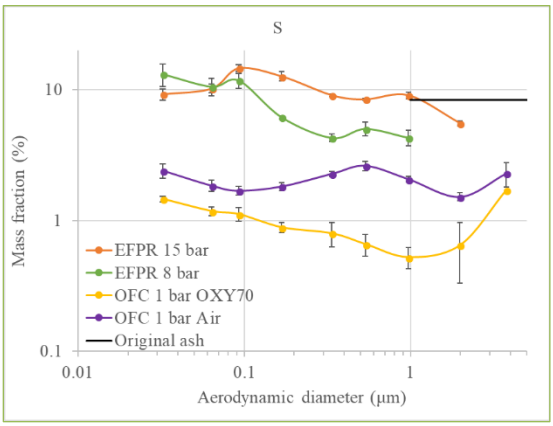
S
EFPR 15 bar
EFPR 8 bar
OFC 1 bar OXY70
OFC 1 bar Air
Original ash
Mass fraction (%)
Aerodynamic diameter (µm)

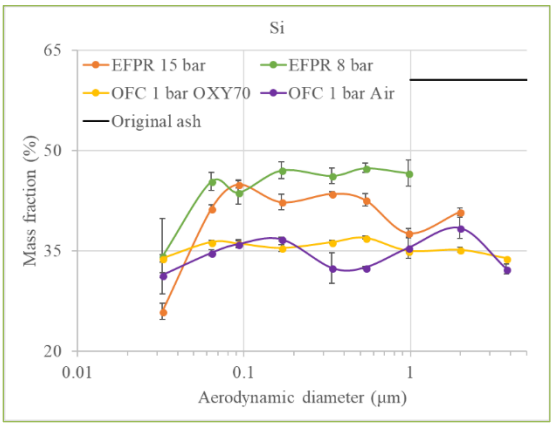
Si
EFPR 15 bar
EFPR 8 bar
OFC 1 bar OXY70
OFC 1 bar Air
Original ash
Mass fraction (%)
Aerodynamic diameter (µm)

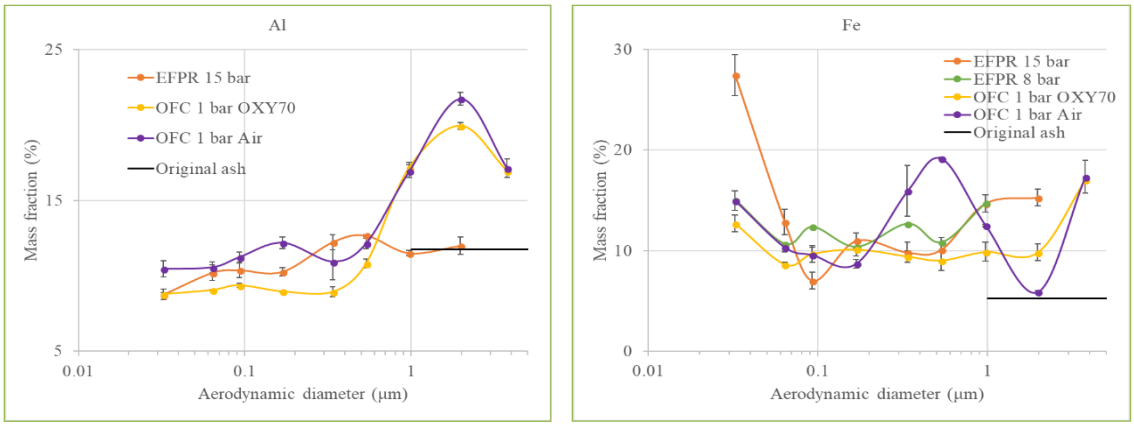

Figure 164. Size segregated aerosol compositions in EFPR (8 and 15 bar) and OFC (1 bar OXY70 and Air)

Figure 164 shows that Na and K are significantly enriched in submicron aerosols at 15 bar in the EFPR test compared with that of OFC OXY70 at 1 bar even though two cases have similar combustion temperatures. Figure 165 shows the equilibrium amounts of abundant species of Na, K, Ca and Mg, at variable pressures from 0.1 to 20 bar and constant temperature of 1900 K. The curves suggest that Na and K are more stable in solid phase as -$AlSiO_3$ salts rather than in the gas phase as hydroxide vapors at higher pressure and the same temperature. This could increase nuclei and condensation of alkali metals at 15 bar and decrease metal vapors for the scavenging process, causing the higher mass fractions of Na, K, Si and S in submicron aerosols at 15 bar (as shown in Figure 164). Some in the literature have reported that high pressure drops alkali metal concentrations in the gas phase, and sulphates are more common in condensed phase[10]. However, other possibilities such as high pressure inhibiting condensation; or reaction of alkali vapors on larger particles; or too short of a residence time to the cooling probe in the EFPR need to be verified.

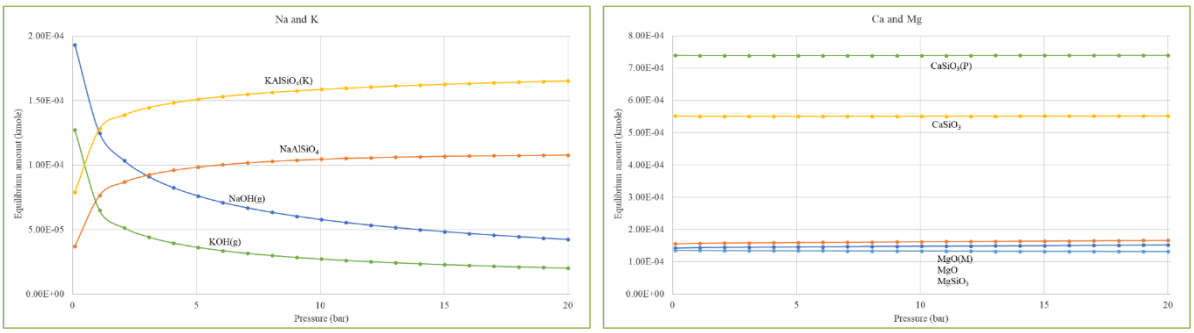

Figure 165. Equilibrium amounts in HSC calculation (P: 0.1 to 20 bar; T = 1900 K)

Calcium and magnesium in Figure 164 also show significant influence from high pressure, at which they greatly deplete compared with 1 bar results. Results shown in Figure 165 do not indicate abundant gas- phase species, but stable equilibrium amounts of Ca and Mg solid species from 0.1 to 20 bar. This may be caused by the decreased volatilization of these alkaline

earth metals at such high pressure leading to less Ca and Mg vapors released. This would also explain the lower submicron aerosol concentrations at higher pressure in Figure 161.

Conclusions from the above analyses are:

1. Scavenging of alkali metals in the submicron size range at atmospheric pressure (1 bar) is consistent with previous conclusions, while the scavenging extent is decreased at high pressure (15 bar) because alkali metals are more stable in condensed solid phase rather than gas phase at such conditions (Figure 165).
2. Higher pressure may decrease volatilization/sublimation of ash volatiles due to their relatively low vapor pressures, which may cause the lower submicron aerosol concentrations in PSDs (Figure 161) and lower mass fractions of alkaline earth metals in size-segregated ash aerosol compositions (Figure 164).

Ash deposits in OFC tests

The compositions of ash deposits in the air case and OXY70 are reported in Figure 166. Elemental relative magnitudes of ash deposits forming the inside deposit layer are roughly consistent with the data of submicron aerosols. The bar shown for Sufco 2 ash represents the normalized mass fraction of original ash with the same elemental set.

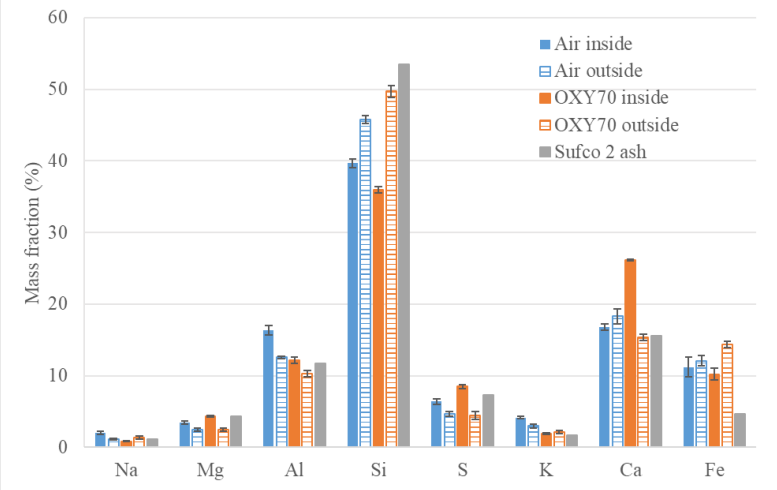

Figure 166. Elemental compositions of ash deposits in Air and OXY70

Figure 167 through Figure 170 are the SEM images of inside and outside deposits. It is shown that inside deposits are more spherical in shape and contain higher amounts of fine particulate than the outside deposits.

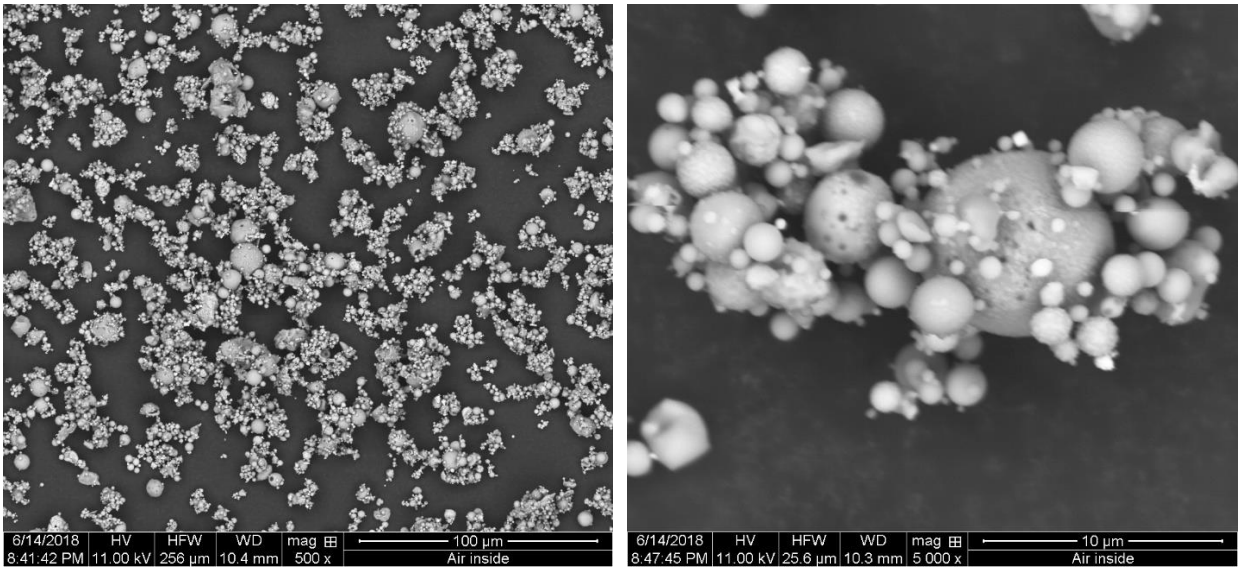

Figure 167. Air inside deposits (left: 500 x; right: 5000 x)

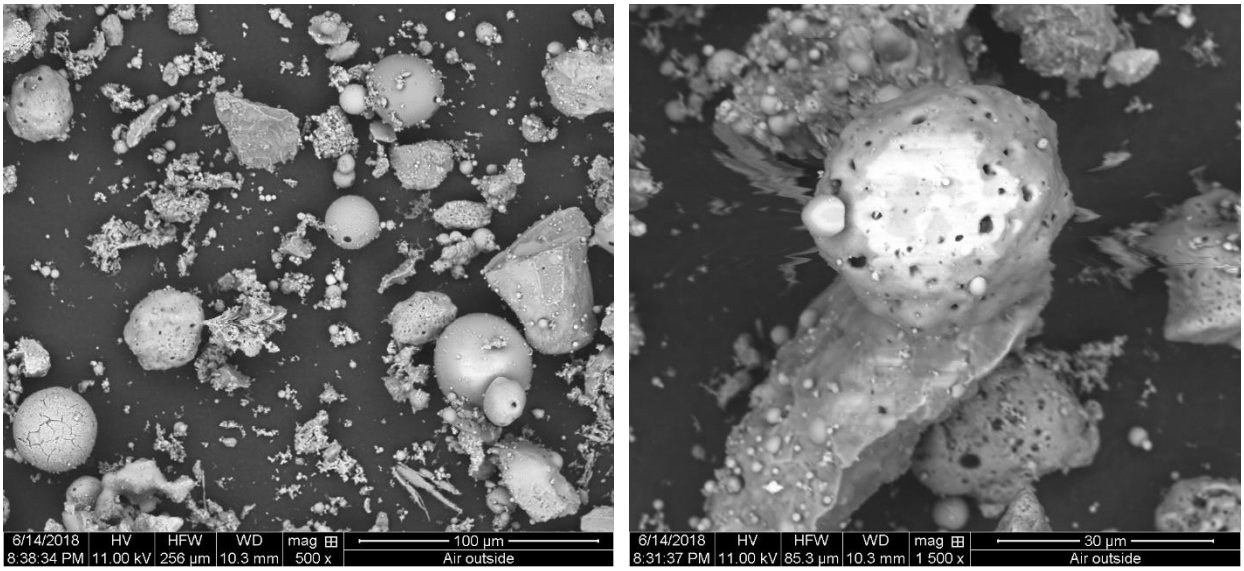

Figure 168. Air outside deposits (left: 500 x; right: 1500 x)

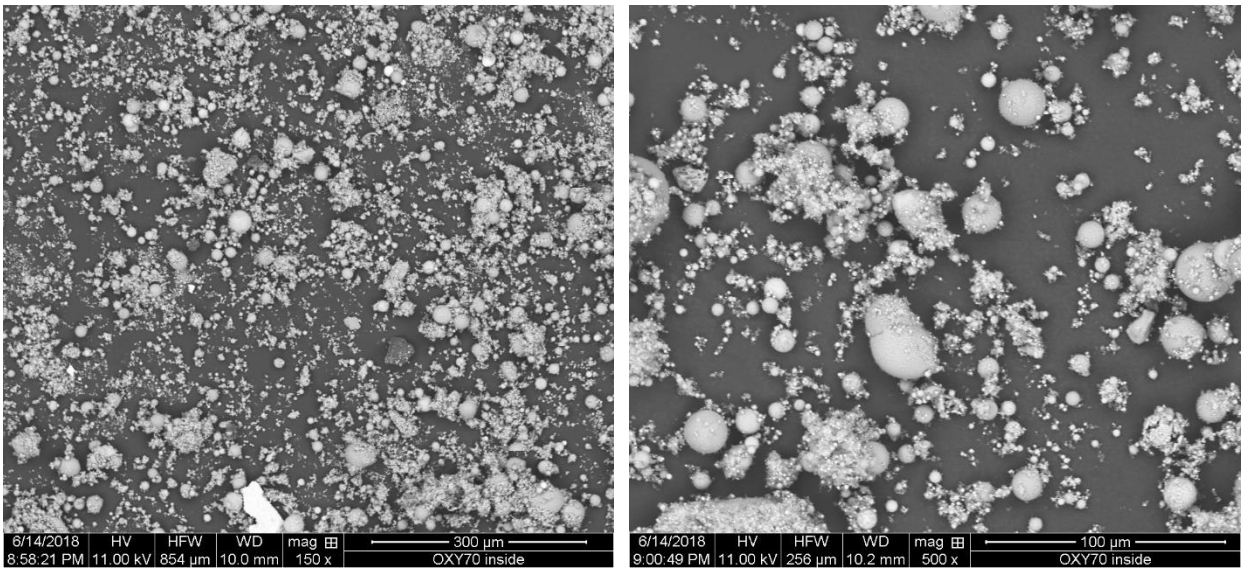

Figure 169. OXY70 inside deposits (left: 150 x; right: 500 x)

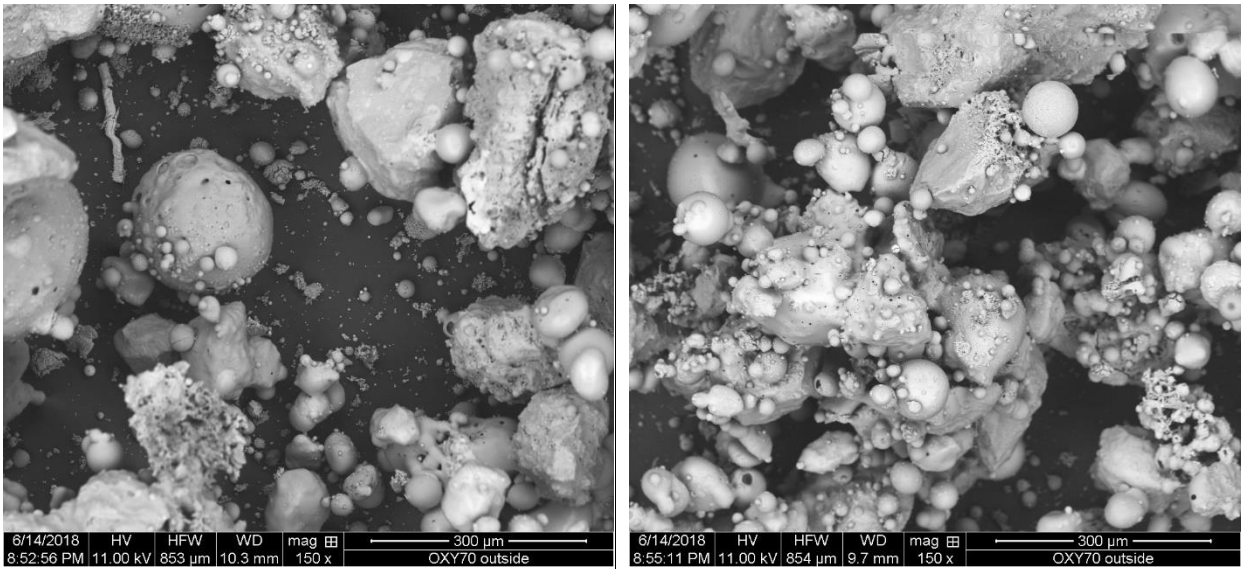

Figure 170. OXY70 outside deposits (left: 150 x; right: 150 x)

Sub-micron particle diffusion and deposition in the sampling lines

This section is concerned with calculations that predict the performance of the particulate sampling system for the pressurized oxy-coal with dry feed tests, and with a description of the piping and instrument system for the dry feed system. Calculations pertinent to the aerosol sampling system show that although turbulent deposition of ultrafine particles, less than 0.1 µm in diameter, onto the walls of the sample lines might have been a problem in preceding coal

slurry tests, sample losses were not significant for particles larger than that. However, results suggested that sample lines be shortened for the dry feed tests.

In the preceding three tests on the EFPR, the ash aerosol sample traveled along a 160-inch-long distance in a ¾-inch tube, from the probe outlet to the manifold. Sample gas in the first 110-inch part of this path is pressurized while the remainder 50-inch length is at atmospheric pressure. After this, the sample is directed through another 65-inch-long ¼ -inch tube to the second-stage air dilution point. Due to such a long travel distance, it is necessary to investigate whether the fine particles are likely to diffuse to and deposit on the walls.

We take conditions of the third test at 15-bar as an example. The flows upstream of the 3 parts are turbulent, in which fine particles are lost at walls by both Brownian and turbulent diffusion.

Table 36. Flow conditions in three parts of the sampling line

Flow path	Length (in)	ID (mm)	Pressure (bar)	Velocity (m/s)	Gas Re number	Particle Re (dp=1um)	Gas mean free path (um)	Residence time (s)
part 1	110	16.5608	15	2.45	19057	1.15	0.00709213	1.14
part 2	50	16.5608	1	36.03	19304	1.17	0.103861	0.035
part 3	65	4.826	1	36.97	6077	1.26	0.10020181	0.045

Brownian diffusivity from Stokes-Einstein expression:

$$\mathrm{D} = {}^{kT}/_{f} \quad (7)$$

The friction factor,

$$f = \frac{3\pi\mu d_p}{C} \quad (8)$$

where the slip correction factor is

$$C = 1 + \frac{2\lambda_p}{d_p}(1.257 + 0.4e^{\frac{-0.55d_p}{\lambda_p}}) \quad (9)$$

The Brownian diffusion time from the sample tube center line to the wall is calculated as:

$$t = \frac{r^2}{2D} \quad (10)$$

For particles with d_p = 0.5 μm, results are reported below:

Table 37. Brownian diffusion in the sampling line (dp = 0.5 μm)

Flow path	Length (in)	ID (mm)	d_p (μm)	Diffusivity (m^2/s)	Diffusion time to wall (s)
part 1	110	16.5608	0.5	6.06E-11	5.66E+05
part 2	50	16.5608	0.5	8.91E-11	3.85E+05
part 3	65	4.826	0.5	8.70E-11	3.35E+04

This rough estimate shows that particle diffusion times from the tube center line to the wall are very much longer than the gas residence times in both ¾ and ¼-inch tubes. This suggests that Brownian diffusion alone from the center line could not cause significant particle loss on walls.

A better, and more precise estimate of the importance of this process can be obtained by considering the effect of turbulence. In turbulent pipe flow, the mass transfer coefficient of particle diffusion is derived as[11]:

$$k = 0.042 u f_F^{\frac{1}{2}} Sc^{-\frac{2}{3}} \quad \textbf{11}$$

where the Fanning friction factor[12],

$$f_F = 0.0791 Re^{-1/4} \quad \textbf{12}$$

and u is the bulk velocity.

The particle number loss rate,η_p, is defined as the ratio (in percent) of the number particles diffusing to walls within a specific sample tube section, to the total number of particles entering the tube:

$$\eta_p = \frac{k n_\infty A}{n_\infty V} \times 100\% \quad \textbf{13}$$

Table 38 shows the particle number loss rate for 0.5μm particles. For those particles, the greatest loss (0.22%) occurs in Part 1 of the sample line, but is still negligible.

Table 38. Particle number loss rate due to turbulent diffusion in the sampling line (dp = 0.5 μm)

Flow path	Length (in)	ID (mm)	d_p (μm)	Sc number	k (m/s)	η_p (%)
part 1	110	16.5608	0.5	35174	7.88E-06	0.21663
part 2	50	16.5608	0.5	346793	2.51E-05	0.021381
part 3	65	4.826	0.5	337440	3.03E-05	0.112235

The effect of particle size is shown in Figure 171 for d_p from 0.01 to 1 μm. The loss rate represents the net particle loss percentage in the entire sampling line. The minimum particle sizes that we measured and collected ranged from 0.0143 μm for the SMPS and 0.0324 μm for the BLPI. The calculation suggests that the very smallest of these might lose ~15% of their number on the walls, although the largest portion of the particle size distribution would not be affected. In any case, the results suggest that sample lines should be kept as short as possible, and modifications to this effect are currently being made.

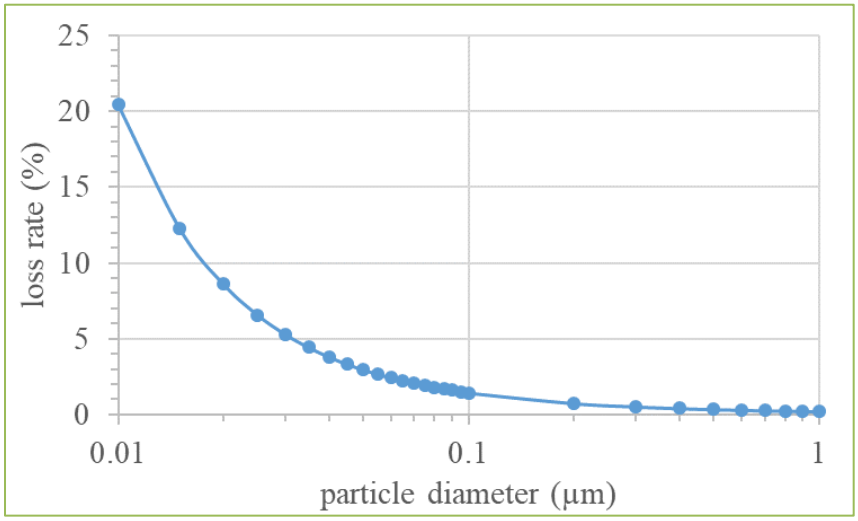

Figure 171. Sub-micron particle loss rate by turbulent diffusion in the sampling line

Modified Aerosol Sampling

In coal slurry tests conducted in DOE Cooperative Agreement No: DE-FE0025168, the ash aerosol sampling probe was inserted into the reaction zone, where the sample entered the probe through the sampling hole at the probe tip located at the combustor centerline. Since slag formed at high temperatures deposited on the inserted probe exposed to the flue gas, the probe in subsequent tests was retracted into the wall space within the sampling port. This avoided direct impact of flue gas. The modified probe configuration is shown by Figure 172. The ceramic tube exit is recessed 1 inch from the wall of the reaction zone and 4.5 inches away from the inner nitrogen tube exit, as shown.

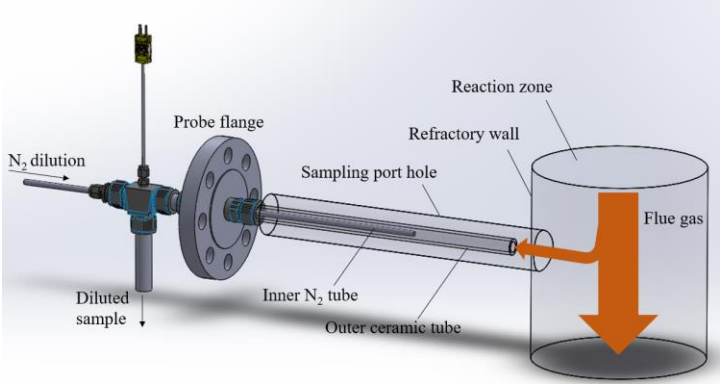

Figure 172. Sketch of the modified aerosol sampling probe in coal slurry tests conducted under DOE Cooperative Agreement No: DE-FE0025168

The sampling system for the dry feed experiments is shown in Figure 173. It adopts the same probe adjustment as in the slurry test described above. However, it has a much shorter sampling line. Downstream of the probe, the diluted sample flows through a pipeline, about 40 inches long to the manifold, which, previously, was around 160 inches long for the slurry tests. In this section of sampling line, the first 35 inches upstream of the critical orifice is pressurized and the remaining 5 inches is at atmospheric pressure. Because the modified sampling line is located directly under the sampling port on EFPR, the manifold is now closer to the second-stage air dilution point. This makes it possible to shorten the length from the manifold outlets to the air dilution point from 65 to 15 inches. Elbows of 45^o replaced those of 90^o in the new system to reduce local particle loss. The particle measurement instruments (SMPS, APS and BLPI) were also moved as close as possible to the combustor, immediately beneath the sampling port and manifold.

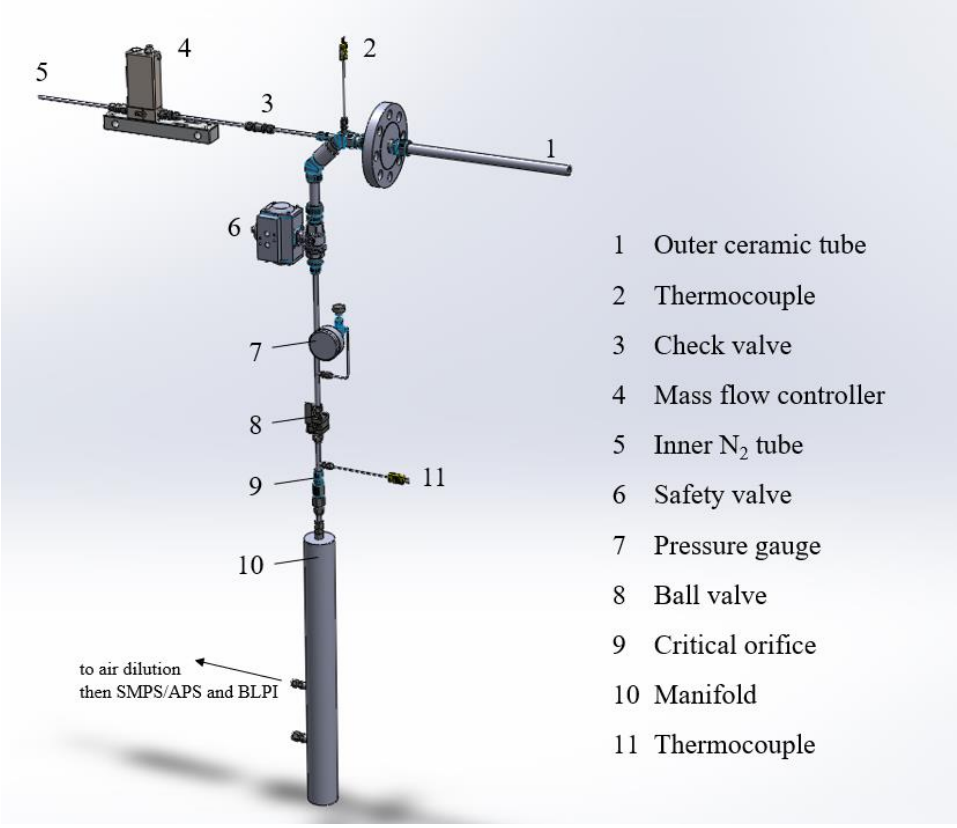

Figure 173. Modified ash aerosol sampling system

The calculation described above suggests that turbulent diffusion is the main cause for particle loss within the sample line, while the Brownian diffusion effect can be neglected. The particle loss rate η_p is defined as the ratio of number of particles diffusing onto walls to the total number of particles entering the tube, $\frac{kn_\infty A}{n_\infty V} \times 100\%$. It is controlled by the mass transfer coefficient k, total wall area A and gas volume flow rate V. The loss rate η_p is reduced with greater tube inner diameter and shorter travel length.

Using the flow conditions of 15-bar tests with a coal slurry in this reactor and calculations which are detailed above, the particle loss rate η_p due to turbulent diffusion in the modified system can be determined. The results of these calculations are reported in Table 39 for particles with d_p = 0.5 μm.

Table 39. Turbulent diffusion in the modified sampling line (dp = 0.5 μm)

Flow path	Length (in)	ID (mm)	pressure (bar)	gas Re number	d_p (μm)	k (m/s)	η_p (%)
part 1	35	16.5608	15	19057	0.5	7.88E-06	0.06893
part 2	5	16.5608	1	19304	0.5	2.51E-05	0.00214
part 3	15	4.826	1	6077	0.5	3.03E-05	0.02590

For particles with d_p from 0.01 to 1 μm, the total loss rates in the sampling line are summed from the three parts and compared with the results in slurry system, in Figure 174. Because the sampling line is greatly shortened, the modified system in future dry feeding tests is expected to have a much lower particle loss rate. That is, below 5% for particles greater than 0.01 μm. The modified system is being built and it will improve the data quality of the particle-measuring instruments.

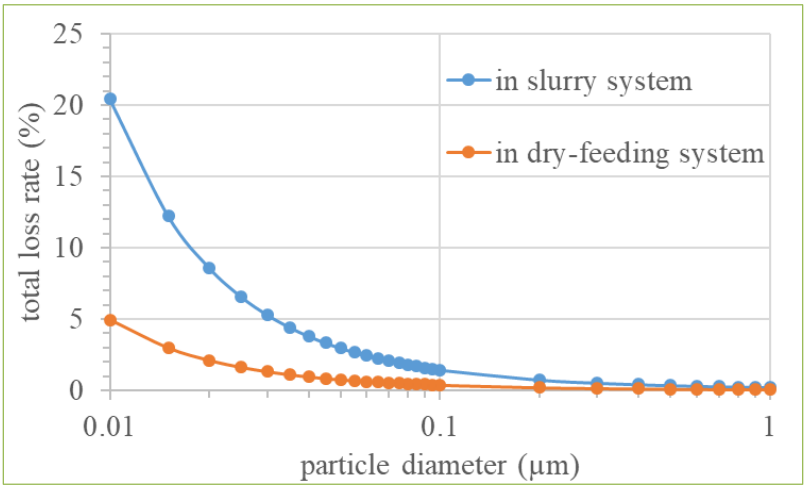

Figure 174. Sub-micron particle loss rate by turbulent diffusion in slurry and planned dry-feeding systems

The modified particle sampling system was subsequently constructed for the EFPR. Figure 175 is a photo showing the main structure installed on the sampling port of the reactor. As described previously, the system is modified from a horizontal configuration adopted during the coal-water slurry test to a vertical arrangement to improve the data quality in future testing with dry pulverized coal. The installed system has certain minor location adjustments due to limited installation space. According to previously reported theoretical calculations, the modified system is expected to have a much lower particle loss rate than its predecessor. Wall losses are predicted to be below 5% for particles greater than 0.01 μm, which is a significant improvement from the wall-loss rates of up to 20% with the original system.

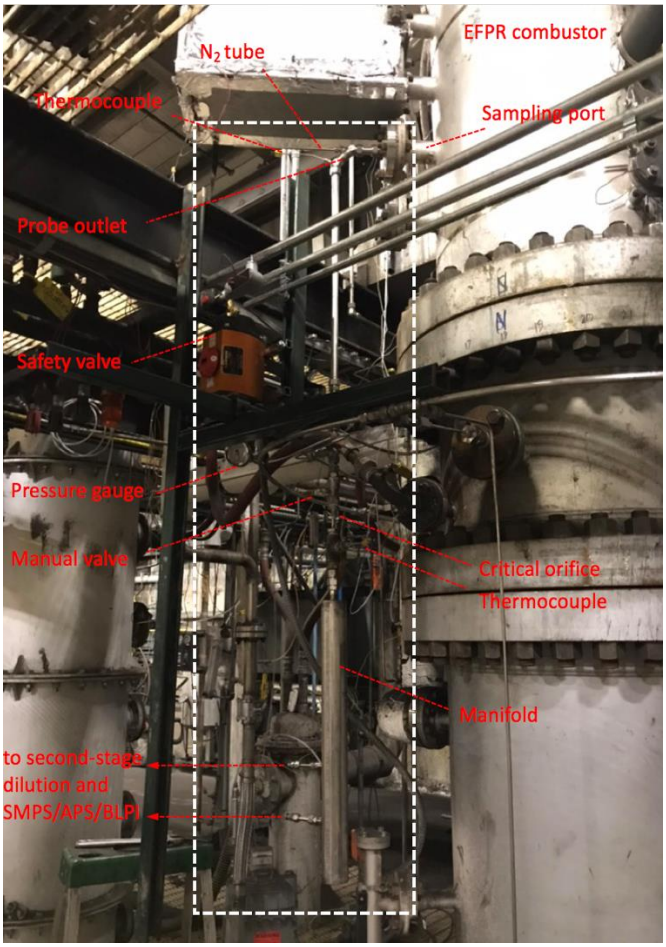

Figure 175. Structure of the particle sampling system installed on the EFPR

Theoretical investigations of pressure impacts on deposition rates

Due to COVID-19, experimental work on the pressurized feed system ceased in mid-March 2020, and the laboratory was temporally closed. As an interim stop gap, theoretical work was then initiated to determine how ash deposition rates at elevated pressures might be determined by extrapolating from ash deposition rate data obtained at atmospheric pressures. The first step is to mine existing, well defined, deposition rate data from 41 tests of air- and oxy-combustion of coal, biomass, petroleum coke and their blend fuels. Although conducted at atmospheric pressure, these test data were leveraged in order to extrapolate well understood deposition mechanisms at atmospheric pressure to pressurized oxy-coal combustion conditions.

The ash deposits sampled from a surface temperature-controlled probe consist of two parts: an outside deposit layer which is loosely bound and can be easily removed by soot-blowing, and an inside layer which tightly sticks to the heat exchanger surfaces. Current correlations on the growth rates of the two deposits are:

$$r_{inside\ deposition} = 48.143C_{PM_1} + 51.642C_{Cl} + 21.388C_{PM_1}C_{Cl} + 4.095,\ R^2 = 0.826; \quad \textbf{14}$$

$$r_{outside\ deposition} = 655.918C_{Na+K} - 512.575C_{Cl} + 343.064C_{Na+K}C_{Cl} - 2.964,\ R^2 = 0.632 \quad \textbf{15}$$

C_{PM_1}, C_{Cl} and C_{Na+K} are the mass concentrations of PM_1, chlorine and alkali metals (Na and K) in the flue gas, respectively. The deposition rates are in unit of g/(m^2hr).

While the correlation for the inside deposit shows promise, the correlation for the outside deposit requires significant improvement in order to be useful. Work is continuing in this direction.

The PM_1 concentration is shown to be an important role in the inside deposition. The mechanism here is that the sub-micron ash particles provide a powdery and sticky layer for larger particles to deposit instead of bouncing off the surface. Several chlorine-rich fuels in the 41 tests produced significantly higher inside deposition rates, therefore, Cl concentration is also taken into account for the correlation. Chlorine is found to be a very effective species causing ash aggregation in the deposits irrespective of the presence of sulfur, which leads to high deposition rate of the hard-to-remove inside layer. With both the overall PM_1 concentration and the essential component Cl being considered, the correlation on inside deposition rate is improved compared to previous work[13]. The outside deposition rate is correlated with concentrations of the alkali metals and chlorine. Na and K contents have been shown to determine the bounce-off behavior of coarse ash particles which are deposited through inertial impaction[13]. When abundant chlorine is present, shedding of the outside deposits is inclined to occur and reduces the deposition rate, of which the relevant mechanism is unclear at present.

Based on the above findings, some estimations on deposition rates in future pressurized oxy-coal combustion could be made, in terms of the chemical effects from ash aerosols. One may assume that the gas volume will be greatly diminished at higher pressure, however, the concentrations also depend on the absolute amounts of pertinent components that are present. As shown in Table 40, yields of $PM_{0.6}$ and PM_1 are greatly reduced at 15 bar (coal water slurry test on EFPR) compared to at 1 bar, with the same Sufco coal being burned at similar peak temperature.

Table 40. PM0.6 and PM1.0 yields in Sufco coal combustion at 1 and 15 bar

	PM0.6 (%)	PM1.0 (%)
1 bar	1.512	1.842
15 bar	0.071	0.085

The PM_1 yield at 15 bar is less than a twentieth of that at 1 bar, and if the gas volume is roughly reduced by a factor of 15, the PM_1 mass concentration at 15 bar will be decreased. Consequently, the impacting ash flux onto the cooling surface will contain less sub-micron particles per unit area, resulting in lower inside deposition rate.

The alkali concentration in the above correlation is calculated as the total input alkali metals by flue gas volume. Figure 176 shows the fractions of Na and K partitioned into ash particles at different sizes. Pressure has little effect on the yields of vaporized alkali metals partitioned into the sub-micron ash but decreases the yields into larger particles. This might suggest that the alkali concentration in the aerosols forming the outside deposits will be reduced at higher pressure, which could increase the rebound behavior and decrease the outside deposition rate.

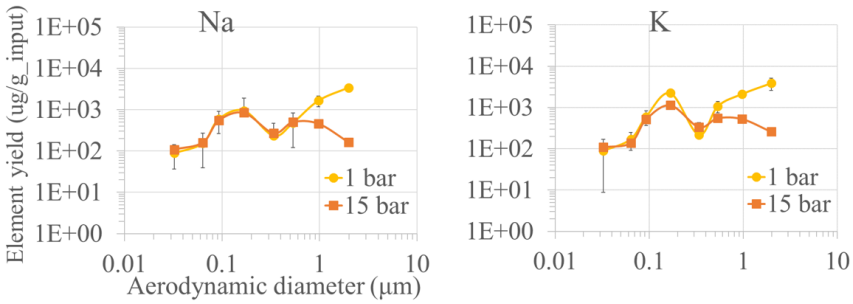

Figure 176. Amounts of Na and K partitioned into ash particles

The above estimations on deposition rates at high pressure have not considered the aerodynamic effects from pressure. One change in pressurized combustion would be that the particle impaction rate is decreased due to the lower gas velocity (if true in a boiler). Chlorine is usually in low amounts in coal, however, its portioning in ash aerosols and deposits at high pressure is unknown. To uncover the complete deposition mechanisms at high pressure, further experimental and simulation work is needed.

Ash Aerosol Sampling

To sample ash aerosols from the reactor under pressure, a sampling system based on a previous design[14] was modified and built. Figure 177 shows its schematic diagram designed for the University of Utah EFPR reactor on the left and the actual system used in these pressurized tests at BYU, on the right. The system was successfully operated on the BYU reactor operated at 100 and 210 psig. Note that the actual tube used connecting parts 2 and 6 in the BYU tests is shorter than the tube shown in the photo.

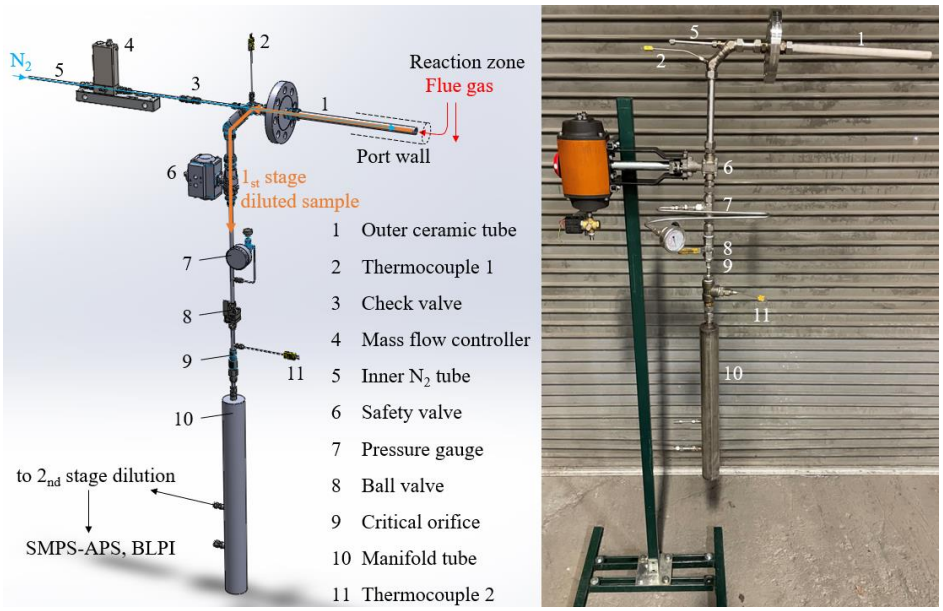

Figure 177. High-pressure ash aerosol sampling system (left: schematic diagram; right: photo of real system).

The sampling system is installed on a port flange of the BYU reactor, with the probe being placed inside the port hole to avoid slag build-up by direct flue gas impact. The probe part consists of an outer ceramic tube and an inner nitrogen steel tube. A stream of flue gas containing ash particles enters the opening of the ceramic tube and is diluted by the injected nitrogen at the probe tip. The diluted sample is then directed through the annulus into the subsequent sampling line. After passing the critical orifice, the sample flow is depressurized to be at atmospheric pressure. A second stage dilution using filtered air further dilutes the sample to a proper concentration before it enters the particle measurement instruments, a Scanning Mobility Particle Sizer (SMPS), an Aerodynamic Particle Sizer (APS) and a Berner Low Pressure Impactor (BLPI).

Because the sample stream is diverted into the sampling port hole, the aerosols are restricted to those particles that follow the gas streamlines. This could cause loss of some particles of large sizes in the sample stream and has been investigated in the original design[14]. In the referenced paper, the CFD simulation at 15 bar (218 psi) suggests that 99 % of particles with d_p (diameter) at 5 µm will follow the flue gas into the probe, and more than 93% of d_p at 10 µm will do so. This simulation has not been performed for the current system at BYU. However, significant differences in the conclusions are not expected because the aerodynamic condition is not greatly changed between the two combustion scenarios at similar temperature and pressure.

Theoretical calculation of the particle loss to the walls by diffusion along the entire sampling line in the 210-psig test on the BYU rig has been performed, where the sampling line was shorter than for the UU EFPR[14]. Figure 178 shows the total diffusion loss percentage in particle number for different d_p. It indicates that the total loss is less than 0.5 % for $d_p > 0.1$ µm and less than 5% for $d_p > 0.01$ µm. Based on these results, the aerosol sample is considered to be

representative in the range of 0.01-10 µm, which is within the measurement range and study scope of this work.

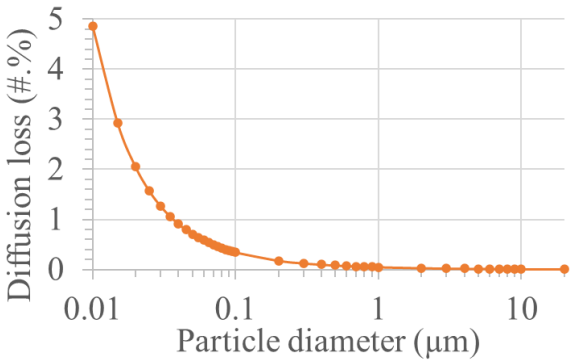

Figure 178. Total particle loss rate by wall diffusion along the sampling line

Figure 179 shows the sampling system mounted on the BYU reactor, through the fifth sampling port from the top. During the 100-psig and 210-psig tests, the sample temperatures of the upstream (thermocouple 1 in Figure 180) and downstream (thermocouple 2) are controlled around 460 and 430 K, respectively. At these temperatures, no water condensation occurred in the cooled sampling line while the dew point of moisture in the sample was indeed increased at elevated pressures.

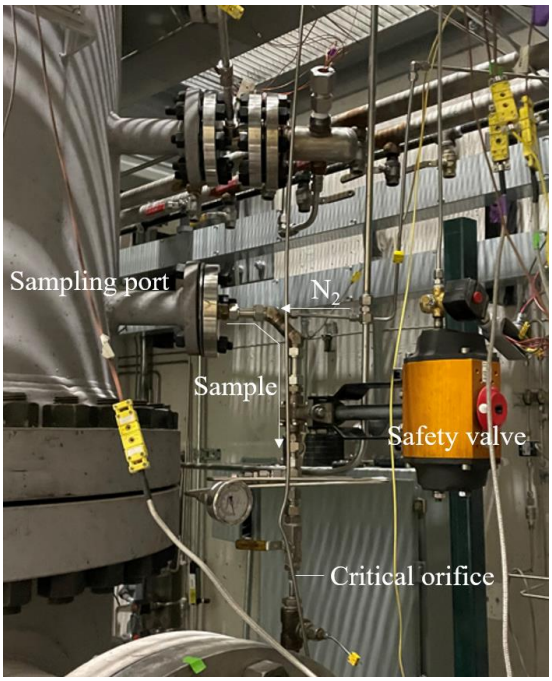

Figure 179. Ash aerosol sampling system mounted on BYU reactor

Figure 180 compares the particle size distributions (PSDs) of ash aerosols formed at two pressures during the BYU tests, with a. showing the mass concentrations based on the flue gas volume, and b. based on the total ash input, which eliminates the effect from gas volume

change between two cases. The results suggest that a higher pressure decreases the PM_1 (sub-micron ash particles) formation which is controlled by mineral vaporization. The coagulation effect on the condensed sub-micron particles at 210 psig is increased compared to 100 psig, producing an accumulation mode at a larger d_p. These results are also true for the 1-2 µm size range. For coarse particles of diameters at 2-20 µm, the higher pressure is shown to increase the formation of these residual ash particles.

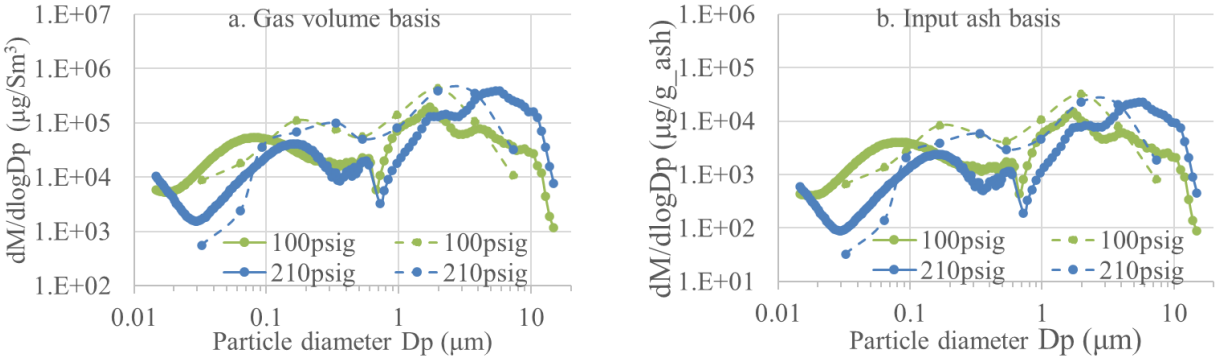

Figure 180. Ash aerosol particle size distributions at 100 and 210 psig

Figure 181 compares the ash aerosol compositions formed at two pressures during the BYU tests. Elevated pressure increased the concentrations of sodium, potassium, sulfur and magnesium in the sub-micron ash and decreased that of calcium, aluminum, and silicon. For all cases, the effects of combustion conditions on elemental composition appear to be diminished as the particle size increases beyond 1 µm. This is reasonable since pressure has been found to affect the super-micron ash aerosol formation only through char fragmentation processes[15–17], which should have an insignificant influence on elemental partitioning.

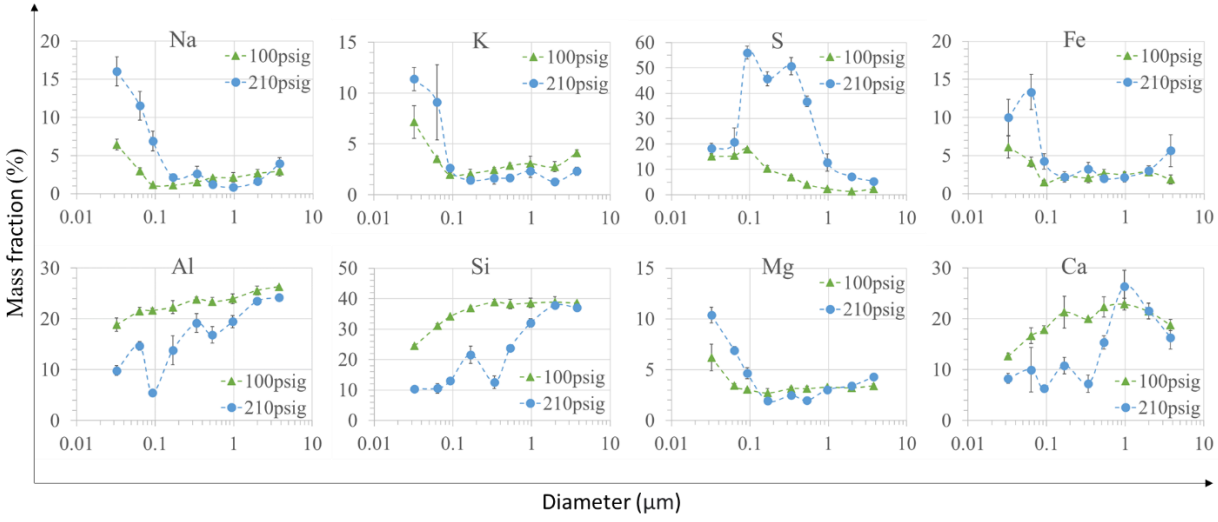

Figure 181. Ash aerosol particle compositions as a function of size at 100 and 210 psig

A scanning electron microscope (SEM) has been used to evaluate the morphology of the particles as shown in Figure 182. The effect of pressure is notable in that it tends to produce

larger quantities of coarse particles. This is also shown in the particle size distribution plots in Figure 180.

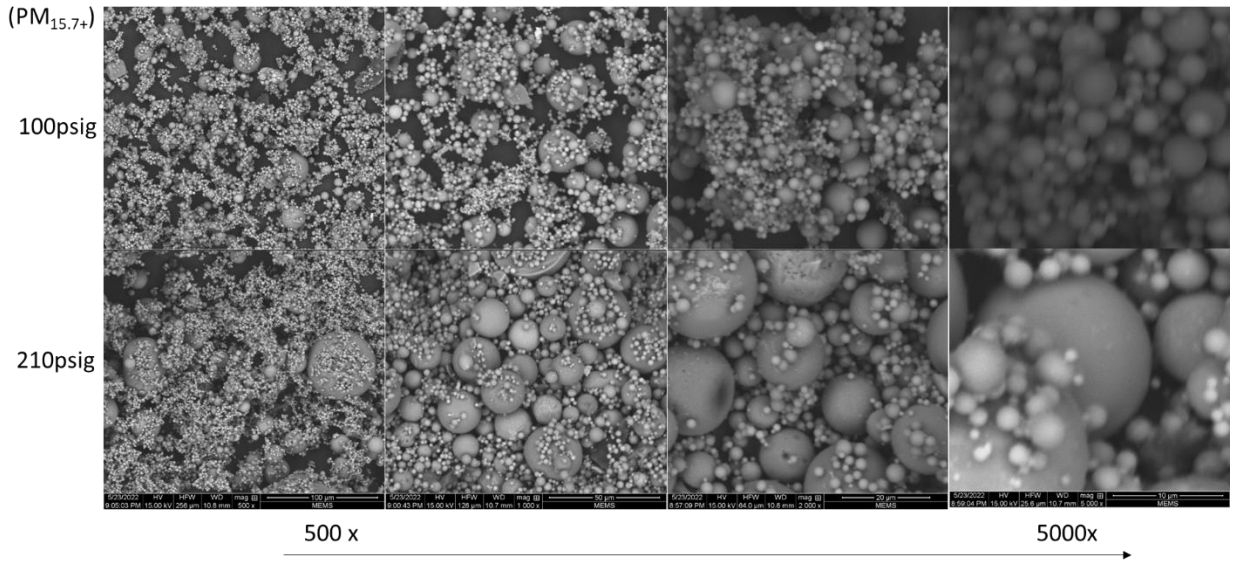

Figure 182. Ash morphology showing the impact of reactor pressure

Subtask 5.2 – EFPR Corrosion Propensity Characterization

One of the goals of this program is to determine the effects of both high temperatures and pressures on corrosion potential on boiler tube surfaces. This is to be accomplished by measuring corrosion rates using a real-time, electrochemical noise-based corrosion monitoring system. A gas-cooled corrosion probe including corrosion sensor elements must be custom designed and manufactured to safely insert into the pressurized reactor. Initial design considerations included suitable sensor element alloys, location and dimensions of the EFPR access ports, and preliminary corrosion probe design.

Materials

The three alloys chosen for the corrosion elements were T22, P91, and 347H. All three alloys are used to some extent in the construction of superheater (SH) tubes. T22 is a low carbon, low chromium alloy that is most common in SH tubes for sub-critical boilers. P91 is commonly used in newer supercritical boilers allowing SH temperatures to extend up to 1100°F. 347H is an advanced high-Ni, high-Cr alloy that sees limited use now but is a targeted material for advanced power plants. The composition and upper temperature limit of these three alloys are recorded in Table 41.

Table 41. Specification of the Materials Used for Corrosion Sensor Elements.

Material	T22	P91	347H
Upper Temperature Limit, °F	1050	1100	1300
C, %	0.11	0.10	0.048
Si, %	0.2	0.32	0.40
Mn, %	0.44	0.47	1.32

Material	T22	P91	347H
Ni, %	-	0.15	9.73
Cr, %	2.21	8.52	17.45
Mo, %	0.95	0.93	-
S, %	0.003	0.002	0.008
P, %	0.01	0.018	0.026
Cu, %	-	0.11	-
Al, %	-	0.01	0.005
Nb/Cb, %	-	0.07	0.63
V, %	-	0.22	0.078
N, %	-	0.044	-
Ta, %	-	-	0.02

REI measured corrosion rates on these three alloys in a prior oxy-coal project with experiments performed at atmospheric pressure. As was done in that project, corrosion rates measurements were targeted for a range from 900°F, a typical SH temperature for sub-critical boilers; and up to the maximum operating temperature of each alloy. In this manner corrosion rates can be compared directly to previous measurements in an atmospheric, oxy-coal environment.

Experience with the particle sampling probe resulted in concern that the slag would freeze the corrosion probe inside the furnace and result in ultimate loss of the probe. To mitigate this risk, two probe bodies were built. Corrosion measurements on T22, the commonly used and least corrosion resistant alloy, was be prioritized to bracket the measurements.

Probe Design

REI previously built and used corrosion probes in several harsh environments. The design for the EFPR was unique in that the probe body was shrunk to 1.5" OD to fit the available EFPR access port. A more difficult challenge was to design the probe for high-pressure and ensure no leakage of potentially harmful gases across the element sensors to the outside of the reactor. The probe was designed with a pressure safety factor of >10. The probe body was constructed from SS316, which has good corrosion resistance but somewhat susceptible to minor corrosion under the target combustion conditions. The higher-pressure rating of the thicker walls ensured the probe body would not fail from the extent of metal wastage expected during the measurement period.

The sensor and probe design are proprietary, but some aspects are mentioned here. The new design includes a back-pressure control valve on the cooling outlet line to maintain a cooling medium pressure slightly above reactor pressure. This ensures minimal potential for leakage across the sensor elements and leakage into the reactor if it occurs. Some movements of the inner probe parts are required for assembly. The new design completely seals around the movable parts so the cooling system is closed. In the case of catastrophic failure such as complete loss of cooling gas and melting of the probe end, all reactor gases would be contained within the closed cooling system.

The preliminary probe design was such that when inserted into the center of the furnace, the orientation of the sensor elements is that of a tube in cross flow. Thus, simulating the condition of a typical SH tube in a utility boiler. When calculating cooling gas requirements (either with CO_2 or N_2), it was discovered that it is not possible to adequately cool this probe with gas. Maximum gas temperatures in experiments with minimal CO_2 introduced as a diluent would exceed 4500°F with inner refractory temperatures of 3000°F, resulting in extraordinarily high heat flux to the cooled probe surface. Therefore, the cross-flow design was abandoned, and a new design was conceptualized with sensor elements placed in the probe face and the probe inserted such that the probe face is flush with the inside reactor walls. This design would mimic flow along boiler tube walls.

Probe Redesign

REI has used a "flush-face" probe design multiple times in the past. The current design is unique in that the probe body decreased in size, and designed for safe operation with the high reactor pressures and prevention of leakage of harmful gases.

A schematic of the general layout is provided in Figure 183. As shown, the corrosion elements are positioned in the tip of the probe. These elements are cooled with gas that flows in through the center of the probe and return through an annulus. The inlet and outlet will be connected to the gas lines with compression fittings. The signal thermocouple lines pass through pressure-fittings in the inlet cap.

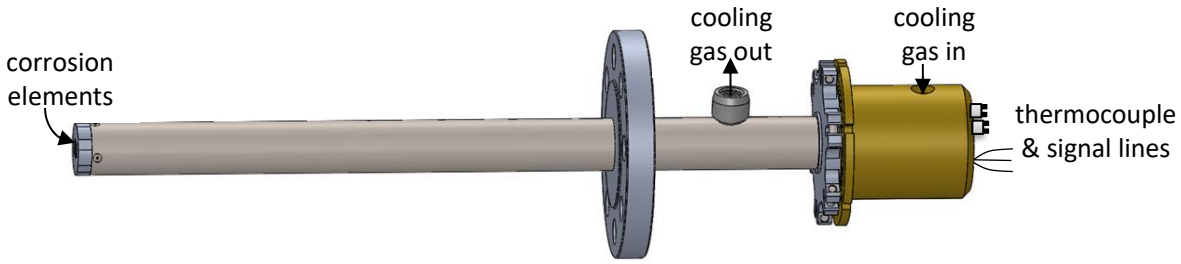

Figure 183. Modified corrosion probe

The smaller probe body of 1.5" OD prevents the use of internal structure that had been used on previous projects. Theoretically, the corrosion element array could be shrunk, but that would result in difficulties machining components and assembling the probe. Therefore, the internal structures were re-designed within the available space. The probe body thickness also needed to be decreased but was still sufficient to reach pressures 2-3 times what was expected to be experienced in the reactor.

Machining of two high-pressure probe bodies was completed at the Precision Machine Shop at Brigham Young University. An image of one of the probes is included in Figure 184. After receipt of the element assembly parts, it was discovered that two minor modifications were necessary to hold the element assembly more securely in position.

Project meetings with Dr. Bill Cox from Corrosion Management, Ltd. were held to discuss operation of the real time electrochemical noise (EN) based corrosion monitors for insertion

into the high-pressure reactor. Some modifications to the probe operation during start-up and shut-down periods were made to ensure that the pressure differential between the reactor and probe internals would be minimized.

Figure 184. Image of completed high-pressure corrosion probe body built at BYU's Precision Machine Shop

Due to the differences in reactor geometry between the EFPR at the University of Utah and the POC at BYU, the corrosion probe designed for the UofU's pressurized oxy-coal reactor was modified to allow measurements to be taken instead in BYU's POC. The corrosion probe is designed to be inserted into the reactor's access port and have a face that is flush with the inner walls of the reactor. Due to the UofU and BYU reactors having different lengths of access ports, modifications to the probe were needed to achieve accurate corrosion measurements. For the probe's face to sit flush with the inner walls of the BYU reactor, the part of the probe that is inserted into the reactor needed to be lengthened by 2 in. This modification was accomplished by moving the probe's flange, intended for mounting the probe to the reactor, 2 inches away from the face that must sit flush with the reactor's wall.

This modification required removing the old flange, which was welded onto the probe, and welding on a new flange at the appropriate distance from the probe's face. During this process, it was decided that a new material be used for the flange that would create a stronger weld to the stainless steel probe body. The old flange was A105 carbon steel, and the new flange was selected to be 316 stainless steel to match the material of the probe, thereby increasing the strength of the weld between the probe piping and the flange. In addition, the flange connections for the cooling gas inlet and the feedthrough section were reinforced along with feedthrough and cooling gas thredolets being redesigned and reinforced. A comparison of the original probe designed for the University of Utah facility and the modified design for the BYU POC is shown in Figure 185.

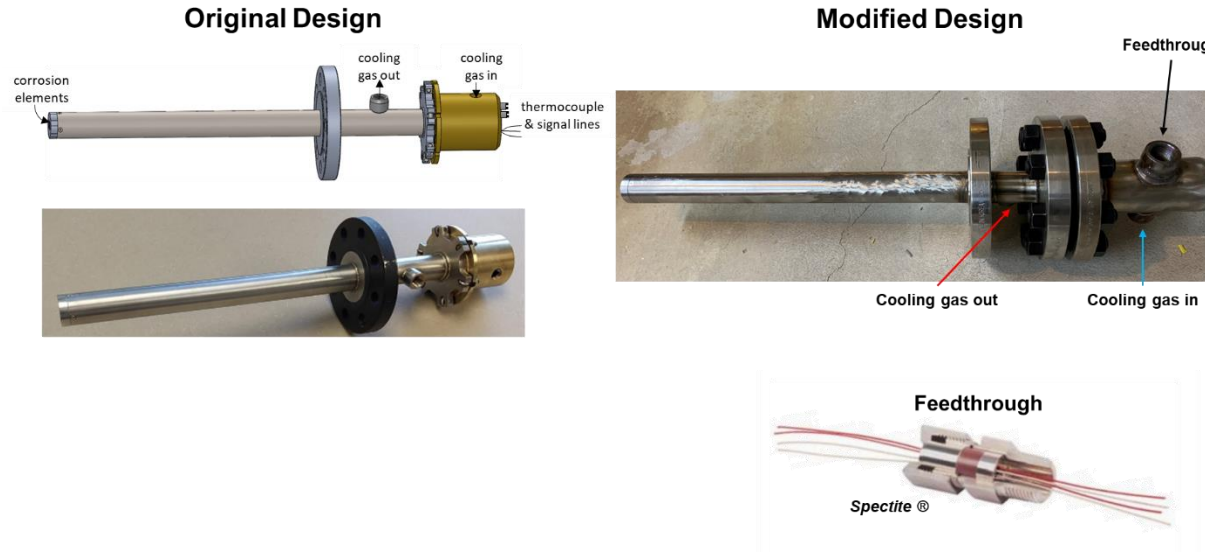

Figure 185. Comparison of the original design for the corrosion probe and the modified design installed in the BYU POC

Realtime Corrosion Monitoring

A plot of temperature measured at the surface of the probe along with real-time corrosion rate is shown in Figure 186 for the test conducted on March 10, 2022. The surface temperature in degrees Fahrenheit is shown in green and corresponds to the left vertical axis. The electrochemical noise corrosion rate (ENCR) represented as a reduction in the metal sensor element in mm/yr is shown in yellow and corresponds to the right vertical axis. An observation from the plot is that peaks in corrosion rates tend to correspond with timeframes where the surface temperature increases significantly. Comparison of Figure 186 with the data in Figure 114 suggests that the increase in coal flow rate at approximately 14:00 corresponds to a steady increase in probe surface temperature and wall temperatures, which also tends to cause a steady rise in corrosion rate. There is a significant spike in corrosion rate and surface temperature at approximately 16:10 and another spike in corrosion rate nearly 10 minutes later. REI's research and experience with corrosion on process tubes in combustion systems has shown that corrosion activity increases when the near-tube environment fluctuates between reducing and oxidizing conditions. It is possible that burner instability produced from greater variability in the fuel transport and resultant fluctuations in the O_2 (as indicated in Figure 110) near the end of the experimental run exacerbated fluctuations in oxidizing vs. reducing conditions in the local environment to which the probe is exposed. It should also be noted that the peaks measured at 0.09 mm/yr would be considered low by industry standards where cause for concern would be rates 5-10 times higher than the rates measured in this test.

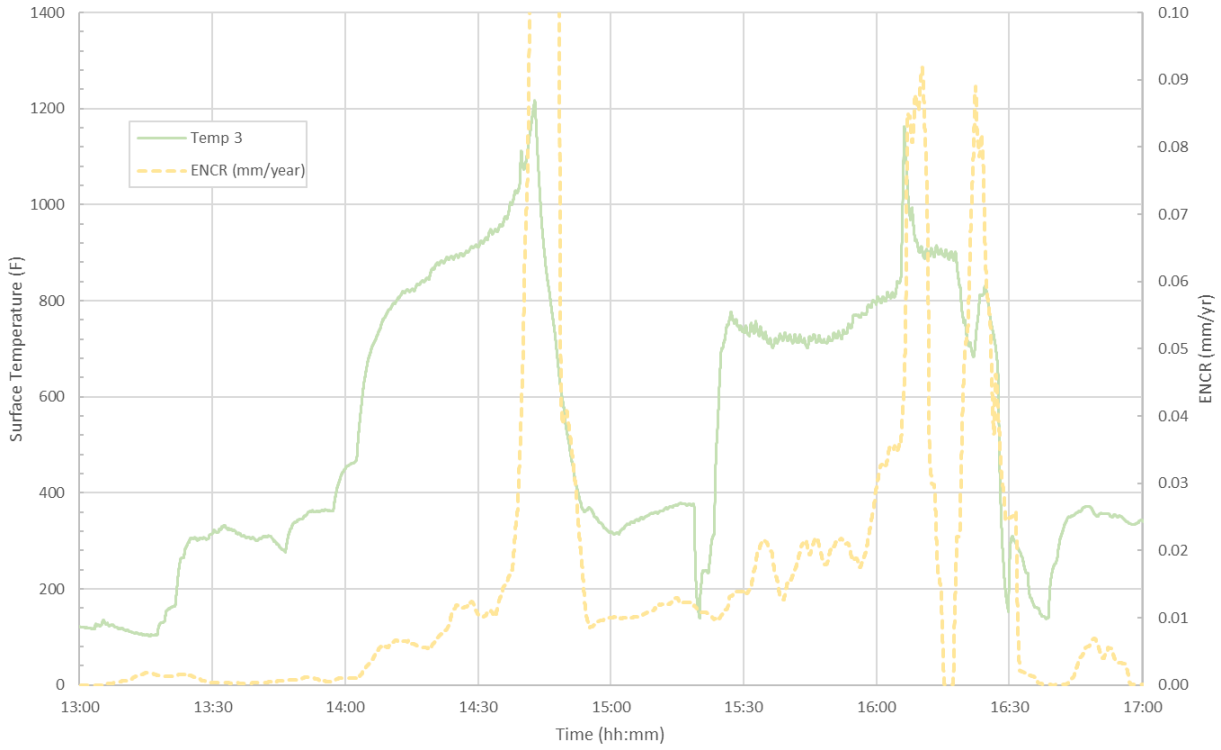

Figure 186. Surface temperature and real-time corrosion rate (ENCR) for the tests on 03/10/22

A plot showing surface temperature and corrosion rate for the test carried out on March 22, 2022 is shown in Figure 187. Although data gathered by the facility does not extend beyond approximately 11:00, the experiment carried on through the afternoon for this test. A disruption in the operation around 11:00 is notable in the Figure 187 plot as surface temperature drops to very low levels before resuming to more typical values in the afternoon. As in the previous dataset, fluctuations in operation which can be interpreted as instability in the burner lead to peaks in temperature and corrosion rate. In addition, a similar trend of increasing corrosion rate with increasing surface temperature is also shown with peaking corrosion rate again occurring near the end of the run. Again, this is likely the result of unstable conditions produced at the end of the run. It has been noted that the instability increases as the coal in the feeder reaches low levels and fluidization becomes more difficult to control.

A plot showing surface temperature and corrosion rate for the test carried on March 29, 2022 is shown in Figure 188. When reviewing this plot with the data shown in Figure 112, it is apparent that the peaks in temperature and corrosion rate between 10:00 and 11:30 are occurring during a period of transient conditions and are therefore less meaningful than the period of more steady operation between 10:30 and 11:45. Coal flow is relatively steady during this period as is the probe temperature measurement. However, instability in the O_2 as shown in Figure 112 occurs where increased corrosion activity is observed. It is suspected that perturbations within the system leading to flame instability caused a change in the local

conditions to which the sensor is exposed, thereby increasing the corrosion rate measured on the sensor elements.

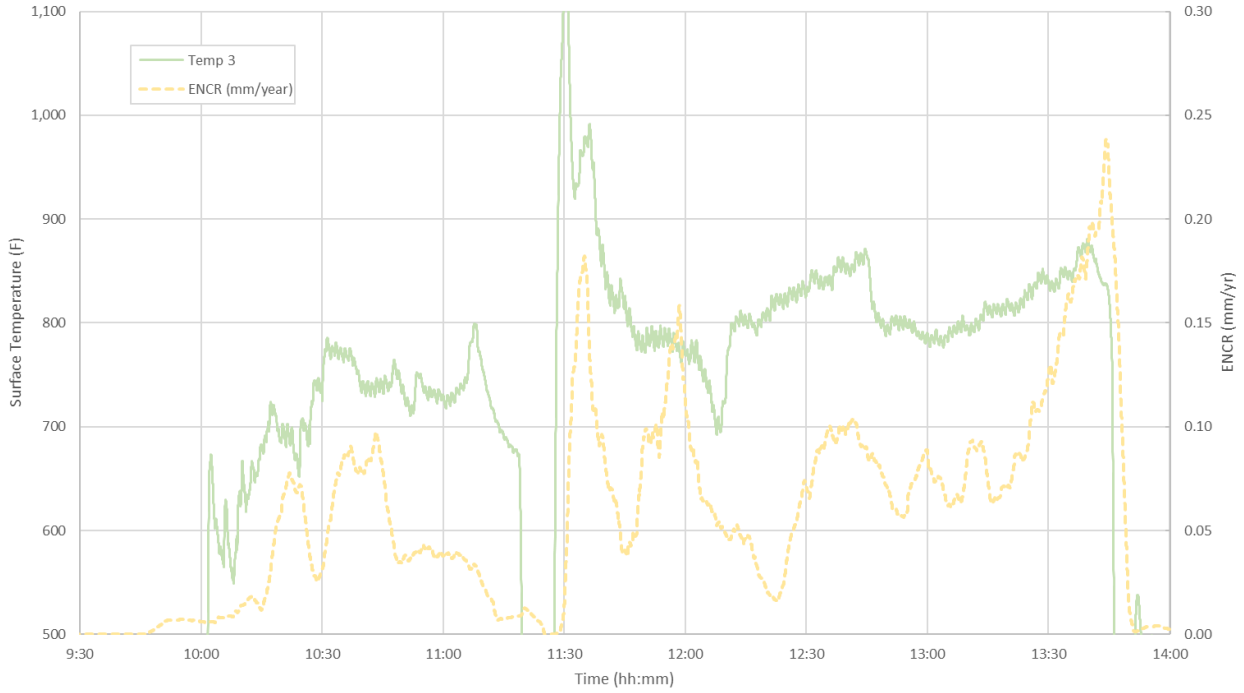

Figure 187. Surface temperature and real-time corrosion rate (ENCR) for the tests on 03/22/22

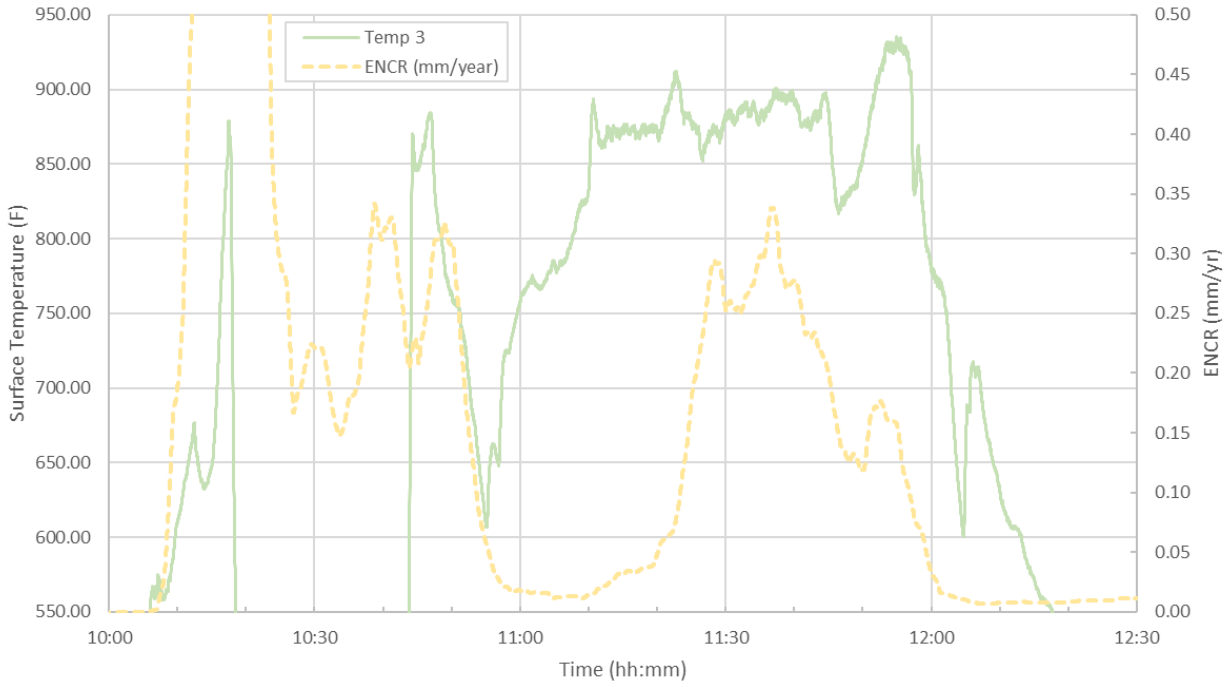

Figure 188. Surface temperature and real-time corrosion rate (ENCR) for the tests on 03/29/22

Task 5 Summary and Conclusions

The dry feed system assembled at the University of Utah was connected to a pressurized candle filter assembly for tests on the functionality of the system to deliver steady and reliable flow rates at values appropriate for the EFPR in high pressure oxy-combustion experiments. Although periods of acceptable coal flow rates appropriate for the capacity of the reactor were recorded, achieving a stable flow rate for a suitable length of time proved to be unattainable.

As part of REI's risk management strategy, REI engaged BYU who were developing a dry feed system for a pressurized oxy-coal combustion facility and had seen reasonable success in achieving consistent coal flow rates. A plan was established to run experiments in the BYU POC that involved REI's real-time corrosion monitoring probe and the UofU ash aerosol sampling system. The BYU facility came equipped with instrumentation providing temperature, heat flux, radiation intensity, gas and particle temperature, and flue gas properties.

Using these capabilities, a test campaign was completed that provided a wealth of unique data that will be valuable for continuing technology development and the development and validation of modeling tools. This data will serve as an excellent resource for validation of models involving turbulent mixing, radiant heat transfer, coal particle combustion, CO chemistry, corrosion, mineral matter transformation and deposition and other important aspects of coal combustion that might arise in the development of pressurized oxy-coal firing for power generation.

Ash aerosol sample data suggest that a higher pressure decreases the PM_1 (sub-micron ash particles) formation which is controlled by mineral vaporization. The coagulation effect on the condensed sub-micron particles at 210 psig increased compared to 100 psig, producing an accumulation mode at a larger d_p, which is also true for the 1-2 μm size range. For coarse particles of diameters at 2-20 μm, the higher pressure is shown to increase the formation of these residual ash particles. SEM data was also used to evaluate the morphology of the particles. The effect of pressure is notable in that it tends to produce larger quantities of coarse particles, which is consistent with the particle size distribution data that has been gathered.

Elevated pressure was shown to increase the concentrations of sodium, potassium, sulfur and magnesium in the sub-micron ash and decreased that of calcium, aluminum, and silicon. For each constituent, the effects of combustion conditions on elemental composition appear to be diminished as the particle size increases beyond 1 μm.

Real-time corrosion data indicate peaks in corrosion rates tend to correspond with timeframes where the metal element surface temperature increases significantly. REI's research and experience with corrosion on process tubes in combustion systems has shown that corrosion activity increases when the near-tube environment fluctuates between reducing and oxidizing conditions. Burner instability produced from greater variability in the fuel transport and resultant fluctuations in the O_2 exacerbated fluctuations in oxidizing vs. reducing conditions in the local environment to which the probe is exposed. Peaks in corrosion rate measured in these tests would be considered low by industry standards.

Task 6 – Model Extension and Validation

Objective: Validate the applicability of the model across a range of scales ensuring that the model can be used with confidence in extension to full-scale applications.

High Pressure Dry Feed Application Validation

A two-step correlation for devolatilization that accommodates pressure effects on volatile yields and resulting char structure currently exists in REI's CFD model, *GLACIER.* The mechanism is based on the Chemical Percolation Devolatilization (CPD) model integrated with a pressure dependent swelling model. The approach provides refined predictions of volatile yield, coal swelling, and resultant char structure and morphology as a function of pressure.

High pressure char combustion data reported by Fluent through DOE's high-pressure coal combustion kinetics project[18] were investigated to validate the mechanism. REI completed a series of CFD simulations under high-pressure conditions which were gathered from the high-pressure coal combustion kinetics project. Model-predicted coal burnout levels were compared against reported burnout measurements in the experiments and interrogated to ensure the model is appropriate for dry-fed coal combustion at high pressures.

The work in this program focused on *high pressure* oxy-combustion processes since the pressure effect on coal devolatilization and char reaction should be properly addressed in modeling. Our approach entailed integration of the CPD model[19] to predict pressure effects on coal devolatilization and the subsequent char reaction based on the extended single film model. The CPD model was implemented into *GLACIER* and model validation work was performed.

Our modeling approach was to call the CPD routine at every time step of each *GLACIER* particle trajectory to evaluate CPD-calculated volatile yield, while the two-step volatile release model based on Ubhayakar et al.[20] and Kobayashi et al.[21] is still used. At the end of each particle iteration, the high temperature volatile yield constant is adjusted so that the overall two step volatile yield match that predicted by CPD. This process is repeated iteratively until *GLACIER* predictions match the CPD-calculated volatile yield.

As part of the U.S. Department of Energy (DOE) initiative to improve the efficiency of coal-fired power plants and reduce the pollution generated by these facilities, DOE has funded the High-Pressure Coal Combustion Kinetics (HPCCK) Projects in the early 2000s[18]. Using SRI's pressurized radiant coal flow reactor, a series of laboratory experiments were conducted on selected pulverized coals at elevated pressures to generate data on burnout, pollutant formation and char formation. We will use this data set to validate our approach. REI modeled SRI's Long Residence Time Radiant Coal Flow Reactor (LRT-RCFR) with two pressure conditions: 1 and 10 atm for comparison purposes. The schematic of the reactor is shown in Figure 189. The reactor has an annulus inlet: core with 0.848 cm ID and sheath flow with 0.176 cm thickness. Coal particles are injected through the core inlet. The wall temperature is maintained at 1873 K. The modeled inlet gas flow rate is 0.537 g/s with O_2 19.5% in Ar at 300K. Pittsburgh #8 coal is injected at 0.0287 g/s with the particle size range of 75 – 106 μm. Coal properties are shown in Table 42.

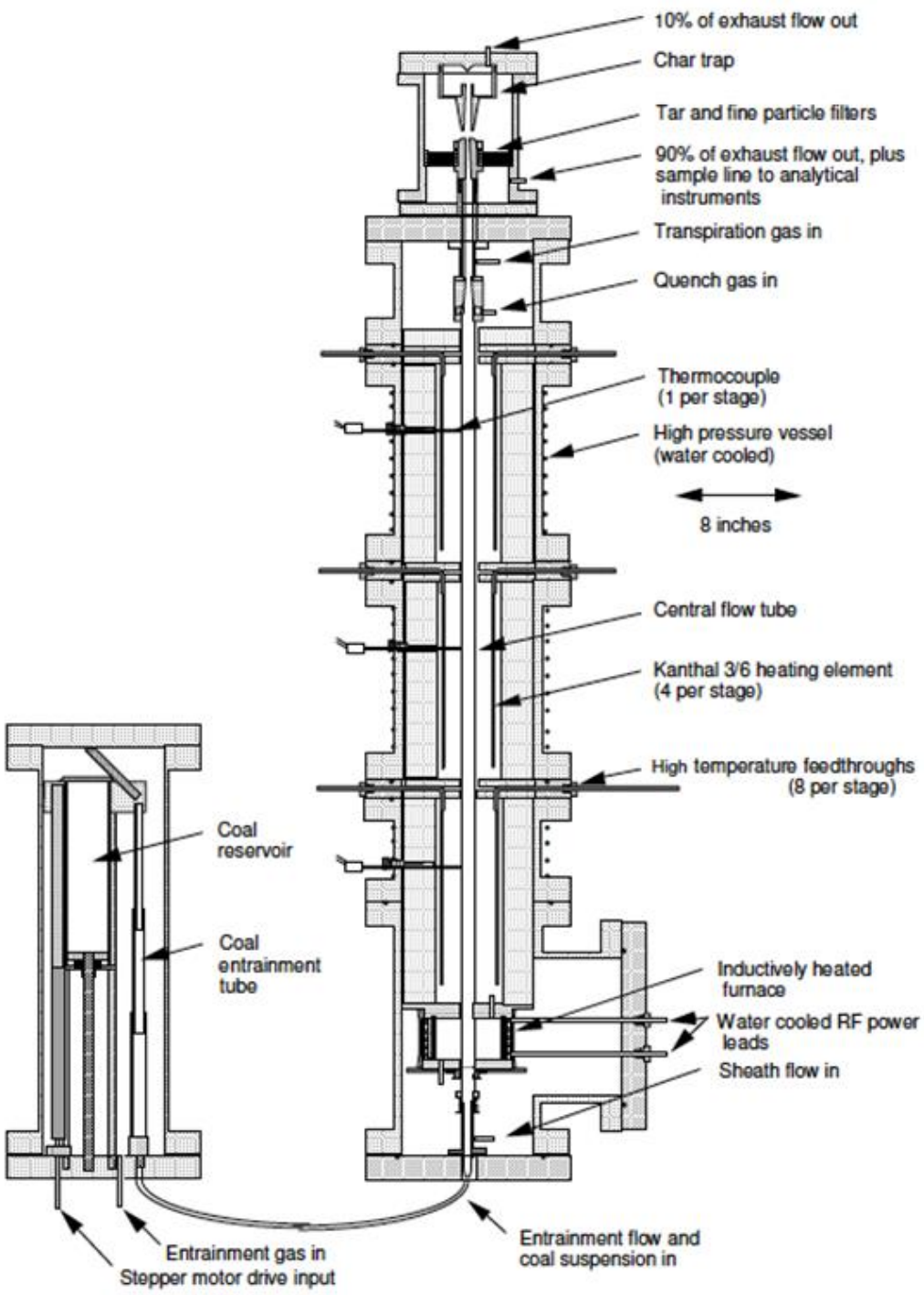

Figure 189. SRI's Long Residence Time Radiant Coal Flow Reactor (LRT-RCFR)[18]

Table 42: Pittsburgh #8 coal properties.

Ultimate Analysis	wt%
C	70.30
H	4.70

O	5.05
N	1.48
S	5.48
Ash	12.30
Moisture	0.70
Sum	*100.00*
Proximate Analysis	**wt%**
M	0.7
Ash	12.3
VM	37.9
FC	49.1
Sum	*100.00*

Figure 190 shows the flue gas temperature profiles from the 1 and 10 atm cases. The 10 atm case shows much higher gas temperatures early in the reactor. Under the same air and fuel mass flow rates, the 10 atm case has a smaller gas volume than the 1 atm case resulting in much lower gas velocities and a longer residence time in the reactor. On the other hand, high velocity in the lower-pressure case pushes the reaction to the later stage of the reactor.

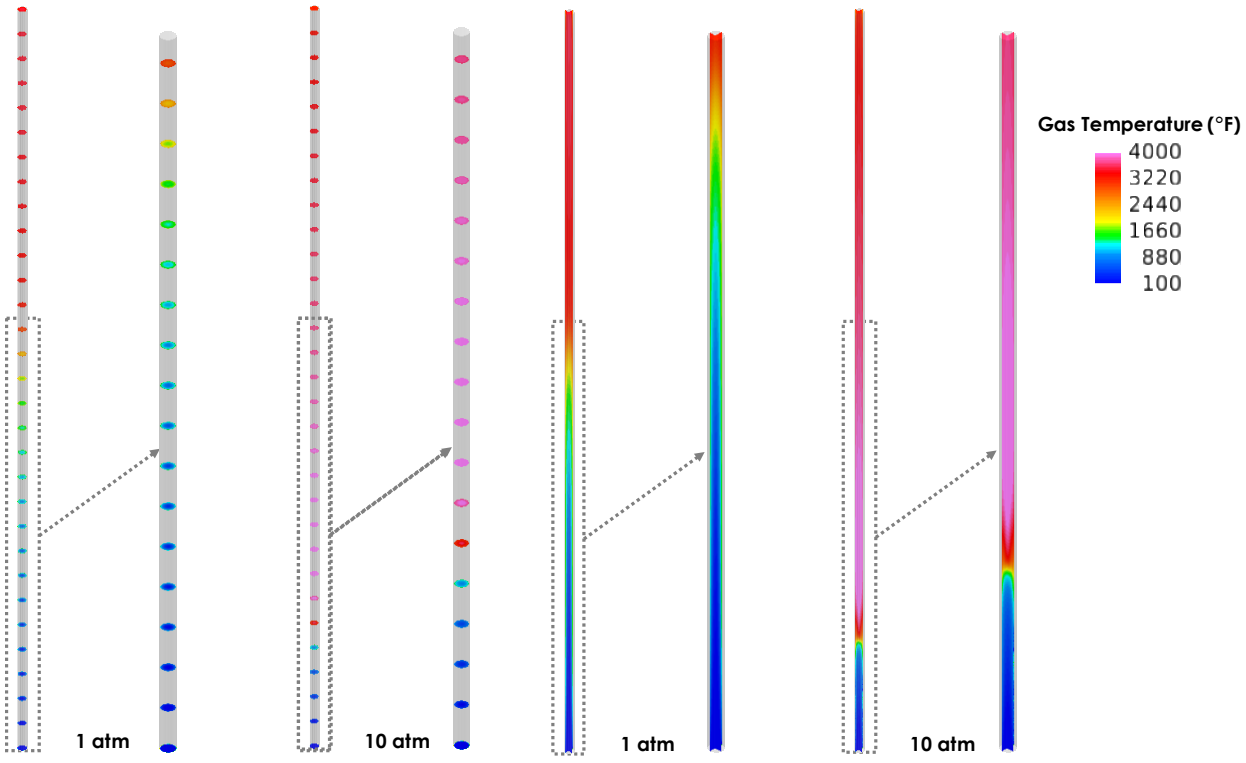

Figure 190: Flue gas temperature profiles at 1 and 10 atm.

Figure 191 and Figure 192 show the particle temperatures and the volatile yields, respectively, as a function of particle residence time and distance for 1 and 10 atm cases. As shown in Figure 191, particles at 1 atm exit the reactor at approximately 0.11 seconds due to high gas velocity

that entrains the particles. At 1 atm, particles heat up quickly and reach peak temperature at about 0.1 second, while, at 10 atm, particles reach peak temperature at approximately 0.55 seconds. In terms of distance, the lower-pressure case reaches peak particle temperature near 0.75 m, while the higher-pressure case reaches peak particle temperature near 0.3 m. The particle heat-up is slow at higher pressure due to slower release of volatiles, but the peak particle temperature occurs earlier in terms of distance due to the relatively lower velocity. This is consistent with the devolatilization behavior shown in Figure 192. The devolatilization begins and completes late for the higher-pressure case, compared with those of the lower-pressure case. Additionally, the total volatile yield is low for the higher-pressure case. High pressure restricts volatile escape resulting in lower overall volatile yield and slows the overall devolatilization process, as well. However, in the lower-pressure case, the higher flue gas velocity from the larger flue gas volume (under identical air and fuel mass flow rates) pushes the start and the completion of the devolatilization later in the reactor. Table 43 summarizes the results with LOI values. The 1 atm case resulted in a much higher LOI value due to low residence time in the reactor. While the 10 atm case, even with more char yield, resulted in complete burnout. As there is significant difference in residence time between these two cases, it is difficult to reach a clear conclusion on pressure effects on char burnout. However, the devolatilization behavior estimated by our modeling approach shows good agreement with observations.

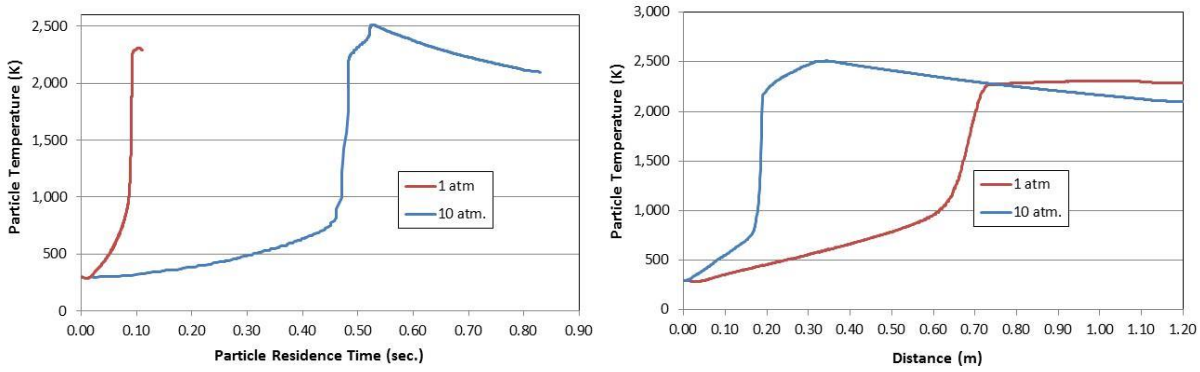

Figure 191: Particle temperature as a function of particle residence time and distance.

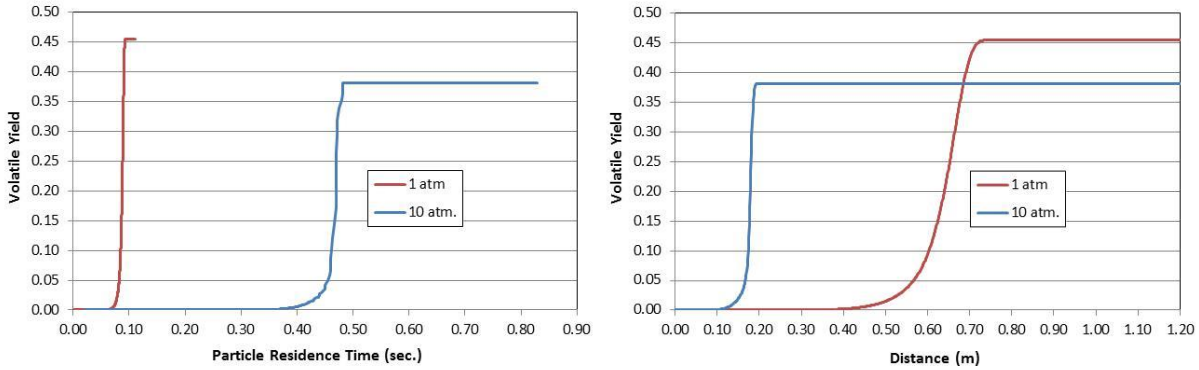

Figure 192: Volatile yields as a function of particle residence time and distance.

Table 43: Simulation results for 1 and 10 atm cases.

Pressure (atm)	Total Particle Residence Time (s)	Residence Time to Complete Devolatilization (s)	Volatile Yield	LOI
1	0.11	0.09	0.45	67%
10	0.83	0.48	0.38	0

Residence times are mass weight averages of all particle trajectories.

In addition, an extension of the CPD model developed by Shurtz et al[22]., which includes pressure effects on coal swelling, has been implemented into *GLACIER*. The swelling ratio d/d_o (d is particle diameter and d_o is initial particle diameter) is commonly used to describe char structure in combustion modeling. The primary swelling ratio correlation was developed for a high heating rate such as that in a pc combustion condition (above ~ 8500 K/s, denoted by subscript "HHR"):

$$\left(\frac{d}{d_o}\right)_{HHR} = s_{var}\, s_P \left(\frac{\dot{T}_{base}}{\dot{T}}\right)^{c_{HR}} + s_{min} \qquad \textbf{16}$$

$$s_{min} = (FC + Ash)^{1/3} \qquad \textbf{17}$$

$$s_P = 1.0 + \{38.89\,(\sigma + 1) - 167.10\}\,\frac{(\log P)^{7.77}}{P^{3.47}} \quad when\ (\sigma + 1) \geq 4.297 \qquad \textbf{18}$$

$$s_P = 1.0 \quad when\ (\sigma + 1) < 4.297\ or\ P \leq 1.0 \qquad \textbf{19}$$

where P is the absolute pressure in atmospheres, FC is the ASTM fixed carbon on a dry basis, and ash is the ASTM ash fraction on a dry basis. The parameter s_{min} represents the theoretical lower limit of swelling at infinitely high heating rates, assuming the apparent particle density is constant and the trends in the volatile yield with coal rank are well-represented by the ASTM volatiles. The pressure factor, s_P is applied when the pressure is higher than 1 atm. and $(\sigma + 1) \geq 4.297$. The parameter s_{var} can be determined from experimental data at an arbitrary standard heating rate (denoted by the subscript "base"), where the heating rate ratio reduces to unity and the coefficient in swelling correlation related to heating rate, c_{HR} can be ignored. A heating rate of 5.8 x 104 K/s was selected to correspond with the average of the heating rates calculated for the Sandia combustion data[23], which had a range from 5.3 x 104 to 6.1 x 104 K/s. Shurtz et al. have developed a correlation for s_{var} and c_{HR} (Table 44) based on the chemical structure parameters that can be obtained from C NMR data used in the CPD model: (a) the average molecular weight per side chain (M_δ) and (b) the total attachments per cluster ($\sigma + 1$).

Table 44: Correlations for s_{var} and c_{HR} with the chemical structure parameter $(\sigma + 1)/M_\delta$

Correlation	Range of applicability
$s_{var} = 1.69\,\frac{\sigma+1}{M_\delta} - 0.0309$	$0.018 \leq \frac{\sigma+1}{M_\delta} \leq 0.207$
$s_{var} = -3.37\,\frac{\sigma+1}{M_\delta} + 1.01$	$0.207 \leq \frac{\sigma+1}{M_\delta} \leq 0.301$
$s_{var} = 0$	$\frac{\sigma+1}{M_\delta} < 0.018\ or\ \frac{\sigma+1}{M_\delta} > 0.301$
$c_{HR} = -191\left(\frac{\sigma+1}{M_\delta}\right)^2 + 68.9\left(\frac{\sigma+1}{M_\delta}\right) - 5.16$	$0.106 < \frac{\sigma+1}{M_\delta} < 0.254$
$c_{HR} = 0$	$\frac{\sigma+1}{M_\delta} < 0.106\ or\ \frac{\sigma+1}{M_\delta} > 0.254$

In addition to the high heating rate correlation, a low heating rate (LHR) correlation for particle heating rates less than 8500 K/s has also been integrated into *GLACIER* according to the manner described by Shurtz[24]. The swelling correlation for low heating rates is a piecewise linear interpolation to approximate Illinois #6 data. Figure 193 provides a visual interpretation of the correlation. The heating rate range is split into two divisions, one from 1 K/s to 1000 K/s and the second from 1000 K/s to the peak at 8500 K/s. Swelling at 1 K/s is assumed to be identical to HHR swelling at 3.37E+04 K/s and swelling at 1000 K/s is assumed to be identical to the HHR swelling at 1.63E+04 K/s. The LHR correlation for each of the two ranges is described by

$$\left(\frac{d}{d_0}\right)_{LHR} = m\,log_{10}(\dot{T}) + b \qquad \textbf{20}$$

where $\dot{T}$ is the LHR heating rate. The slope *m* and intercept *b* are calculated for each of the two LHR ranges by matching HHR swelling at 1.63E+04 K/s and 3.37E+04 K/s. Although the

correlation is developed for Illinois #6 at 1 atmosphere pressure, it is assumed to be a reasonable general approximation. In industrial applications, heating rates are generally in the HHR range.

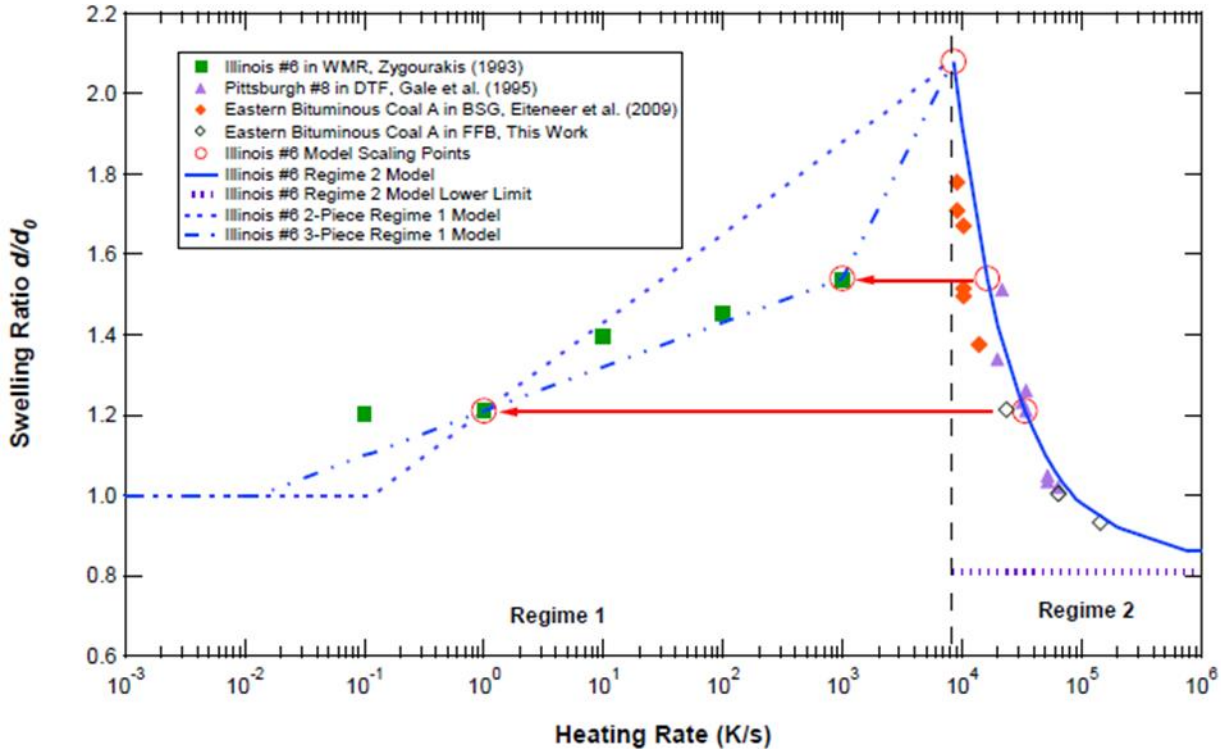

Figure 193. Visual interpretation of the LHR piecewise linear interpolation correlation.

The swelling model is implemented into *GLACIER* in an iterative manner. Along each particle trajectory, the maximum particle heating rate encountered during the devolatilization process is used to calculate a swelling ratio, and the swelling ratio calculated at the end of a particle iteration is used during the following particle iteration. This process is repeated until convergence is reached. The particle is assumed to swell linearly with devolatilization; the maximum diameter is reached at the end of devolatilization.

A high or elevated temperature and/or a high-pressure environment can push the char reaction to a diffusion-controlled regime according to the scaling law discussed in the research from DOE Cooperative Agreement No: DE-FE0025168. However, the scaling law can indicate only relative behavior and the actual reaction regime can be decided by the mixed reaction modes. Therefore, an extended single film char oxidation mechanism developed previously under oxy-firing conditions[25] was used in this development.

Figure 194 shows modeled coal particle swelling and data vs. particle heating rate at 1 atmosphere pressure as reported by Shurtz. Figure 195 shows current model swelling vs. heating rate at 1 and 10 atmospheres pressure. At 1 atmosphere, the current model agrees very well with Shurtz's plot. At 10 atmospheres, the model predicts a large increase in swelling

over that of 1 atmosphere. Zeng[26] notes a report indicating swelling increases of 3 – 30 times at 8 atmospheres pressure over that at 1 atmosphere pressure for Illinois #6 coal, so a large increase in particle swelling at 10 atmospheres appears to be reasonable.

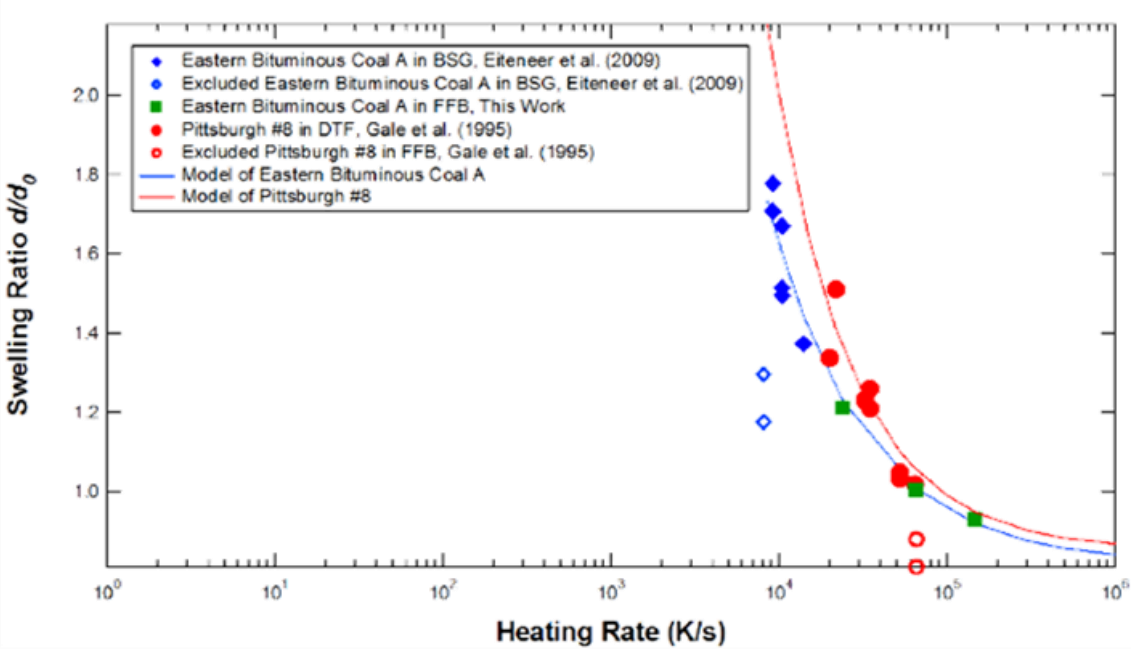

Figure 194. Bituminous coal swelling ratio vs. heating rate. Comparison of data and Shurtz's model at 1 atmosphere pressure (Shurtz, 2011).

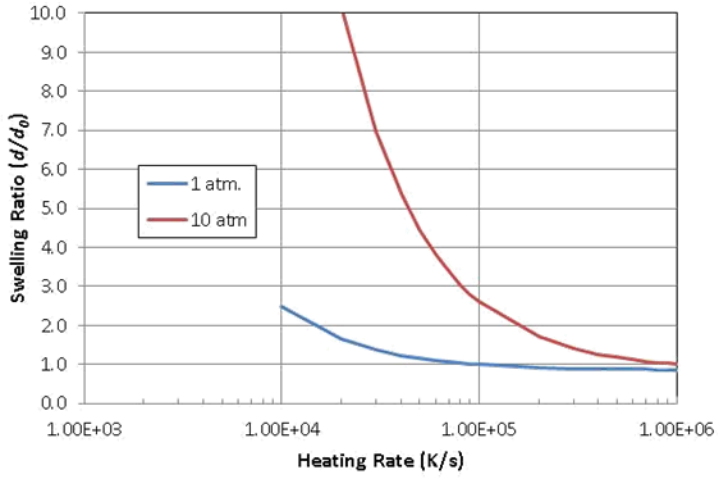

Figure 195. *GLACIER* model Pittsburgh #8 swelling at 1 and 10 atmospheres pressure.

Particle swelling vs. residence time for the four particle diameters included in the model is plotted in Figure 196. At 1 atmosphere, the swelling ratio for all particles is ~ 2.5. The swelling occurs over a time span of approximately 15 ms during devolatilization. At 10 atmospheres, the

swelling occurs over a somewhat shorter time of ~10 ms, also during the devolatilization process. Swelling is also larger at 10 atmospheres and more dependent on initial particle size, varying from 2.8 for initial 75 µm particles to 4.6 for initial 105 µm particles. At 1 atmosphere, particle residence time in the reactor is shorter due to the lower gas density and resulting higher gas velocity. Residence time is longer for larger particles due to the greater particle response time to the effect of gas heating and increasing gas velocity in the combustion zone.

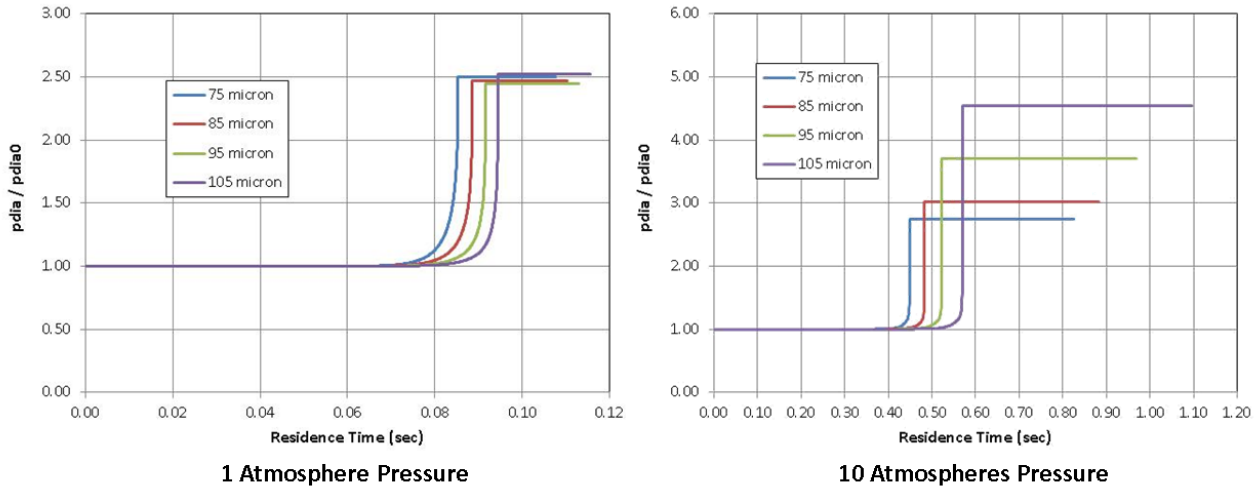

Figure 196. Swelling ratio as a function of particle diameter vs. residence time at 1 and 10 atmospheres pressure.

Model particle swelling vs. heating rate as a function of initial particle diameter is shown in Figure 197. At 1 atmosphere pressure, the particle heating rate falls in the LHR region, very near the peak, and all sizes are clustered. At 10 atmospheres pressure, heating rates fall in the very steep slope section of the HHR region. In this section, relatively small changes in heating rate will have a large impact on swelling.

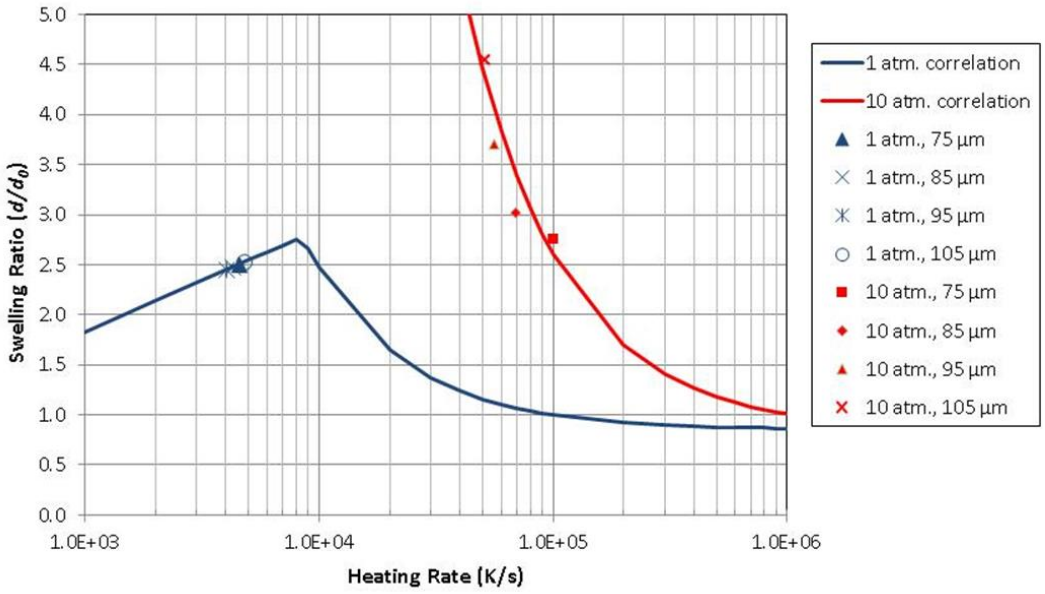

Figure 197. Model particle swelling vs. heating rate as a function of initial particle diameter.

The results reported above are compared with the updated model results in Table 45. The previous results were obtained with a constant swelling factor of 1.1, a typical value used in industrial furnace models where heating rates are high. In the drop tube, however, the calculated heating rates are not as high, and the swelling model predicts significantly larger swelling ratios. The larger swelling in the updated model is associated with higher volatile yield at both pressures and higher burnout at 1 atmosphere pressure. This underscores the importance of the swelling model, especially at high pressure where swelling is increased.

Table 45. Comparison of Previous and Current Case Results

Pressure (atm)	Previous Results, Swelling = 1.1		Current Results, Swelling Model	
	Volatile Yield	LOI	Volatile Yield	LOI
1	0.45	67%	0.56	0%
10	0.38	0%	0.44	0%

Figure 198 shows particle burnout vs. residence time for each initial particle size. Initial burnout occurs with devolatilization, followed by char oxidation with some overlap between the two processes. Distinction between the two processes is evident in the 1 atmosphere plot of Figure 198 where the slope of the burnout curve decreases. Devolatilization occurs very quickly while char oxidation is somewhat slower. In addition, a flat flame burner (FFB) model described by Zeng where data also suggests incomplete burnout is in process. Since data indicates unburned fuel at the actual volatile yield, it can be expected that the greater char fraction at low volatile yield should produce some unburned carbon.

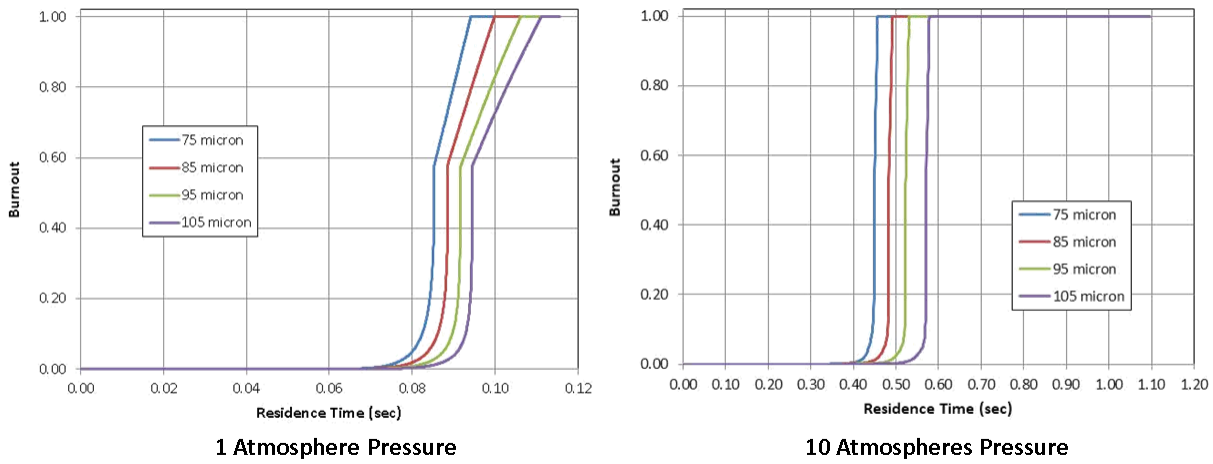

Figure 198. Burnout vs. residence time for each particle size.

Task 6 Summary and Conclusions

High pressure char combustion data produced in prior DOE-funded work were investigated to validate the two-step correlation for devolatilization that accommodates pressure effects on volatile yields and resulting char structure that currently exists in REI's CFD modeling tools. Model-predicted coal burnout levels were compared against experimental data and interrogated to ensure the model is appropriate for dry-fed coal combustion at high pressures.

The work in this program focused on *high pressure* oxy-combustion processes since the pressure effect on coal devolatilization and char reaction should be properly addressed in modeling. Our approach entailed integration of the CPD model to predict pressure effects on coal devolatilization and the subsequent char reaction based on the extended single film model.

The implemented modeling approach evaluates CPD-calculated volatile yield, while the existing two-step volatile release model is applied. At the end of each particle iteration, the high temperature volatile yield constant is adjusted so that the overall two-step volatile yield match that predicted by CPD. This process is repeated iteratively until CFD model predictions match the CPD-calculated volatile yield.

A data set from SRI's Long Residence Time Radiant Coal Flow Reactor (LRT-RCFR) was used for model validation under 2 pressure conditions, 1 atm and 10 atm. Particle heat-up is slow at higher pressure due to slower release of volatiles, but the peak particle temperature occurs earlier in terms of distance due to the relatively lower velocity. Devolatilization begins and completes late for the higher-pressure case, compared with the lower-pressure case. Additionally, the total volatile yield is low for the higher-pressure case. High pressure restricts volatile escape resulting in lower overall volatile yield and slows the overall devolatilization process, as well. In the lower-pressure case, the higher flue gas velocity from the larger flue gas volume pushes the start and the completion of the devolatilization later in the reactor.

The 1 atm case resulted in a much higher LOI value due to low residence time in the reactor. While the 10 atm case, even with more char yield, resulted in complete burnout. As there is

significant difference in residence time between these two cases, it is difficult to reach a clear conclusion on pressure effects on char burnout. However, the devolatilization behavior estimated by our modeling approach shows good agreement with observations.

An extension of the CPD model, which includes pressure effects on coal swelling, has been implemented into REI's CFD Model. Model results indicate larger swelling associated with higher volatile yield at both pressures and higher burnout at 1 atmosphere pressure, which underscores the importance of incorporating a swelling model, especially at high pressure where swelling is increased.

Summary: Overall Results and Conclusions

The execution of the project resulted in the successful completion of the proposed tasks and milestones as described in the preceding report. This report documents: the collection of key data from oxy-coal combustion testing under multiple pressures using unique equipment tailored for this application; the development and validation of mechanistic descriptions of relevant oxy-coal combustion physics and chemistry for integration into a CFD modeling framework; application of advanced modeling tools for burner design and performance evaluation at laboratory scale. More specifically key results and conclusions of the individual project tasks include the following:

Task 2 Design, construction and shakedown of a dry feeding system: Project partner Southeast University developed a design for a pulverized coal dry feed system based on design specifications from the University of Utah. Although SEU had demonstrated controlled feed of coal powder under pressurized conditions for gasification applications using a similar design, this would be the first time that this design would be used for oxy-coal combustion. The design centered on a cone-shaped pressure vessel approximately 5 feet high and 2 feet diameter. The vessel serves both as the fuel hopper and as an integral part of the feed system. Three pressurized gas lines carrying CO_2 are used to pneumatically convey the pulverized fuel and balance the pressure around the system. REI and the University of Utah carried out both physical model and CFD-based assessments to gain an understanding of behavior of coal particles in the fluidization zone and within the hopper overall. Prior to combustion tests in the UofU entrained flow pressurized reactor (EFPR), non-reacting or "cold" tests were conducted in order to obtain operational experience with coal transport using the pressurized system. A relationship between pressure drop between the coal hopper and the reactor, and coal flow rate was developed from the cold tests. Over the course of many experiments attempting to stabilize a coal flow rate appropriate for the combustor, it became clear that a system pressure drop of 4 psi would produce the target coal flow rate near 60 lb/h (approximately 200 kW firing rate with the Utah bituminous coal. Although the target coal feed could be achieved with this dP, it was observed that maintaining such a low dP corresponded to unstable coal transport. Instability and unpredictable coal flows would conflict with achieving the stated objectives for pressurized oxy-coal experiments. As it became apparent that the problems encountered with unstable coal flow at the University of Utah facility would not be solved under the program's time and budget constraints, REI invoked its risk management strategy and sought alternatives for performing pressurized oxy-coal experiments. This resulted in a collaboration between REI and Brigham Young University who had developed a pressurized dry coal feed system of their own in a separate DOE-funded project.

Task 3 Pressurized Reactor Preparation: Prior to operation of the BYU Pressurized Oxy-Coal Combustor (POC) for this program, there were many maintenance and upgrade activities that were required. Portions of the reactor were disassembled or removed for cleaning. During the last phase of testing for a preceding DOE program, it was determined that the coal feed rate was most impacted by the pressure differential between the pressurized fluidized bed feeder and the POC. This pressure differential proved to be difficult to maintain within the desired threshold when the operating pressure of the POC was not steady. To rectify this problem, the

PID control on reactor pressure was tuned using the throttling valve. This proved to be a critical fix for operating at steady fuel feed rates.

Modifications to the furnace and ancillary equipment were necessary to install the REI corrosion/deposition probe on the POC. The plumbing on the CO_2 delivery system was reconfigured to provide a CO_2 stream for probe cooling with its own pressure regulator for the probe. The CO_2 exhaust was plumbed from the probe into the reactor ventilation system, which included safety measures to ensure any breach of flue gas through sensor elements would be properly contained. Additional maintenance on the reactor and feed system was performed to prepare the system for pressurized oxy-coal experiments.

Task 4 Design, Installation, and Shakedown of EFPR Burner: Burner design concepts for dry pulverized coal-fed pressurized combustion were initiated with a survey of the literature on firing systems for pressurized combustors. Commercial experience with dry feed burner concepts for high pressure combustion of pulverized coal is limited, but REI applied its experience with atmospheric pressure commercial dry feed systems and with high pressure gasifiers to develop burner design concepts. Conceptual designs were focused on producing stable flames and a heat flux profile suitable for the tolerances of the combustion equipment. The impact of burner design features (including fuel/oxidant mixing related to velocities and velocity differentials) on behaviors including recirculation patterns and flame locations/shapes heat release profiles, flame stability, flame temperatures, peak burner and wall temperatures was evaluated. A CFD modeling approach was developed to evaluate the impact of specific design features. For example, the impact of a burner register layout with pure O_2 in the center and fuel introduced through a concentric annular opening was determined to release too much heat close to burner, while the utilization of lower velocity inlets from larger pipe diameters resulted in delayed heat release and high heat fluxes in a relatively small volume near the midpoint of the furnace's axial length. A specific burner configuration/operation was identified for further testing. In the final design that was fabricated for testing, the fuel is transported through a center pipe encircled by a stream of pure O_2, followed by an outer annulus of an O_2/CO_2 mixture. When firing with natural gas, air is routed through the center tube and the outer annulus; and natural gas is routed through the inner annulus. This arrangement provides cooling of the two inner tubes that do not come in contact with the burner's water jacket. The design and geometry of the burner was chosen specifically to accommodate both modes of operation and improved the efficiency in switching between reactor idle during standby mode and pressurized oxy-coal combustion experiments.

Task 5 Pressurized Testing with Minimal CO_2 for Coal Transport: The dry feed system designed by SEU and assembled at the University of Utah was connected to a pressurized candle filter assembly for tests on the functionality of the system to deliver steady and reliable flow rates at values appropriate for the EFPR in high pressure oxy-combustion experiments. During these "cold" tests of coal transport, a stable flow rate was achieved for brief time intervals, but consistent flow for a suitable length of time proved to be unattainable.

REI engaged BYU who were developing a dry feed system for a pressurized oxy-coal combustion facility and had seen reasonable success in achieving consistent coal flow rates. A plan was

established to run experiments in the BYU POC that included REI's real-time corrosion monitoring probe and the UofU ash aerosol sampling system. The BYU facility came equipped with instrumentation providing temperature, heat flux, radiation intensity, gas and particle temperature, and flue gas properties. Using these capabilities, a test campaign was completed that provided a unique data set that will serve as an excellent resource for validation of models involving turbulent mixing, radiant heat transfer, coal particle combustion, CO chemistry, corrosion, mineral matter transformation and deposition and other important aspects of coal combustion that might arise in the development of pressurized oxy-coal firing for power generation.

Task 6 – Model Extension and Validation: High pressure char combustion data produced in prior DOE-funded work were investigated to validate the two-step correlation for devolatilization that accommodates pressure effects on volatile yields and resulting char structure that currently exists in REI's CFD modeling tools. Model-predicted coal burnout levels were compared against experimental data and interrogated to ensure the model is appropriate for dry-fed coal combustion at high pressures.

The mechanism is based on the Chemical Percolation Devolatilization model integrated with a pressure dependent swelling model. The approach provides refined predictions of volatile yield, coal swelling, and resultant char structure and morphology as a function of pressure. The pressure effect on coal devolatilization and char reaction should be properly addressed in modeling. The implemented modeling approach evaluates CPD-calculated volatile yield, while the existing two-step volatile release model is applied. Data under 2 pressure conditions were used as a basis of comparison with the model. The devolatilization behavior estimated by the modeling approach showed good agreement with observations. An extension of the CPD model, which includes pressure effects on coal swelling, was implemented into REI's CFD Model. Model results indicate larger swelling associated with higher volatile yield at both pressures and higher burnout at 1 atmosphere pressure, which underscores the importance of incorporating a swelling model, especially at high pressure where swelling is increased.

PRODUCTS

Publications, conference papers and presentations

Davis, K., Chiodo, A. *Characterizing Impacts of Dry Coal Feeding in High Pressure Oxy-Coal Combustion Systems*. Poster presentation at 2017 NETL CO_2 Capture Technology Project Review Meeting, Pittsburgh, PA, August 25, 2017

Davis, K., Chiodo, A., Whitty, K., & Wendt, J. *Characterizing Impacts of Dry Coal Feeding in High Pressure Oxy-Coal Combustion Systems*. 2018 NETL CO_2 Capture Technology Project Review Meeting, Pittsburgh, PA, August 14, 2018

Dobo, Z., Backman, M., Whitty, K., "Pilot-Scale Oxy-Coal Combustion at Elevated Temperatures and Pressures – Demonstration and Flame Radiation Measurements," Poster presentation at the *4th MÉB Combustion Conference of the Hungarian Section of the Combustion Institute*, 10 November 2018, Miskolc, Hungary (2018).

Chiodo, A., Davis, K., Li, X., Wang, Y., Wendt, J. *Sub-Micron Ash Aerosol Formation in Oxy-Coal Combustion at Atmospheric and Elevated Pressures*. 44th International Technical Conference on Clean Energy in Clearwater, FL

Chiodo, A., Davis, K. *Design, Construction, and Assessment of Dry Coal Feeding in a High Pressure Oxy-coal System*. 44th International Technical Conference on Clean Energy in Clearwater, FL

Chiodo, A., Davis, K., Li, X., Wang, Y., Wendt, J. *Sub-Micron Ash Aerosol Formation in Oxy-Coal Combustion at Atmospheric and Elevated Pressures*. 2019 International Pittsburgh Coal Conference in Pittsburgh PA

Davis, K., Chiodo, A., Whitty, K., & Wendt, J. *Characterizing Impacts of Dry Coal Feeding in High Pressure Oxy-Coal Combustion Systems*. DOE-NETL'S 2020 FE R&D Project Review Meeting – Transformative Power Generation, Held virtually, September 28, 2020

Li, X., Wang, Y., Wendt, J. *Characteristics of the sub-micron ash aerosol generated during oxy-coal combustion at atmospheric and elevated pressures*. Proceedings of the Combustion Institute Volume 38, Issue 3, 2021, Pages 4063-4071

Davis, K., Chiodo, A., Whitty, K., Li, X., Wang, Y., Wendt, J. *Characterizing Impacts of Dry Coal Feeding in High Pressure Oxy-Coal Combustion Systems*. 2021 DOE/FE Spring R&D Project Review Meeting, Held virtually, May 11, 2020

Website(s) or other Internet site(s)

Characterizing Impacts of Dry Coal Feeding in High Pressure Oxy-Coal Combustion Systems: https://www.netl.doe.gov/projects/project-information.aspx?p=FE0029162

Technologies or techniques
Nothing to report.

Inventions, patent applications, and/or licenses
Nothing to report

Other Products
Nothing to report.

REFERENCES

1. Davis, K. A. & Chiodo, A. P. *Characterizing Impacts of High Temperatures and Pressures in Oxy-Coal Combustion Systems*. (2018).

2. Tuia, J. Correlation Pressure, Transport Gas Velocities, and Solids Mass Flowrates in High Pressure Fluidized Bed Coal Feed Systems. (Brigham Young University, 2019).

3. Perry, R., Green, D., & Maloney, J. *Perry's chemical engineers' handbook. McGraw-Hill*. (McGraw-Hill, 1999).

4. Krarnes, J., Büttner, H. & Ebert, F. Submicron particle generation by evaporation of water droplets. *J. Aerosol Sci.* **22**, S15–S18 (1991).

5. Wu, H., Bryant, G. & Wall, T. The effect of pressure on ash formation during pulverized coal combustion. *Fuel Energy Abstr.* **43**, 43 (2002).

6. Wang, X. *et al.* Characterization of organic and black carbon aerosol formation during coal combustion: An experimental study in a 1 MW pilot scale coal combustor. *Fuel* **180**, 653–658 (2016).

7. Liu, H., Wang, Y. & Wendt, J. O. L. Particle Size Distributions of Fly Ash Arising from Vaporized Components of Coal Combustion: A Comparison of Theory and Experiment. *Energy & Fuels* **32**, 4300–4307 (2018).

8. Petela, R. Prediction of the product size in the agglomeration of coal particles in a water-oil emulsion. *Fuel* **70**, 509–517 (1991).

9. Kijo–Kleczkowska, A. Combustion of coal–water suspensions. *Fuel* **90**, 865–877 (2011).

10. Mojtahedi, W. & Backman, R. *The fate of sodium and potassium in the pressurized fluidized-bed combustion and gasification of peat*. *J. Inst. Energy* **62**, (1989).

11. Friedlander, S. K. *Smoke, Dust, and Haze: Fundamentals of Aerosol Dynamics*. (Oxford University Press, USA, 2000).

12. Brockmann, J. E., McMurry, P. H. & Liu, B. Y. H. On Simultaneous Coagulation and Diffusional Loss of Free Molecule Aerosols in Turbulent Pipe Flow. *Aerosol Sci. Technol.* **1**, 163–178 (1982).

13. Wang, Y., Li, X. & O. L. Wendt, J. On Ash Deposition Rates from Air and Oxy-Combustion of Pulverized Coal, Petroleum Coke, and Biomass. *Energy & Fuels* **33**, 5849–5858 (2019).

14. Li, X., Wang, Y. & Wendt, J. O. L. Characteristics of the sub-micron ash aerosol generated during oxy-coal combustion at atmospheric and elevated pressures. in *Proceedings of the Combustion Institute* **38**, (2021).

15. Wu, H., Bryant, G., Benfell, K. & Wall, T. An Experimental Study on the Effect of System Pressure on Char Structure of an Australian Bituminous Coal. *Energy & Fuels* (2000).

doi:10.1021/ef990066j

16. Wall, T. F. *et al.* The effects of pressure on coal reactions during pulverised coal combustion and gasification. *Prog. Energy Combust. Sci.* **28**, 405–433 (2002).

17. Wu, H. Ash formation during pulverised coal combustion and gasification at pressure. (University of Newcastle, 2000).

18. Orsino, S. *High Pressure Coal Combustion Kinetics Project*. (2005).

19. Fletcher, T. H., Kerstein, A. R., Pugmire, R. J. & Grant, D. M. Chemical percolation model for devolatilization. 2. Temperature and heating rate effects on product yields. *Energy & Fuels* **4**, 54–60 (1990).

20. Ubhayakar, S. K., Stickler, D. B., Von Rosenberg, C. W. & Gannon, R. E. Rapid devolatilization of pulverized coal in hot combustion gases. *Symp. Combust.* **16**, 427–436 (1977).

21. Kobayashi, H., Howard, J. B. & Sarofim, A. F. Coal devolatilization at high temperatures. *Symp. Combust.* **16**, 411–425 (1977).

22. Shurtz, R. C., Kolste, K. K. & Fletcher, T. H. Coal Swelling Model for High Heating Rate Pyrolysis Applications. *Energy & Fuels* **25**, 2163–2173 (2011).

23. Fletcher, T. H. & Hardesty, D. R. *Compilation of Sandia coal devolatilization data: Milestone report. Milestone report*. (1992).

24. Shurtz, R. C. Effects of Pressure on the Properties of Coal Char Under Gasification Conditions at High Initial Heating Rates. (Brigham Young University, 2011).

25. Geier, M., Shaddix, C. R., Davis, K. A. & Shim, H.-S. On the use of single-film models to describe the oxy-fuel combustion of pulverized coal char. *Appl. Energy* **93**, 675–679 (2012).

26. Zeng, D. Effects of Pressure on Coal Pyrolysis at High Heating Rates and Char Combustion. (Brigham Young University, 2005).